Semiconductors, Vol. 34, No. 4, 2000, pp. 371–375. Translated from Fizika i Tekhnika Poluprovodnikov, Vol. 34, No. 4, 2000, pp. 385–388.

ATOMIC STRUCTURE AND NONELECTRONIC PROPERTIES OF SEMICONDUCTORS

Thermodynamics of Complex Formation and Defect Clustering in Semiconductors

S. V. Bulyarskiĭ, V. V. Svetukhin, and P. E. L'vov

Ul'yanovsk State University, Ul'yanovsk, 432700 Russia

Submitted December 25, 1998; accepted for publication September 22, 1999

Abstract—Characteristics of complex defects in semiconductors are calculated by the method of minimizing the free energy for the actual crystal. The influence of the electron subsystem on the impurity solubility is considered. The modeling of solidus curves is carried out in terms of binary association and clustering. © *2000 MAIK "Nauka/Interperiodica".*

INTRODUCTION

Point defects and their associations strongly affect the electrical properties of semiconductors [1, 2].

In most publications, the method of quasi-chemical reactions, which follows from the mass action law, is used to calculate the concentration of point defects. However, in order to apply this method, it is necessary to analyze a large number of reactions and to calculate the corresponding number of equilibrium constants. In some cases, the final result can depend on the selection of the initial set of equations [3]. In addition, the search for numerical values of equilibrium constants is rather intricate, and the result is ambiguous.

In studying the equilibrium systems, it is preferable to use the method of minimization of the Gibbs free energy. This approach was developed in [4, 5]. However, the possibility of degeneracy of the electron subsystem as well as the probability of cluster formation was not taken into account in these works. We were able to obviate these weaknesses in the framework of the model proposed below.

1. FREE ENERGY OF THE CRYSTALLIZING SOLUTION

Let us consider a melt of several substances, at a temperature below the melting point of one of the components. The precipitation of crystals of a certain composition should proceed in this solution.

We can conveniently use the terminology proposed in [4, 5] for calculation of the Gibbs free energy for this system. We will consider every lattice site or interstice as the site, and the site type will be indicated by the superscript. The particle type (the interstitial or substitutional defects, vacancies, etc.) shall be denoted by the subscript. We denote the total number of sites in the sublattice β by N^β. Let $N^\beta_{\alpha q}$ be the total number of particles of the type α at the β site in the charge state q, with q running through all values for this defect with its own sign (we consider that the elementary charge is equal to unity). We denote the total number of sites for the crystal by $N = \sum_\beta N^\beta$.

The formation of different complexes or clusters of defects is possible in the bulk of crystals. We shall denote the type of complexes or clusters by the subscript k, and their number, by N_k. No restrictions will be imposed on the cluster (complex) size and composition, since it is not necessary to distinguish between clusters and complexes of defects in terms of thermodynamics. We shall consider the number of simple defects of the $\binom{\beta}{\alpha q}$ type in the cluster of k type as equal to $m^\beta_{\alpha q k}$.

2. FREE ENERGY OF THE SYSTEM

Let us represent the Gibbs free energy of the system in the form

$$G = G_S(N^\alpha_{\beta q}, N_k) + G_L(N_{\alpha L}) + G_e, \qquad (1)$$

where G_S is the energy of the crystal with defects, G_L is the energy of the melt, and G_e is the energy of free electrons and holes; in this case, the α, β, and q indices run through all possible values.

We now express the free energy G_S by analogy with [5]. However, we will take into account the

1063-7826/00/3404-0371$20.00

formation of clusters:

$$G_S = \sum_{\alpha\beta q} N^{\beta}_{\alpha q} g^{\beta}_{\alpha q} + \sum_k N_k \left(g_k + \sum_{\alpha\beta q} g^{\beta}_{\alpha q} m^{\beta}_{\alpha q k} \right) - kT \ln \left[\prod_{\beta\alpha q} \frac{N^{\beta}! (r^{\beta}_{\alpha q})^{N^{\beta}_{\alpha q}}}{N^{\beta}_{\alpha q}! \prod_k N_k! \left(\prod_{\gamma\delta s} m^{\delta}_{\gamma s k}! \right)^{N_k}} \prod_k P_k^{N_k} \right]. \quad (2)$$

Here, $g^{\beta}_{\alpha q} = g^{\beta}_{\alpha} + \varepsilon^{\beta}_{\alpha q}$ is the energy of the defect $\binom{\beta}{\alpha q}$, where g^{β}_{α} is the energy of formation of the neutral defect and $\varepsilon^{\beta}_{\alpha q}$ is the energy of ionization; and P_k is the probability of formation of the type k cluster anywhere in the crystal.

When calculating the configurational entropy, we considered that the sites and particles of the same type are identical, including the position of the latter inside the clusters. Permutation of particles and sites does not necessarily bring about the formation of clusters. For this reason, the probabilities P_k appear in expression (2). Let us consider $m^{\beta}_{\alpha q k}$ particles, which are located in the volume V^{β}. The probability of these particles entering the volume v^{β} equals

$$P^{\beta}_{\alpha q k} = \left(\frac{v^{\beta}}{V^{\beta}} \right)^{m^{\beta}_{\alpha q k}} \left(1 - \frac{v^{\beta}}{V^{\beta}} \right)^{N^{\beta}_{\alpha} - m^{\beta}_{\alpha q k}}.$$

Taking into account that $v^{\beta} = \sum_{\gamma q} m^{\beta}_{\gamma q k} v^{\beta}_0$ and $V^{\beta} = N^{\beta} v^{\beta}_0$, the probability of cluster formation can be represented as

$$P_k = N \prod_{\alpha q \beta} P^{\beta}_{\alpha q k} = N \prod_{\alpha q \beta} \left(\frac{\sum_{\gamma s} m^{\beta}_{\gamma s k}}{N^{\beta}} \right)^{m^{\beta}_{\alpha q k}} \times \left(1 - \frac{\sum_{\gamma s} m^{\beta}_{\gamma s k}}{N^{\beta}} \right)^{\sum_{\alpha} N^{\beta}_{\alpha} - m^{\beta}_{\alpha q k}}, \quad (3)$$

where N^{β}_{α} is the total number of defects $\binom{\beta}{\alpha}$ in the crystal, and v^{β}_0 is the unit cell volume in the sublattice β. The multiplier N accounts for the possibility of formation of the cluster anywhere in the crystal.

Let us consider the energy of free electrons and holes of the crystal, which are distributed over the continuous states of the conduction and valence bands. In order to take into account the contribution of rearrangement of electrons within the bands to the thermodynamic probability, we divide the mth band into intervals $(\varepsilon^m_l, \varepsilon^m_{l+1})$, which contain $Q^m_l = Q^m(\varepsilon^m_l, \varepsilon^m_{l+1})$ electronic states. Here, once n^m_l is the total number of electrons with the energy between ε^m_l and ε^m_{l+1}, the total number of transmutations of the electrons in bands is given by

$$W_m = \prod_l \frac{Q^m_l!}{n^m_l! (Q^m_l - n^m_l)!}. \quad (4)$$

Generally speaking, it is not necessary to consider all of the bands of the crystal, since most of the processes in semiconductors occur in two bands, namely, in the conduction and valence bands. For this reason, we shall consider the m index to run only through the values $m = \{v, c\}$, which correspond to these bands. Because of this, it make sense to pass on to the electron-hole formalism denoting the number of electrons and holes in the l subband by $n_l \equiv n^c_l$ and $p_l \equiv Q^v_l - n^v_l$.

Hence, G_e takes the form

$$G_e = \sum_l \varepsilon^c_l n_l + \sum_l \varepsilon^v_l p_l - kT \times \ln \left[\prod_l \frac{Q^c_l!}{n_l! (Q^c_l - n_l)!} \prod_l \frac{Q^v_l!}{p_l! (Q^v_l - p_l)!} \right]. \quad (5)$$

3. CALCULATION OF EQUILIBRIUM CONCENTRATION OF DEFECTS AND CHARGE CARRIERS

When minimizing free energy (1), the laws of conservation of the particle number of each type and the law of the charge conservation should be taken into account:

$$\varphi_{\alpha} = N_{\alpha} - \sum_{\beta q} N^{\beta}_{\alpha q} - \sum_{\beta q k} N_k m^{\beta}_{\alpha q k} - N_{\alpha L} = 0, \quad (6)$$

$$\varphi^e = \sum_l n_l - \sum_l p_l - \sum_{\alpha\beta q} q N^{\beta}_{\alpha q} - \sum_{k q \alpha\beta} q m^{\beta}_{\alpha q k} N_k = 0. \quad (7)$$

In addition, the coupling equation for a total number of lattice sites should be taken into account:

$$\varphi^{\beta} = N^{\beta} - \sum_{\alpha q} N^{\beta}_{\alpha q} - \sum_{\alpha q k} m^{\beta}_{\alpha q k} N_k = 0. \quad (8)$$

We shall derive the minimum of free energy by the method of Lagrangian undetermined multipliers. For this purpose, we use the functional

$$\Phi = G + \sum_{\alpha} \lambda_{\alpha}\varphi_{\alpha} + \sum_{\beta} \lambda^{\beta}\varphi^{\beta} + \lambda^{e}\varphi^{e}. \quad (9)$$

Using the conventional procedure, we can derive a number of relationships.

(i) Differentiation of the functional Φ with respect to n_l leads to the expression for the number of electrons in the subband l:

$$n_l = \frac{Q^c(\varepsilon_l, \varepsilon_l + \Delta\varepsilon_l)}{1 + \exp\left[\dfrac{\varepsilon_l - \lambda^e}{kT}\right]}. \quad (10)$$

Since the initial division of the band into intervals is arbitrary and $\Delta\varepsilon_l$ is as small as desired, the following expansion is valid:

$$Q^c(\varepsilon, \varepsilon + \Delta\varepsilon_l) = Q^c(\varepsilon_l, \varepsilon_l) + \left(\frac{dQ^c(\varepsilon)}{d\varepsilon}\right)_{\varepsilon = \varepsilon_l} \Delta\varepsilon_l. \quad (11)$$

It is obvious that $Q^c(\varepsilon_l, \varepsilon_l) = 0$. In this case, the total number of electrons in the band is given by

$$n = \sum_{l} \frac{\left(\dfrac{dQ^{\varepsilon}(\varepsilon_l, x)}{d\varepsilon}\right)_{\varepsilon = \varepsilon_l} \Delta\varepsilon_l}{1 + \exp\left[\dfrac{\varepsilon_l + \lambda^e}{kT}\right]}. \quad (12)$$

The derivative in the numerator represents the density of states, which we denote by $N_c(\varepsilon_l)$. By tending $\Delta\varepsilon_l$ to zero and passing from the sum to the integral, we derive

$$n = \int_{\varepsilon^c_{\min}}^{\varepsilon^c_{\max}} \frac{N_c(\varepsilon)d\varepsilon}{1 + \exp\left[\dfrac{\varepsilon_l + \lambda^e}{kT}\right]}. \quad (13)$$

We now clarify the physical meaning of the Lagrangian multiplier λ^e. To this end, we express the free energy in the form $G = \Phi - \sum_{\alpha}\lambda_{\alpha}\varphi_{\alpha} - \lambda^e\varphi^e$. In this case,

$$\varepsilon_F \equiv \frac{\partial G}{\partial n} = -\lambda^e. \quad (14)$$

Thus, λ^e coincides with the Fermi level, to within a sign.

Since the Fermi level is located within the forbidden band at high temperatures and for moderate doping levels, we may assume that the upper limit of the conduction band $\varepsilon^c_{\max}$ is equal to infinity (similarly to $\varepsilon^v_{\min}$ of the valence band). If the energy of electrons and holes is measured from the bottom of the conduction band, as is usually done, $\varepsilon^c_{\min}$ becomes equal to zero and $\varepsilon^v_{\max}$ becomes equal to the bandgap taken with the opposite sign.

Let us suppose that the density of states in the bands is proportional to the square root of the energy. In this case, the concentrations of electrons and holes are expressed in terms of the Fermi integrals:

$$n = N_c(T)\Phi_{1/2}\left(\frac{\varepsilon_F}{kT}\right), \qquad p = N_v(T)\Phi_{1/2}\left(\frac{-E_g - \varepsilon_F}{kT}\right). \quad (15)$$

(ii) Differentiating the functional Φ with respect to $N_{\alpha L}$, we derive the equation

$$\lambda_{\alpha} - \left(\frac{\partial G_L}{\partial N_{\alpha L}}\right)_T = 0. \quad (16)$$

According to the definition of the chemical potential, we find that $\lambda_{\alpha} = \mu_{\alpha L}$. The chemical potential can be expressed in terms of the activity in the known manner; thus, for λ_{α}, we have

$$\lambda_{\alpha} = \mu^0_{\alpha L} + kT\ln a_{\alpha L}. \quad (17)$$

(iii) In view of (17), the number of elementary defects $\begin{pmatrix}\beta\\ \alpha q\end{pmatrix}$ is defined by the dependence

$$N^{\beta}_{\alpha q} = r^{\beta}_{\alpha q} a_{\beta L} \exp\left[\frac{-(g^{\beta}_{\alpha} + \varepsilon^{\beta}_{\alpha}) + \mu^0_{\alpha L} + \lambda^{\beta} - q\varepsilon_F}{kT}\right]. \quad (18)$$

From (18), it follows that the total number of particles $\begin{pmatrix}\beta\\ \beta\end{pmatrix}$ is given by

$$N^{\beta}_{\beta} = a_{\beta L}\exp\left(\frac{-g^{\beta}_{\beta} + \mu^0_{\beta L} + \lambda^{\beta}}{kT}\right). \quad (19)$$

Expressing λ^{β} from this equation, we arrive at the dependence

$$N^{\beta}_{\alpha q} = N^{\beta}_{\beta} r^{\beta}_{\alpha q} \frac{a_{\alpha L}}{a_{\beta L}} \times \exp\left[\frac{-(g^{\beta}_{\alpha} + \varepsilon^{\beta}_{\alpha q}) + \mu^0_{\alpha L} + g^{\beta}_{\beta} - \mu^0_{\beta L} - q\varepsilon_F}{kT}\right], \quad (20)$$

$$N^{\beta}_{\alpha} = \sum_{q} N^{\beta}_{\alpha q} = N^{\beta}_{\beta}\frac{a_{\alpha L}}{a_{\beta L}}\exp\left[\frac{-g^{\beta}_{\alpha} + \mu^0_{\alpha L} + g^{\beta}_{\beta} - \mu^0_{\beta L}}{kT}\right] \times \sum_{q} r^{\beta}_{\alpha q}\exp\left[\frac{-\varepsilon^{\beta}_{\alpha q} - q\varepsilon_F}{kT}\right]. \quad (21)$$

The Fermi level ε_F in (20) is calculated from charge conservation law (7) and depends on temperature.

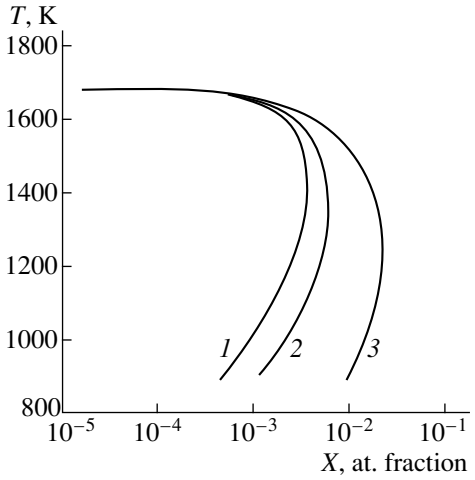

Fig. 1. The solidus curves plotted for the parameter of the binary association g_2 = (*1*) 0 (clustering is absent), (*2*) –0.42, and (*3*) –0.62 eV.

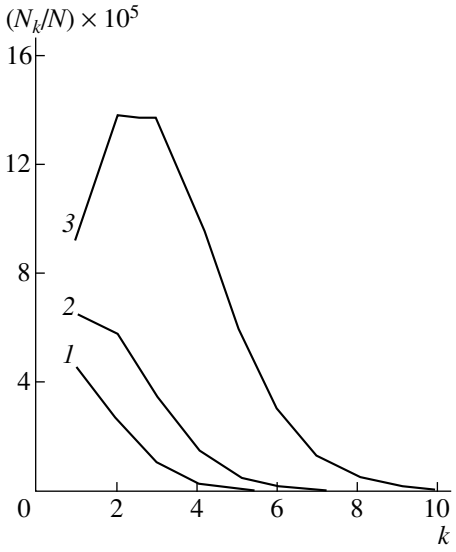

Fig. 2. Size distribution for clusters at temperatures of T = (*1*) 1154 (X = 0.00024), (*2*) 1198 (X = 0.00068), and (*3*) 1207 (X = 0.00181) K. Corresponding impurity concentrations are parenthesized.

Let us find the distribution of defects over the charge states. The probability that the defect $\binom{\beta}{\alpha}$ has the charge state q is given by

$$f^{\beta}_{\alpha q} = \frac{N^{\beta}_{\alpha q}}{\sum\limits_{s} N^{\beta}_{\alpha s}} = \frac{1}{1 + \sum\limits_{s \neq q} \frac{r^{\beta}_{\alpha s}}{r^{\beta}_{\alpha q}} \exp\left[\frac{\varepsilon^{\beta}_{\alpha s} - \varepsilon^{\beta}_{\alpha q} + \varepsilon_F (s-q)}{kT}\right]}. \quad (22)$$

Hence, the distribution of defects $\binom{\beta}{\alpha}$ is given by the function, which converts to the Fermi distribution in the case of two charge states.

(iv) We find the number of clusters of the kth type from the formula

$$N_k = N \prod_{\alpha\beta q} \left(\frac{a_{\alpha L}}{a_{\beta L}}\right)^{m^{\beta}_{\alpha q k}} \frac{1}{m^{\beta}_{\alpha q k}!} \times \left(\frac{\sum\limits_{\gamma s} m^{\beta}_{\gamma s k}}{N^{\beta}}\right)^{m^{\beta}_{\alpha q k}} \exp\left(-N^{\beta}_{\alpha} \frac{\sum\limits_{\gamma s} m^{\beta}_{\gamma s k}}{N^{\beta}}\right) \times \exp\left[\frac{-m^{\beta}_{\alpha q k}(g^{\beta}_{\alpha q} - g^{\beta}_{\beta} - \mu^{0}_{\alpha L} + \mu^{0}_{\beta L} + q\varepsilon_F) - g_k}{kT}\right]. \quad (23)$$

Here, we used the first remarkable limit in formula (3) assuming that $N^{\beta}_{\alpha} \gg m^{\beta}_{\alpha k}$. Formula (23) is consistent with the mass action law:

$$N_k = N \exp\left[\frac{-g_k}{kT}\right] \times \prod_{\alpha\beta} \frac{1}{m^{\beta}_{\alpha q k}!} \left(\frac{\sum\limits_{\gamma} m^{\beta}_{\gamma q k}}{N^{\beta}}\right)^{m^{\beta}_{\alpha q k}} (N^{\beta}_{\alpha q})^{m^{\beta}_{\alpha q k}}. \quad (24)$$

Here, the exponential function involving $N^{\beta}_{\alpha}/N^{\beta}$ is ignored, since $N^{\beta}_{\alpha} \ll N^{\beta}$.

Let us consider the effect of clustering on dissolution of the impurity in a semiconductor crystal. For simplicity, we ignore the ionization of impurity.

Simulation of dissolution of the impurity in terms of the formation of binary complexes yielded the solidus curves, which are shown in Fig. 1 (the impurity concentration is given in atomic fractions). The computations were carried out using formulas (20), (23), and (24). Solidus curves were calculated for various values of the complex-formation energy; in this case, the ultimate solubility increased with increasing energy of association.

The problem of the association of defects whose number in a cluster is arbitrary is more complex. The computations can also be performed using formula (23). When considering the cluster formation, we assume that the cluster energy depends linearly on the particle number in the cluster; i.e.,

$$g_i = -g_0(i-1), \quad (25)$$

where the free energy of a single atom in the cluster g_0 is expressed in terms of an enthalpy h_0 and entropy s_0 as $g_0 = h_0 - s_0T$.

The distribution functions of the cluster size for various temperatures at $h_0 = 0.87$ eV and $s_0 = -1.7 \times 10^{-3}$ eV/K are shown in Fig. 2. As can be seen from Fig. 2, the cluster number increases compared to the monomer number with an increase in temperature.

REFERENCES

1. V. I. Fistul', *Physics and Chemistry of Semiconductors* (Metalurgiya, Moscow, 1995).
2. V. M. Glazov and V. S. Zemskov, *Physicochemical Principles of Semiconductor Doping* (Nauka, Moscow, 1967; Israel Program for Scientific Translations, Jerusalem, 1968).
3. S. V. Bulyarovskiĭ and V. I. Fistul', *Thermodynamics and Kinematics of Interacting Defects in Semiconductors* (Nauka, Moscow, 1997).
4. C. V. Bulyarskiĭ and V. P. Oleinikow, Phys. Status Solidi B **141**, K7 (1987).
5. C. V. Bulyarskiĭ and V. P. Oleinikow, Phys. Status Solidi B **146**, 439 (1988).

Translated by N. Korovin

Semiconductors, Vol. 34, No. 4, 2000, pp. 376–380. Translated from Fizika i Tekhnika Poluprovodnikov, Vol. 34, No. 4, 2000, pp. 389–393.

ATOMIC STRUCTURE AND NONELECTRONIC PROPERTIES OF SEMICONDUCTORS

Highly Efficient *n*-$(Bi, Sb)_2Te_3$ Thermoelectric Materials for Temperatures Below 200 K

V. A. Kutasov, L. N. Luk'yanova, and P. P. Konstantinov

Ioffe Physicotechnical Institute, Russian Academy of Sciences, Politekhnicheskaya ul. 26, St. Petersburg, 194021 Russia

Submitted November 3, 1999; accepted for publication November 9, 1999

Abstract—The possibility of using an *n*-type $Bi_{2-x}Sb_xTe_3$ solid solution in thermoelectric refrigerators at $T <$ 200 K is considered. It is shown that, if the material under consideration is optimized for the above temperature region, the temperature dependence of the Seebeck coefficient α becomes less pronounced, and the crystal-lattice thermal conductivity κ_L decreases as compared to what is observed in a conventional *n*-$Bi_2Te_{3-y}Se_y$ solid solution. These factors and a high mobility of charge carriers μ_0 bring about an increase in the parameter $\beta \sim ZT$, where Z is the thermoelectric efficiency. © *2000 MAIK "Nauka/Interperiodica".*

$Bi_2Te_{3-y}Se_y$ ($0 < y \le 0.3$) *n*-type solid solutions, which are widely used at temperatures close to room temperature, are conventionally employed at lower temperatures ($T < 200$ K) as well. For the region of low temperatures, the optimal concentration of charge carriers is provided by introducing an excess concentration of Te [1–3]. This method of doping makes it possible to eliminate additional scattering of carriers, which arises at low temperatures if metal chalcogenides are introduced. A further decrease in the scattering of charge carriers is possible in an *n*-$Bi_{2-x}Sb_xTe_3$ ($0 < x <$ 0.5) system, because Sb atoms are close in size to Bi atoms and, thus, introduce minimal variations in the crystal-lattice parameters in Bi_2Te_3-based quasi-binary alloys [4]. The use of more complex alloys with the simultaneous replacement of atoms in anionic (Te) and cationic (Bi) sublattices of Bi_2Te_3 [1, 5] made it possible to obtain the *n*-type materials that efficiently performed at room temperature. In [2], it was shown that, in the temperature range of 150 K $< T <$ 180 K, the thermoelectric efficiency Z in an *n*-$Bi_{2-y}Sb_yTe_3$ ($y =$ 0.7–0.8) solid solution was higher than Z in the conventionally used *n*-$Bi_2Te_{3-y}Se_y$ ($y = 0.3$) compound. Thus, a system of *n*-$Bi_{2-x}Sb_xTe_3$ solid solutions is of interest not only at room but also at lower temperatures.

In this work, we studied the thermoelectric properties of a system of *n*-$Bi_{2-x}Sb_xTe_3$ ($x \le 0.4$) solid solutions, with the samples obtained by planar crystallization (vertical zone equalization). Temperature dependences of the Seebeck coefficient α, electrical conductivity σ, and thermal conductivity κ were measured in the temperature range of 80–300 K for the $Bi_{2-x}Sb_xTe_3$ samples enriched in Te or doped with TeI_4 donor impurity [1].

In $Bi_{2-x}Sb_xTe_3$ solid solutions enriched in Te with charge-carrier concentrations optimized for $T < 200$ K, the power parameter $\alpha^2\sigma$ is larger than that in $Bi_2Te_{3-y}Se_y$ (see Fig. 1, curves *1*, *2*, *6*). Such a dependence $\alpha^2\sigma = f(T)$ is accounted for by a higher electrical conductivity σ (and, consequently, higher mobility) in the region of low temperatures in $Bi_{2-x}Sb_xTe_3$ solid solutions as compared to those in $Bi_2Te_{3-y}Se_y$ (Fig. 2, curves *1*, *6*).

In the case of an increase in the charge-carrier concentration n and the doping with TeI_4, the quantity $\alpha^2\sigma$ decreases owing to an increase in the number of scattering centers and an additional scattering by iodine atoms (Fig. 1, curves *3*–*5*).

In a $Bi_{2-x}Sb_xTe_3$ solid solution, the temperature dependence of the Seebeck coefficient (see table) became less pronounced as x increased from 0.2 to 0.4 (Fig. 2, curves *7*, *8*). The slope $s_1 = d\ln\alpha/d\ln T$

Slopes of temperature dependences $s_1 = d\ln\alpha/d\ln T$, $|s_2| = d\ln(m/m_0)^{3/2}\ \mu_0/d\ln T$, $|s_3| = d\ln\mu_0/d\ln T$, $|s_4| = d\ln\kappa_L/\ d\ln T$, and $|s_5| = d\ln\beta/d\ln T$ in $Bi_{2-x}Sb_xTe_3$ and $Bi_2Te_{3-y}Se_y$ solid solutions for the temperature region of $ds < 200$ K

x	n, 10^{19} cm^{-3}	s_1	s_2	s_3	s_4	s_5
$Bi_{2-x}Sb_xTe_3 + Te$						
0.2	0.86	0.75	1.71	1.86	0.84	1.53
	0.83	0.77	1.99	1.87	0.92	1.42
0.4	0.84	0.57	1.49	1.54	0.74	1.49
$Bi_{2-x}Sb_xTe_3 + TeI_4$						
0.2	0.76	0.69	1.45	1.51	0.81	1.72
0.4	0.83	0.5	1.64	1.21	0.8	1.66
$Bi_{2-x}Sb_xTe_3 + Te$						
0.3	0.35	0.54	1.71	1.45	0.74	1.53

1063-7826/00/3404-0376$20.00 © 2000 MAIK "Nauka/Interperiodica"

decreases with an increase in x in the solid solution; this is true for the samples that either contain an excess of Te or are doped with TeI_4. However, in a sample doped with TeI_4, a low value of electrical conductivity (Fig. 2, curve *4*) brings about a decrease in the parameter $\alpha^2\sigma$. Thus, the form of the dependence $\alpha^2\sigma(T)$ in a $Bi_{2-x}Sb_xTe_3$ solid solution is indicative of the possibility of increasing the product ZT, which defines the efficiency of a thermogenerator or the cooling efficiency of a thermoelectric refrigerator. Therefore, it is of considerable interest to analyze in detail the parameter

$$ZT \approx \beta = \frac{2(2\pi)^{3/2}}{h^3 e} k_0^{7/2} \left(\frac{m}{m_0}\right)^{3/2} \mu_0 T^{5/2} \kappa_L^{-1}, \qquad (1)$$

where m, μ_0, and κ_L are the density-of-state effective mass, the mobility with allowance made for degeneracy, and the thermal conductivity of the crystal lattice, respectively.

The parameter β was analyzed for isotropic scattering of charge carriers, in which case the energy dependence of the relaxation time is described by a power function; i.e., we have

$$\tau = \tau_0 E^{r_{\text{eff}}}, \qquad (2)$$

where τ_0 is a factor independent of energy and r_{eff} is the effective scattering parameter accounting for special features of scattering in solid solutions as compared to the pure acoustic mechanism of scattering [6, 7].

The product $(m/m_0)^{3/2}\mu_0$ (Fig. 3) appearing in (1) was determined from the data on α and σ with allowance made for r_{eff} using the method reported in [8, 9] in accordance with expressions for the concentration and mobility of charge carriers as applicable to semiconductors with extrinsic conduction.

In a $Bi_{2-x}Sb_xTe_3$ solid solution with an excess of Te, the product $(m/m_0)^{3/2}\mu_0$ is larger than that in $Bi_2Te_{3-y}Se_y$ for close values of the slopes $|s_2|$ in the samples with optimal charge-carrier concentrations for $T < 200$ K (Fig. 3, curves *1*, *2*, *6*). As the content of the second component in a $Bi_{2-x}Sb_xTe_3$ solid solution increases, the quantity $(m/m_0)^{3/2}\mu_0$ decreases (Fig. 3, curves *1*, *2*, *4*, *5*). Doping with TeI_4 brings about a decrease in $(m/m_0)^{3/2}\mu_0$ as a result of a decrease in the mobility (Fig. 3, curves *4*, *5*).

The mobility μ_0 with allowance made for degeneracy and the averaged density-of-state effective mass m/m_0 were calculated from the product $(m/m_0)^{3/2}\mu_0$ in accordance with [8]. In order to determine the charge-carrier concentration, we used the concentration dependence of the Seebeck coefficient $\alpha = f(n)$ derived from the data on galvanomagnetic coefficients measured in a low magnetic field in $Bi_2Te_{3-y}Se_y$ solid solutions [9]. The calculated concentrations of charge carriers in the samples of the solid solution optimized for $T < 200$ K were equal to $\sim 0.8 \times 10^{19}$ cm^{-3} and exceeded those in

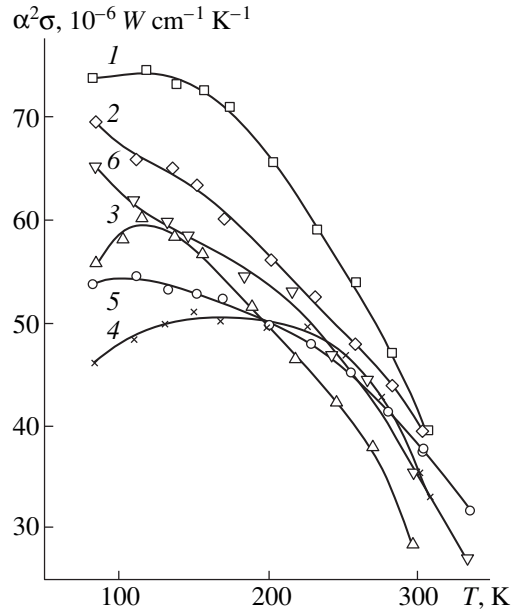

Fig. 1. Temperature dependence of the power parameter $\alpha^2\sigma$ in (*1–5*) $Bi_{2-x}Sb_xTe_3$ and (*6*) $Bi_2Te_{3-y}Se_y$ solid solutions for x = (*1*, *3*, *4*) 0.2 and (*2*, *5*) 0.4 and (*6*) y = 0.3. Curves *1–3* correspond to the compounds containing an excess of Te, and curves *4* and *5* correspond to the compounds doped with TeI_4.

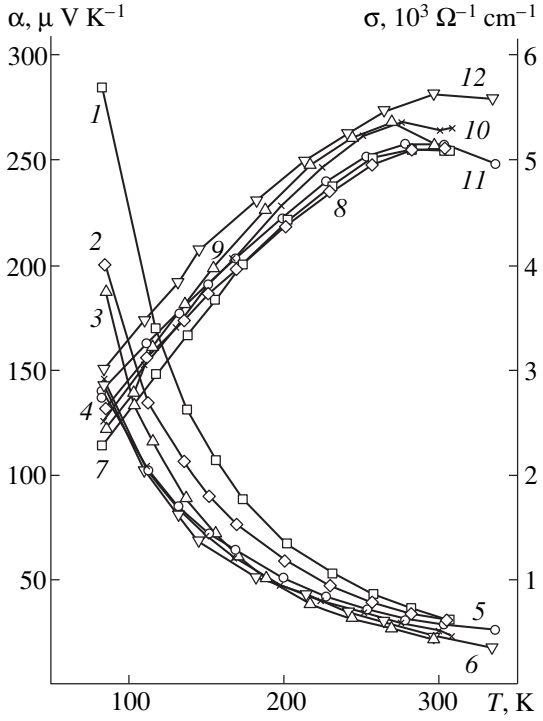

Fig. 2. Temperature dependences of (*1–6*) electrical conductivity σ and (*7–12*) Seebeck coefficient α in (*1–5*, *7–11*) $Bi_{2-x}Sb_xTe_3$ and (*6*, *12*) $Bi_2Te_{3-y}Se_y$ solid solutions. Curves *1*, *3*, *4*, *7*, *9*, and *10* correspond to x = 0.2; curves *2*, *5*, *8*, and *11* correspond to x = 0.4; curves *6* and *12* correspond to y = 0.3; curves *1–3*, *6–9*, and *12* correspond to the compounds with an excess of Te; and curves *4* and *10* correspond to the compounds doped with TeI_4.

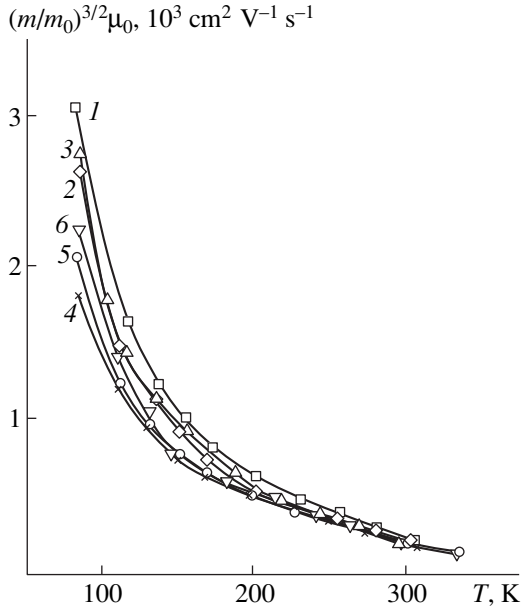

Fig. 3. Temperature dependence of the product $(m/m_0)^{3/2}\mu_0$ in (*1*–*5*) $Bi_{2-x}Sb_xTe_3$ and (*6*) $Bi_2Te_{3-y}Se_y$ solid solutions. The curves are labeled here and in the figures to follow in the same way as in Fig. 1.

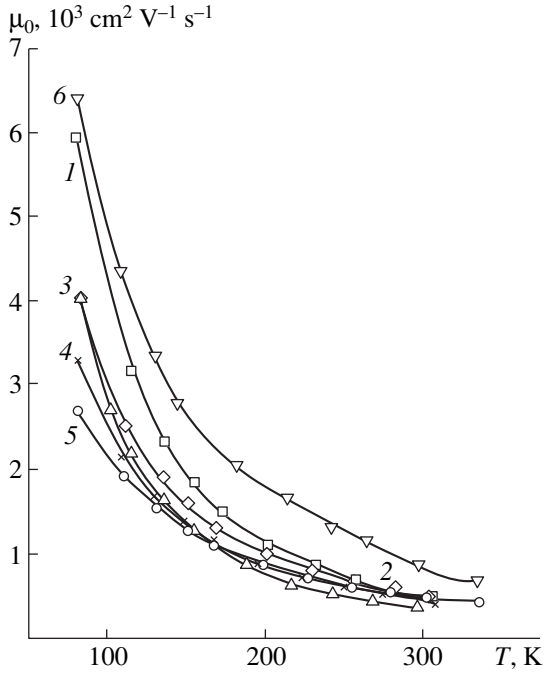

Fig. 4. Temperature dependence of mobility μ_0 with allowance made for degeneracy in (*1*–*5*) $Bi_{2-x}Sb_xTe_3$ and (*6*) $Bi_2Te_{3-y}Se_y$ solid solutions.

$Bi_2Te_{3-y}Se_y$ ($\sim 0.3 \times 10^{19}$ cm^{-3}). Despite a large difference in the charge-carrier concentrations, the charge-carrier mobilities within the range of low temperatures in the optimized samples of $Bi_{2-x}Sb_xTe_3$ and $Bi_2Te_{3-y}Se_y$ solid solutions differ insignificantly; the same is true for the corresponding slopes (see table and Fig. 4, curves *1*, *6*). It follows from a comparison of the samples with close values of the carrier concentrations ($n \approx 8 \times 10^{19}$ cm^{-3}) at $T = 80$ K that the carrier mobilities in a $Bi_{2-x}Sb_xTe_3$ are higher ($\mu_0 \approx 6000$ cm^2 V^{-1} s^{-1}) than those in $Bi_2Te_{3-y}Se_y$ ($\mu_0 \approx 4600$ cm^2 V^{-1} s^{-1}); this is a result of the fact that Sb atoms introduce lower distortions in crystal lattice in comparison with those introduced by Se atoms. As the content x of the second component and the concentration n in a solid solution decrease, μ_0 and the product $(m/m_0)^{3/2}\mu_0$ decrease owing to an enhancement of scattering of charge carriers (curves *1*, *2* and *1*, *3*). In the case of doping with TeI_4, a decrease in mobility is also observed.

In the $Bi_{2-x}Sb_xTe_3$ ($x = 0.2$) sample with high charge-carrier mobility μ_0, the effective mass m/m_0 depends very slightly on T in the region of low temperatures (Fig. 5, curve *1*). For $x = 0.4$, an increase in the effective mass m/m_0 is observed, as in the case of $Bi_2Te_{3-y}Se_y$ (curves *2*, *6*). An increase in m/m_0 at low temperatures in a $Bi_{2-x}Sb_xTe_3$ solid solution for lower charge-carrier concentrations than in the case of $Bi_2Te_{3-y}Se_y$ can be explained by the temperature dependence of the ratio of the components of the effective-mass tensor m/m_0 in $Bi_{2-x}Sb_xTe_{3-y}Se_y$ in accordance with [10]. The small value of m/m_0 in a $Bi_2Te_{3-y}Se_y$ solid solution, as well as a high mobility μ_0, is related to a low concentration of charge carriers as compared to the case of $Bi_{2-x}Sb_xTe_3$. As the charge-carrier concentration increases, m/m_0 increases too (Fig. 5, curve *3*), which brings about an increase in the product $(m/m_0)^{3/2}\mu_0$. In the $Bi_{2-x}Sb_xTe_3$ ($x = 0.4$) sample doped with TeI_4 (Fig. 5), m/m_0 also increases at low temperatures; however, in this case, low mobility does not make it possible to attain large values of $(m/m_0)^{3/2}\mu_0$.

The data on thermal conductivity κ were used to calculate the crystal-lattice thermal conductivity κ_L (Fig. 6). In determination of the electronic thermal conductivity κ_e, the Lorentz number L was calculated for r_{eff} as

$$L = \left(\frac{k}{e}\right)^2 \left[\frac{(r+7/2)F_{r+5/2}(\eta)}{(r+3/2)F_{r+1/2}(\eta)} - \frac{(r+5/2)^2 F^2_{r+3/2}(\eta)}{(r+3/2)^2 F^2_{r+1/2}(\eta)}\right], \quad (3)$$

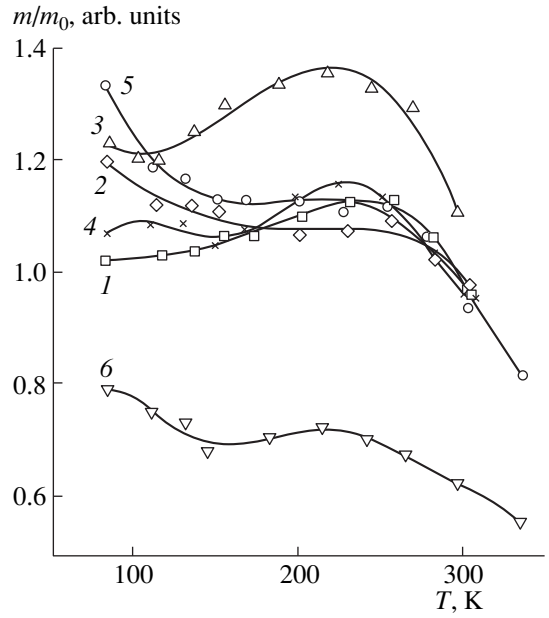

Fig. 5. Temperature dependence of the density-of-state effective mass m/m_0 in (*1–5*) $Bi_{2-x}Sb_xTe_3$ and (*6*) $Bi_2Te_{3-y}Se_y$ solid solutions.

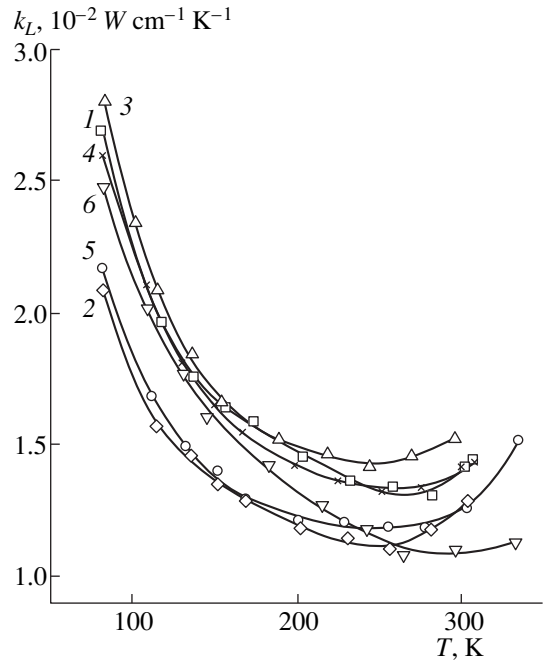

Fig. 6. Temperature dependence of the crystal-lattice thermal conductivity κ_L in (*1–5*) $Bi_{2-x}Sb_xTe_3$ and (*6*) $Bi_2Te_{3-y}Se_y$ solid solutions.

where $F_r(\eta)$ is the Fermi integral having the form of

$$F_r(\eta) = \int_0^\infty [x^r / e^{x-\eta}]dx. \quad (4)$$

The use of r_{eff} in calculations of the Lorentz number L makes it possible to take into account the possible ambipolar diffusion of charge carriers in the temperature range of $T > 250$ K by relying on the temperature dependence $r_{\text{eff}} = f(T)$ [6, 7].

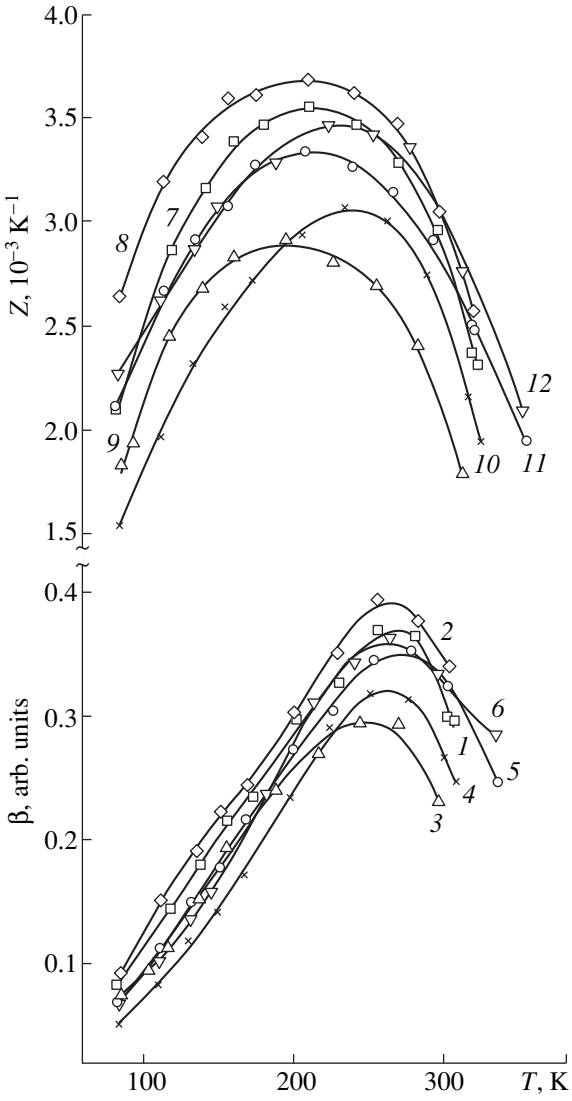

Fig. 7. Temperature dependence of (*1–6*) the parameter β and (*7–12*) the thermoelectric efficiency Z in (*1–5* and *7–11*) $Bi_{2-x}Sb_xTe_3$ and (*6, 12*) $Bi_2Te_{3-y}Se_y$ solid solutions with (*1, 3, 4, 7, 9,* and *10*) $x = 0.2$; (*2, 5, 8,* and *11*) $x = 0.4$, (*6, 12*) $y = 0.3$ for the compounds (*1–3, 6–9, 12*) containing an excess of Te and (*4, 10*) doped with TeI_4.

The crystal-lattice thermal conductivity κ_L in a $Bi_{2-x}Sb_xTe_3$ solid solution with an excess of Te increases with an increase in x from 0.2 to 0.4, because the phonon scattering by the atoms of the second component becomes more pronounced. The smallest values of κ_L and the slope $|s_3| = d\ln\kappa_L/d\ln T$ were observed in the $Bi_{2-x}Sb_xTe_3$ ($x = 0.4$) sample (Fig. 6, curve *2*), which ensured an increase in the parameter β calculated according to (1) (Fig. 7, curve *2*). The small value of κ_L was also observed in $Bi_{2-x}Sb_xTe_3$ ($x = 0.4$) doped with

TeI_4 (Fig. 6, curve *5*). However, a decrease in mobility and a larger slope $|s_3| = d\ln\kappa_L/d\ln T$ (see table) as compared to the sample enriched in Te bring about a decrease in the parameter β (Fig. 7, curve *5*).

An increase in the parameter $\beta \sim ZT$ for smaller slopes s_4 (see table) in $Bi_{2-x}Sb_xTe_3$ solid solutions, especially for $x = 0.4$ (Fig. 7; curves *1*, *2*), indicates that the thermoelectric efficiency of this material exceeds that of $Bi_2Te_{3-y}Se_y$. For $Bi_{2-x}Sb_xTe_3$ with $x = 0.4$, $\langle Z\rangle = 3.1 \times 10^{-3}$ K^{-1} in the range of 80 K < T < 200 K (Fig. 7, curve *8*). In a $Bi_2Te_{3-y}Se_y$ solid solution optimized for T < 200 K, the corresponding mean value $\langle Z\rangle = 2.85 \times 10^{-3}$ K^{-1} (Fig. 7, curve *12*). It is noteworthy that $Bi_{2-x}Sb_xTe_3$ solid solutions (x = 0.4) exhibit a high thermoelectric efficiency in the entire temperature range under consideration; thus, $\langle Z\rangle = 3.3 \times 10^{-3}$ K^{-1} for 200 K < T < 300 K (Fig. 7, curve *8*).

As a result of studying $Bi_{2-x}Sb_xTe_3$ ($0.2 < x < 0.4$) solid solutions containing an excess of Te, we showed that, in the range of optimal concentrations of charge carriers, these compounds are promising materials for use in thermoelectric refrigerators in the range of both 80 K < T < 200 K and 200 K < T < 300 K. An increase in the thermoelectric efficiency Z occurs owing to the attainment of high mobility μ_0, and an increase in the averaged density-of-states effective mass m/m_0 in the low-temperature region and a decrease in the thermal conductivity of crystal lattice κ_L are observed.

REFERENCES

1. M. H. Ettenberg, W. A. Jesser, and F. D. Rossi, in *Proceeding of XV International Conference on Thermoelectrics* (Pasadena, CA, USA), 1996, p. 52.
2. A. I. Anukhin, in *Proceeding of XVI International Conference on Thermoelectrics, Dresden, Germany, 1997*, p. 159.
3. V. A. Kutasov, M. V. Vedernicov, P. P. Konstantinov, *et al.*, Pis'ma Zh. Tekh. Fiz. **18**, 542 (1992) [Sov. Tech. Phys. Lett. **18**, 542 (1992)].
4. B. M. Gol'tsman, V. A. Kudinov, and I. A. Smirnov, *Semiconductor Thermoelectric Bi_2Te_3-based Materials* (Nauka, Moscow, 1972).
5. W. M. Yim and F. D. Rossi, Solid-State Electron. **15**, 1121 (1972).
6. V. A. Kutasov and L. G. Luk'yanova, Fiz. Tverd. Tela (Leningrad) **26**, 2501 (1984) [Sov. Phys. Solid State **26**, 1515 (1984)].
7. V. A. Kutasov and L. G. Luk'yanova, Fiz. Tverd. Tela (Leningrad) **28**, 899 (1986) [Sov. Phys. Solid State **28**, 502 (1986)].
8. V. A. Kutasov, L. G. Luk'yanova, and P. P. Konstantinov, Fiz. Tverd. Tela (St. Petersburg) **41**, 187 (1999) [Phys. Solid State **41**, 164 (1999)].
9. G. T. Alekseeva, P. P. Konstantinov, V. A. Kutasov, *et al.*, Fiz. Tverd. Tela (Leningrad) **33**, 3539 (1991) [Sov. Phys. Solid State **33**, 1988 (1991)].
10. V. A. Kutasov and L. G. Luk'yanova, Fiz. Tverd. Tela (Leningrad) **29**, 2966 (1987) [Sov. Phys. Solid State **29**, 1705 (1987)].

Translated by A. Spitsyn

Semiconductors, Vol. 34, No. 4, 2000, pp. 381–385. Translated from Fizika i Tekhnika Poluprovodnikov, Vol. 34, No. 4, 2000, pp. 394–398.

ATOMIC STRUCTURE AND NONELECTRONIC PROPERTIES OF SEMICONDUCTORS

Tunneling Spectroscopy of Impurity Atoms in a Single-Crystal Semiconductor Matrix

A. V. Kartavykh*, N. S. Maslova, V. I. Panov**, V. V. Rakov*, and S. V. Savinov****

** Institute of Chemical Problems of Microelectronics, Moscow, 109017 Russia*

*** Faculty of Physics, Moscow State University, Vorob'evy gory, Moscow, 119899 Russia*

Submitted June 28, 1999; accepted for publication November 16, 1999

Abstract—Impurity atoms of two of the most important classes (so-called "shallow" and "deep" impurities) have been studied by scanning tunneling microscopy/spectroscopy in a single-crystal matrix of III–V semiconductors. This was done in order to determine the potentialities of the techniques in solving analytical and technological problems of semiconductor materials science. *© 2000 MAIK "Nauka/Interperiodica".*

INTRODUCTION

Scanning tunneling microscopy/spectroscopy (STM/STS) is widely used to analyze the surface relief pattern and electronic properties of atomic-scale surface structures [1–3]. The capabilities of the method most clearly manifest themselves in studies of localized states, in particular those formed by impurity atoms or atomic defects in a crystal lattice with band electronic structure [4, 5]. Among the advantages of the technique, mention should be made of the following. The spatial resolution is high and is comparable to the size of the outermost electron shells of separate atoms; the scanning field (scanning image range) can be fairly large, up to tens of micrometers in size; and information about the local density of electronic states can be obtained by measuring the tunneling conductivity for a sample area under study. The last fact is of fundamental importance as a basis for tunneling spectroscopy, a method that makes it possible to study the spatial distribution of the energy spectra of the tunneling current over local areas of the atomic surface.

The most important, from the practical standpoint, localized states in semiconductor crystals arise at impurity atoms and atomic defects distorting the periodicity of charge density distribution. For this reason, any information about the effect of localized states related to separate impurity atoms on the electronic properties of materials is very important. Here, the key point is the influence exerted by a separate impurity atom on the material properties in devices of submicrometer and, in the near future, nanometer size, in which the impurity distribution nonuniformity can change device parameters drastically.

In this work, an attempt was made to study impurity atoms representing the two most important classes (so-called shallow and deep) in a single-crystal matrix of III–V semiconductors in order to determine the capabilities of scanning tunneling microscopy/spectroscopy in solving applied analytical and technological problems of semiconductor materials science.

1. "SHALLOW" (HYDROGEN-LIKE) Te IMPURITY IN GaAs MATRIX

Tellurium (Group VI of the periodic table of elements) is a well-known substitutional donor impurity in the arsenic sublattice. After valence bonding in the GaAs crystal lattice, a Te atom loses five electrons donated into the valence band from the initial configuration [Kr] $4d^{10}5s^25p^4$. Thus, a Te atom in a crystal is commonly regarded as a system consisting of a 5*s* electron weakly bound in the field of a positively charged [Kr] $4d^{10}$ core.

A solution of the Schrödinger equation, similar to that for a free hydrogen atom ($p^+ - 1s_e$) residing in an isotropic medium and having an electron with effective electron mass m_n^*, yields an estimate for the ionization energy of the ground state of an *s* electron

$$E_i = R(1/\vartheta^2)(m_n^*/m_e) = 6.8 \times 10^{-3}\ \text{eV}.$$

Here, R = 13.6 eV is the Rydberg constant, ϑ = 11.6 is the dielectric constant of GaAs, and $m_n^* = 0.067m_e$ is the effective electron mass in the GaAs crystal lattice [6]. The adequacy of even such a simple estimate is evidenced by the good agreement between the calculated and experimental Te ionization energies. The experimental energy ($E_x \sim 5.95$ meV) [7] corresponds to formation of a "shallow" donor level in the forbidden gap of GaAs. With allowance made for corrections to the Bohr model, the localization radius of an outer *s* electron $r \propto m_e/m_n^*$ is approximately equal to 7 nm.

Thus, a Te atom occupying an As site in the GaAs lattice is characterized by a strongly delocalized distribution of density of states related to an outer electron and having a spherical symmetry, with the electron

1063-7826/00/3404-0381$20.00

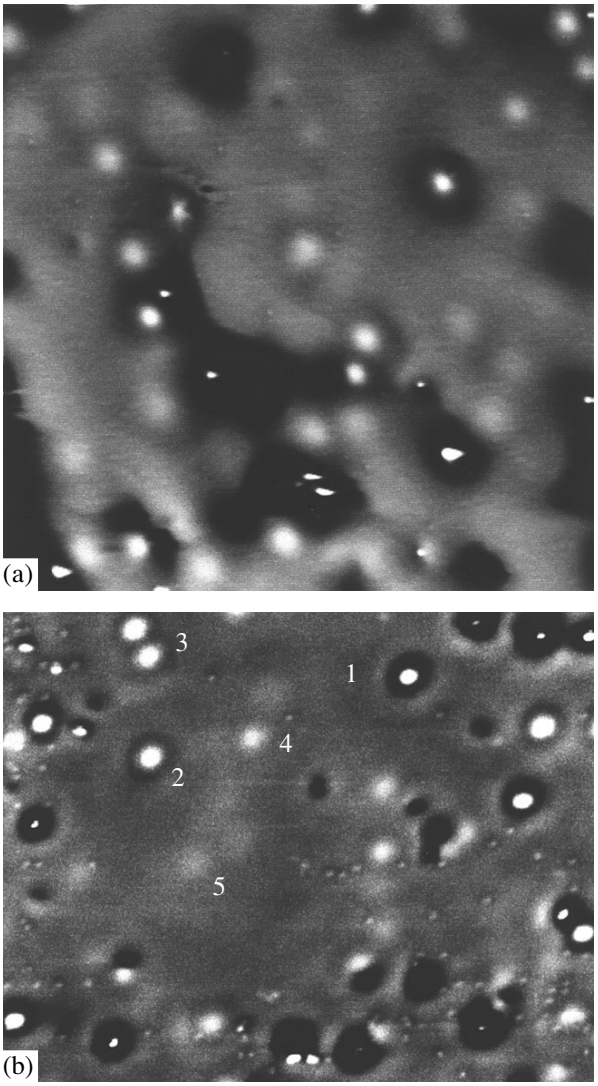

Fig. 1. STM images (taken at 4.2 K) of the (110) surface of a GaAs single crystal doped with Te to a level of 8.9×10^{17} cm^{-3}: (a) it is clearly seen that the wave functions of outer 5*s* electrons of neighboring Te atoms overlap, the image size is 80×80 nm, the tunneling voltage is –2.5 V, and the tunneling current is 10 pA; (b) illustration of the "transparency" of the single-crystal matrix for tunneling electrons, numbers 1–5 denote images of impurity atoms located at different distances from the surface under study, the image dimension is 70×50 nm, the tunneling voltage is –1 V, and the tunneling current is 40 pA.

cloud extending to 15–20 GaAs crystal-lattice constants a (a = 0.565 nm). With the spatial distribution of the impurity assumed to be chaotic, an estimate readily follows that a partial overlap of 5*s* electron states of neighboring Te atoms sets in on attaining a critical impurity concentration in the crystal equal to $\approx 4.5 \times 10^{17}$ cm^{-3}.

As the object of the study we chose a single-crystal GaAs sample with a concentration of electrically active Te equal to 8.9×10^{17} cm^{-3}, found from the Hall coefficient. Measurements were done at 4.2 K on a scanning tunneling microscope equipped with a cleaving device for *in situ* sample cleaning [8]. Upon cleavage, the scanned surface was a (110) atomically clean surface. The obtained scanning images are shown in Figs. 1a and 1b, with the STM image having the form of a two-dimensional pattern of electronic-state density distribution in the vicinity of the Fermi level, increasing from dark to light areas in the image.

Since the tunneling current is determined by the local density of electronic states, the outer 5*s* orbitals of Te atoms, possessing an additional electron with respect to host atoms, appear in scanning images as light spots. As can be seen from Fig. 1a, the charge density of neighboring Te impurity atoms does start to partly overlap at a Te concentration approximately corresponding to theoretical estimates. This confirms the assumption on a chaotic impurity distribution in the sample under study.

Figure 1b illustrates the depth resolution of the tunneling microscope for the GaAs single crystal under study. Numbers 1 to 5 denote images belonging to Te atoms introduced into, respectively, first, second, etc., atomic planes counting from the sample surface. Thus, the single-crystal matrix is "transparent" for tunneling electrons to distances comparable to four lattice constants (≈2.0–2.5 nm).

The inset in Fig. 2 shows a separate impurity atom against the background of rows of Ga and As atoms. The localization region of the outer electron of Te does have a nearly spherical symmetry. The size of this region, close to the calculated value, can be readily evaluated from the known crystal-lattice constant.

In the case of a substantial delocalization of the electron density of the defect, the spatial resolution of the tunneling microscope allowed its use in the local spectroscopy mode, which is of much interest. Figure 2 shows tunneling conductivity spectra for local regions designated as I and II in the inset. In fact, these spectra are numerically differentiated current–voltage characteristics $(dI/dV)/(I/V)$ of selected areas of the sample surface, taken at a fixed tunneling gap and stationary microscope tip over a chosen area of the surface.

The (*ab*) and (*de*) portions of the tunneling conductivity curves correspond to the excitation of collectivized electrons of the GaAs matrix from the conduction (E_c) and valence (E_v) bands, respectively. The spectra taken from regions I and II differ markedly in the (*bd*) portion corresponding to the forbidden band E_g of the semiconductor. In spectrum I (impurity-free single-crystal matrix), there is practically no current at voltages corresponding to the forbidden band. At the same time, in spectrum II corresponding to a Te atom on the surface, the tunneling current is nonzero. This is indicative of the existence of a tunneling channel in the case of excitation of an outer electron. The tunneling conductivity spectrum shows a broad peak resolved into a doublet g_1g_2 in the range from –1 to 0 V.

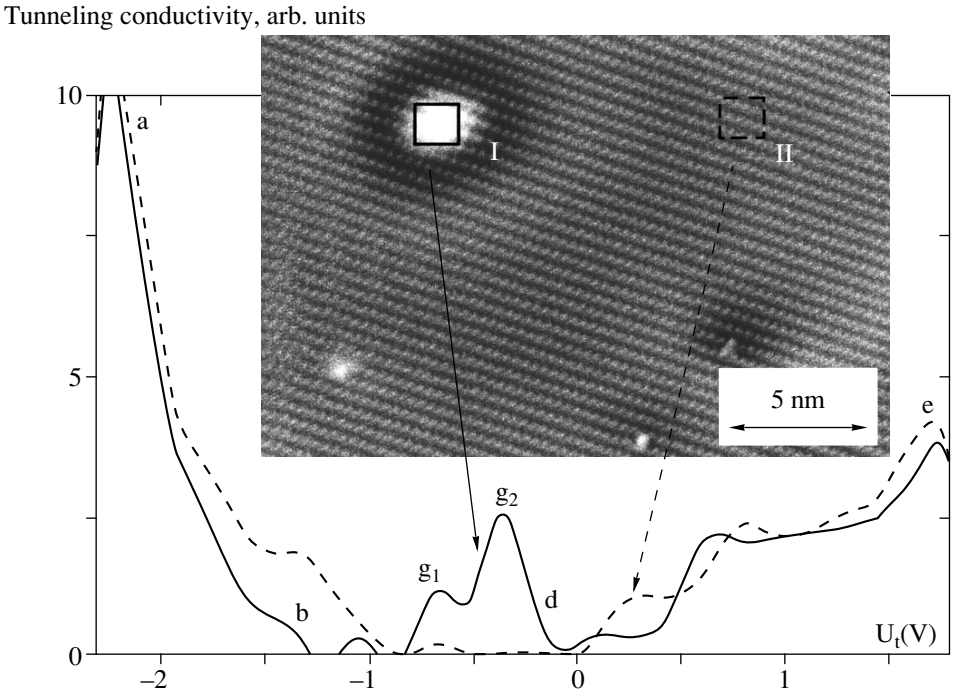

Fig. 2. Differential conductivity as a function of sample bias voltage (tunneling spectra) for local areas shown in the inset: I corresponds to the defect-free single-crystal matrix and II corresponds to the electron shell of a Te atom occupying a site in the As sublattice. The inset shows the STM image of a separate Te atom at a tunneling voltage of –1.5 V and a tunneling current of 20 pA. Image dimensions amount to 22×12 nm.

The specific shape of the tunneling-conductivity curves may be associated with the resonance mechanism of electron tunneling through the "impurity" channel (level) in the forbidden band, first described in our previous work [9]. The peak positions cannot yet be directly related to the ionization energy of the Te atom in the GaAs lattice. This fact points to the complicated physical characteristics of the phenomena occurring at the surface near the tunneling gap.

Quantitative interpretation of the "impurity" state of each atom requires consideration of corrections for the effect exerted by the Coulomb potential of the charge accumulating at the STM tip because of a finite relaxation time of nonequilibrium electrons. Such a charge affects the relative position of the impurity level in the forbidden band and its possible splitting due to distortion of the outermost electron shell of the atom.

2. CR TRANSITION METAL AS IMPURITY IN AN INAS MATRIX

Chromium is a typical transition element in the periodic table of elements. The group of transition elements (metals) is characterized by similar chemical properties due to the partial filling of outer *d* orbitals with electrons. An incomplete *d* shell can, with close probabilities, both donate electrons (down to d^0 configuration) and accept them (up to the completed shell d^{10}) in the formation of chemical bonds. Consequently, such elements have a wide range of oxidation states (valences). The complex symmetry of the *d* shell leads to strict directionality of chemical bonds formed by an atom in compounds (complexes); this symmetry is also preserved when an atom of a *d* element occupies the site in a semiconductor crystal lattice. In this case, the size of a localized state is limited, to a first approximation, by the nearest-neighbor ligands. For a Cr atom, such a quasi-molecule consists of the nearest host atoms occupying the vertices of a circumscribed octahedron (coordination number 6). Consequently, the perturbing potential includes contributions not only from the impurity atom itself but also from the surrounding lattice atoms shifted from the initial equilibrium positions (the Jahn–Teller effect). In such centers, electrons are strongly localized and, as a rule, the effective mass approximation is inapplicable.

The electronic configuration of a Cr atom is [Ar] $3d^5 4s^1$. According to the valence-bond theory, in the case when a Cr atom substitutes As in an InAs lattice site, configuration of Cr changes to [Ar] $3d^1$, which corresponds to a *d* shell electron localized in the vicinity of a closed-shell electronic–nuclear system [Ar]. According to the coordination theory, the localized state has the form of a collective electron cloud surrounding the Cr atom and representing the mixed electron density of chemical bonds of the central atom and

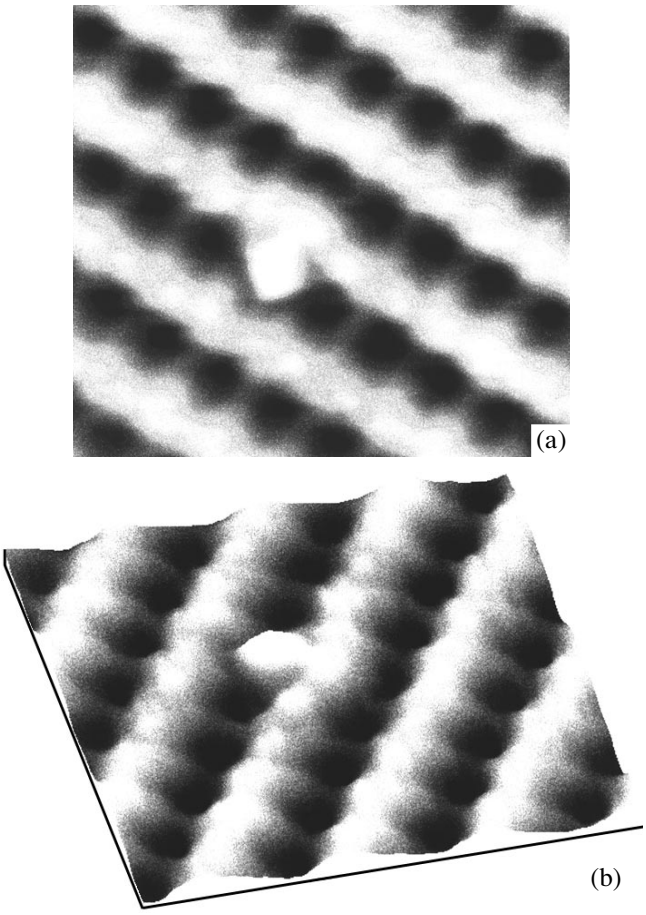

Fig. 3. (a) STM image of a localized state of a Cr impurity atom at the (110) surface of an InAs single crystal at 4.2 K and (b) the corresponding quasi-three-dimensional image. Image dimensions correspond to 2.9×2.6 nm, the tunneling voltage is –1 V, and the tunneling current is 20 pA.

its nearest neighbors. In this case, there is, on average, a single electron from the *d* shell of the impurity atom per each of the six bonds (configuration rearrangement $3d^5 4s^1 \longrightarrow 3d^6 4s^0$ followed by sp^3d^2 hybridization). The crystal-field theory accounts for a deformation of the hybrid electron cloud, which leads to energy-level splitting in the localized state. All the aforementioned approaches describe the real situation with a varied extent of approximation.

In view of the above, the Bohr model is inapplicable to describing quantum-mechanically a transition element impurity in a crystal. At present, an approximate solution to the Schrödinger equation can be obtained only numerically if the wave functions of all atoms belonging to the "molecular cluster" are accounted for. However, even this can only be done in the case of a matrix composed of atoms–ligands of the same kind [10]. Typically, such a solution corresponds to an energy level that has a localized wave function, is split off from E_c (for donor atom) or E_v (for acceptor), and lies deep in the forbidden band. In connection with this, atoms of transition elements are a particular case of deep impurities in semiconductors.

The procedure used to study the Cr impurity in the InAs matrix was similar to that in the case of Te impurity in the GaAs matrix. An atomically clean (110) surface of an InAs:Cr single crystal was scanned at 4.2 K. An STM image of a surface area is shown in Fig. 3a. For better clarity, the corresponding three-dimensional image is shown in Fig. 3b. Here, atomic rows of As possessing higher electron affinity are represented by white and the In sublattice by black color. It can be readily seen that the Cr impurity occupies the arsenic sublattice site at the surface under study. In contrast to the "shallow" Te impurity (see the inset in Fig. 2), the action of the perturbing potential introduced by the Cr atom is limited to only two lattice constants of the semiconductor matrix. A region of increased electron density is observed near the impurity atom. Most likely, this region is associated with the spatial localization of an unpaired electron at the hybrid orbital of the ruptured bond between the Cr atom and the "upper" In atom removed in sample cleavage. The elongated shape of the electron cloud demonstrates the directionality of the chemical bond, which is characteristic of a hybrid orbital involving the *d* electron state.

The characteristic size of the localized state associated with the *d* orbital can be determined from Fig. 3 to be about 0.5 nm. We note that estimating the characteristic energy of Coulomb repulsion in terms of the Hubbard model yields $U \sim e^2/a_0 \sim 0.5$–1 eV if the radius of the localized state a_0 is ~0.5 nm. In this case, the Coulomb repulsion energy is comparable to the bandgap. This leads to a strong influence of the Coulomb interaction within a site on the impurity-state energy and the spectra of tunneling conductivity near an impurity atom. Hence, one can expect a strong dependence of the STM image of impurity atoms on the applied voltage; also, the appearance of additional peaks in tunneling conductivity spectra in the vicinity of the band edges is expected. Therefore, different impurity atoms must exhibit individual features in STM images and STS spectra.

CONCLUSION

This work was devoted to the low-temperature STM/STS experimental study of localized electron states introduced by impurity atoms into semiconductor single crystals. In the first stage, the well-known impurities, Te and Cr, in GaAs and InAs crystals, respectively, were chosen as objects of study. In terms of the physics of semiconductors, Te and Cr are typical representatives of different classes of electrically active defects introducing "shallow" (Te) and "deep" (Cr) energy levels into the forbidden band of a crystal. In terms of crystal chemistry, these impurity centers differ fundamentally in the binding force of the outer electrons and, correspondingly, the size of the region in

which the perturbing potential introduced into the atomic lattice of the crystal is localized.

The obtained results demonstrate the unique properties of the STM method, which can be used to study impurity states in a crystal, with separate atoms resolved. It is shown that atoms of hydrogen-like (Te) and transition-metal (Cr) impurities, occupying the sites in the As sublattice, produce STM images with strained crystal lattice regions of different size and also with different sizes, shapes, and symmetries of the regions of localization of their outermost electron shells. Experimental estimates of these parameters agree satisfactorily with the predictions of theoretical quantum-mechanical models.

A tunneling spectrum of the localized electron state associated with a separate impurity atom was measured for the first time for Te. We believe that theoretical and experimental development of the STM method in this direction deserves particular attention. The possibility of identifying, in principle, separate impurity atoms, using the characteristics of their tunneling spectra, could serve as the basis for developing a new method of material analysis.

REFERENCES

1. G. Binning, H. Rohrer, C. Gerber, *et al.*, Phys. Rev. Lett. **50**, 120 (1983).
2. N. S. Maslova and V. I. Panov, Usp. Fiz. Nauk **157**, 185 (1989).
3. C. S. Jiang, T. Nakayama, and M. Aono, Jpn. J. Appl. Phys., Part 2 **36**, L1336 (1997).
4. R. S. Goldman, R. M. Feenstra, B. G. Briner, *et al.*, Appl. Phys. Lett. **69**, 3698 (1996).
5. C. Domke, Ph. Ebert, M. Heinrich, *et al.*, Phys. Rev. B: Condens. Matter **54**, 10288 (1996).
6. O. Madelung, *Physics of III–V Compounds* (Wiley, New York, 1964; Mir, Moscow, 1967).
7. S. S. Strel'chenko and V. V. Lebedev, *III–V Compounds: A Reference Book* (Metallurgiya, Moscow, 1984).
8. S. I. Oreshkin, V. I. Panov, S. V. Savinov, *et al.*, Instrum. Exp. Tech. **40** (4), 566 (1997).
9. A. Depuydt, N. S. Maslova, V. I. Panov, *et al.*, Appl. Phys. A **66**, S171 (1998).
10. O. Madelung, *Introduction to Solid State Theory* (Springer-Verlag, Berlin, 1978; Nauka, Moscow, 1985).

Translated by M. Tagirdzhanov

Semiconductors, Vol. 34, No. 4, 2000, pp. 386–388. Translated from Fizika i Tekhnika Poluprovodnikov, Vol. 34, No. 4, 2000, pp. 399–401.

ELECTRONIC AND OPTICAL PROPERTIES OF SEMICONDUCTORS

Saturation of Interband Absorption in Semiconductors

A. O. Melikyan and G. R. Minasyan

Armenian State Engineering University, Yerevan, 375009 Armenia

Submitted April 22, 1999; accepted for publication October 12, 1999

Abstract—The nonlinear absorption factors in a direct-gap semiconductor are calculated both for the pump and probe waves using the density matrix formalism. The key feature of the calculation is the consideration of the carrier dispersion. It is shown for the first time that the dispersion law defines the saturation behavior of the absorption factor. The intensity and frequency dependences of the absorption factors calculated differ significantly from those obtained previously. It is also shown that the conventional theory of nonlinear interband absorption based on the kinetic equations for carriers leads to the correct results only in the limit of small pump intensities. © *2000 MAIK "Nauka/Interperiodica".*

The nonlinear wave interaction in direct-gap semiconductors is currently being studied intensively in connection with four-wave mixing in optical amplifiers based on bulk semiconductors [1–16].

The saturation effect at high pump power levels plays an important role in the lowering of the efficiency of four-wave mixing in semiconductor optical amplifiers. The absorption saturation was directly observed in the experiment with the absorption of pump and probe waves in bulk InGaAsP in [1]. The multiphoton interband absorption [17], spectral hole burning [3, 4], and carrier heating are the main mechanisms of the nonlinear light absorption in semiconductors. The first mechanism is inefficient in the case of a single-photon interband resonance and thus will not be discussed here. The theoretical studies of two remaining mechanisms were carried out using the third-order nonlinear susceptibility or by numerical solution of the rate equation [3, 4, 6]. The absorption saturation in a direct-gap semiconductor with a parabolic dispersion law of carriers was first calculated in [18]. There are also some papers where the density-matrix and Maxwell equations were numerically solved [7]. However, to our knowledge, simple analytical results for the intensity-dependent interband absorptivity remain to be obtained. In this paper, we present the results of such calculations.

Carrier heating is of major importance in the case of nondegenerate four-wave mixing. However, as will be shown below, it has a negligible effect on the nonlinear absorption under the conditions of the experiment [1] (the injection is absent and detuning of pump and probe waves is zero). Thus, from the density-matrix equations [7] at a fixed temperature with consideration of only the mechanism of spectral hole burning, we have

$$\begin{aligned}
\dot{\rho}_c(k) &= -\frac{1}{\tau_c}\rho_c(k) \\
&+ \frac{i}{\hbar}[d^*(k)E^*(k)\rho_{cv}(k) - d(k)E\rho_{cv}^*(k)] \\
&+ \Lambda_c(k) + \frac{1}{\tau_c}\rho_{c0}(k), \\
\dot{\rho}_{cv}(k) &= \left[i(\omega - \omega_k) - \frac{1}{\tau}\right]\rho_{cv}(k) \\
&- \frac{i}{\hbar}d(k)[\rho_c(k) + \rho_v(k) - 1]E, \\
\dot{\rho}_v(k) &= -\frac{1}{\tau_v}\rho_v(k) \\
&+ \frac{i}{\hbar}[d^*(k)E^*(k)\rho_{cv}(k) - d(k)E\rho_{cv}^*(k)] \\
&+ \Lambda_v(k) + \frac{1}{\tau_v}\rho_{v0}(k).
\end{aligned} \tag{1}$$

Here, $\rho_c(k)$ and $\rho_v(k)$ designate the respective populations of the electron and hole states with the wave vector **k** in the conduction and valence bands; the nondiagonal matrix element $\rho_{cv}(k)$ defines the polarization. According to [7], the dipole moment of the transition $d(k)$ is defined by the expression

$$|d(k)|^2 = \frac{e^2}{6m_0\omega^0(k)}\left(\frac{m_0}{m_c} - 1\right)\frac{\varepsilon_g(\varepsilon_g + \Delta_0)}{\varepsilon_g + 2\Delta_0/3}. \tag{2}$$

Here, e is the elementary charge, m_0 is the free electron mass, Δ_0 is the spin-orbit splitting, and $\omega(k)$ is the transition rate,

$$\hbar\omega(k) = \varepsilon_g + \varepsilon_c(k) - \varepsilon_v(k),$$

where ε_g is the energy gap, $\varepsilon_c(k)$ and $\varepsilon_v(k)$ are the carrier energies. The external field is represented in (1) by the strength E and the frequency ω. The parameters $\Lambda_c(k)$

1063-7826/00/3404-0386$20.00

and $\Lambda_v(k)$ describe the injection, and $\rho_{c0}(k)$ and $\rho_{v0}(k)$ are the steady-state electron and hole populations. The relaxation times τ_c and τ_v are defined as

$$\frac{1}{\tau_c} = \frac{1}{\tau_{1c}} + \frac{1}{\tau_{hc}} + \frac{1}{\tau_s}, \quad \frac{1}{\tau_v} = \frac{1}{\tau_{1v}} + \frac{1}{\tau_{hv}} + \frac{1}{\tau_s},$$

Here, τ_{1c} and τ_{1v} define the electron hole scattering, τ_{hc} and τ_{hv} define the carrier scattering by phonons, and τ_s is the recombination time. Finally, τ in (1) is the relaxation time of a dipole.

From the time-independent solution to system (1), it follows that

$$\mathrm{Im}\,\rho_{cv}(k) = \frac{d(k)EW(k)}{\hbar\tau} \times \frac{1}{[\omega - \omega(k)]^2 + \tau^{-2} + 2(\tau_v + \tau_c)\tau^{-1}[d(k)E/\hbar]^2}, \tag{3}$$

where

$$W(k) = 1 - \rho_{c0}(k) - \rho_{v0}(k) - \tau_c\Lambda_c(k) - \tau_v\Lambda_v(k).$$

In the absence of injection and at room temperature, we may assume that $W = 1$.

Using (3), we introduce the imaginary part of the susceptibility χ'',

$$\chi'' = \frac{1}{E}\mathrm{Im}\,P = \frac{1}{E}\int d(k)\,\mathrm{Im}\,\rho_{cv}(k)\frac{d^3k}{(2\pi)^3} \tag{4}$$

(P is the polarization induced by an external field, in which all orders of resonance interband nonlinearity are taken into account), and intensity-dependent absorption factor α,

$$\alpha = \frac{8\pi^2}{\lambda n'}\chi'' \tag{5}$$

(λ is the wavelength and n' is the real part of the refractive index). In the spectral region of interest $\chi'' \ll n'$; thus, we can ignore the intensity dependence of n'.

One can see from (3)–(5) that the intensity dependence of α is defined by the dispersion law $\omega(k)$. It is noteworthy that the dependence $d(k)$ is also defined by the dispersion law, as follows from (2). Assuming the parabolic isotropic dispersion law for the electrons and heavy holes [19] in InGaAsP, we can write

$$\hbar\omega(k) = \varepsilon_g + \frac{\hbar^2k^2}{2\mu}, \tag{6}$$

where μ is the reduced mass. The same approximation was used in [19] to calculate the infrared absorption in a split band. Performing integration in the complex plane and ignoring the contributions of the nonresonance poles, which appear due to the dependence $d(k)$, we finally have

$$\alpha = \frac{\alpha_0\sqrt{1-\gamma}}{\sqrt{\sqrt{1 + I/I_s} - \gamma}}. \tag{7}$$

Here, I is the pump intensity; $\gamma = \delta\tau(1 + \delta^2\tau^2)^{-1/2}$; $\delta = (\hbar\omega - \varepsilon_g)/\hbar$, α_0 is the linear (for $E \longrightarrow 0$) absorption factor,

$$\alpha_0 = \frac{\pi d^2}{\sqrt{2}n'\lambda\hbar}\left(\frac{2\mu}{\hbar}\right)^2\sqrt{\sqrt{\frac{1}{\tau^2} + \delta^2} + \delta}, \tag{8}$$

which, for $\delta \gg \tau$, yields the well-known dependence

$$\alpha \sim \sqrt{\omega - \varepsilon_g/\hbar},$$

and I_s is the saturation intensity,

$$I_s = \frac{c\hbar^2(1 + \delta^2\tau^2)}{4\pi\tau(\tau_c + \tau_v)d^2}. \tag{9}$$

The expression similar to (7) could be obtained in [18]; however, the result reported only in [18] was valid for the particular case of the exact resonance.

Comparing expression (7) with the absorption coefficient obtained in [4], we see that expression (4.8) in [4] can be derived from (7) by the expansion of the square roots in a power series for low intensities

$$\alpha_A = \frac{\alpha_0}{1 + I/4I_s(1-\gamma)}. \tag{10}$$

The rate-equation approach also yields a similar dependence of the absorption factor on the pump intensity: $\alpha = \alpha_0(1 + aI)^{-1}$. Since expression (10) was derived for small I, it cannot describe the process in the saturation mode. For this reason, the dependence of the type I^{-1} for the saturated absorption does not occur. In contrast to this, a more general approach used here and based on the correct calculation of the integral in (4) results (according to (7)) in a very different saturation behavior for high intensities

$$\alpha \sim I^{-1/4}. \tag{11}$$

The weak intensity dependence of the absorption factor can be explained as follows. As the pump intensity increases, the electrons with high detuning values $\omega - \omega(k)$ participate in the absorption (see (4)). Along with this, the contribution of phase volume of the electrons involved in the absorption also increases, resulting in partial compensation for the saturation effect. Actually, although the integrand in (4) decreases with the increase in intensity as $1/I$ [see (3)], the contribution of the phase volume increases, since the product $k^2\mathrm{Im}\,\rho_{cv}(k)$ attains its maximum for $k = k_0$

$$k_0 = \left(\frac{2\mu}{\hbar}\right)^{1/2}\left[\delta^2 + \tau^{-2} + 2(\tau_c + \tau_v)^{-1}\left(\frac{Ed}{\hbar}\right)^2\right]^{1/4},$$

and the main contribution to the integral is in the vicinity of this point. In the early works devoted to this problem [3, 4], an approximate integration over k was performed under the assumption that the main contribution comes from the vicinity of the resonance point $k_0' = (2\mu\delta/\hbar)^{1/2}$. The comparison of k_0 and k_0' shows that the approximation adopted in [3, 4] is justified only in the case of low intensities. Thus, the saturation behavior in the early theories differs from that obtained by us (7).

The absorption factor of a probe wave at the pumping frequency was calculated on the basis of this approach. To obtain the desired value, we replace E in (1) by $E + E_1$, where E_1 is the field strength of the low-intensity wave. The linear term of the expansion of $\mathrm{Im}\rho$ in E_1 yields the desired parameter; i.e.,

$$\alpha_{pr} = \frac{d(\alpha E)}{dE} = \frac{\alpha_0\sqrt{1-\gamma}}{\sqrt{\sqrt{1+J}-\gamma}} \times\left[1-\frac{J}{2\sqrt{1+J(\sqrt{1+J}-\gamma)}}\right], \quad (12)$$

where $J = I/I_s$. It is readily seen that the saturation behavior of α_{pr} at high intensities is the same as for α

$$\alpha_{pr} \sim I^{-1/4}.$$

To compare these results with the experimental data [1], consideration must be given to the propagation effects, since the sample thickness in the experiment was comparable to the absorption length. We hope to return to this issue in the future.

The contribution of heating of carriers can be evaluated from the calculation of their concentration. With the same approach for the carrier concentration in the conduction band as for the calculation of the absorption factor, we have

$$n_c = \int\rho_c(k)\frac{d^3k}{(2\pi)^3} = \frac{\alpha_0 n'\tau_c d}{2\hbar\omega} I\frac{\sqrt{1-\gamma}}{\sqrt{\sqrt{1+I/I_s}-\gamma}}.$$

Substituting the numerical values of parameters from [1, 5, 7, 20] and taking account of the uncertainty in the evaluation of the relaxation times, we obtain $n_c \sim 10^{16}$–10^{17} cm^{-3} at $I = I_s$. If n_c in InGaAsP is 10^{16} cm^{-3} in the absence of the pumping, the quasi-equilibrium carrier temperature in the experiment [1] is only 5–10% above room temperature. At the same time, this mechanism of nonlinearity is critical in the case of injection, when the carrier concentration is $\sim 10^{21}$ cm^{-3}.

REFERENCES

1. M. N. Islam, E. P. Ippen, E. K. Burkhardt, *et al.*, Appl. Phys. Lett. **47**, 1042 (1985); J. Appl. Phys. **59**, 2619 (1986).
2. H. A. MacKenzie, D. J. Hagan, and H. A. Al-Attar, IEEE J. Quantum Electron. **QE-22**, 1328 (1986).
3. J. P. Agraval, IEEE J. Quantum Electron. **QE-23**, 860 (1987).
4. J. P. Agraval, Phys. Rev. **106**, 1345 (1957).
5. R. Frankenberger and R. Schrimpe, Appl. Phys. Lett. **57**, 2520 (1990).
6. J. Mark and J. Mørk, Appl. Phys. Lett. **61**, 2281 (1992).
7. A. Uskov, J. Mørk, and J. Mark, IEEE J. Quantum Electron. **30**, 1769 (1994).
8. A. D'Ottavi, E. Iannone, A. Mecozzi, *et al.*, Appl. Phys. Lett. **65**, 2633 (1994).
9. M. Willatzen, J. Mark, J. Mørk, *et al.*, Appl. Phys. Lett. **64**, 143 (1994).
10. J. Zhou, N. Park, J.W. Dawson, *et al.*, IEEE Photonics Technol. Lett. **6**, 50 (1994).
11. A. D'Ottavi, A. Mecozzi, S. Scotti, *et al.*, Appl. Phys. Lett. **67**, 2753 (1995).
12. A. Grindt, A. Knorr, M. Hofmann, *et al.*, Appl. Phys. Lett. **66**, 550 (1995).
13. A. D'Ottavi, F. Martelli, P. Spano, *et al.*, Appl. Phys. Lett. **68**, 2186 (1996).
14. N. C. Kothari and D. J. Blumenthal, IEEE J. Quantum Electron. **32**, 1810 (1996).
15. J. Mørk, A. Mecozzi, and C. Hultgren, Appl. Phys. Lett. **68**, 449 (1996).
16. I. Kolchanov, S. Kindt, K. Peterman, *et al.*, IEEE J. Quantum Electron. **32**, 712 (1996).
17. H. Minassian and S. Avetissian, Phys. Rev. B: Condens. Matter **34**, 963 (1986).
18. Yu. L. Klimontovich and É. V. Pogorelova, Zh. Éksp. Teor. Fiz. **50** (3), 605 (1966) [Sov. Phys. JETP **23** (3), 402 (1966)].
19. D. A. Parshin and A. R. Shabaev, Zh. Éksp. Teor. Fiz. **92** (4), 1471 (1987) [Sov. Phys. JETP **65** (4), 827 (1987)].
20. S. Adachi, *Physical Properties of III–V Semiconductor Compounds* (Wiley, New York, 1993).

Translated by Yu. Aleshchenko

Semiconductors, Vol. 34, No. 4, 2000, pp. 389–397. Translated from Fizika i Tekhnika Poluprovodnikov, Vol. 34, No. 4, 2000, pp. 402–410.

ELECTRONIC AND OPTICAL PROPERTIES OF SEMICONDUCTORS

Scattering of Phonons by a Spatially Correlated System of Fe Atoms and the Low-Temperature Anomaly of Thermal Conductivity in HgSe:Fe Crystals

I. G. Kuleev*, A. T. Lonchakov, and I. Yu. Arapova**

Institute of Metal Physics, Ural Division, Russian Academy of Sciences, ul. S. Kovalevskoi 18, Yekaterinburg, 620219 Russia

** e-mail: kuleev@imp.uran.ru*

*** e-mail: arapova@imp.uran.ru*

Submitted July 12, 1999; accepted for publication October 12, 1999

Abstract—The thermal conductivity κ of HgSe:Fe samples with various content N_{Fe} of Fe impurity was studied in the temperature range of 8–60 K. It was found that the dependence of the thermal conductivity κ on N_{Fe} is unconventional at low temperatures. For $T < 12$ K, the value of κ first decreases with an increase in the Fe concentration up to $N_{Fe} = 5 \times 10^{18}$ cm^{-3} and then increases and attains a maximum for $N_{Fe} = (1–2) \times 10^{19}$ cm^{-3}. A further increase in Fe concentration brings about a steady decrease in thermal conductivity. The electron- and phonon-related thermal conductivity of HgSe:Fe crystals with consideration of the effects caused by the ordering of trivalent Fe ions was analyzed. It is shown that both the electron- and phonon-related contributions to thermal conductivity at low temperatures are increasing functions of Fe concentration in the range of $5 \times 10^{18} < N_{Fe} < (1–2) \times 10^{19}$ cm^{-3}. However, the electronic contribution is too small to account for the experimental increase in thermal conductivity. An analysis of the lattice contribution to thermal conductivity showed that an anomalous increase in thermal conductivity is caused by a reduction in the Rayleigh scattering of phonons by a system of Fe ions with mixed valence and is related to the spatial ordering of Fe^{3+} ions. © *2000 MAIK "Nauka/Interperiodica".*

1. INTRODUCTION

In [1, 2], temperature dependences of thermal conductivity κ(*T*) in HgSe crystals with various concentrations of shallow donor impurities were studied. The dependences κ(*T*) calculated [2] in the context of the Callaway theory [3] were in good quantitative agreement with experimental data. It was established that, as the concentration of chaotically located shallow donor impurities increases, thermal conductivity decreases owing to an increase in the probability of the Rayleigh scattering of phonons.

As distinct from semiconductors doped with shallow-level donors, Fe impurity in HgSe:Fe crystals forms a resonance *d* level against the background of a continuous spectrum of the conduction band [4]. For the Fe concentration of $N_{Fe} \geq N^* = 4.5 \times 10^{18}$ cm^{-3}, the conduction-band states located below the Fe *d* level are found to be filled, the Fermi level is pinned at this position, and a mixed-valence state formed from the Fe^{3+}–Fe^{2+} ions is formed in the HgSe:Fe crystals. In this case, the concentrations of conduction electrons and trivalent Fe ions are stabilized in such a way that $n_e = N_{Fe^{3+}} = N_+$, and the concentration of neutral (in the crystal lattice) ions $N_{Fe^{2+}} - N_0 = N_{Fe} - N_{Fe^{3+}}$ increases with increasing the concentration of Fe. Under the conditions of the mixed-valence state, the Coulomb repulsion of positive charges at Fe ions (the *d* holes) results in spatial correlations in their positions: the higher the concentration of N_{Fe}, the larger the number of unoccupied sites for the redistribution of *d* holes and the higher the degree of ordering in a correlated system of Fe^{3+} ions [5]. In this case, the scattering of conduction electrons by a correlated system of Fe^{3+} ions is reduced, and the mobility increases.

The phenomena of electron transport in HgSe:Fe crystals containing the Fe impurity with mixed valence have been well studied by now, both experimentally and theoretically [4–10]. Much less attention has been paid to the special features of the phonon-momentum relaxation in systems containing mixed-valence states. So far, only one work [11] has been concerned with the influence of correlation effects on the phonon-subsystem properties in a system of Fe ions with mixed valence in HgSe:Fe crystals. It was established [11] that, for $T < 12$ K, the dependence of thermal emf on the concentration of Fe impurity exhibits a portion of anomalous increase in the concentration range of $5 \times 10^{18} < N_{Fe} < (1–2) \times 10^{19}$ cm^{-3}. It was shown that an anomalous increase in thermal power is caused by a reduction of the scattering of phonons by the spatially correlated system of trivalent Fe ions.

Table

Sample no.	N_{Fe}, 10^{19} cm^{-3}	n_e, 10^{18} cm^{-3}	μ, 10^4 cm^2/(V s)		N_i, 10^{18} cm^{-3}
			T = 4.2 K	T = 10 K	
1	0	2.1	3.0	3.0	2.1
2	0.1	3.0	2.8	2.8	3.0
3	0.3	4.0	2.9	2.9	4.0
4	0.5	4.8	5.1	4.9	5.0
5	0.8	4.7	6.10	5.7	8.0
6	1	4.7	8.3	7.65	10
7	1	4.85	8.0	7.15	10
8	2	4.9	6.4	5.85	20
9	5	4.8	5.95	5.45	50
10	10	5.1	4.5	4.25	100
11	40	6.2	2.5	2.4	400

The objective of this work was to study the influence of interimpurity Coulomb correlations in a system of Fe ions with mixed valence on the Rayleigh scattering of phonons and the thermal conductivity of HgSe:Fe crystals at low temperatures. We show that an increase in the degree of spatial ordering of Fe ions results not only in an increase in the electron mobility [6] and thermoelectric power [11] but also in an appreciable increase in thermal conductivity at fairly low temperatures for the concentration range of 5×10^{18} cm^{-3} < $N_{Fe} < 2 \times 10^{19}$ cm^{-3}.

In order to experimentally observe an anomalous increase in thermal conductivity, two conditions should be met. First, the lattice-related contribution κ_{ph} to the thermal conductivity of the samples under investigation should exceed the electron-related contribution κ_e. Second, the main mechanism of the phonon-momentum relaxation should be that of the Rayleigh scattering. According to studies of thermal emf [1] and thermal conductivity [2], these conditions are fulfilled in HgSe:Fe crystals in the temperature range of $5 < T <$ 15 K. According to [2], the electronic contribution to the thermal conductivity of HgSe crystals diminishes as the temperature decreases and amounts to less than 1% of the total thermal conductivity at $T \lesssim 10$ K. It is shown in [1] that the mechanism of Rayleigh scattering plays an important role in the momentum relaxation of the phonon system and largely defines the magnitude of thermal emf in HgSe:Fe crystals at low temperatures; in fact, the thermal emf measured in the temperature range of 7–20 K decreases by more than 20 times as the Fe concentration increases from 1×10^{18} to 4×10^{20} cm^{-3}.

In what follows, we report the results of measurements and quantitative analysis of the dependences of thermal conductivity on temperature and Fe concentration.

2. EXPERIMENTAL DATA

Thermal conductivity $\kappa(T)$ was measured in the temperature range of $7.5 < T < 60$ K in 11 HgSe:Fe crystals with an Fe concentration ranging from 0 to 4×10^{20} cm^{-3}. We measured the thermal conductivity by the absolute method (the steady-heat-flux method), which was described in detail elsewhere [1, 2]. The (Au + 0.012%Fe)-Cu thermocouples were used as temperature sensors. The main characteristics of the samples studied (the Fe concentration N_{Fe} and the concentration n_e and mobility μ of electrons at T = 4.2 and 10 K) are listed in the table. The typical dimensions of the samples were 8 mm × 2.0 mm × 0.9 mm. The measured temperature difference did not exceed 10% of the mean temperature of the sample. As can be seen from the table, the concentration of electrons exceeds that of Fe in samples *2* and *3*, in which $N_{Fe} < N^*$ and the Fermi level is below the Fe donor level. This is related to the presence of charged native defects whose concentration N_d is typically ~$(1–2) \times 10^{18}$ cm^{-3} in HgSe:Fe crystals. Therefore, in the samples with $N_{Fe} < N^*$, the electron concentration n_e is equal to the total concentration of charged centers; i.e., we have $n_e = N_d + N_{Fe^{3+}} = N_i$. For $N_{Fe} > N^*$, the Fermi level is pinned to the Fe donor level, and the electron concentration is virtually independent of N_{Fe} (see table).

Figure 1 shows the temperature dependences of the overall thermal conductivity $\kappa(T) = \kappa_{ph}(T) + \kappa_e(T)$ for samples 1–11. As can be seen, the dependences $\kappa(T)$ for HgSe:Fe crystals with low ($N_{Fe} < N^*$) and high ($N_{Fe} > N^*$) Fe concentrations are radically different. For the samples of the first group (samples *1–3*), an increase in $\kappa(T)$ with decreasing temperature is clearly pronounced and is attributed to a decrease in the probability of phonon-phonon scattering (Fig. 1a). For sample *1* with the lowest concentration of native defects, a phonon-related peak at $T \approx 15$ K is observed. It is noteworthy that the position of the peak and the values of $\kappa(T)$ for sample *1* are consistent with the data obtained for the HgSe crystal with $N_i \approx 10^{18}$ cm^{-3} [1]. For HgSe:Fe crystals *9–11* with a high Fe concentration, the shape of the curve $\kappa(T)$ becomes radically different, and an increase in the thermal conductivity related to a repression of the phonon-phonon scattering is not observed. Moreover, the magnitude of $\kappa(T)$ decreases only slightly as the temperature is lowered in the range of 7–30 K (Fig. 1a). Such dependences are typical of the lattice-related thermal conductivity of the crystals in the case where the dominant mechanism of phonon-momentum relaxation involves the Rayleigh scattering of phonons by point defects [12, 13].

For HgSe:Fe samples with intermediate Fe concentrations $(0.5–2) \times 10^{19}$ cm^{-3}, the shape of the $\kappa(T)$ curve in the range of 15–60 K is defined by competition between the phonon–phonon and Rayleigh mechanisms of phonon scattering. As a result, the thermal

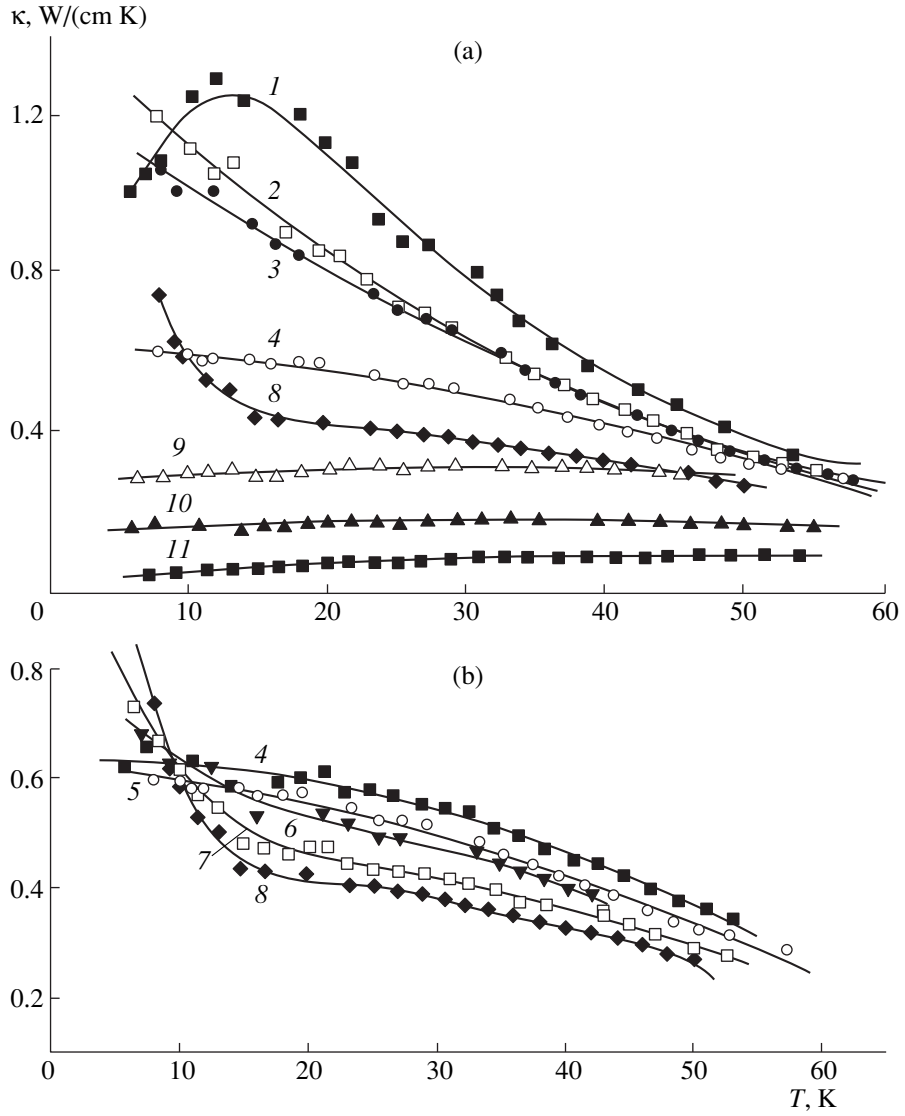

Fig. 1. Experimental dependences of thermal conductivity κ on the temperature T in HgSe:Fe crystals with various Fe concentrations. The curves are numbered in accordance with the sample numbers in the table.

conductivity in samples 4–18 increases with a decrease in the temperature; however, this decrease is less pronounced than in the case of samples 1–3 (Fig. 1b). It is also evident that the thermal conductivity of samples 4 and 5 at $T > 15$ K is much larger than that of samples 6 and 8. However, in the crystals with $N_{Fe} = (1–2) \times 10^{19}$ cm^{-3}, $\kappa(T)$ increases rapidly with decreasing temperature for $T < 15$ K and becomes larger than the thermal conductivity of samples 4 and 5 with $N_{Fe} \approx (5–8) \times 10^{19}$ cm^{-3} at $T < 11$ K. This experimental result is inconsistent with available theoretical concepts, according to which an increase in the Fe concentration should bring about a rise in the role of the Rayleigh phonon scattering and, thus, a decrease in the thermal conductivity for a given temperature. This concentration "anomaly" of the thermal conductivity is more clearly illustrated in Fig. 2 showing the dependences of κ on the impurity concentration N_i. The latter is equal to the concentration of charged centers for samples 1–3 and is equal to the Fe concentration N_{Fe} for samples 4–11. As can be seen from Fig. 2, the dependence $\kappa(N_i)$ at $T = 8$ K is nonmonotonic; as N_i increases, the thermal conductivity first decreases to the value $\kappa_{min} \approx 0.6$ W/(cm K) for $N_i = 5 \times 10^{18}$ cm^{-3} and then increases and attains a maximum $\kappa_{max} \approx 0.75$ W/(cm K) for $N_{Fe} \approx (1–2) \times 10^{19}$ cm^{-3}. A further increase in the Fe concentration results in a steady decrease in $\kappa(N_i)$, which is evidently caused by an increase in the probability of Rayleigh phonon scattering by Fe^{2+} ions that are neutral in the lattice. The fact is that, for $N_{Fe} > N^*$, the Fermi level is pinned to the Fe donor level, and, as the Fe concentration increases,

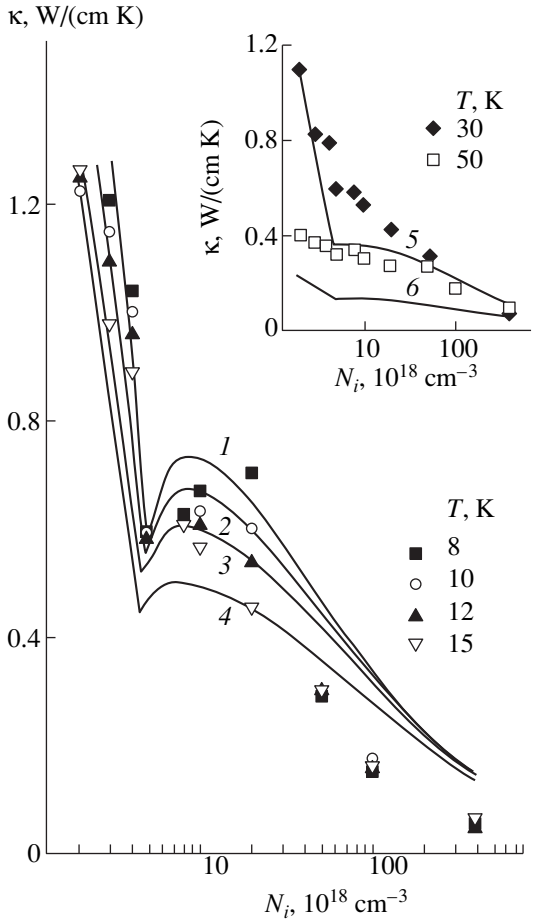

Fig. 2. The calculated (the lines) and experimental (the graphic characters) dependences of thermal conductivity on Fe concentration at several temperatures indicated. The following values of the phonon-scattering parameters were used in calculations: $E_1 = 0.7$ eV, $c_L = 0.6$, $c_H = 2$, $c_{R+} = 3$, $c_{R0} = 0.1$, and $c_U = 0.5$.

the Fe^{3+} ion concentration remains unchanged; it is only the Fe^{2+} ion concentration that increases. Thus, instead of an expected decrease in thermal conductivity in the range of Fe concentrations $(0.5–2) \times 10^{19}$ cm^{-3}, an increase in κ is observed; this increase amounts to ~25% of κ_{min} at $T \approx 8$ K. It is noteworthy that an increase in $\kappa(N_{Fe})$ occurs in the same concentration range where an anomalous increase in thermal emf [11] and electron mobility [4–6] is observed. Therefore, we may assume that an increase in κ is also related to an increase in the degree of spatial ordering of Fe^{3+} ions. It is notable that, in sample *4* with $N_{Fe} = 5 \times 10^{18}$ cm^{-3}, the mixed-valence state of Fe ions is already realized, because electron mobility (see table) appreciably exceeds the value of 3×10^4 cm/(V s) characteristic of electron-momentum relaxation at a chaotic ion system with $N_i = 5 \times 10^{18}$ cm^{-3} [6, 14]. For a HgSe sample with such a donor concentration, thermal conductivity [2] is equal to $\kappa \approx 0.5$ W/(cm K), which is smaller than $\kappa_{min} \approx 0.6$ W/(cm K) for sample *4*. Thus, the magnitude of an increase in thermal conductivity in a HgSe:Fe system with the mixed-valence state of Fe ions with respect to the thermal conductivity of HgSe containing a chaotic system of ions with $N_i = 5 \times 10^{18}$ cm^{-3} can substantially exceed the value of $(\kappa_{max} - \kappa_{min}) \approx 0.15$ W/(cm K).

An anomalous increase in $\kappa(N_i) = \kappa_{ph}(N_i) + \kappa_e(N_i)$ with increasing N_i may be related either to electron or to phonon components of thermal conductivity. For samples *10* and *11*, we managed to single out the electron component $\kappa_e(T)$ of thermal conductivity using the graphical method suggested in [1]. We found that, for $T \approx 10$ K, the value of κ_e did not exceed 10^{-2} W/(cm K), which is consistent with the estimate based on the Wiedemann–Franz relation $\kappa_e = en_e\mu TL$, where μ is the electron mobility and L is the Lorentz number. As shown in [9], the following expression is valid for HgSe:Fe crystals at $T < 30$ K within a wide concentration range:

$$L = L_0 = \frac{\pi^2}{3}\left(\frac{k_B}{e}\right)^2.$$

Estimations of the electronic thermal conductivity for samples *6* and *7*, which have the highest electron mobility, on the basis of the Wiedemann–Franz law and the data listed in the table yield a value of $\kappa_e(N_i)$ no larger than $(1.5–2) \times 10^{-2}$ W/(cm K) at $T = 10$ K. Thus, the magnitude of the electronic contribution to the thermal conductivity is found to be an order of magnitude less than the experimentally observed increase in thermal conductivity $(\kappa_{max} - \kappa_{min}) \approx 0.15 \times 10^{-2}$ W/(cm K). Consequently, this increase is caused by the lattice-related component alone. Therefore, we may assume that the main cause for the low-temperature anomaly of thermal conductivity, as well as of thermal emf [11], is the effect of the diminution of phonon scattering by a spatially correlated system of Fe^{3+} ions.

In what follows, we report the results of the quantitative analysis of the dependences of thermal conductivity on temperature and Fe concentration with allowance made for the phonon drag of electrons. In the calculations, we take into account the scattering of electrons by the correlated system of Fe^{3+} ions, the alloying potential, and acoustic phonons, as well as the main mechanisms of the phonon-momentum relaxation. The phonon scattering by a spatially ordered system of Fe^{3+} ions is also accounted for.

3. ELECTRONIC THERMAL CONDUCTIVITY

Studies of the thermal emf of HgSe:Fe crystals [11] showed that the effect of the phonon drag of electrons plays an important role and defines to a great extent the thermal emf at temperatures lower than 20 K. Therefore, in analyzing the thermal conductivity of these crystals, we proceed from the following expression

obtained in [15] with allowance made for the effects of both the drag of electrons by phonons and their mutual drag:

$$\kappa = \kappa_{\rm ph} + L_0\sigma T\left\{1 + \left(\frac{k_B T}{\varepsilon_F}\right)\right.$$
$$\left.\times [D_F\Gamma C_2 + A_{\rm ph}(\varepsilon_F)(D_5 + D_A - 2D_4)]\right\}. \quad (1)$$

Here, $\sigma = en\mu$ is electrical conductivity, $A_{\rm ph}(\varepsilon_{\rm F})$ is the parameter defining the contribution of phonon drag to thermal emf

$$\alpha_{\rm ph} = -\frac{k_B}{e}A_{\rm ph}(\varepsilon_F),$$

and Γ is the mutual-drag parameter equal to the ratio of the mean free-path time to the time it takes for the momentum transferred by electrons to the phonon subsystem to be returned back to electrons; the coefficients D_i were defined in [15]. Estimations show that, for $T \approx 10$ K, we have $A_{\rm ph}(\varepsilon_{\rm Fe}) < 0.1$–$0.2$, $\Gamma \approx 10^{-3}$, and $k_{\rm B}T/\varepsilon_{\rm F} \approx 10^{-2}$ for HgSE:Fe crystals (the values of the parameters are the same as in [11]); thus, the contribution of electron-phonon drag to electronic thermal conductivity may be ignored.

A nonmonotonic dependence of thermal conductivity $\kappa(N_{\rm Fe})$ in HgSe:Fe crystals is observed at temperatures below 15 K. In this temperature range, elastic scattering of electrons by a correlated system of Fe^{3+} ions and by the alloying potential [6, 7] is dominant, and the effective Lorentz factor is equal to $L \approx L_0$ [9]. Therefore, in order to estimate the electronic thermal conductivity κ_e, we can use the Wiedemann–Franz law. Taking into account the results reported in [6], we can represent the expression for κ_e as

$$\kappa_e = \kappa_e^*\frac{\mu}{\mu^*}\frac{n_e}{N^*}T, \quad (2)$$

where n_e is electron concentration; $\kappa_e^* \approx 5.3 \times 10^{-4}$ W/(cm K) and $\mu^* = 3 \times 10^4$ cm^2/(V s) are the thermal conductivity and mobility, respectively, of electron gas with $n_e = N^*$ in the case of electron scattering by a chaotic system of ions with concentration of $N_i = N^*$; and

$$\mu = \mu^*\left(\frac{1 + 2\varepsilon_d/\varepsilon_g}{1 + 2\varepsilon_F/\varepsilon_g}\right)^2$$
$$\times \Phi_{\rm BH}^*\left\{\Phi_c + \Lambda\left[2\left(\frac{N_0}{N_+}\right)^{1/2}\Phi_{+0} + \frac{\Lambda}{2}\frac{N_0}{N_+}\right]\right\}^{-1}. \quad (3)$$

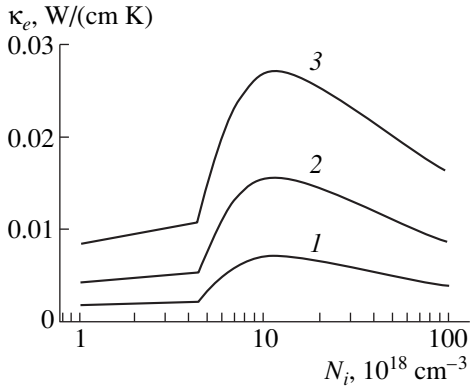

Fig. 3. Calculated dependences of electronic thermal conductivity on Fe concentration for T = (*1*) 4, (*2*) 10, and (*3*) 20 K.

Here, $\varepsilon_d = \varepsilon_{\rm F} = 210$ meV, $\varepsilon_g = 220$ MeV, $\Phi_{\rm BH}^* \approx 2.26$ [6], $\Lambda = 0.1$ is the alloying-scattering parameter, and

$$\Phi_c(k_F) = 2\int_0^1 \frac{x^3 S(2k_F x)}{(x^2 + b_s^{-1})^2}dx, \quad (4)$$
$$\Phi_{+0} = 1 - b_s^{-1}\ln(1 + b_s), \quad b_s = (2k_F r_s)^2.$$

The structure factor $S(q)$ characterizing the degree of spatial ordering in a correlated system of Fe^{3+} ions was determined in [6]; for a chaotic system of ions, $S(q) = 1$ and $\Phi_c = \Phi_{\rm BH}$. In the case of arbitrary Coulomb correlations, the structure factor is calculated to the Percus-Yevick approximation for a model system of hard spheres. The use of this approximation is justified by the fact that, if the mixed-valence state of Fe^{2+}–Fe^{3+} ions is formed at the Fermi level ($N_{\rm Fe} > N^*$), the most closely spaced d holes (positive charges at Fe ions) are the first to be removed. This ensures the highest gain in free energy and gives rise to a correlation sphere around each Fe^{3+} ion; this sphere has a radius of $r_c = d$ (d is the diameter of the hard sphere) and does not contain any other d holes [5]. In such a system, the degree of ordering is characterized by the packing factor $\eta = \pi d^3 N_+/6$, which is equal to the ratio of the volume occupied by hard spheres to the total volume of the system.

As the temperature increases, the migration of d holes between Fe^{2+} and Fe^{3+} ions is intensified, a system of Fe^{3+} ions becomes more and more chaotic, and the degree of spatial ordering and the radius of the correlation sphere decrease. In the approximation of "soft spheres" [10], variations in the packing factor $\eta(T)$ and the diameter $d(T)$ are defined by the following expressions:

$$d(T) = d_0\left(1 - \frac{\Delta r(T)}{d_0}\right),$$
$$\frac{\Delta r}{d_0} = \beta_1[\sqrt{1 + \beta_2 T} - 1]. \quad (5)$$

Here, d_0 is the diameter of a hard sphere at $T = 0$; and β_1 and β_2 are the parameters that generally depend on the concentrations N_+ and N_0, the packing factor, and the screening radius; these parameters were defined in [10].

Expressions (2)–(5) make it possible to analyze the dependences of electronic thermal conductivity both on temperature and on the Fe concentration. Figure 3 shows the dependences $\kappa_e(N_{\mathrm{Fe}})$ for HgSe:Fe crystals in the absence of native defects at several temperatures. As can be seen from Fig. 3, these dependences are nonmonotonic and differ from the dependence of electron mobility $\mu(N_{\mathrm{Fe}})$ [5, 6]. In the concentration range of $1 \times 10^{18} < N_{\mathrm{Fe}} < 4.5 \times 10^{18}$ cm^{-3}, the mobility decreases owing to an increase in the effective mass of charge carriers as the Fermi level rises, whereas the electronic thermal conductivity increases (albeit moderately) in this range owing to an increase in the charge-carrier concentration. In the concentration range of $4.5 \times 10^{18} < N_{\mathrm{Fe}} < (1–2) \times 10^{19}$ cm^{-3}, electronic thermal conductivity rises steeply and increases by about a factor of 3 at $T \approx 10$ K, which is caused by an increase in the degree of spatial ordering in a correlated system of Fe^{3+} ions and by a suppression of electron scattering. However, the absolute values of κ_e in the region of the peak are equal to about 2×10^{-2} W/(cm K), which is by an order of magnitude less than the experimentally measured increase in thermal conductivity in this concentration range.

Thus, an increase in electronic thermal conductivity with an increase in the degree of spatial ordering in a correlated system of Fe^{3+} ions cannot account for the experimentally observed increase in thermal conductivity of HgSe:Fe crystals.

4. LATTICE-RELATED THERMAL CONDUCTIVITY

In analyzing the lattice contribution to the thermal conductivity of HgSe:Fe crystals, we will follow [2] and use an approach suggested by Callaway [12]; this approach is the best developed and is widely used in actual calculations [2, 14, 15], because it makes it possible to limit the number of adjustable parameters to a minimum. In this approach, allowance is made for a specific role of the normal phonon-scattering processes that bring about only the redistribution of momentum between phonons rather than phonon-momentum relaxation. In this model, the phonon-related thermal conductivity is given by

$$\kappa_{\mathrm{ph}} = \left(\frac{k_B T}{\hbar}\right)^3 \frac{k_{\mathrm{B}}}{2\pi^2 s}(J_1 + \beta J_2), \qquad (6)$$

where $s = 3(1/s_l + 2/s_t)^{-1}$ is the mean velocity of sound, with s_l and s_t denoting the velocities of longitudinal and transverse sound; and

$$J_1 = \int_0^{x_d} dx \frac{f(x)}{\nu_{\mathrm{ph}}(x)}, \quad J_2 = \int_0^{x_d} dx \frac{\nu_{\mathrm{ph}N}(x)}{\nu_{\mathrm{ph}}(x)} f(x), \quad \beta = \frac{J_2}{J_3},$$

$$J_3 = \int_0^{x_d} \nu_{\mathrm{ph}N}(x)[1 - \nu_{\mathrm{ph}N}(x)/\nu_{\mathrm{ph}}(x)] f(x) dx, \qquad (7)$$

$$f(x) = x^4 \exp x (\exp x - 1)^{-2}.$$

Here, $x = \hbar\omega_q/k_{\mathrm{B}}T$, $x_d = \Theta_d/T$, with Θ_d standing for the Debye temperature; $\nu_{\mathrm{ph}N}(x)$ is the phonon relaxation rate in normal scattering processes (the Herring mechanism); and $\nu_{\mathrm{ph}}(x)$ is the total relaxation rate for phonons. As studies of thermal conductivity [2] and the drag-related thermal emf [11] showed, the following mechanisms mainly contribute to the phonon-momentum relaxation at low temperatures:

The Umklapp processes with the rate of $\nu_{\mathrm{ph}U} = B_U T^3 \omega^2 \exp(-\Theta_d/aT) = \Lambda_U x^2$, where $\Lambda_U = B_U \exp(-T_U/T)$, $\Theta_d = 151$, $B_U = (2.2 \pm 0.4) \times 10^{-17}$ s/K^3 [2], and $T_U = 123$ K, which corresponds to the limiting energy of longitudinal phonons at the edge of the Brillouin zone.

The Herring mechanism: the relaxation rate is $\nu_{\mathrm{ph}N} = B_N T^3 \omega^2 = \Lambda_N x^2$, where $B_N = (3 \pm 0.8) \times 10^{-22}$ s/K^3 [2].

The phonon scattering by electrons with the rate of $\nu_{\mathrm{ph}e} = \nu^0_{\mathrm{ph}e} x$, with

$$\nu^0_{\mathrm{ph}e} = \frac{E_1^2 m(\varepsilon)}{2\pi p \hbar^3} q_T.$$

Scattering at the sample's boundaries with the rate of $\nu_{\mathrm{ph}L} = c_L s/(L_1 L_2)^{1/2} = \nu^0_{\mathrm{ph}L} c_L$, where $c_L = f/(2 - f)$, f is a fraction of phonons scattered diffusely by the sample's boundaries, and L_1 and L_2 define the cross section of the sample.

The Rayleigh mechanism: the relaxation rate for phonons scattered by chaotically distributed Fe^{3+} charged centers and Fe^{2+} neutral (in the lattice) centers is given by the following expression [11, 16, 17] derived to the point-defect approximation:

$$\nu_{\mathrm{ph}R} = \nu_{\mathrm{ph}R+} + \nu_{\mathrm{ph}R0} = c_{R+}\Lambda_{R+}(N_+ + c_{R0}N_0)x^4. \quad (8)$$

Here, $\Lambda_{R+} = A_+ s^4 q_T^4$, with the constant A_+ defining the probability of phonon scattering at native defects in HgSe crystals; on analyzing the experimental data [2], the estimate $A_+ = 12.1 \times 10^{-40}$ cm^4/s was obtained. According to [2, 12], the value of A_+ can vary by more than an order of magnitude for dissimilar impurities owing to differences in the phonon-scattering cross sec-

tion. The parameter c_{R+} is the ratio of the probability of scattering by Fe^{3+} ions to that by native defects in HgSe crystals. The constant $c_{R0} = A_0/A_+$ is, in fact, the ratio of the cross section for phonon scattering by neutral (in the lattice) Fe^{2+} ions to that by charged Fe^{3+} ions. According to the estimates obtained in [11] from the analysis of the phonon component of thermal emf for HgSe:Fe crystals, $c_{R+} = 2$ and $c_{R0} = 0.15$. The point-defect approximation is justified for substitutional impurities, isotopes, vacancies, and interstitial atoms whose perturbing effect is localized within a unit cell. It is obvious that this approximation is valid for Fe^{2+} substitutional impurity. In the case of scattering of long-wavelength acoustic phonons, a point defect manifests itself as a small portion of the crystal with differing density and elastic properties. The point-defect approximation for charged centers in semiconductors is widely used in actual calculations [2, 12, 13], although its applicability is not quite evident. In fact, the range of a charged-center potential in semiconductors is defined by screening radius r_s. For HgSe:Fe crystals with $n_e = N^* = 4.5 \times 10^{18}$ cm^{-3}, $r_s \approx 5 \times 10^{-7}$ cm $\approx 10a_0$ (a_0 is the lattice constant), and the mean distance between Fe^{3+} ions is $R_+ \approx 6 \times 10^{-7}$ cm. Therefore, the perturbing effect of Fe^{3+} ions (variation of the force constants and the lattice distortion) spans over a large number of unit cells rather than a single unit cell. Since the cross section of Rayleigh phonon scattering is proportional to the square of the perturbed region of a crystal [18], the probability of phonon scattering by Fe^{3+} ions is bound to be much higher than that by Fe^{2+} ions. Therefore, the value of $c_{R0} = 0.15$ obtained in [11] is not surprising. A comprehensive study of the influence of various impurities on the thermal conductivity of Ge and Si crystals has shown [12, 13] that doping with neutral impurities suppresses thermal conductivity much less than in the case of doping with charged impurities; this suppression becomes more pronounced with decreasing temperature. Thus, the results of these studies are consistent with the inference [11] that neutral impurities scatter phonons much less effectively than do charged impurities.

In calculating the rate of phonon relaxation at a correlated system of Fe ions, we take into account the spatial ordering of Fe^{3+} ions in terms of the structure factor $S(q)$ similarly to what was done in [11]. In this case, the following expression can be derived for the rate of phonon relaxation at a mixed-valence state of Fe ions:

$$\nu_{phR}(x) = c_{R+}(N_+ J(q) + c_{R0}N_0)\Lambda_{R+}x^4,$$
$$J(q) = \int_0^1 uS(2qu)du. \tag{9}$$

At low temperatures ($T \le 10$ K), the long-wavelength acoustic phonons contribute largely to both thermal conductivity and the phonon component of thermal emf. Therefore, in calculating the relaxation rate $\nu_{phR}(x)$ in [11], the structure factor $S(q)$ was expanded in a series in terms of powers of q up to the q^4 terms, and analytical expressions were obtained for $J(q)$ and $\nu_{phR}(x)$ [$J(q) = \tilde{S}(x)$]. However, this approximation is found to be inadequate for calculating the thermal conductivity at higher temperatures (see Fig. 4). For large q, the quantity $\tilde{S}(x)$ increases steadily, whereas $J(q)$ tends to a constant value remaining smaller than unity. In this work, in order to simplify numerical calculations, we used an interpolation formula for $J(q)$. This formula was obtained by expanding the direct correlation function $C(q)$ in a series in powers of q and integrating directly the structure factor $S(q) = [1 - nC(q)]^{-1}$; thus, we have

$$\tilde{J}(q) = S(0) + [1 - S(0)] \times \frac{1}{\pi}[\arctan(2u_\tau - \xi) - \arctan(-\xi)], \tag{10}$$

where $\xi = (1 + 1.7\eta)\sqrt{S(0)/S_{(1)}}$. The quantities $S(0)$ and $S_{(1)}$ were defined in [11]. As can be seen from Fig. 4, there is a reasonable agreement between the quantities $\tilde{J}(q)$ and $J(q)$ in the entire range of wave vectors q. The resulting expression for the phonon-relaxation rate in HgSe:Fe crystals with allowance made for the spatial ordering of the correlated system of Fe^{3+} ions can be written as

$$\nu_{ph}(x) = c_L\nu^0_{phL} + \nu^0_{phe}x + c_H\Lambda_H x^2 + c_U\Lambda_U x^2 + c_{R+}[N_+\tilde{J}(q) + c_{R0}N_0]\Lambda_{R+}x^4. \tag{11}$$

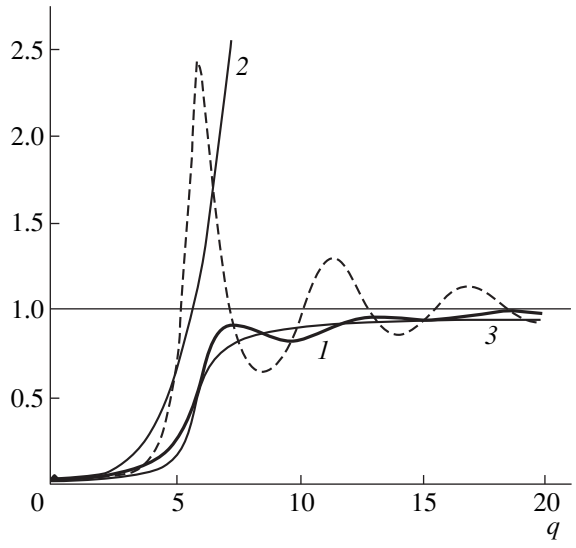

Fig. 4. The dependences of the functions (*1*) $J(q)$, (*2*) $\tilde{S}(q)$, (*3*) $\tilde{J}(q)$, and (the dashed line) $S(q)$ on the wave vector q.

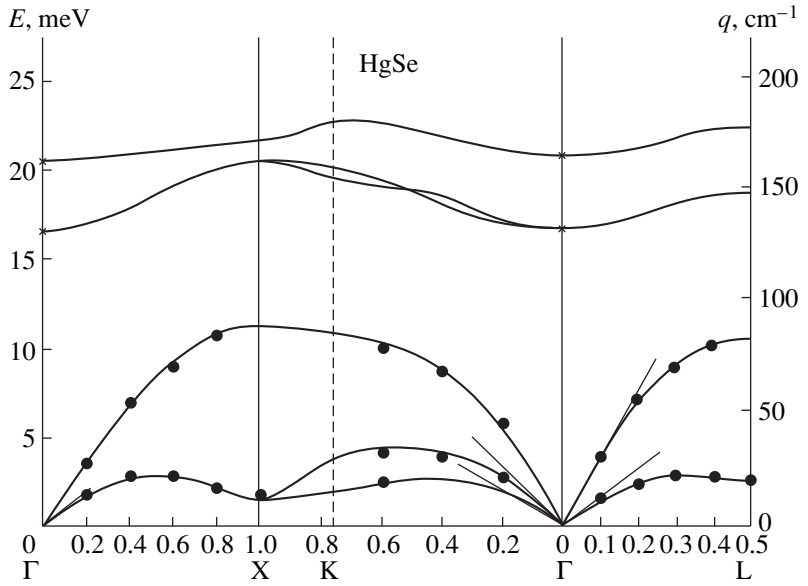

Fig. 5. Phonon spectrum of HgSe crystals [18].

In (11), the adjustable parameters c_H, c_U, c_{R+}, and c_{R0} appear explicitly; they characterize the difference between the properties of HgSe crystals with native defects [2] and those of HgSe:Fe crystals studied in this work. For the parameters of phonon scattering reported in [2], we have $c_H = c_{R+} = 1$. Formulas (6)–(11) make it possible to calculate the dependences of lattice-related thermal conductivity on temperature and Fe concentration for HgSe:Fe crystals.

5. DISCUSSION OF RESULTS

In calculating the thermal conductivity, we used the same values of the parameters as in [11]; i.e., we have $m(\varepsilon) = m_n(1 + 2\varepsilon/\varepsilon_g)$; $\varepsilon_g = 0.22$ eV; the effective mass of an electron at the bottom of the conduction band $m_n = 0.02m_0$, where m_0 is the mass of a free electron; and $s = 1.95 \times 10^5$ cm/s. The results of calculations of the dependence $\kappa(N_{Fe})$ are shown by solid lines in Fig. 2. The values of the phonon-scattering parameters $E_1 = 0.7$ eV, $c_L = 0.6$, $c_H = 2$, $c_{R+} = 3$, $c_{R0} = 0.1$, and $c_U = 0.5$ used in calculating the dependence $\kappa(N_{Fe})$ virtually coincide with those obtained in [11]. As can be seen from Fig. 2, agreement between the calculated dependences $\kappa(N_{Fe})$ and experimental data at $T < 15$ K is quite satisfactory. For a given temperature, the contributions of normal phonon-scattering processes, the Umklapp processes, and the phonon-electron interaction to the phonon-relaxation rate remain constant. The entire variation in thermal conductivity is caused by changes in the Fe concentration and by the influence of native defects. Therefore, in the absence of a spatial correlation for the samples with $N_{Fe} < 5 \times 10^{18}$ cm^{-3} (in which case the Fermi level is below the *d* level of Fe), an increase in the charged-center concentration $N_i = N_{Fe} + N_d$ brings about an enhancement in the Rayleigh scattering of phonons and, correspondingly, a rather sharp decrease in thermal conductivity. In the range of Fe concentrations of 5×10^{18} cm^{-3} $< N_{Fe} <$ (1–2) $\times 10^{19}$ cm^{-3}, the Fermi level is pinned at the Fe donor level (see table) and an increase in the Fe concentration brings about an increase in the concentration of neutral (in the lattice) Fe^{2+} ions and, correspondingly, an increase in the degree of spatial ordering of Fe^{3+} ions. As a result, the Rayleigh phonon scattering by a correlated system of Fe^{3+} ions is depressed and thermal conductivity increases in the aforementioned concentration range. An increase in $\kappa(N_{Fe})$ at $T = 8$ K amounts to 25% of κ_{min}. A steady decrease in thermal conductivity with $N_{Fe} > 2 \times 10^{19}$ cm^{-3} is caused by an increase in the probability of the Rayleigh scattering of phonons by neutral (in the lattice) Fe^{2+} ions with increasing Fe^{2+} concentration. A certain spread of experimental points with respect to the calculated curve is caused by the presence of uncontrolled native defects in the samples [14].

As the temperature increases, both the phonon-phonon scattering processes and the *d*-hole migration between charged and neutral (in the lattice) Fe ions are enhanced (see Section 3). Furthermore, the degree of spatial ordering in a system of Fe ions with mixed valence decreases; as a result, at $T > 15$ K nonmonotonic dependence $\kappa(N_{Fe})$ is observed no more, although the characteristic kinks in the curves $\kappa(N_{Fe})$ persist up to $T \approx 20$ K (Fig. 2).

It is noteworthy that, in order to explain an unconventional dependence of lattice-related thermal conductivity on Fe concentration, we made a number of simplifying assumptions: first, we adopted the Debye

approximation for the acoustic-phonon spectrum, and, second, we used the average velocity of sound $s = 3(1/s_l + 2/s_t)^{-1}$ for the three branches of the phonon spectrum. However, the use of these approximations for HgSe is justified only at fairly low temperatures $T < 10$ K, in which case the long-wavelength phonons with $\omega_q = sq$ contribute largely to the thermal conductivity. In an analysis of thermal conductivity in a wider temperature range, one should take into account the contributions of longitudinal and transverse phonons separately. In fact, the dispersion curves for transverse phonons in HgSe crystals involve two extrema and extended flat portions [18] (see Fig. 5). This gives rise to the emergence of two peaks in the density of states for transverse phonons; the most important of these peaks is the low-energy one. The latter corresponds to the phonons near the boundary of the Brillouin zone; the energy of these phonons is $\hbar\omega_{g/2} \approx k_B T_g$, where $T_g \approx$ 30–35 K and the wave vector $g/2$ corresponds to the boundary of the Brillouin zone [18]. The phonons with wave vectors corresponding to the peaks in the density of states contribute only slightly to thermal conductivity, because the group velocity of these phonons is given by $\partial\omega_q/\partial q \approx 0$. However, they can appreciably affect the relaxation rates for long-wavelength phonons both in the normal-scattering processes and in the Umklapp processes. In connection with this, the Umklapp processes for transverse phonons are expected to be frozen out at significantly lower temperatures than in the case of longitudinal phonons. According to a model suggested by Holland [8, 19], it is necessary to set off a region of the Debye spectrum $\omega_1 < \omega_{max}$ ($q \le q_{max}$) for transverse phonons and take into account separately the contribution of short-wavelength phonons in the range of anomalous dispersion $q_{max} < q < g/2$. Since the highest frequency of transverse phonons is $\hbar\omega_{max} \approx k_B T_{max}$ ($T_{max} = 50$ K) and $\hbar\omega_{g/2} \approx k_B T_g$, we may expect that the anomalous-dispersion region of the phonon spectrum (Fig. 5) contributes significantly to thermal conductivity even at $T > 15$ K. Analysis of the temperature dependence $\kappa(T)$ in the context of the Callaway model [3] without considering the contribution of short-wavelength transverse phonons supports the above assumption. For $T \le 12$ K, the results of calculation of $\kappa(T)$ are in good agreement with experimental data, whereas, for $T \ge 15$ K, the theoretical curves run below the experimental points, with this discrepancy increasing as the temperature increases (see the insert in Fig. 2). Therefore, in order to adequately interpret the dependence $\kappa(T)$ in a wide temperature range, we should take into account the special features of the phonon spectrum in HgSe:Fe crystals (Fig. 5) in terms of the modified Holland approach developed in [19]. However, this approach requires further consideration and will be reported in our forthcoming publication.

6. CONCLUSION

In this work, our main concern was with the quantitative explanation of a new effect consisting of a depression of phonon scattering by a spatially correlated system of Fe^{3+} ions. This effect is the cause of an anomalous dependence of thermal conductivity on Fe concentration at low temperatures, in which case the short-wavelength transverse phonons are frozen out to a great extent. Consequently, it is hoped that the use of the Debye approximation to the phonon spectrum, which we adopted in analyzing the dependence of lattice-related thermal conductivity on Fe concentration, is well substantiated.

REFERENCES

1. S. A. Aliev, L. L. Korenblit, and S. S. Shalyt, Fiz. Tekh. Poluprovodn. (Leningrad) **8**, 705 (1966) [Sov. Phys. Semicond. **8**, 565 (1966)].
2. C.R. Whitset, D.A. Nelson, and J.G. Broerman, Phys. Rev. B: Solid State **7**, 4625 (1973).
3. J. Callaway, Phys. Rev. **113** (4), 1046 (1959).
4. I. M. Tsidil'kovskiĭ, Usp. Fiz. Nauk **162**, 63 (1992).
5. I. G. Kuleev, Fiz. Tverd. Tela (St. Petersburg) **39**, 250 (1997) [Phys. Solid State **39**, 219 (1997)].
6. I. G. Kuleev, I. I. Lyapilin, and I. M. Tsidil'kovskiĭ, Zh. Éksp. Teor. Fiz. **102**, 1652 (1992) [Sov. Phys. JETP **75**, 893 (1992)].
7. I. G. Kuleev, I. I. Lyapilin, A. T. Lonchakov, and I. M. Tsidil'kovskiĭ, Zh. Éksp. Teor. Fiz. **103**, 1447 (1993) [JETP **76**, 707 (1993)].
8. I. G. Kuleev, I. I. Lyapilin, A. T. Lonchakov, and I. M. Tsidil'kovskiĭ, Fiz. Tekh. Poluprovodn. (St. Petersburg) **28**, 937 (1994) [Semiconductors **28**, 544 (1994)].
9. I. G. Kuleev, I. I. Lyapilin, A. T. Lonchakov, and I. M. Tsidil'kovskiĭ, Zh. Éksp. Teor. Fiz. **106**, 1205 (1994) [JETP **79**, 653 (1994)].
10. I. G. Kuleev, I. I. Lyapilin, and I. M. Tsidil'kovskiĭ, Fiz. Tverd. Tela (St. Petersburg) **37** (8), 2360 (1995) [Phys. Solid State **37** (8), 1291 (1995)].
11. I. G. Kuleev, A. T. Lonchakov, I. Yu. Arapova, and G. I. Kuleev, Zh. Éksp. Teor. Fiz. **114** (7), 199 (1998) [JETP **87** (1), 106 (1998)].
12. B. M. Mogilevskiĭ and A. F. Chudnovskiĭ, *Thermal Conductivity of Semiconductors* (Nauka, Moscow, 1972).
13. V. S. Oskotskiĭ and I. A. Smirnov, *Defects in Crystals and Thermal Conductivity* (Nauka, Moscow, 1972).
14. I.G. Kuleyev, N.K. Lerinman, and L.D. Sabirzyanova, Semicond. Sci. Technol. **12**, 840 (1997).
15. I. G. Kuleev, Fiz. Met. Metalloved. **87** (6), 5 (1999).
16. J. W. S. Rayleigh, *The Theory of Sound*, 2nd ed. (Macmillan, London, 1896; Gostekhizdat, Moscow, 1955).
17. P.G. Klemens, Proc. Phys. Soc. London **68**, 1113 (1955).
18. H. Kepa and T. Giebultowicz, Phys. Scr. **25**, 807 (1982).
19. M. Asen-Palmer, K. Bartkowski, E. Gmelin, *et al*., Phys. Rev. B: Condens. Matter. **56** (15), 9431 (1997).

Translated by A. Spitsyn

Semiconductors, Vol. 34, No. 4, 2000, pp. 398–404. Translated from Fizika i Tekhnika Poluprovodnikov, Vol. 34, No. 4, 2000, pp. 411–417.

ELECTRONIC AND OPTICAL PROPERTIES OF SEMICONDUCTORS

Activation-Controlled Conduction and Metal–Insulator Transition in the Impurity Band of Narrow-Gap *p*-$Hg_{1-x}Cd_xTe$ Doped Crystals

V. V. Bogoboyashchiĭ*, S. G. Gasan-zade, and G. A. Shepel'skiĭ****

** State Polytechnical Institute, Kremenchug, 315024 Ukraine*

*** Institute of Semiconductor Physics, National Academy of Sciences of Ukraine, Kiev, 252650 Ukraine*

Submitted February 8, 1999; accepted for publication October 22, 1999

Abstract—Metal–insulator transition and hopping conduction are studied in narrow-gap copper-doped *p*-$Hg_{1-x}Cd_xTe$ crystals in a wide range of temperatures, compositions *x*, and impurity concentrations. It is shown that, as distinct from wide-gap semiconductors, a characteristic size of shallow acceptor wave function responsible for the hopping mechanism of conduction is determined by the effective mass of a heavy, rather than light, hole. The presence of low-temperature ε_2-conduction over the delocalized states of positively charged acceptors near the metal–insulator transition is established. *© 2000 MAIK "Nauka/Interperiodica".*

INTRODUCTION

Low-temperature activation-controlled conduction in the impurity band is studied to date in a number of semiconductors and dielectrics. Several monographs are devoted to this problem [1–3]. However, some important issues still remain unclear to this day. In particular, the nature of ε_2-conduction is not well understood. The next important question concerns the characteristic size of the shallow acceptor wave function in the case of a degenerate valence band. As is known, in semiconductors with cubic crystallographic structure, the valence band is degenerate at the point with $k = 0$ and consists of light- and heavy-hole subbands, which are characterized by effective masses m_{lh} and m_{hh}, respectively. As a result, the dependence of the shallow acceptor wave function on the distance r to its center is rather complicated. According to modern concepts, for $m_{lh}/m_{hh} \ll 1$, the change of wave-function amplitude for the bound state in the immediate vicinity of an acceptor is determined mainly by the heavy hole mass m_{hh}. Here, the value of $a_h = \hbar/\sqrt{2m_{hh}E_A}$ is a characteristic size (E_A is the acceptor level energy) [4]. On the contrary, for large distances ($r \gg a_h$), the asymptotic behavior of wave function depends heavily on m_{lh}, and the characteristic size increases up to $a_l = \hbar/\sqrt{2m_{lh}E_A}$ [2]. Therefore, it would be reasonable to consider that it is this value that determines the probability of the hole hops between the impurity states [2].

Actually, it is shown in [5] by an example of gallium-doped *p*-Ge that the radius of the acceptor state, which determines the probability of carrier hops, is constant and is close to the value of a_l for a wide range of acceptor concentrations $N_A = 7.5 \times 10^{14}$–10^{17} cm^{-3}. However, contradictory data exist. Based on the analysis of conductivity studies of heavily compensated *p*-InSb [7, 8], it was concluded in [6] that the effective radius of the acceptor state decreases with increasing N_A.

A possible reason for the contradictions indicated above is apparently related to the fact that InSb is an inappropriate object for such studies, since, within this context, InSb is in an intermediate position between narrow-gap and wide-gap semiconductors. This becomes clear from what follows.

Actually, the metal–insulator transition in the uncompensated semiconductors of *p*-type represents a modification of the Mott transition. It occurs at the moment the impurity bands merge, which are analogues of the lower and upper Hubbard bands formed by the neutral and positively charged acceptor states as a result of attachment of the excessive hole [1]. The transition point is determined by the ratio of the overlap integral for wave functions of neighboring acceptors and the repulsion energy of holes localized at the native center (the Hubbard energy U). The acceptor concentration at the transition point satisfies the Mott criterion [1]:

$$N^{1/2}a \simeq 0.25. \tag{1}$$

The overlap integral

$$J = \frac{2}{3}\frac{e^2}{\varepsilon a}\frac{r}{a}\exp\left(-\frac{r}{a}\right) \tag{2}$$

(here, ε is the dielectric constant and $a = \hbar(2m^*E_A)^{1/2}$ for a simple band with the effective mass m^*), calculated for the hydrogen-like center as a function of interimpurity distance [2], has the maximum for $r = a$. It can

be easily verified in this case that the ratio J/E_A in the maximum is independent of a.

The situation is different in the case of a semiconductor with the degenerate valence band. Here, the ionization energy of a single-charged acceptor is determined mainly by the heavy hole mass [4], and $E_A = e^2/(3\varepsilon a_h)$ in the limit of $m_{lh}/m_{hh} \longrightarrow 0$. At the same time, for $r \gg a_h$, the overlap integral J, to within a numerical factor on the order of 12, is described by expression (2), if we assume that $a = a_l$. Therefore, for $r \gg a_h$, the ratio J/E_A is small and may be no greater than $0.7a_h/a_l$ (or $0.7\sqrt{m_{lh}/m_{hh}}$) at its maximum value.

On the other hand, a width B of the impurity band is determined solely by the value of overlap integral J [1], without regard for the Coulomb interaction of charged impurities. As it will be shown below, in this case, at the point of the Mott transition, $B = (2/3)E_A$ and the ratio $J/B \approx 0.22$, so that $J/E_A \approx 1/7$. Consequently, in order that the overlap of asymptotic tails of wave functions could induce the Mott transition, the fulfillment of the following condition is necessary: $0.7\sqrt{m_{lh}/m_{hh}} > 1/7$, i.e., $m_{lh}/m_{hh} > 0.04$.

In p-Ge, where $m_{lh} = 0.042m_0$ and $m_{hh} = 0.379m_0$ [9], the ratio $m_{lh}/m_{hh} > 0.11$; therefore, this material behaves as a typical wide-gap semiconductor, and $a = a_l$ in it. In the narrow-gap semiconductors, e.g., $Hg_{1-x}Cd_xTe$, where $m_{lh}/m_{hh} \ll 1$, the overlap of tails of the bound hole wave functions is small, and the Hubbard bands are narrow. As a result, these bands merge only if the distance between the impurity atoms becomes comparable to the radius of heavy hole localization a_h. The ratio m_{lh}/m_{hh} in InSb has an intermediate value of 0.04–0.08 [10-12], and for this reason a depends on the mean distance between acceptors.

On the basis of the reasoning given above, we come to the conclusion that $Hg_{1-x}Cd_xTe$ can be a promising material for the studies of general laws of hopping conduction in semiconductors with a degenerate valence band. The bandgap for this semiconductor and the effective mass of light hole heavily depend on its composition x, whereas m_{hh} remains practically constant. As a result, the ratio m_{lh}/m_{hh} can attain very small values (for $x = 0.2$, it is close to 10^{-2}). Varying x, one can thus change the value of m_{lh} in a wide range, practically without changing m_{hh} in this case. This should provide the possibility of the reliable determination of the contributions of light and heavy holes to the conduction in the impurity band. There is another advantage of $Hg_{1-x}Cd_xTe$: the activation-controlled conduction in this material is observed for the very high acceptor concentrations, which exceed 10^{-17} cm^{-3} [13, 14]. Therefore, within a good accuracy, the condition for weak compensation is realized that allows us to ignore the broadening of the acceptor band owing to the influence of charged impurity centers.

However, the advantages of $Hg_{1-x}Cd_xTe$ listed above have not yet been realized, since low-temperature conduction studies were only carried out for crystals with intrinsic defects of the acceptor type (mercury vacancies V_{Hg}). The low-temperature conduction of such crystals has an additional feature. Regions of hopping conduction with a constant activation energy (regions of ε_2 and ε_3 conduction) are not observed at all, and the conduction with a variable activation energy (conduction according to Mott [15]) replaces the band ε_1 conduction at unusually high temperatures $T \simeq$ 20–25 K [13]. The presence of activation-controlled impurity conduction for such large values of N_A contradicts the concept of the critical importance of a_l in the transition to the metallic conduction in the impurity band. Actually, for p-$Hg_{1-x}Cd_xTe$ crystals with $x \approx 0.2$, the value $a_l \approx 2 \times 10^{-6}$ cm can be obtained. Then, the conduction in the acceptor band should already be metallic for the concentrations of vacancies of about 2×10^{15} cm^{-3}. Contradictions can be eliminated if one assumes that, in narrow-gap $Hg_{1-x}Cd_xTe$, the metal–insulator transition in the acceptor band is determined predominantly by the localization radius a_h of the heavy hole. In fact, as $a_h \simeq 2$ nm, the Mott transition in this case could correspond to $N_A \approx 10^{18}$ cm^{-3}. Thus, undoped p-$Hg_{1-x}Cd_xTe$ is not quite convenient for determining the parameters of the hole bound state. Doped crystals can be more suitable for these aims; as is shown below, conduction over the acceptor states in these crystals has a constant activation energy.

In this work, specific studies of the conductivity of copper-doped uncompensated $Hg_{1-x}Cd_xTe$ crystals were carried out in a wide range of temperatures, compositions x, and impurity concentrations. Copper was selected as the main impurity for a number of reasons. First, it produces only one shallow acceptor level in the $Hg_{1-x}Cd_xTe$ gap, which is well described by the effective mass method. The latter allows us to exclude the features related to the multiply charged defects. Second, copper is introduced easily, controllably, and in large amounts into the $Hg_{1-x}Cd_xTe$ crystals by diffusion at comparatively low temperatures ($T < 300$°C) [16], which is especially important because it allows us to circumvent the Hg-vacancy generation.

METHODS OF SAMPLE PREPARATION AND MEASUREMENTS

The electrical conductivity of crystals with compositions x in the range of 0.19–0.30 was measured. The copper concentration varied in the range from 10^{16} to 10^{18} cm^{-3}. The bandgap at $T = 0$ changed approximately from 0.038 eV for $x = 0.19$ to 0.225 eV for $x = 0.30$, and the localization radius a_l varied from 38 to 11.5 nm, respectively. At the same time, the value of a_h varied insignificantly due to the independence of m_{hh} on x [17]. This allowed us to identify a branch of the valence

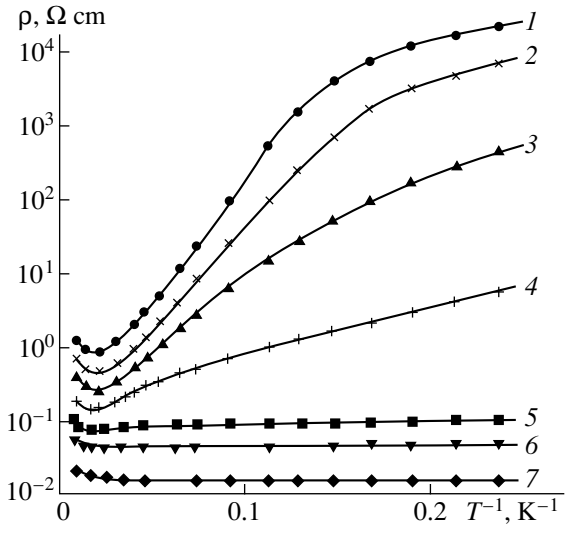

Fig. 1. Temperature dependences of resistivity ρ for doped p-$Hg_{1-x}Cd_xTe$ crystals ($x = 0.21$) with $N_A = (1)\ 2.2 \times 10^{16}$, $(2)\ 3.2 \times 10^{16}$, $(3)\ 6.7 \times 10^{16}$, $(4)\ 1.4 \times 10^{17}$, $(5)\ 3.5 \times 10^{17}$, $(6)\ 6.5 \times 10^{17}$, and $(7)\ 2.0 \times 10^{18}$ cm^{-3}.

band, which determines the radius a of the state in the Mott criterion (1) by measuring a dependence of the acceptor critical concentration on the crystal composition.

The compositionally homogeneous $Hg_{1-x}Cd_xTe$ wafers obtained by the method of vertical planar crystallization from the stoichiometric melts were selected. The wafers were subjected to a homogenizing annealing at 550°C for a week in saturated Hg vapors in order to reduce the vacancy concentration and to improve the structure. After that, the annealing temperature was lowered in increments, down to 250°C. As a result, all the wafers had the n-type conduction with electron concentration $n = (1–2) \times 10^{14}$ cm^{-3} at 77 K. The dislocation density in such a material did not exceed 3×10^5 cm^{-2}. The total concentration of residual impurities was estimated to be of about 2×10^{15} cm^{-3}. The composition of wafers was determined to no worse than $x = 0.001$ of the molar fraction. Rectangular samples with dimensions of about 0.1 cm × 0.3 cm × 1.2 cm were cut from the central part of the wafer. After sample etching in a solution of Br_2 in HBr, a copper in the amount ranging from 10^{15} to 10^{17} cm^{-2} was evaporated in a vacuum onto the sample surface. Then the samples were annealed in an atmosphere of saturated Hg vapor at 200°C for 3 days, which allowed us to obtain the homogeneously doped crystals [16]. As a result, five series of samples of practically identical composition (within each series) were obtained; these samples contained various amounts of copper (10^{16}–10^{18} cm^{-3}) and identical concentrations of donors $N_D \approx 10^{15}$ cm^{-3}. The concentration of mercury vacancies in such crystals was negligibly small.

For eliminating surface effects, the samples were treated in a solution of Br_2 in HBr directly before measurements and then rinsed in distilled water. The resistivity was measured in the temperature range of 4.2–125 K. In some cases, the temperature of measurements was 2.5 K. The Cu concentration was determined in the course of individual measurements of the Hall coefficient in a magnetic field of up to 3 T at 77 K.

EXPERIMENTAL RESULTS AND DISCUSSION

The results of measurements of ρ for several samples having the composition $x = 0.210 \pm 0.002$ and containing various amounts of impurities are shown in Fig. 1. A general shape of dependences $\rho(T)$ obtained and trends of their change with N_A increase are characteristic of weakly compensated semiconductors. For comparatively light doping ($N_A < 6 \times 10^{16}$ cm^{-3}), both the ε_1-conduction regions in the valence band and the regions with impurity conduction over acceptor states are well distinguished. The temperature at which the change of charge transport mechanism occurs is almost independent of N_A in this concentration range and is equal to 7–8 K. The activation energy of impurity conduction increases here as N_A increases, whereas the value of E_A decreases in the region of ε_1 conduction.

The situation alters for $N_A < 6 \times 10^{16}$ cm^{-3}. The transition point to the other conduction mechanism rapidly shifts to higher temperatures, so that, for $N_{Cu} > 1.4 \times 10^{17}$ cm^{-3}, it is above 50 K. The temperature region of ε_1 conduction narrows sharply and becomes weakly pronounced, and, for $N_A > (2–3) \times 10^{17}$ cm^{-3}, practically disappears. The activation energy of impurity band conduction reduces with increasing N_A and, for $N_A = 3.8 \times 10^{17}$ cm^{-3}, tends to zero (the Mott transition). If we assume the contributions of various conduction mechanisms to be additive and separate them in the range of mixed electrical conduction, one can show that the activation energy of impurity band conduction is independent of temperature in the temperature and Cu-concentration ranges studied. It is seen especially well by the example of samples with intermediate impurity concentration $N_A \approx (1–2) \times 10^{17}$ cm^{-3} (Fig. 1).

Thus, the low-temperature impurity-band conduction of doped p-$Hg_{0.8}Cd_{0.2}Te$ radically differs from the conduction in undoped crystals with mercury vacancies [13, 14]. Consequently, the absence of ε_2- and ε_3-conduction regions is a specific feature of the latter. The obvious reason for this difference is as follows: the mercury vacancy, as distinct from the Cu impurity atom, is a doubly charged acceptor. As a result, the levels of Cu and V_{Hg} are susceptible to the influence of composition fluctuation to a different extent. Actually, according to [18], the composition fluctuations of a

solid solution induce the broadening of the acceptor state band, which is described by a split Gaussian distribution with the variance

$$D[E_A] = \frac{1}{2}\gamma_1^2 + \frac{5}{2}\gamma_2^2, \quad (3)$$

where $\gamma_1 = 0.55$, $\gamma_2 = 0.13$,

$$\gamma = 0.5\left|\frac{\partial E_v}{\partial x}\right|\sqrt{\frac{x}{\pi N a^3}},$$

and N is the site concentration in the metal sublattice. Consequently, without regard for the Coulomb interaction, the rms difference of energy levels of two acceptors is equal to

$$\langle E_A\rangle = \sqrt{2D[E_A]} \approx 0.31\left|\frac{\partial E_v}{\partial x}\right|\sqrt{\frac{c}{\pi N a^3}}. \quad (4)$$

In the case of the simple acceptor and the effective mass approximation, one should consider the localization radius a as being equal to a_h [18]. Therefore, assuming for $Hg_{0.79}Cd_{0.21}Te$ $|\partial E_v/\partial x| = 0.35$ meV [19], $\varepsilon = 17.5$ [20], $m_{hh} \approx 0.4m_0$ [17], and $N = 1.5 \times 10^{22}$ cm^{-3}, we find that, for Cu impurity ($E_A \approx 8$ meV), the spread energy is $\langle E_A\rangle \simeq 1.1$ meV. This value only exceeds that of k_BT in the temperature range studied by a factor of 2 or 3; therefore, the composition fluctuations only slightly influence the activation energy of hopping conduction in the copper-doped crystals.

It is more complicated to estimate the broadening of levels that are produced by Hg vacancies. For this purpose, it is necessary to calculate the radius of the corresponding state. To do this, one can conveniently use the variational method, which is employed for calculations of the ionization energy of helium atoms [21]. We ignore the exchange effects and calculate a mean value of the Hamiltonian for the system of two holes bound by one acceptor with the nucleus charge Ze in the state with a wave function in the form $\Psi(x_1, x_2) = \varphi_1(x_1)\varphi_2(x_2)$. Here, $\varphi(x)$ is the wave function of the ground state of the hole bound by the acceptor with the effective charge of nucleus Z^*e. The result is then minimized with respect to the parameter Z^*.

Employing as $\varphi(x)$ the wave functions obtained in [18] in the limit of $m_{lh}/m_{hh} \longrightarrow 0$ and assuming that $a = a_h/Z^*$ [21], we obtain for the ground state energy

$$\varepsilon_{AZ} \approx -1.95(Z^*)^2 E_{A1}, \quad (5)$$

$$Z^* \approx 1.01Z - 0.27, \quad (6)$$

where $E_{A1} = Zm_{hh}e^4/9\varepsilon^2\hbar^2$ is the ionization energy of a simple acceptor.

In the case of neutral vacancy, when $Z = 2$, we use relationship (6) to obtain $Z^* = 1.75$. Then, the radius of the acceptor state in expression (4) should be considered equal to $a \approx 6\varepsilon\hbar^2/7m_{hh}e^2$, which yields 2.7 meV for the spread energy of the lower state of V_{Hg}. This value already exceeds, by a factor of 4 to 8, the energy k_BT; therefore, the fluctuations of composition suppress the hops between neighboring vacancies. As a result, the Mott conduction in p-$Hg_{1-x}Cd_xTe$ crystals with Hg vacancies can exceed the ε_3 conduction even at rather high temperatures.

Let us consider in detail the features of the charge transport over the impurity acceptor states in the copper-doped p-$Hg_{1-x}Cd_xTe$. The dependence of parameters ε and ρ_0 for the Arrhenius-type law

$$\rho = \rho_0^* \exp(\varepsilon/k_BT) \quad (7)$$

on the impurity concentration in the samples of various composition x is shown in Figs. 2 and 3. It is seen that dependence ε on the reciprocal interimpurity distance $r^{-1} = N_{Cu}^{1/3}$ has two kinks rather than one, as other semiconductors have. One of these is a conventional point of the Mott transition, where ε vanishes. At the other point (for lower Cu concentrations), a steady increase of ε with $N_{Cu}^{1/3}$ changes by jumping into its steady decrease. The preexponential factor ρ_0^* at this point (for $r = N_{Cu}^{-1/3} \approx 2.5 \times 10^{-6}$) also decreases abruptly by almost an order of magnitude (Fig. 3), whereas, at the Mott-transition point, the dependence of the value ρ_0^* on N_{Cu} does not experience any singularities.

The threshold impurity concentration depends on the solid solution composition and increases with an increase in x (Fig. 2). Considering the dependence of ε on $N_{Cu}^{1/3}$ to be linear below the transition, we find that the Mott transition occurs for N_{Cu} equal to 2.6×10^{17}, 3.8×10^{17}, 4.9×10^{17}, and 6.1×10^{17} cm^{-3} for $x = 0.19$, 0.22, 0.26, and 0.30, respectively. Such behavior of the Mott-transition point should be ascribed solely to an increase in the binding energy of a hole at the acceptor E_A with an increase in x. Actually, the activation energy of ε_1 conduction grows markedly with an increase in x (Fig. 4). For $N_{Cu} = (1.6–1.8) \times 10^{17}$ cm^{-3} in the temperature range where $\rho < 100$ Ω cm, the value of $\varepsilon_1 \approx 5.5$ meV for $x = 0.19$ and increases up to 7.8 meV for $x = 0.30$. In this region, $p > N_D$, so that the contribution of impurity donors to the condition for electrical neutrality

$$N_D + p = N_A \quad (8)$$

can be ignored, which corresponds to the weak compensation approximation. For $\rho > 100$ Ω cm, the relationship between N_D and p is replaced by the opposite one ($p < N_D$); therefore, the influence of compensating donors on the Fermi energy becomes substantial, and the activation energy ε_1 increases to 7–11 meV. Correspondingly, a kink appears in the dependence of ε_1 on $1/T$ for the samples with $x \geq 0.26$ (Fig. 4).

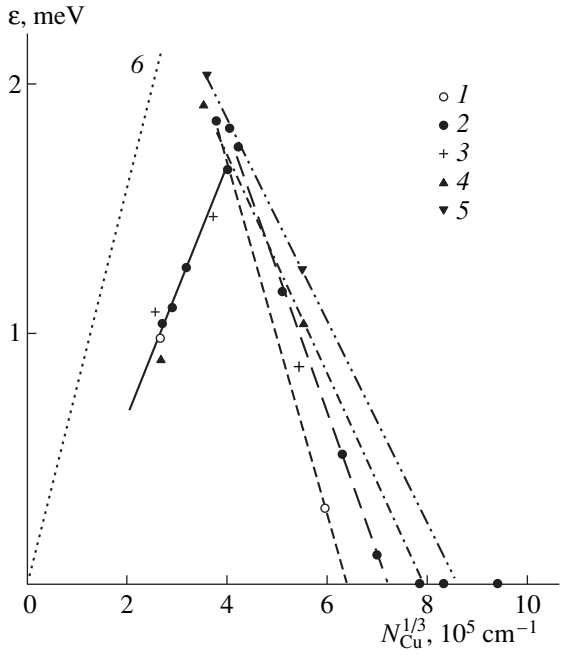

Fig. 2. Dependence of the conduction activation energy ε in the impurity band on the impurity concentration N_{Cu} in p-$Hg_{1-x}Cd_xTe$ crystals with x = (*1*) 0.19, (*2*) 0.21, (*3*) 0.226, (*4*) 0.26, and (*5*) 0.30. (*6*) is the dependence of $\varepsilon_3(N_A)$ calculated according to data [2] for $K \longrightarrow 0$ and T = 4.2 K.

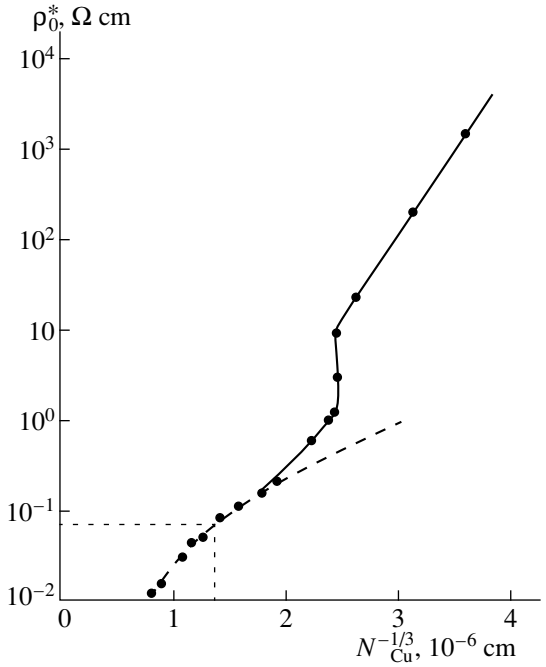

Fig. 3. Dependence of the preexponential factor ρ_0^* on the impurity concentration N_{Cu} in p-$Hg_{1-x}Cd_xTe$ crystals (T = 4.2 K, x = 0.21). Points are experimental, the dashed line is the dependence $\rho_0^* \propto 1/N_{Cu}$, and the Mott-transition point is indicated by the dotted line.

In order to correctly estimate E_A from measurements of ε_1, we should consider the actual form of the density of states in the impurity band for the compensation condition according to [2]; the dependence of the integrated density of states in the valence band and of hole mobility on temperature should be also taken into account. As a result, the ionization energy of Cu in p-$Hg_{1-x}Cd_xTe$ increases from 6–7 meV for x = 0.19 to 10–11 meV for x = 0.30. Correspondingly, the calculated value of localization radius for heavy holes a_h decreases from 3.7–4.0 to 3.0–3.1 nm. In fact, this coincides with estimates of a_h obtained above from the experiment based on the Mott criterion (1).

Thus, in the range of the Mott transition in copper-doped narrow-gap p-$Hg_{1-x}Cd_xTe$ crystals with $x < 0.3$, and, correspondingly, $m_{lh}/m_{hh} < 0.045$, the overlap of the wave function tails for bound holes actually turns out to be infinitesimal.

Another singular point in Figs. 2 and 3, which corresponds to $N_{Cu} \approx 6 \times 10^{16}$ cm^{-3}, separates the regions with different behavior of parameters ρ_0^* and ε. In the region $N_{Cu} < 6 \times 10^{16}$ cm^{-3}, the logarithm of ρ_0^* is proportional to $N_{Cu}^{-1/3}$, which, as is known, is directly indicative of the presence of ε_3 conduction. An increase in ε with increasing $N_{Cu}^{1/3}$ in the same concentration region is also indicative of the fact mentioned above. In this case, ρ_0^* coincides with the value of ρ_{03} calculated in [2]:

$$\rho_{03} = \rho_0 \exp\left(\frac{1.73}{N_A^{1/3} a}\right). \quad (9)$$

Comparing the data in Fig. 3 for the region $N_{Cu} > 6 \times 10^{16}$ cm^{-3} with relationship (9) for $N_A = N_{Cu}$, we can estimate the value of the localization radius for a bound hole, which determines the hopping charge transport over the states in the middle of the impurity band. For $x \approx 0.22$, this value turns out to be approximately equal to 3.7 nm, which is very close to the localization radius of a heavy hole a_h, which in turn is equal under these conditions to 3.4 nm. Thus, for concentrations of $N_{Cu} > 1.6 \times 10^{16}$ cm^{-3}, i.e., for $r > 10a_h$, the light holes do not affect the charge transport in the acceptor band in p-$Hg_{1-x}Cd_xTe$ crystals with $x < 0.3$. This result turns out to be no less important than that obtained above on the data of the Mott transition, since, under light doping, the concept of the localization radius of impurity state is quite appropriate [2].

In the region $N_{Cu} > 6 \times 10^{16}$ cm^{-3} after the abrupt change of ρ_0^*, the dependence $\rho_0^*(N_A)$ gradually

becomes less steep and, for $N_{Cu} > 1.7 \times 10^{17}$ cm^{-3}, smoothly changes for inversely proportional. In this case, the Mott transition does not affect the dependence of ρ_0^* on N_A at all. Since the quantity $1/\rho_0^*$ has the meaning of the impurity electrical conductivity in the limit of the equiprobable distribution of impurity holes over the acceptor band (including the upper Hubbard band), one can conclude that, for $N_{Cu} > 6 \times 10^{16}$ cm^{-3}, the charge transport is accomplished over the localized states beyond the percolation threshold, both above and also below the Mott transition (the ε_2 conduction).

Actually, the impurity band is rather narrow, and the effective mass of delocalized holes is correspondingly large, so that near the Mott-transition point, their scattering by the charged acceptors is apparently insignificant. Therefore, the fact of proportionality between$1/\rho_0^*$ and N_{Cu} for $N_{Cu} > 1.6 \times 10^{17}$ cm^{-3} allows us to conclude that, under these conditions, the largest part of states in the upper Hubbard band is delocalized. Then, a sharp increase in ρ_0^* for concentrations lower than 1.6×10^{17} cm^{-3} is indicative of a fast reduction of the number of delocalized states in this band, and the abrupt change in ρ_0^* for $N_{Cu} \approx 6 \times 10^{16}$ cm^{-3} indicates that they completely disappear.

To confirm this, we evaluate the critical concentration of acceptors, starting from the similarity with the metal–insulator transition in the acceptor band. It follows from relationships (5) and (6) that, for light doping, all the states in the upper Hubbard band of the *p*-type semiconductor are localized as well as those in the lower band. With an increase in N_A, the overlap of the wave functions of neighboring acceptors increases too, and, as a result, delocalized states can appear in the central part of the upper band in accordance with the Anderson mechanism. On the other hand, delocalized states in this band can appear as a result of its overlap with the valence band (this mechanism is similar to that of the Mott transition). In the first case, the critical concentration can be evaluated using the Anderson localization criterion, which practically coincides with (1). In accordance with (6), for a simple acceptor, we have $Z^* \approx 0.74$; therefore, the localization radius for a heavy hole in the upper Hubbard band is approximately equal to $4a_h/3$ (i.e., is about 4.5 nm for $x = 0.21$). If we consider that the overlap of states in the upper band, as well as in the lower band, is determined solely by heavy holes, we find from (9) that the Anderson transition in the band should be observed for $N_{Cu} \approx 1.6 \times 10^{17}$ cm^{-3}. In fact, this coincides with the onset of the inversely proportional dependence of ρ_0^* on N_A. For larger values of N_A, the majority of states in the upper Hubbard zone are delocalized.

In the case of the second delocalization mechanism, which is related to the overlap of the upper Hubbard band with the valence band, we use the obvious similarity with the mechanism of the Mott transition to determine the transition criterion and equate the width B of the Hubbard band to a double energy of the hole attachment to the neutral acceptor. This energy can be easily found with the use of relationships (5) and (6) assuming that $Z = 1$. In this case, the energy of the acceptor ground state with two holes is $\varepsilon_{A1} \approx -1.07E_{A2}$. Consequently, the energy of the hole attachment, which is equal to the difference $E_{A1} - \varepsilon_{A1}$, is about $0.07E_{A1}$; thus, in the moment of band merging, $B \approx 0.14E_{A1}$. Let us assume in the first approximation that the overlap integral for acceptor states in both Hubbard bands has form (2) obtained for the hydrogen-like centers. We also take into account that the radius of a state in the upper band is one-third larger than in the lower band and that the width B of the impurity band is proportional to the overlap integral J. Then, from relationships (1) and (2), we find that, at the Mott-transition point, the width B of the upper Hubbard band is twice as large as the width of the lower band, and, consequently, is about $(2/3)E_{A1}$. Thus, calculating J with the use of (2), we find that, at the Mott-transition point, an approximate equality $J/B \approx 0.22$ is valid for each of the bands. This is similar to the estimate $J/B \approx 1/4$, obtained in [2] within the context of the percolation theory.

By virtue of the analogy indicated above, we assume that, at the moment of upper Hubbard band merging with the valence band, the width of the former is also determined by the relationship $J/B \approx 0.22$. Then, after relevant transformations, we obtain the delocal-

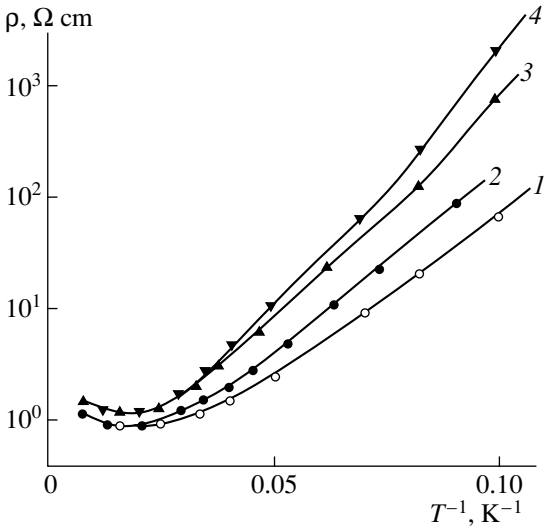

Fig. 4. Temperature dependences of resistivity ρ for doped *p*-$Hg_{1-x}Cd_xTe$ crystals in the region of ε_1 conduction. x = (*1*) 0.19, (*2*) 0.21, (*3*) 0.26, and (*4*) 0.30. $N_{Cu} = 1.7 \times 10^{16}$ cm^{-3}.

ization criterion of the upper Hubbard band in the form of

$$N_A^{1/3} a \approx 0.18. \quad (10)$$

For $a = 4.5$ nm, we find from (10) that the critical concentration of the acceptor impurity, at which the upper Hubbard band merges with the valence band, is equal to $N_{Cu} \simeq 6.4 \times 10^{17}$ cm^{-3}. This practically coincides with the point at which ρ_0^* undergoes the abrupt change in Fig. 3.

CONCLUSION

The results of studies allow us to make the following conclusions.

(i) The effective radius of the acceptor state, which determines the probability of bound hole hopping between the impurities, is ambiguously defined in semiconductors with the degenerate valence band. In the limiting case, it coincides with the localization radius of a light hole a_l in wide-gap semiconductors with $m_{lh}/m_{hh} > 0.04$, whereas, in narrow-gap materials with $m_{lh}/m_{hh} < 0.04$, it is close to the value of a_h.

(ii) Single crystals of narrow-gap p-$Hg_{1-x}Cd_xTe$ semiconductor are a convenient object for studying the general tendencies of conduction over the acceptor states due to the possibility of gradually changing the bandgap and relationship m_{lh}/m_{hh}, as well as due to the high values of acceptor critical concentrations corresponding to the Mott transition.

(iii) In the copper-doped p-$Hg_{1-x}Cd_xTe$ crystals with $x \approx 0.2$ and $N_{Cu} > 10^{16}$ cm^{-3} (i.e., for a mean distance between impurities $r < 10a_h$), the hopping conduction is determined solely by the localization radius a_h of heavy holes.

(iv) The feature of the relationship of ε_2- and ε_3-conductivity parameters for narrow-gap $Hg_{1-x}Cd_xTe$ solid solutions is as follows: for a given impurity concentration, one of the conduction mechanisms is completely dominant in the entire temperature range. The change of the dominant mechanism occurs only if the acceptor concentration in the crystal is changed. As a result, one can distinctly observe the moment of delocalized-state appearance in the upper Hubbard band and confidently identify it with the moment of its merging with the valence band. In this case, the ε_2 conduction is observed only in the region where only a fraction of states in the upper Hubbard band are delocalized.

REFERENCES

1. N. F. Mott and É. A. Davis, *Electronic Processes in Non-Crystalline Materials* (Clarendon, Oxford, 1971; Mir, Moscow, 1974).
2. B. I. Shkalovskiĭ and A. L. Éfros, *Electronic Properties of Doped Semiconductors* (Nauka, Moscow, 1982; Springer-Verlag, New York, 1984).
3. I. M. Tsidil'kovskiĭ, *Electron Spectrum of Zero-gap Semiconductors* (Ural'skiĭ Rabochiĭ, Sverdlovsk, 1991).
4. B. L. Gel'mont and M. I. D'yakonov, Fiz. Tekh. Poluprovodn. **5**, 2191 (1971) [Sov. Phys. Semicond. **5**, 1905 (1971)].
5. H. Fritzsche and M. Cuevas, Phys. Rev. **119**, 1238 (1960).
6. E. M. Gershenzon, I. N. Kurilenko, and L. B. Litvak-Gorskaya, Fiz. Tekh. Poluprovodn. **8**, 1186 (1974) [Sov. Phys. Semicond. **8**, 768 (1974)].
7. E. M. Gershenzon, I. N. Kurilenko, and L. B. Litvak-Gorskaya, Fiz. Tekh. Poluprovodn. **8**, 1057 (1974) [Sov. Phys. Semicond. **8**, 689 (1974)].
8. H. Fritzsche, Phys. Rev. **99**, 408 (1960).
9. P. I. Baranskiĭ, V. P. Klochkov, and I. V. Potykevich, *Semiconductor Electronic* (Naukova Dumka, Kiev, 1975).
10. S. Zwerdling, W. H. Kleiner, and J. P. Theriault, J. Appl. Phys. **22**, 2118 (1961).
11. D. M. S. Bagguley, M. L. A. Robinson, and R. A. Stradling, Phys. Lett. **6**, 143 (1963).
12. G. Dresselhaus, A. F. Kip, C. Kittel, *et al.*, Phys. Rev. **100**, 580 (1955).
13. A. I. Elizarov and V. I. Ivanov-Omskiĭ, Fiz. Tekh. Poluprovodn. **15**, 927 (1981) [Sov. Phys. Semicond. **15**, 531 (1981)].
14. A. I. Elizarov, V. V. Bogoboyashchiĭ, and N. N. Berchenko, Fiz. Tekh. Poluprovodn. **18**, 455 (1984) [Sov. Phys. Semicond. **18**, 283 (1984)].
15. N. F. Mott, Philos. Mag. **19**, 835 (1969).
16. V. V. Bogoboyashchiĭ, A. I. Elizarov, V. A. Petryakov, *et al.*, Fiz. Tekh. Poluprovodn. **21**, 1469 (1987) [Sov. Phys. Semicond. **21**, 893 (1987)].
17. V. V. Bogoboyashchiy, Proc. SPIE-Int. Soc. Opt. Eng. **3486**, 325 (1997).
18. B. L. Gel'mont, A. R. Gadzhiev, B. L. Shklokovskiĭ, *et al.*, Fiz. Tekh. Poluprovodn. **8**, 2377 (1974) [Sov. Phys. Semicond. **8**, 1549 (1974)].
19. C. K. Shin and W. E. Spicer, J. Vac. Sci. Technol. B **5**, 1231 (1987).
20. A. V. Lyubchenko, E. A. Sal'kov, and F. F. Sizov, *Physical Basics of Semiconductor Infrared Photoelectronics* (Naukova Dumka, Kiev, 1984).
21. L. D. Landau and E. M. Lifshitz, *Quantum Mechanics: Non-Relativistic Theory*, 3rd ed. (Nauka, Moscow, 1974; Pergamon, Oxford, 1977).

Translated by T. Galkina

Semiconductors, Vol. 34, No. 4, 2000, pp. 405–409. Translated from Fizika i Tekhnika Poluprovodnikov, Vol. 34, No. 4, 2000, pp. 418–424.

ELECTRONIC AND OPTICAL PROPERTIES OF SEMICONDUCTORS

Cathodoluminescence and Raman Scattering in $Ga_{1-x}Al_xP$ Epitaxial Films

L. K. Vodop'yanov, V. I. Kozlovskiĭ, and N. N. Mel'nik

Lebedev Institute of Physics, Russian Academy of Sciences, Leninskiĭ pr. 53, Moscow, 117924 Russia

Submitted September 27, 1999; accepted for publication October 25, 1999

Abstract—Low-temperature cathodoluminescence and Raman scattering of $Ga_{1-x}Al_xP$ epitaxial layers ($0 \le x \le 0.8$) grown by liquid phase epitaxy on the GaP(100) substrate are studied. The obtained cathodoluminescence spectra indicate that the dependence of the indirect energy gap on the composition parameter x is nonlinear. This nonlinearity can be described by the parabolic function with the inflection parameter $b = 0.13$. Raman scattering studies show that the phonon spectrum of $Ga_{1-x}Al_xP$ consists of one (Al–P)-like vibrational mode and three (Ga–P)-like modes. © *2000 MAIK "Nauka/Interperiodica".*

INTRODUCTION

Layers of $Ga_{1-x}Al_xP$ solid solution are of interest in relation to the development of green-emission photodiodes, as well as of the barrier layers in quantum-confined $Ga_{1-x}Al_xP/GaP/AlP/Ga_{1-x}Al_xP$ structures [1]. The crystal lattice parameters of the end-member binary compounds of this solid solution practically coincide (mismatch $\Delta a/a < 0.001$ [2]), which is conducive to the growth of isomorphous heterostructures with a low concentration of defects. However, luminescent properties and the phonon spectrum of these layers have hardly been studied.

The composition dependence of the emission energy peak only in the narrow range $0.55 < x < 0.75$ of compositions at room temperature has been reported in [3]. These results, as well as the absorption spectra measured also at room temperature, indicate that the energy gap E_g is a linear function of x. However, according to [4], the dependence of E_g on x is not linear for some $Ga_{1-x}Al_xP$ alloys. In this work, we measured the low-temperature cathodoluminescence (CL) spectra for the $Ga_{1-x}Al_xP$ solid solution in a wide range of compositions; these spectra indicate that the dependence $E_g(x)$ is nonlinear.

Only a few papers have been devoted to the study of the phonon spectra of $Ga_{1-x}Al_xP$. Results of analysis of the lattice reflectivity spectra for the bulk $Ga_{1-x}Al_xP$ crystals, which may differ from similar spectra of the epitaxial films due to the difference in the growth conditions of the solid solution, were reported in [5]. Raman scattering (RS) of the $Ga_{1-x}Al_xP$ bulk crystals only in the narrow composition range $x < 0.23$ was studied in [6]. In [7], Raman spectra were excited by the radiation directed along the normal to the surface of the thin film grown by metal-organic chemical vapor deposition (MOCVD) on the GaP substrate. Because thin films of the alloy are partly transparent for the emission lines of a Kr laser, the very strong peaks from the GaP substrate prevail in the spectra. This hampers the observation of fine effects related to the composition rearrangement of the phonon spectrum. In this work, we measured the Raman spectra related to the long-wavelength optical phonons of the $Ga_{1-x}Al_xP$ epitaxial films in the wide composition range $x = 0$–0.8 using the micro-Raman technique [8]. This technique permitted us to observe vibrational excitations in thin epitaxial layers.

EXPERIMENT

$Ga_{1-x}Al_xP$ epitaxial films with x varying from 0 to 0.8 were grown on the GaP(100) substrate by liquid phase epitaxy from the Ga-rich melt at the State Institute of Rare Metals. The thickness of the grown layers varied from 3 to 10 μm. CL and RS measurements of the $Ga_{1-x}Al_xP$ films were performed without any additional surface treatment, except for $Ga_{1-x}Al_xP$ with $x = 0.8$. In the latter case, the surface of the epitaxial layer was coated with protective film to avoid surface hydrolysis in the air ambience. The protective film was removed just before the measurements of the CL spectra. Composition of the $Ga_{1-x}Al_xP$ films was predetermined by the composition of the AlP/GaP mixture in the liquid phase. According to [3], the composition of the epitaxial layers of the GaP–AlP system virtually coincides with the composition of the initial mixture in the liquid phase. Electron probe microanalysis of the sample with $x = 0.5$ confirmed the validity of such an assumption.

1063-7826/00/3404-0405$20.00

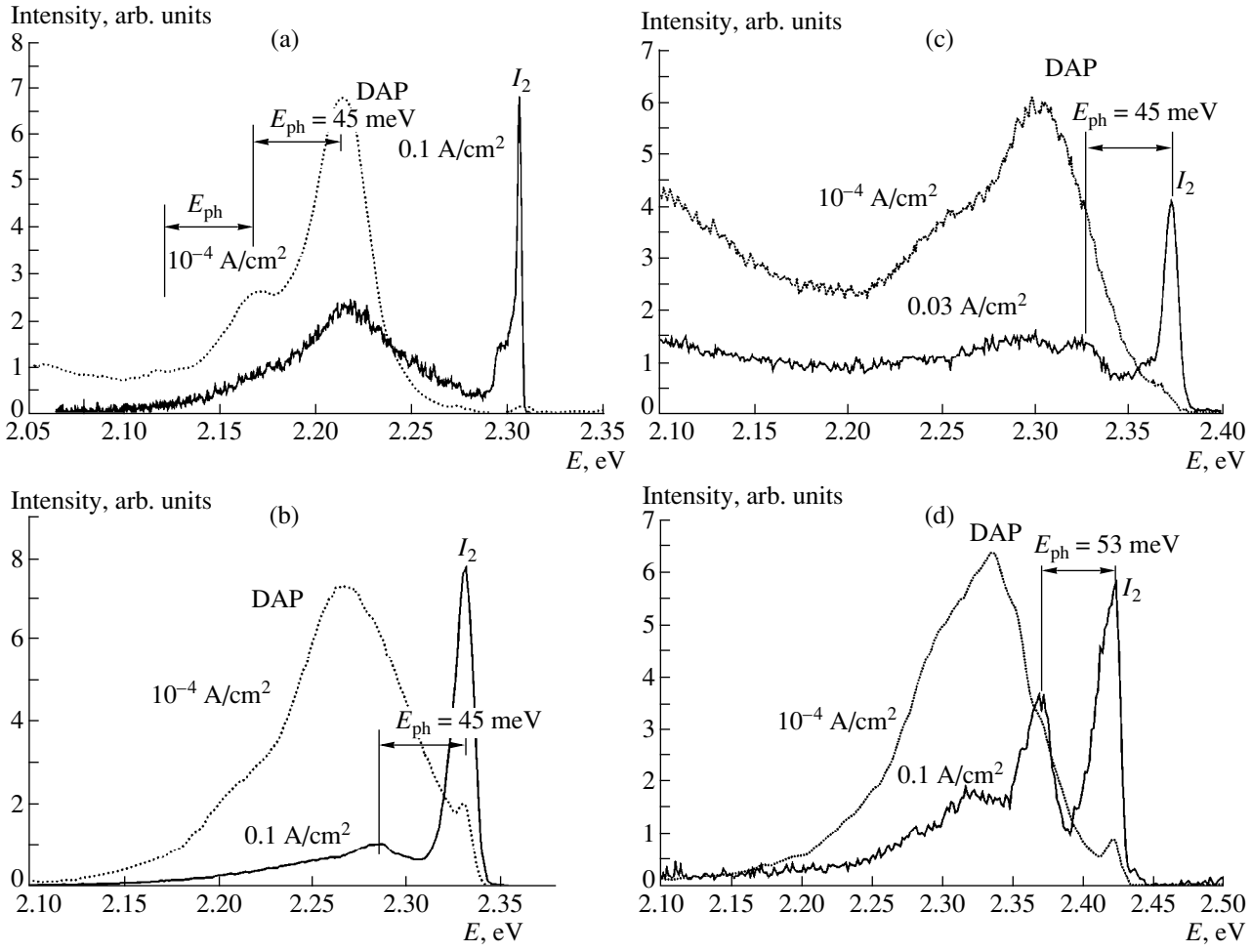

Fig. 1. Cathodoluminescence spectra of the $Ga_{1-x}Al_xP$ epitaxial films at T = 14 K, the electron energies (a, b) E_e = 30 and (c, d) 10 keV. (a) x = 0 (GaP), (b) x = 0.25, (c) x = 0.5, and (d) x = 0.7. The current densities of the electron beam j_e are indicated.

Cathodoluminescence was studied at the electron energy of 10 and 30 keV and the current of 1 μA. The diameter of the electron spot on the surface of the sample was varied from 1 mm to 30 μm. The sample was cooled to $T \le 14$ K with the help of a cryogenerator of the closed-type, operating in the McMahon cycle. The emission from the sample surface excited by the electron beam was analyzed. The spectra were recorded using a PGS-2 spectrograph with an attached photometer having a dispersion of 0.7 nm/mm.

The Raman spectra were excited by the 4880 Å line of an Ar laser. The micro-Raman technique was used; i.e., the laser beam was focused onto a cleaved surface of the epitaxial layer. This allowed us to decrease the influence of the GaP substrate on the RS spectra of the epitaxial layer. The size of the focused spot (1–3 μm) was smaller than the layer thickness. The spectra were recorded with a U-1000 spectrometer using backscattering configuration.

CATHODOLUMINESCENCE

CL spectra of pure GaP are shown in Fig. 1a. The most intense line for the electron beam diameter d_e = 1 mm, which corresponds to the current density j_e = 10^{-4} A/cm^2, is the emission line of the donor–acceptor pairs (DAP) with a peak near the energy of 2.21 eV [8]. The structure on the lower energy side of this line may be related to the corresponding phonon replicas. Because the half-width of the zero–phonon part of the emission line is rather large and the fine structure is not resolved, it is possible only to estimate the phonon energy from the energy position of the phonon replicas [$E_{ph} \approx 45$ meV (360 cm^{-1})]. The emission of DAP is saturated when the current density increases (d_e decreases) to 0.1 A/cm^2 and the narrow line (I_2) becomes distinct on the higher energy side of spectrum. This line may be assigned to the emission of excitons bound by neutral donors [8]. We note that the phonon replicas of the I_2 line are not evident in the spectrum.

CL spectra for three $Ga_{1-x}Al_xP$ compositions (x = 0.25, 0.5, and 0.7) are shown in Figs. 1b, 1c, and 1d, respectively. As one can see, the emission spectrum of the solid solution has approximately the same structure as that of pure GaP, although the lines are distinctly broadened and shifted towards a higher energy as x increases. Due to the broadening of the zero-phonon emission line of DAP, it is difficult to assess the variation in E_{ph} with x on the basis of the DAP line structure. However, as x increases, the intensity of the phonon replica of the more narrow I_2 line also increases. For the sample with $x = 0.7$, the energy difference between the zero-phonon line and its phonon replica is E_{ph} = 53 meV, which is much larger than that for the GaP sample (45 meV). Thus, rearrangement of the $Ga_{1-x}Al_xP$ phonon spectrum with x is observed. This rearrangement has been studied in detail by the RS method (see below).

The dependence of the energy position $E(I_2)$ of the I_2 peak on the parameter x of $Ga_{1-x}Al_xP$ layers is shown in Fig. 2. One can see that this dependence is nonlinear and that it may be approximated by a parabolic function with an inflection parameter equal to 0.13. Assuming that the energy difference between the emission peak I_2 and the edge of the indirect energy gap is nearly the same for all compositions of solid solution and is equal to 32 meV [8], we obtain the following dependence of the indirect energy gap on x: E_g^X (in eV) = 2.338 + $0.19x - 0.13x(1 - x)$.

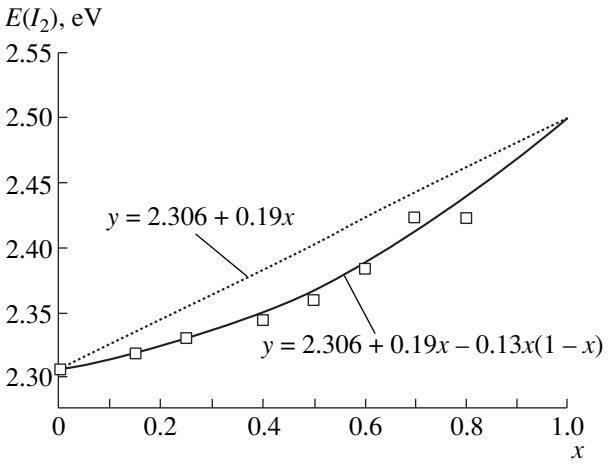

Fig. 2. Composition variation of the emission peak position on the short-wavelength line $E(I_2)$ in the cathodoluminescence spectra of $Ga_{1-x}Al_xP$ at T = 14 K and j_e = 0.1 A/cm^2. Dots represent the experimental data; the dashed line, the linear approximation; the solid line, the parabolic approximation with the inflection parameter equal to 0.13.

RAMAN SCATTERING

The typical RS spectra of the $Ga_{1-x}Al_xP$ solid solution with x = 0.15, 0.4, 0.6, and 0.8 are illustrated in Fig. 3. In the high-frequency part of the spectrum, two bands of AlP-like vibrations appear. The intensity of the band at $\omega \approx 440$ cm^{-1} increases with the AlP content, and its position virtually does not change. The second band shifts towards higher energies as x increases. In the low-frequency part of the spectrum where GaP-like modes are evident, a more complicated pattern is observed. A set of bands appears with not necessarily well-resolved frequencies and with intensities varying with x. Figure 4 shows the spectrum of the sample with x = 0.25; this spectrum was taken in a more narrow spectral interval. It is seen that many RS bands are not clearly pronounced: they appear as a shoulder at a wing of a more intense peak or against the noise background. To determine the true parameters of such bands, the computer program of the contour separation was used.

To explain the experimentally observed RS bands, we have to determine their origin (longitudinal or transverse phonons). For this purpose, polarization measurements were performed. Tensors of the RS effective cross sections for the polar zinc-blende cubic crystals were calculated in [9]. According to the selection rules following from the analysis of these tensors, only longitudinal phonons must manifest themselves in the polarized spectra (with parallel polarization of the exciting and scattered light) for excitation in the ⟨111⟩ direction. In the depolarized spectra (cross polarizations), both longitudinal and transverse phonons may appear.

An example of the spectrum of the alloy with x = 0.5 is shown in Fig. 5. The upper curve is related to the polarized spectrum $Z(X, X)\bar{Z}$, and the lower one, to the depolarized spectrum $Z(X, X)\bar{Z}$. It is seen that the intensity of the bands at $\omega \approx 405$ and ~480 cm^{-1} in the second case is significantly lower, which permits us to relate them to LO phonons.

As a result of the analysis of the $Ga_{1-x}Al_xP$-film experimental spectra, the dependences of the TO- and LO-phonon frequencies on the alloy composition x were obtained (Fig. 6). It can be seen that the AlP-like vibrations (two upper curves) exhibit classical two-mode behavior as the phonon spectrum is transformed. For low concentration of Al, the TO and LO branches converge to the local mode frequency $\omega \sim 440$ cm^{-1} of Al substituting P in the GaP lattice. This is in good agreement with the value $\omega = 438$ cm^{-1} experimentally obtained in [10]. For the GaP-like vibrations, three TO branches and one LO branch are observed. It is significant that, as the Ga concentration decreases, the TO and LO branches do not converge to the gap-mode of Ga in the AlP lattice. One of the plausible reasons for such behavior could be related to the absence of the energy gap between the allowed acoustic and optical energy bands in the AlP lattice. Unfortunately the phonon spectrum of this compound has not been studied. We do not know the origin of the fragment of the branch in the

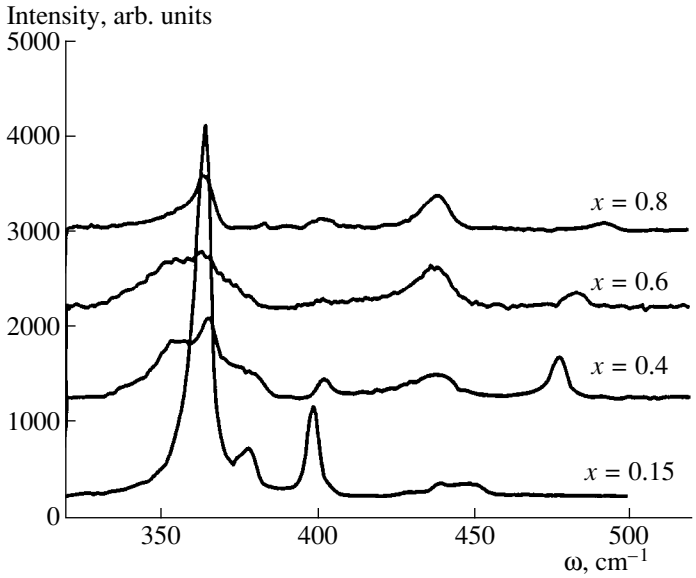

Fig. 3. Raman spectra of the $Ga_{1-x}Al_xP$ epitaxial films for different values of the composition parameters x = 0.15, 0.4, 0.6, and 0.8. Spectra are excited by the 488 nm line of an Ar laser.

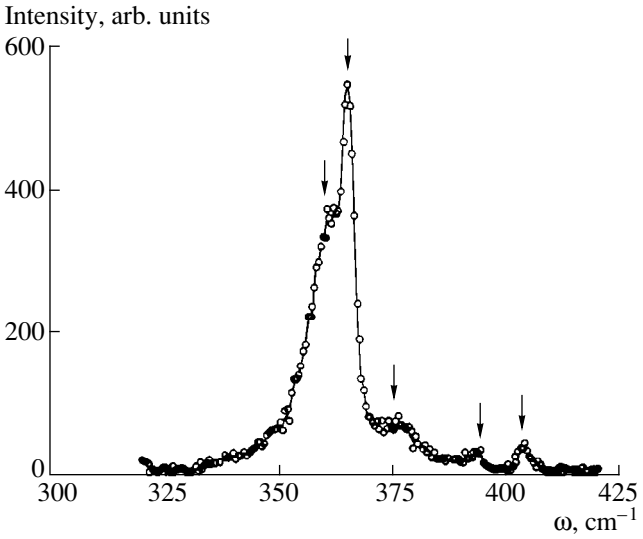

Fig. 4. Raman spectrum of the $Ga_{0.75}Al_{0.25}P$ epitaxial film.

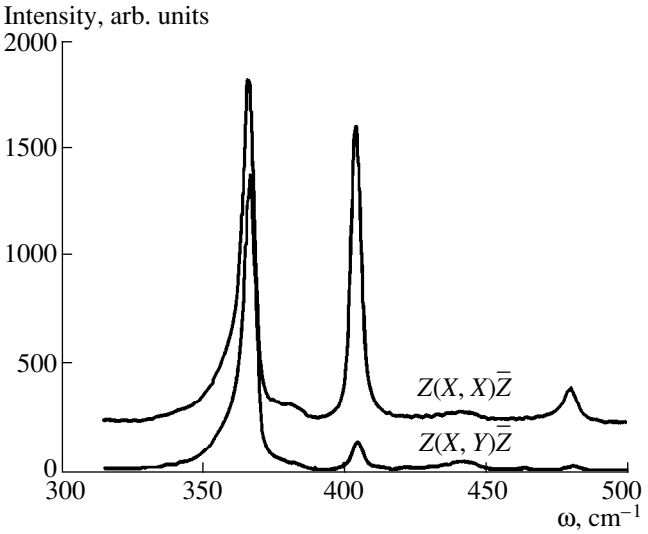

Fig. 5. Polarized $Z(X, X)\bar{Z}$ and depolarized $Z(X, Y)\bar{Z}$ Raman spectra of the $Ga_{0.5}Al_{0.5}P$ epitaxial film.

vicinity of $\omega \approx 393$ cm^{-1} that is observed for the alloy compositions x = 0.15–0.25. We should note a good agreement between the concentration dependences of the TO-branches obtained from the RS and infrared measurements [5]. Thus, two independent optical methods show the existence of three branches of transverse optical phonons in a system of (GaAl)P alloys.

A similar rearrangement of the phonon spectrum was previously observed in the well-studied system of $Hg_{1-x}Cd_xTe$ alloys [11, 12]. This behavior is explained on the basis of the quasi-molecular model, according to which the alloy crystal structure is considered to originate from five tetrahedral basic cells with a shared anion in the tetrahedron center and different configurations of cations in the tetrahedron vertexes. For each Hg–Te and Cd–Te vibration, four vibrational modes are possible, depending on the cell configuration. As the elementary cells are assumed to be noninteracting (in view of the predominantly covalent short-range nature of the bond in the tetrahedral compounds), the frequencies of these modes are independent of the alloy composition. The concentration dependence of the vibrational spectrum of the crystal is determined by the ratio

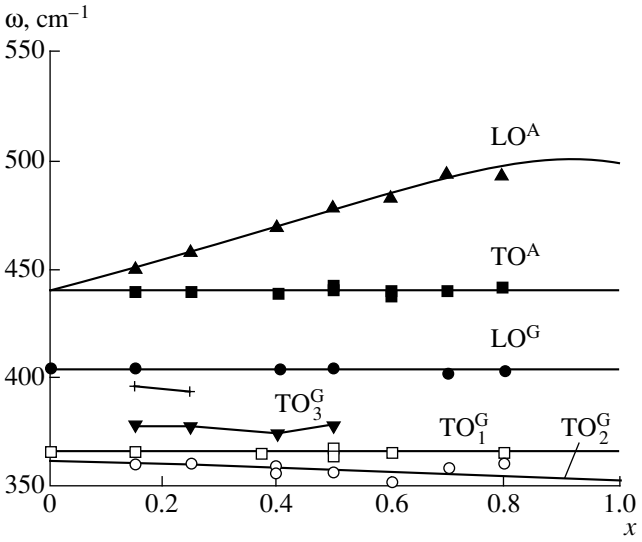

Fig. 6. Composition (x) variation of the $Ga_{1-x}Al_xP$ phonon spectrum.

of the number of cells with different configurations. However, not all modes may be resolved by measuring the vibrational spectrum, because, for different elementary cells, the mode splitting largely depends on the cation mass ratio as well as on the cation to anion mass ratio for each pair. This is probably the reason why, in the system of $Ga_{1-x}Al_xP$ alloys in our experiment, we observe one mode of Al–P-like and three modes of Ga–P-like vibrations.

CONCLUSION

In conclusion, the low-temperature cathodoluminescence studies of the $Ga_{1-x}Al_xP$ epitaxial layers in the composition range of $0 \le x \le 0.8$ provide evidence of the nonlinear dependence of the indirect energy gap on the solid solution composition at an inflection parameter equal to 0.13. Raman scattering studies show that the $Ga_{1-x}Al_xP$ phonon spectrum consists of one Al–P vibrational mode and three Ga–P modes.

ACKNOWLEDGMENTS

We thank A.A. Shlenskiĭ and L.V. Druzhinina from the State Institute of Rare Metals for growing the (GaAl)P films.

This work was supported by the Russian Foundation for Basic Research (project nos. 97-02-16791 and 96-15-96596) and by the State Scientific and Technical Program “Physics of Quantum and Wave Processes,” section “Fundamental Spectroscopy” (project no. 0.8.02.73).

REFERENCES

1. F. Issiki, S. Fukatsu, and Y. Shiraki, Appl. Phys. Lett. **67**, 1048 (1995).
2. V. I. Gavrilenko, A. M. Grekhov, D. V. Korbutyak, and V. G. Litovchenko, *Optical Properties of Semiconductors: A Handbook* (Naukova Dumka, Kiev, 1987).
3. H. Sonomura, T. Nanmori, and T. Miyauchi, Appl. Phys. Lett. **24**, 77 (1974).
4. S. S. Strel’chenko and V. V. Lebedev, *III–V Compounds: A Handbook* (Metallurgiya, Moscow, 1984).
5. G. Lucovsky, R. D. Burnham, and A. S. Alimonda, Phys. Rev. B: Solid State **14**, 2503 (1976).
6. B. X. Baĭramov, V. N. Bessolov, É. Yane, *et al.*, Pis’ma Zh. Tekh. Fiz. (Leningrad) **6**, 1432 (1980) [Sov. Tech. Phys. Lett. **6**, 618 (1980)].
7. G. Armelles, J. M. Calleja, and E. Múnoz, Solid State Commun. **65**, 779 (1988).
8. A. Bergh and P. J. Dean, *Light Emitting Diodes* (Clarendon, Oxford, 1976; Mir, Moscow, 1979).
9. R. Loudon, Adv. Phys. **13**, 423 (1964).
10. D. Hon, W. Fost, W. G. Spitzer, *et al.*, Phys. Rev. Lett. **25**, 1184 (1970).
11. S. P. Kozyrev, V. N. Pyrkov, and L. K. Vodop’yanov, Fiz. Tverd. Tela **34**, 3695 (1992) [Sov. Phys. Solid State **34**, 1978 (1992)].
12. S. P. Kozyrev, L. K. Vodop’yanov, and R. Triboulet, Phys. Rev. B: Condens. Matter **58** (3), 1374 (1998).

Translated by I. Kucherenko

Semiconductors, Vol. 34, No. 4, 2000, pp. 410–414. Translated from Fizika i Tekhnika Poluprovodnikov, Vol. 34, No. 4, 2000, pp. 425–429.

ELECTRONIC AND OPTICAL PROPERTIES OF SEMICONDUCTORS

Participation of the Electron Subsystem of a Crystal in the Reactions of Defect-Complex Decomposition in Semiconductors

N. I. Boyarkina

Institute of Physics of Semiconductors, Siberian Division, Russian Academy of Sciences, Novosibirsk, 630090 Russia

Submitted July 12, 1999; accepted for publication October 27, 1999

Abstract—The reactions of defect-complex decomposition in semiconductors are considered. The contribution from the electron subsystem to the reaction rate is taken into account by adding a change in the electron-subsystem energy of a crystal (as a result the reaction) to the energy barrier of the reaction. The theoretical and experimental data are compared by the example of the reactions of *E*-center decomposition in the *n*-type phosphorus-doped silicon. The dependence of temperature of isochronous annealing of *E* centers on a donor-impurity concentration is explained. The first stage of annealing ($T_{ann} \approx 400$ K) in a low-resistivity silicon is caused by the decomposition of the *E* center and can be explained using the model of a vacancy as the double acceptor center with a negative correlation energy and values of vacancy charge-exchange levels $E_V(0/-) = E_c - 0.09$ eV, $E_V(-/--) = E_c = -0.39$ eV. From the comparison between calculated and experimental data, the dissociation energy of *E* center and the degeneracy factor are obtained to be $U_{a0} \approx 0.96$ eV and $g_E^-/g_E^0 = 1/16$, respectively.

1. INTRODUCTION

In a number of studies (see, for example, [1, 2]), attention was drawn to the fact that, as a rule, the defects participating in quasi-chemical reactions in semiconductors are electrically charged and must affect the rates of forward and reverse reactions and, consequently, the concentrations of particular types of complexes.

In particular, the reactions between charged centers were considered in study [3] in which the expressions were obtained for the rate constants of formation and decomposition reactions for defect complexes in semiconductors. In a theoretical consideration of the decomposition reactions for multicharged centers carried out in [3], the energy expenditure associated with capturing and ejecting charge carriers by initial components of the reaction were taken into account by adding this expenditure to the energy barrier of the reaction.

However, the disappearance and appearance of a multicharged center in any of its possible charge states violates the quasi-equilibrium distribution of these centers over charge states. For example, even in the case of the "electron-neutral" reaction considered in [3],

$$C^0 \longrightarrow A^0 + B^0 \qquad (1)$$

(here, A, B, and C are the reactants; the superscripts indicate their charge states), a change in the concentration of any neutral multicharge centers (A, B, or C) causes a change in the distribution of this center over charge states. The reestablishment of the quasi-equilibrium according to a Fermi-level position by means of exchanging electrons between reactants and allowed bands (the conduction and valence bands) is associated with energy expenditure, which is neglected in this work.

Here, we propose a way for taking into account the energy expenditure associated with rearrangement of the crystal electron subsystem in the reactions of defect-complex decomposition in semiconductors.

2. CONSIDERATION OF THE CONTRIBUTION FROM THE ELECTRON SUBSYSTEM OF A CRYSTAL TO THE RATE OF REACTION OF A DEFECT-COMPLEX DECOMPOSITION

Our consideration is based on the example of the reaction, as a result of which a two-particle defect complex C decomposes into its constituents:

$$C \xrightarrow{\nu_C} A + B, \qquad (2)$$

where ν_C is the rate constant of this reaction.

Following [3], we assume that reaction (2) proceeds simultaneously along the mutually independent channels differing in charge states *Z* of decomposing complex C:

$$C^Z \xrightarrow{\nu_C^Z} A + B + Ne, \qquad (3)$$

where ν_C^Z is the rate constant of this reaction and the term *Ne* characterizes the "electron yield" of this reaction (*N* is the function of the parameters *Z* and ν_C^Z;

e stands for the electron). The charge states of formed centers A and B are specified by their charge-state functions.

The rates of reactions (2) and (3) can be written as

$$\frac{d[\mathrm{C}]}{dt} = -\nu_\mathrm{C}[\mathrm{C}], \tag{4}$$

$$\frac{d[\mathrm{C}^Z]}{dt} = -\nu_\mathrm{C}^Z[\mathrm{C}^Z], \tag{5}$$

where [C] and [C^Z] are the total and *Z*-charge-state concentrations of complex C, respectively. It is evident that

$$[\mathrm{C}] = \sum_Z [\mathrm{C}^Z]. \tag{6}$$

From relationships (4) and (6), we obtain

$$\begin{aligned}\frac{d[\mathrm{C}]}{dt} &= \sum_Z \frac{d[\mathrm{C}^Z]}{dt} \\ &= -\sum_Z \nu_\mathrm{C}^Z[\mathrm{C}^Z] = -\sum_Z \nu_\mathrm{C}^Z f_\mathrm{C}^Z[\mathrm{C}],\end{aligned} \tag{7}$$

where f_C^Z is the probability of finding complex C in charge state *Z*. Comparing relationships (4) and (7), we express the constant ν_C as

$$\nu_\mathrm{C} = \sum_Z \nu_\mathrm{C}^Z f_\mathrm{C}^Z. \tag{8}$$

As reaction (3) proceeds, the concentrations of centers A, B, and C vary. Following these variations, the centers exchange charges for reestablishing the violated quasi-equilibrium. We assume that this charge exchange progresses reasonably fast, so that its time τ_{rc} is much less than the reaction time τ_r. Qualitatively, this assumption follows from the known adiabatic approximation. The energy spent by the reactants in the charge exchange amounts to a fraction of the reaction energy barrier. This energy is equal to a variation in the electron-subsystem energy of a crystal as a result of this reaction. In this case, the expression for rate constants ν_C^Z is written as

$$\nu_\mathrm{C}^Z = \theta_\mathrm{C}^Z \exp\left(-\frac{\delta w_\mathrm{C}^{Ze}}{kT}\right), \tag{9}$$

where θ_C^Z is the rate constant for the reaction of decomposition of complex C in charge state *Z*, without taking into account a contribution from the electron subsystem of a crystal, and δw_C^{Ze} is the change in electron-subsystem energy as a result of reaction (3) per one decomposed complex C. For the constant θ_C^Z, we use expression (2.12) from [3] to obtain

$$\theta_\mathrm{C}^Z = \theta_{\mathrm{C}0}^Z \exp\left(-\frac{U_\mathrm{C}^Z}{kT}\right), \tag{10}$$

where U_C^Z is the energy barrier of the reaction of decomposition of complex C in charge state *Z* without taking into account the electron-subsystem contribution and $\theta_{\mathrm{C}0}^Z$ is the preexponential factor depending on the reaction radius and the frequency of oscillation of defects, which are the components of the complex.

A change δw_C^{Ze} in the electron-subsystem energy of a crystal as a result of reaction (3) is determined by a change in concentrations of charged centers A, B, and C. For the sake of definiteness, we consider a crystal with the *n*-type conduction. As complex C decays in amounts equal to δ[C] and centers A and B are formed in amounts of δ[A] = δ[B] = δ[C], the following number of electrons pass from the conduction band to the levels of newly formed centers A and B:

$$\begin{aligned}\delta n_\mathrm{A} &= (f_\mathrm{A}^- + 2f_\mathrm{A}^{--} + \ldots - f_\mathrm{A}^+ - 2f_\mathrm{A}^{++} - \ldots)\delta[\mathrm{A}], \\ \delta n_\mathrm{B} &= (f_\mathrm{B}^- + 2f_\mathrm{B}^{--} + \ldots - f_\mathrm{B}^+ - 2f_\mathrm{B}^{++} \ldots)\delta[\mathrm{B}],\end{aligned} \tag{11}$$

and the number of electrons equal to

$$\delta n_\mathrm{C} = (f_\mathrm{C}^- + 2f_\mathrm{C}^{--} + \ldots - f_\mathrm{C}^+ - 2f_\mathrm{C}^{++} - \ldots)\delta[\mathrm{C}] \tag{12}$$

pass into the conduction band from decomposed complexes C.

In this case, a change in the electron-subsystem energy per one decomposed complex C amounts to

$$\delta w_\mathrm{C}^{Ze} = (\Delta W_\mathrm{A}^{Ze} + \Delta W_\mathrm{B}^{Ze} + \Delta W_\mathrm{C}^{Ze})/\delta[\mathrm{C}], \tag{13}$$

where

$$\begin{aligned}\Delta W_\mathrm{A}^{Ze} &= [-[\varepsilon_\mathrm{A}^- f_\mathrm{A}^- + (\varepsilon_\mathrm{A}^- + \varepsilon_\mathrm{A}^{--}) f_\mathrm{A}^{--} + \ldots] \\ &\quad + [\varepsilon_\mathrm{A}^+ f_\mathrm{A}^+ + (\varepsilon_\mathrm{A}^+ + \varepsilon_\mathrm{A}^{++}) f_\mathrm{A}^{++} + \ldots]]\delta[\mathrm{A}],\end{aligned} \tag{14}$$

$$\begin{aligned}\Delta W_\mathrm{B}^{Ze} &= [-[\varepsilon_\mathrm{B}^- f_\mathrm{B}^- + (\varepsilon_\mathrm{B}^- + \varepsilon_\mathrm{B}^{--}) f_\mathrm{B}^{--} + \ldots] \\ &\quad + [\varepsilon_\mathrm{B}^+ f_\mathrm{B}^+ + (\varepsilon_\mathrm{B}^+ + \varepsilon_\mathrm{B}^{++}) f_\mathrm{B}^{++} + \ldots]]\delta[\mathrm{B}],\end{aligned} \tag{15}$$

$$\begin{aligned}\Delta W_\mathrm{C}^{Ze} &= [[\varepsilon_\mathrm{C}^- f_\mathrm{C}^- + (\varepsilon_\mathrm{C}^- + \varepsilon_\mathrm{C}^{--}) f_\mathrm{C}^{--} + \ldots] \\ &\quad - [\varepsilon_\mathrm{C}^+ f_\mathrm{C}^+ + (\varepsilon_\mathrm{C}^+ + \varepsilon_\mathrm{C}^{++}) f_\mathrm{C}^{++} + \ldots]]\delta[\mathrm{C}].\end{aligned} \tag{16}$$

Eventually, we can express the change in the electron-subsystem energy as

$$\begin{aligned}\delta w_\mathrm{C}^{Ze} &= -[\varepsilon_\mathrm{A}^- f_\mathrm{A}^- + (\varepsilon_\mathrm{A}^- + \varepsilon_\mathrm{A}^{--}) f_\mathrm{A}^{--} + \ldots] \\ &\quad + [\varepsilon_\mathrm{A}^+ f_\mathrm{A}^+ + (\varepsilon_\mathrm{A}^+ + \varepsilon_\mathrm{A}^{++}) f_\mathrm{A}^{++} + \ldots]\end{aligned}$$

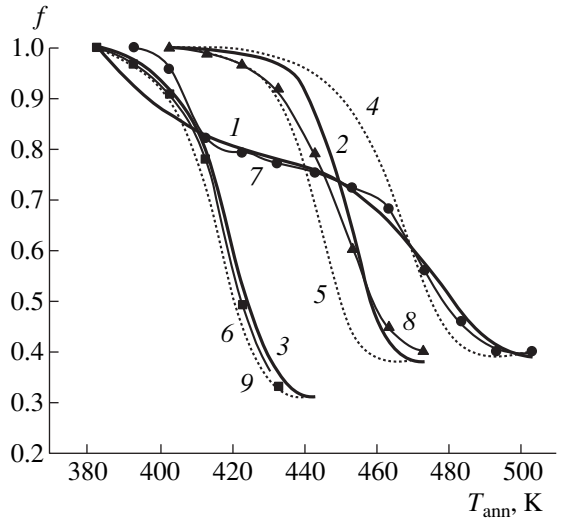

Fig. 1. Fraction of the unrecovered concentration of electrons in the conduction band of an irradiated *n*-type silicon as a function of isochronous-annealing temperature T_{ann}. Curves *1–6* represent the calculation; dots and curves *7–9* drawn through them are experimental [1]. Resistivity of initial silicon ρ = (*1*), (*4*), and (*7*) 0.1; (*2*), (*5*), and (*8*) 1.0; and (*3*), (*6*), and (*9*) 10 Ω cm. An initial pre-annealing electron concentration n_{rad} = (*1*), (*4*), and (*7*) 500×10^{14}; (*2*), (*5*), and (*8*) 37×10^{14}; and (*3*), (*6*), and (*9*) 2.1×10^{14} cm^{-3}.

$$\begin{aligned} &-[\varepsilon_B^- f_B^- + (\varepsilon_B^- + \varepsilon_B^{--}) f_B^{--} + \ldots] \\ &+[\varepsilon_B^+ f_B^+ + (\varepsilon_B^+ + \varepsilon_B^{++}) f_B^{++} + \ldots] \\ &+[\varepsilon_C^- f_C^- + (\varepsilon_C^- + \varepsilon_C^{--}) f_C^{--} + \ldots] \\ &-[\varepsilon_C^+ f_C^+ + (\varepsilon_C^+ + \varepsilon_C^{++}) f_C^{++} + \ldots]. \end{aligned} \tag{17}$$

It can be seen that δw_C^{Ze} depends on temperature and on the Fermi-level position in the forbidden band but is the same for all the charge states of decomposing complex C; i.e., $\delta w_C^{Ze} = \delta w_C^e$. Expressions (9) and (8) take the form

$$\nu_C^Z = \theta_C^Z \exp\left(-\frac{\delta w_C^e}{kT}\right), \tag{18}$$

$$\nu_C = \sum_Z \theta_C^Z f_C^Z \exp\left(-\frac{\delta w_C^e}{kT}\right). \tag{19}$$

3. ANNEALING OF *E* CENTERS: CALCULATION AND COMPARISON WITH THE EXPERIMENT

In order to compare the result obtained with the experimental data, we consider a particular example of the decomposition of the *E* center in silicon (the complex consisting of vacancy *V* and an atom of the doping donor impurity D from Group V of elements):

$$E \xrightarrow{\nu_E} V + \mathrm{D}, \tag{20}$$

where ν_E is the rate constant for this reaction. From formulas (19), (17), and (10), we obtain the expression for ν_E:

$$\nu_E = \exp(-\delta w_E^e / kT)(\theta_E^0 f_E^0 + \theta_E^{-1} f_E^-), \tag{21}$$

where

$$\delta w_E^e = \varepsilon_E f_E^- + \varepsilon_D f_D^+ - \varepsilon_V^- f_V^- - (\varepsilon_V^- + \varepsilon_V^{--}) f_V^{--}; \tag{22}$$

$$\theta_E^Z = \theta_{E0}^Z \exp\left(-\frac{U_E^Z}{kT}\right), \quad Z = -1, 0. \tag{23}$$

The results of calculations of recovery of the electron concentration in the conduction band of a silicon crystal with various levels of doping during isochronous annealing of *E* centers are shown in Fig. 1. The calculations were performed according to formulas (21)–(23). The annealing was assumed to proceed by the mechanism of decomposition of a complex into its constituents. The activation energy for the annealing of the *E* center in both charge states [neutral (U_E^0) and negative (U_E^-)] was taken to be the same and equal to U_{a0} = 0.96 eV. In Fig. 1, we present a fraction of the unrecovered electron concentration

$$f = \frac{n_0 - n_T}{n_0 - n_{rad}},$$

where n_0, n_{rad}, and n_T are the electron concentrations before the irradiation, following the irradiation, and following the annealing at temperature $T = T_{ann}$, respectively, and where $(n_0 - n_{rad})/n_0 \approx 0.25$ is the degree of compensation after irradiation.

Experimentally, the annealing of the *E* center was investigated in many studies (see, for example, [1, 4–8]). The authors of [4] proposed a mechanism for annealing the *E* center by means of its migration as a whole to sinks and obtained a value of annealing-activation energy for the neutral *E* center to be equal to (0.93 ± 0.05) eV. In [5], from the results of isochronous annealing for a high-resistivity silicon (ρ ≥ 50 Ω cm) irradiated with γ-quanta, the annealing process was found to correspond to a first-order reaction with activation energies $E_a \approx 0.94$ eV for the phosphorus-doped silicon and $E_a \approx 1.5$ eV for the arsenic-doped silicon. The authors of [1] presented some reasoning in favor of another mechanism, namely, the dissociation of the *E* center into its constituents: an atom of the doping donor impurity and a vacancy migrating across the crystal following the *E*-center dissociation. In study [6], based on the analysis of results for annealing *E* centers introduced into the arsenic-doped silicon by electron irradi-

ation, it was concluded that the dominant process in the *E*-center removal is its dissociation.

An experimentally observed increase in temperature of the corresponding isochronous-annealing stage of *E* centers with increasing donor concentration was explained in [1] by the influence of a charge state of the centers on the rate of their thermal decomposition. In the same study, the activation energies for *E*-center annealing were estimated as $E_a \approx 0.9$–1.2 eV in the neutral state and as $E_a \approx 1.2$–1.6 eV in the negative charge state.

The experiments with the annealing of *E* centers (see, for example, [1]) showed that a low-resistivity silicon ($\rho \le 1\ \Omega$ cm) is annealed in two stages: at $T_{\text{ann}} \approx 400$ K and at $T \approx 460$ K, with both stages caused by *E*-center annealing, as was assumed in [1] and shown in [7].

On the assumption that $U_E^- = U_E^0 = U_{a0}$, an effective activation energy U_a^{eff} for the *E*-center-annealing process is determined by the following expression:

$$U_a^{\text{eff}} = U_{a0} + \delta w_E^e + U_{\text{m}V}, \tag{24}$$

where U_{a0} is the dissociation energy for a complex without taking into account an electron-subsystem contribution; δw_E^e is the change in the electron-subsystem energy of a crystal as a result of the reaction; and $U_{\text{m}V}$ is the migration energy for a vacancy released on the decomposition of the complex ($U_{\text{m}V^-} = U_{\text{m}V^{--}} =$ 0.18 eV, and $U_{\text{m}V^0} = 0.38$ eV).

Thus,

$$\begin{aligned} U_a^{\text{eff}} &= U_{a0} + \varepsilon_E f_E^- + \varepsilon_{\text{P}} f_{\text{P}}^+ - \varepsilon_V^- f_V^- \\ &\quad - (\varepsilon_{\text{P}}^{--} + \varepsilon_V^-) f_{\text{V}}^{--} + U_{\text{m}V}. \end{aligned} \tag{25}$$

It can be seen that U_a^{eff} depends on the Fermi-level position and temperature. The dependence of characteristics of annealing on the doping level of a material is caused by the fact that an effective activation energy U_a^{eff} of the process depends on the Fermi-level position. The same reason can account for different kinetics of annealing of the *E* center in a material irradiated with different doses and, thus, differently compensated (see, for example, Fig. 3 in [8]).

The effective activation energy also varies in the course of annealing. The annealing stage at $T_{\text{ann}} \approx 400$ K in a low-resistivity silicon is caused by a variation in U_a^{eff}, when the Fermi level passes through the level corresponding to a change in the vacancy charge state ($E_c - \varepsilon_V^{--}$) or ($E_c - \varepsilon_V^-$). In this case, the variation δU_a^{eff} in the activation energy is equal to either ε_V^{--} or ε_V^-, respectively. The Fermi-level position found from experimental data [1] for which this variation in U_a^{eff} takes place amounts to $\varepsilon_{\text{F}} \approx 0.24$ eV. The variation δU_a^{eff} in activation energy is defined by this value. However, it follows from the calculations that such a value of δU_a^{eff} is insufficient for observing the annealing stage at $T_{\text{ann}} \approx 400$ K.

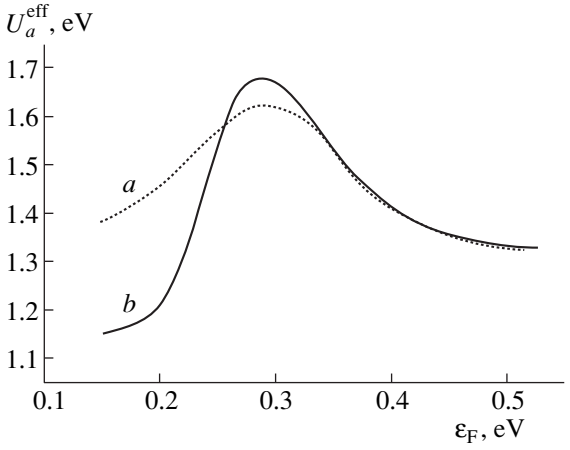

Fig. 2. Calculation of an effective activation energy (U_a^{eff}) for the process of the annealing of the *E* center as a function of the Fermi-level position (ε_{F}) in the energy gap of *n*-Si at temperature $T = 390$ K ($U_{a0} = 0.96$, $g_E^-/g_E^0 = 1/16$) for the cases when a vacancy represents: (*a*) a conventional double acceptor center, and (*b*) a double acceptor center with the negative correlation energy.

A better agreement with the experiment was obtained if the concept of the vacancy as a system $\{V^0, V^-, V^{--}\}$ with a negative correlation energy (see [9]) was used. In this case, $f_V^- \ll 1$ and position of the energy level in the forbidden band, such that a value U_a^{eff} changes when the Fermi level passes through this energy level, amounts to $(\varepsilon_V^- + \varepsilon_V^{--})/2 = 0.24$ eV. In this case, the variation δU_a^{eff} in the activation energy amounts to $(\varepsilon_V^- + \varepsilon_V^{--})/2 = 0.48$ eV. If we assume that $\varepsilon_V^- = E_c - E_V(0/-) = 0.09$ eV, we obtain $\varepsilon_V^{--} = E_c - E_V(-/--) = 0.39$ eV. In Fig. 2, we show the dependence of U_a^{eff} on the Fermi level position ε_{F}. These dependences were calculated by formula (25) at $T = 390$ K for the cases:

(a) a vacancy is a double acceptor center

$$\begin{aligned} E_V(0/-) &= E_c - \varepsilon_V^- = E_c - 0.24\ \text{eV}, \\ E_V(-/--) &= E_c - \varepsilon_V^{--} = E_c - 0.09\ \text{eV}; \end{aligned} \tag{26}$$

(b) a vacancy is a double acceptor center with a negative correlation energy

$$E_V(0/-) = E_c - \varepsilon_V^- = E_c - 0.09 \text{ eV},$$
$$E_V(-/--) = E_c - \varepsilon_V^{--} = E_c - 0.39 \text{ eV}. \quad (27)$$

Curves *1–3* in Fig. 1 represent the results of calculations to recovery of the electron concentration in the conduction band of *n*-Si on annealing of the *E* center, on the assumption that a vacancy is a double acceptor center with a negative correlation energy. Dotted curves *4–6* are the result of calculations carried out on the assumption that a vacancy is a conventional double acceptor center. The results of calculations performed without taking into account an electron-subsystem contribution and activation energies of annealing of the *E* center equal to 1.19 eV in the neutral state and to 1.6 eV in the negative charge state (see [1]) virtually coincide with the results obtained, with allowances made for an electron-subsystem contribution and the vacancy model as a conventional double acceptor center (curves *4–6* in Fig. 1). In Fig. 1, we also show experimental data obtained in [1] on annealing of *n*-Si irradiated with electrons; these are curves *7–9* drawn through experimental points. It can be seen that the results of calculations (curves *1–3*) agree well with the experimental data on annealing of the *E* center in the irradiated *n*-Si (curves *7–9*).

4. CONCLUSION

Using the mechanism proposed in this study for the participation of the electron subsystem of a crystal in the reactions of defect-complex decomposition in semiconductors, we explained the dependence of the temperature corresponding to effective annealing of *E* centers in irradiated *n*-Si on the donor-impurity concentration. Using the model of a vacancy as a double acceptor center with a negative correlation energy, we explained the two-stage annealing of *E* centers in a low-resistivity silicon. Values of certain parameters were determined for *E* centers and a vacancy in the phosphorus-doped *n*-Si: the dissociation energy $U_{a0} \simeq 0.96$ eV of the *E* center, the degeneracy factor $g_E^-/g_E^0 = 1/16$, $E_V(0/-) = E_c - \varepsilon_V^- = E_c - 0.09$, $E_V(-/--) = E_c - \varepsilon_V^{--} = E_c - 0.39$ eV.

The satisfactory agreement between the calculated and experimental data favors the proposed mechanism of participation of the electron subsystem of a crystal in the reactions of the defect-complex decomposition in semiconductors.

ACKNOWLEDGMENTS

We thank S.S. Shaĭmeev, L.N. Safronov, and A.V. Vasil'ev for their helpful participation in discussions.

This work was supported by the Russian Foundation for Basic Research, project no. 96-15-97272.

REFERENCES

1. L. C. Kimerling, H. M. DeAngelis, and C. P. Carnes, Phys. Rev. B: Condens. Matter **3**, 427 (1971).
2. A. I. Baranov, A. V. Vasil'ev, and L. S. Smirnov, Fiz. Tekh. Poluprovodn. (Leningrad) **20**, 1132 (1986) [Sov. Phys. Semicond. **20**, 713 (1986)].
3. A. I. Baranov, A. V. Vasil'ev, V. F. Kuleshov, *et al.*, Preprint (Chernogolovka, 1985).
4. G. D. Watkins and J. W. Cobett, Phys. Rev. A: Gen. Phys. **134**, 1359 (1954).
5. M. Hirata, M. Hirata, and H. Saito, J. Appl. Phys. **37**, 1867 (1966).
6. A. O. Evwaraye, J. Appl. Phys. **48**, 1840 (1977).
7. A. O. Evwaraye, Appl. Phys. Lett. **29**, 476 (1976).
8. L. C. Kimerling and C.P. Carnes, J. Appl. Phys. **42**, 3548 (1971).
9. G. A. Baraff, E. O. Kane, and M. Schlüter, Phys. Rev. B: Condens. Matter **21**, 5662 (1980).

Translated by V. Bukhanov

Semiconductors, Vol. 34, No. 4, 2000, pp. 415–417. Translated from Fizika i Tekhnika Poluprovodnikov, Vol. 34, No. 4, 2000, pp. 430–432.

ELECTRONIC AND OPTICAL PROPERTIES OF SEMICONDUCTORS

Bandgap and Intrinsic Carrier Concentration in HgCdMnTe and HgCdZnTe

O. A. Bodnaruk, A. V. Markov, S. É. Ostapov*, I. M. Rarenko, and A. F. Slonetskiĭ

Fed'kovich State University, ul. Kotsyubinskogo 2, Chernovtsy, 274012 Ukraine

** e-mail: ostap@chdu.cv.ua*

Submitted April 27, 1999; accepted for publication October 28, 1999

Abstract—The main band parameters of HgCdMnTe and HgCdZnTe quaternary solid solutions were theoretically and experimentally studied. Empirical formulas were proposed for the bandgap and intrinsic carrier concentration in a wide range of temperatures and compositions. Calculated values were found to conform well to experimental data. © *2000 MAIK "Nauka/Interperiodica".*

HgCdTe solid solutions have a number of unique physical properties, which make such materials promising for the development of infrared radiation detectors. However, the instability of this material hinders its widespread application. This instability was theoretically shown in [1] to be caused by a marked difference in the Cd and Hg atomic radii. Hence, the material stability can be increased by introducing Mn or Zn, whose atomic radius is closer to that of Hg atoms.

Although such materials as HgCdMnTe and HgCdZnTe are promising, their basic parameters, first of all, the bandgap, intrinsic carrier concentration, and effective electron mass are not adequately studied.

The basic band parameters of HgCdMnTe and HgCdZnTe quaternary solid solutions can be calculated by the method proposed in [2], where an initial solution was considered as a combination of three ternary ones. However, since that calculation is rather cumbersome, we use a simpler method (see [3]), where a quaternary material is represented as a set of two ternary ones. For instance, the expression for the HgCdMnTe bandgap is written as

$$E_g(\mathrm{Hg}_z\mathrm{Cd}_x\mathrm{Mn}_y\mathrm{Te}) = 0.5E_g(\mathrm{Hg}_{1-u}\mathrm{Cd}_u\mathrm{Te}) + 0.5E_g(\mathrm{Hg}_{1-w}\mathrm{Mn}_w\mathrm{Te}), \quad (1)$$

where $u = 2x$, $w = 2y$, and $z = 1 - x - y$. Using the empirical formulas for HgCdTe [4], HgZnTe [5], and HgMnTe [6] bandgaps, the values of E_g in $\mathrm{Hg}_{1-x-y}\mathrm{Cd}_x\mathrm{Mn}_y\mathrm{Te}$ and $\mathrm{Hg}_{1-x-y}\mathrm{Cd}_x\mathrm{Zn}_y\mathrm{Te}$ are respectively given by

$$E_g(x, y, T) = -0.302 + 5.125\times10^{-4}T - (x + 2.287y)\times10^{-3}T + 1.93(x + 2,197y) - 1.62(x^2 + 2.728y^2) + 0.272(12.235x^3 - y^3), \quad (2)$$

and

$$E_g(x, y, T) = -0.301 + 1.93x + 2.29\times10^{-2}y^{1/2} + 2.731y - 1.62x^2 + 5.35\times10^{-4}T \times (1 - 2x - 0.35y^{1/2} - 1.28y) + 3.328x^3 - 1.248y^2 + 2.132y^3. \quad (3)$$

The accuracy of formula (2) was checked by comparing it with the data in [7] at $T = 7$ K (see Fig. 1) and [8] at $T = 300$ K. Formula (3) was checked by comparison with the data in [9] for HgCdZnTe (see Table 1).

As follows from Fig. 1 and Table 1, empirical formulas (2) and (3) quite accurately describe HgCdMnTe and HgCdZnTe bandgaps at various compositions and temperatures.

Using (2) and (3), we calculated the intrinsic carrier concentration, Fermi level position, and effective electron mass for studied materials. The calculation technique based on the *k–p* method was outlined in detail in [6].

The calculated carrier concentrations were compared to the data [10] of Hall measurements in HgCdMnTe and HgCdZnTe crystals grown by modi-

Table 1. Comparison of the results of calculations by formula (3) to the data of [9] for HgCdZnTe at $T = 95$ K

Composition		E_g, eV		
x	y	Calculation [9]	Experiment [9]	Calculation by formula (3)
0.07	0.17	0.322	0.328	0.301
0.07	0.20	0.382	0.383	0.374
0.12	0.18	0.416	0.409	0.406
0.07	0.16	0.282	0.277	0.276

1063-7826/00/3404-0415$20.00 © 2000 MAIK "Nauka/Interperiodica"

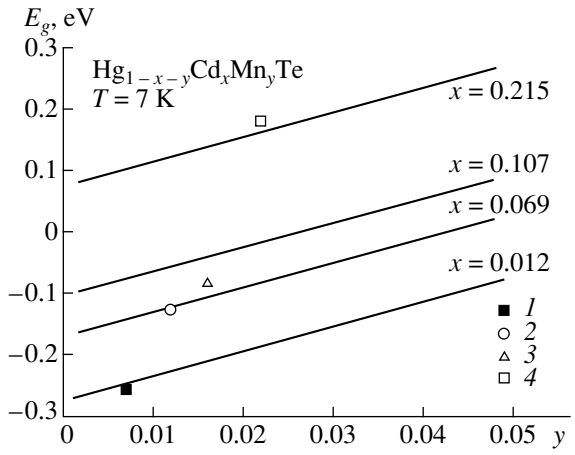

Fig. 1. Dependences of the HgCdMnTe bandgap on Mn content, calculated by formula (2) (solid lines) and according to the experimental data of [7] (dots). Mole fractions Cd (x) and Mn (y) are (*1*) 12 and 7, (*2*) 6.9 and 1.2, (*3*) 10.7 and 1.6, and (*4*) 21.5 and 2.2%.

fied zone melting. Ingots 12–20 mm in diameter and 12–18 cm long had axial and radial inhomogeneities $\Delta x_L \lesssim \pm 0.01$ and $\Delta x_R \lesssim \pm 0.005$, respectively, in the fairly homogeneous region in the middle of the sample. Mechanical and chemical treatment of the samples to be measured did not differ from the conventional procedure for HgCdTe wafers and did not introduce any damaged layers. The HgCdTe composition determined using a Camscan-4DV microanalyzer was found to vary along the sample within $\Delta x = \pm 0.003$.

Calculated concentrations of intrinsic carriers in comparison with the Hall measurements are plotted in Figs. 2 and 3. As is evident, a reasonably good agreement with the experimental data is observed in the domain of intrinsic conduction. An additional comparison with the data of [9] shows that the values of n_i coincide within 3–4%, notwithstanding the different bandgap calculation techniques.

The above estimates show that the conduction band instability is low in the considered materials (a parabolic equivalent of the effective mass differs from the exact values by no more than 30%), which allows us to apply the parabolic approximation to calculate the intrinsic carrier concentration. The least-squares method was used to find the following empirical relationships for the concentration n_i.

For $Hg_{1-x-y}Cd_xMn_yTe$ within the ranges of $0 \le x \le 0.5$, $0.03 \le y \le 0.2$, and $50 \le T \le 350$ K,

$$n_i(x, y, T)$$

$$= [5.84 - 4.42x + 2.87y + 2.53 \times 10^{-3}(1 + x + y)] \quad (4)$$

$$\times 10^{14} E_g^{0.75} T^{1.5} \exp(-E_g/2kT),$$

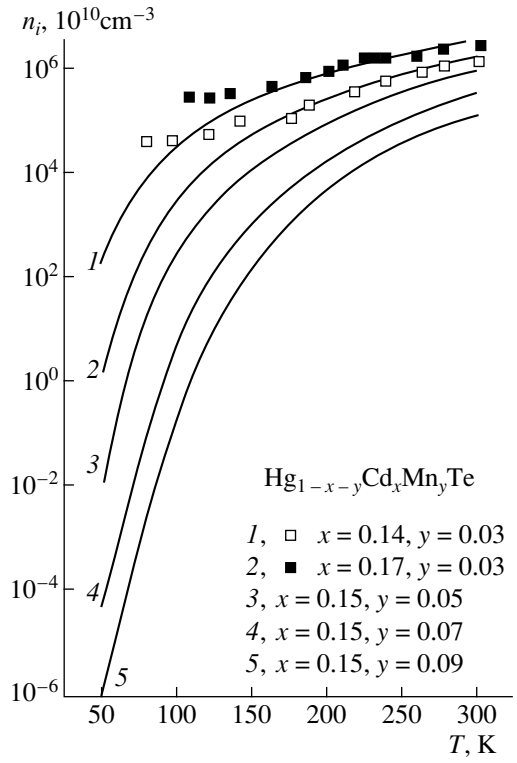

Fig. 2. Calculated and experimental temperature dependences of the intrinsic carrier concentration in the $Hg_{1-x-y}Cd_xMn_yTe$ solid solution.

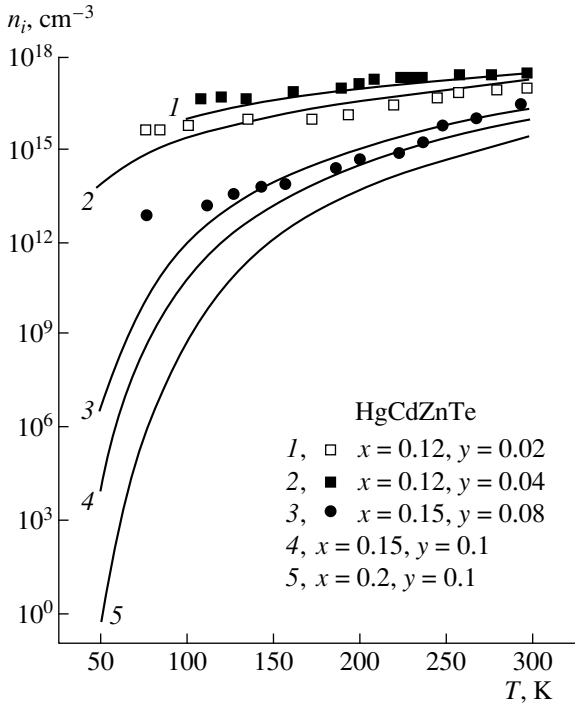

Fig. 3. Calculated and experimental temperature dependences of the intrinsic carrier concentration in the $Hg_{1-x-y}Cd_xZn_yTe$ solid solution.

Table 2. Coefficients *A*, *B*, *C*, and *D* in formula (6) for HgCdMnTe and HgCdZnTe

Material	*A*	*B*	*C*	*D*
HgCdMnTe	6.48	−4.42	−6.54	1.42×10^{-3}
HgCdZnTe	5.84	−4.42	2.87	2.53×10^{-3}

and for $Hg_{1-x-y}Cd_xZn_yTe$ within the ranges of $0 \le x \le 0.5$, $0.03 \le y \le 0.5$, and $50 \le T \le 350$ K,

$$n_i(x, y, T) = [6.48 - 4.42x - 6.54y + 1.42 \times 10^{-3}(1 + x + y)] \times 10^{14} E_g^{0.75} T^{1.5} \exp(-E_g/2kT). \quad (5)$$

Thus, the intrinsic carrier concentration in HgCdMnTe and HgCdZnTe in the parabolic approximation is given by the empirical formula

$$n_i(x, y, T) = [A + Bx + Cy + DT(1 + x + y)] \times 10^{14} E_g^{0.75} T^{1.5} \exp(-Eg/2kT) \quad (6)$$

with coefficients *A*, *B*, *C*, and *D* listed in Table 2.

The use of formula (6) with these coefficients to calculate the intrinsic carrier concentration in HgCdMnTe and HgCdZnTe in the parabolic approximation yields an error no greater than 4% in the temperature range 50–350 K for a variety of compositions.

REFERENCES

1. A. Sher, A. Chen, W. Spicer, *et al.*, J. Vac. Sci. Technol., A **3**, 105 (1985).
2. C. K. Williams, T. N. Glisson, J. R. Hauses, *et al.*, J. Electron. Mater. **7**, 639 (1978).
3. S. E. Ostapov, O. A. Bodnaruk, I. N. Gorbatiuk, *et al.*, in *Proceedings of School-Conf: PPMSS, Chernovtsi, Ukraine, 1995* (Ruta, Chernovtsi, 1995), p. 158.
4. G. L. Hansen, J. L. Schmit, and T. N. Cusselman, J. Appl. Phys. **53**, 7099 (1982).
5. K. Joswikowski and A. Rogalski, Infrared Phys. **28**, 101 (1988).
6. O. A. Bodnaruk, I. N. Gorbatyuk, S. E. Ostapov, *et al.*, Fiz. Tekh. Poluprovodn. (St. Petersburg) **26**, 468 (1992) [Sov. Phys. Semicond. **26**, 264 (1992)].
7. S. Takeyama and S. Narita, J. Phys. Soc. Jpn. **55**, 274 (1986).
8. U. Debska, M. Dietl, G. Grabecki, *et al.*, Phys. Status Solidi A **64**, 707 (1981).
9. N. L. Bazhenov, A. M. Andrukhin, and V. I. Ivanov-Omskiĭ, Infrared Phys. **34** (4), 357 (1993).
10. O. A. Bodnaruk, I. N. Gorbatyuk, S.E. Ostapov, *et al.*, Neorg. Mater. **31** (10), 1347 (1995).

Translated by A. Kazantsev

Semiconductors, Vol. 34, No. 4, 2000, pp. 418–421. Translated from Fizika i Tekhnika Poluprovodnikov, Vol. 34, No. 4, 2000, pp. 433–435.

ELECTRONIC AND OPTICAL PROPERTIES OF SEMICONDUCTORS

Fission of Longitudinal Autosolitons in InSb in a Magnetic Field

I. K. Kamilov*, A. A. Stepurenko, and A. S. Kovalev

Institute of Physics, Dagestan Scientific Center, Russian Academy of Sciences, ul. 26 Bakinskikh Komissarov 94, Makhachkala, 367003 Dagestan, Russia

**e-mail: kamilov@datacom.ru*

Submitted June 28, 1999; accepted for publication October 28, 1999

Abstract—The behavior of longitudinal autosolitons in InSb in a weak magnetic field was studied. It is shown experimentally that a weak longitudinal magnetic field affects significantly the behavior of longitudinal autosoliton in InSb samples. In all samples, sharp changes in the current due to fission of longitudinal autosoliton were observed for certain values of a magnetic field. It was found that the magnitude of initial autosoliton current took a different stable value under the effect of a magnetic field. The initial value of the autosoliton current is recovered if a magnetic field of opposite orientation is applied to the sample. © *2000 MAIK "Nauka/Interperiodica".*

It is known that the homogeneous state of nonequilibrium electron-hole plasma (EHP) is disturbed under high-intensity excitation; as a result, inhomogeneous steady states (thermal-diffusion autosolitons) are formed in the plasma [1–4]. In a dense EHP, these inhomogeneities have the form of current sheets extended along the electric field (longitudinal autosolitons) [5, 6], whereas autosolitons in the shape of electric-field sheets perpendicular to the lines of current (transverse autosolitons) [7–9] are formed in a low-density EHP.

Experiments with *n*-GaAs show [10–14] that a nonequilibrium EHP formed in the samples as a result of impact ionization or injection is stratified in an electric field **E** into current filaments and electric-field domains. Autosolitons traveling in a photogenerated EHP heated by an electric field were experimentally observed in *n*-Ge [15, 16].

As shown in [17, 18], a nonequilibrium EHP can be formed in InSb by thermal generation and both longitudinal and transverse autosolitons appear in this EHP as a result of excitation by an electric field. Due to the asymmetry of EHP in InSb (the relation between effective masses of holes and electrons is given by the inequality $m_p^* \gg m_e^*$), transverse autosolitons move from cathode to anode and give rise to oscillations of current in an external circuit of the sample. It was shown in [19] that a magnetic field of moderate magnitude brings about a significant variation in the frequency and amplitude of these oscillations.

In [6], heating of a uniformly generated dense EHP was considered. It was shown that, irrespective of the mechanisms of the momentum and energy relaxation, uniform distribution of EHP became unstable towards fluctuations with the wave vector $k_0 \approx (lL)^{-1/2}$ directed perpendicularly to the lines of current. In such an EHP, current filaments are observed even at a low level of heating.

In this work, we studied the behavior of longitudinal autosolitons in InSb samples subjected to a longitudinal magnetic field that had a strength as high as $H = 1.4 \times 10^4$ A/m and was excited in a coil. Samples having concentration of charge carriers (holes) $p = (2–4) \times 10^{12}$ cm^{-3} and mobility $\mu_p \approx 4000$ cm^2 V^{-1} s^{-1} at 77 K were used in the experiments. The applied magnetic field was weak both for holes ($\mu_p H/c \approx 5 \times 10^{-3}$) and for electrons (the ratio between the electron and hole mobilities was $\mu_e/\mu_p \sim 100$, so that $\mu_e H/c \approx 0.5$). A nonequilibrium EHP was formed in the samples by Joule heating under the effect of a slowly varying electric field. The EHP was excited on a further increase in the electric-field strength. As a result, longitudinal autosolitons in the form of current filaments appeared in the hot zone of EHP (μ_e and $\mu_p \propto T^{3/2}$) and transverse autosolitons in the form of moving sheets of strong electric field appeared in the EHP zone with lower temperature and density [17].

The dependence of longitudinal-autosoliton current on the strength of parallel and antiparallel magnetic fields (**H** $\uparrow\uparrow$ **E** and **H** $\downarrow\uparrow$ **E**) was studied. Variations in the autosoliton current in relation to the magnetic field were recorded with a strip-chart recorder.

In what follows, we report experimental results for an InB-b1 sample that had dimensions of 5.1 mm ×

1.9 mm × 1.3 mm and a resistance of $R = 7.9$ kΩ. In the presence of autosolitons, the resistance was $R^{AS} = 3.5–5.5$ kΩ, depending on the excitation level.

Figure 1 shows the current-voltage characteristic $I(U)$ of the InSb-b1 sample. Hysteresis in current, which is indicative of an autosoliton origin of current filaments, is characteristic of the $I(U)$ curve [20]. The initial values of the current of longitudinal autosolitons, whose behavior in a magnetic field was studied, are indicated by the numbered points in the $I(U)$ curve.

Figure 2 shows the dependences of the longitudinal-autosoliton current on the magnetic field. The numeral at the origin of a curve indicates the number of the point in the $I(U)$ characteristic; the value of current at this point was taken as initial.

It can be seen from Fig. 2a that the dependence of autosoliton current on the magnetic-field strength is sublinear. As the strength of the parallel magnetic field increases (curve I, **H** ↑↑ **E**), the current sharply increases at a certain value of H and then again varies smoothly. If the magnetic-field strength is decreased, a reverse drastic change (a decrease) in current is observed, but now at a lower value of magnetic-field strength. Similar hysteresis-type behavior of current with drastic changes in the course of forward and reverse variations in magnetic-field strength is also observed in the case of an antiparallel magnetic field (curve II, **H** ↓↑ **E**).

We also observed the following phenomenon: in the course of forward- and reverse-directed variations in the magnetic-field strength, the autosoliton current acquired a different initial value, which is then preserved on subsequent forward and reverse variations in a magnetic field having parallel (**H** ↑↑ **E**) or antiparallel (**H** ↓↑ **E**) orientations. This can be seen from Fig. 2b. As the magnetic-field strength increases and decreases (curve II, **H** ↓↑ **E**), the autosoliton current undergoes two hysteresis sharp changes and returns again to point *11*. However, under the same conditions, curve I' (**H** ↑↑ **E**) finally arrives at point *11*'; i.e., the initial autosoliton current becomes larger. The value of this initial autosoliton current (point *11*') is retained at zero magnetic field and on forward- and reverse-directed variations of the magnetic field for both parallel and antiparallel orientations. In this case, curves I' (**H** ↑↑ **E**) and II' (**H** ↓↑ **E**) describing the autosoliton-current variations become dissimilar. If the measurements of current-voltage characteristics are repeated (Fig. 1), the autosoliton current at point *11* returns to its previous value.

In some cases, the initial autosoliton current acquires a new value if the magnetic-field strength varies in forward and reverse directions for a certain magnetic-field orientation, whereas the value of initial autosoliton current is recovered on forward and reverse variations of magnetic field having another orientation.

As can be seen from Fig. 2c, curve I (**H** ↑↑ **E**) describing the variations in the autosoliton current is

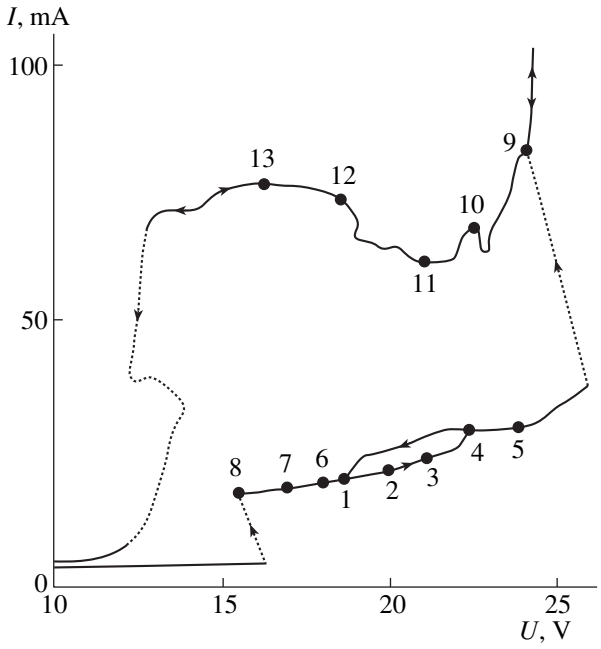

Fig. 1. Current-voltage characteristics of the InSb-*b*1 sample.

reproduced on the forward- and reverse-directed changes in the magnetic-field strength. The initial value of current (Fig. 2c, point *9*) remains unchanged. Curve II (**H** ↓↑ **E**) describing the variations in the autosoliton current on forward and reverse runs of magnetic-field strength reaches point *9*' in this case. A repeated forward and reverse variation in the strength of the magnetic field with the same orientation induces the autosoliton-current curve to return to point *9*'; i.e., curve II' is reproduced. A switching-off of the magnetic field does not affect the new value of initial autosoliton current at all. A forward variation in the magnetic field with **H** ↑↑ **E** orientation results in curve I' for autosoliton current, whereas, for a reverse variation in H, curve I is obtained; i.e., the original value of initial autosoliton current is recovered (point *9*).

Similar experimental results were obtained in studies of the behavior of longitudinal-autosoliton current under a magnetic field in numerous other samples.

The observed sharp changes in the longitudinal-autosoliton current for certain values of magnetic-field strength are most likely caused by fission or coalescence of autosolitons [20].

Longitudinal autosolitons are, in fact, localized domains with elevated temperature and a large temperature gradient $\nabla T \approx 4 \times 10^5$ K/cm [19]. In a longitudinal magnetic field ($H = 8 \times 10^3$ A/m), the presence of transverse temperature gradient in a longitudinal autosoliton gives rise to transverse potential difference $E_\perp \approx 0.4$ V [19] as a result of the Nernst-Ettingshausen effect.

The existence and stability of a hot autosoliton is defined by dynamic balance between the thermal-diffu-

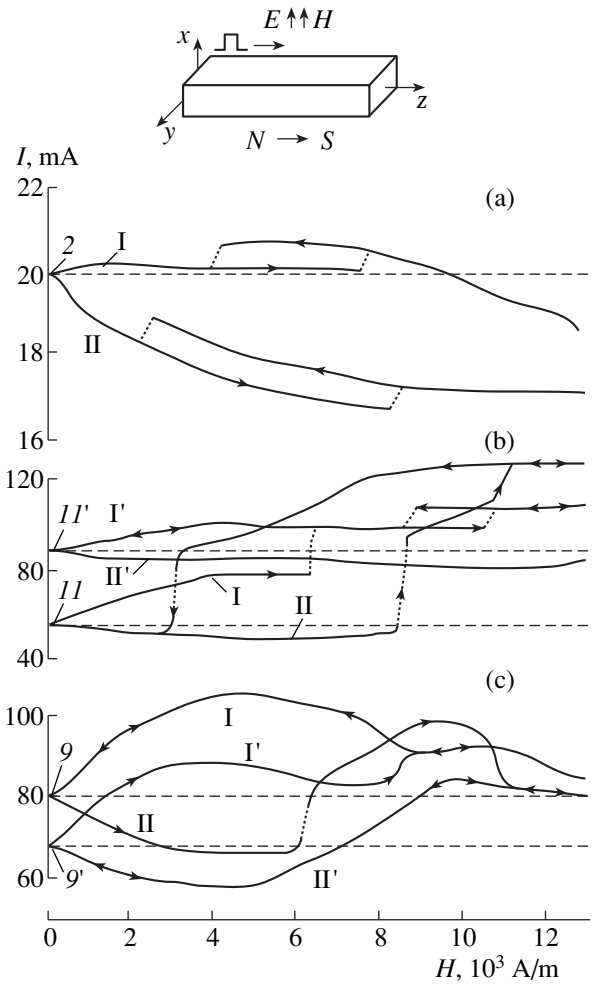

Fig. 2. Variations in the longitudinal-autosoliton current in the InSb-b1 sample subjected to a longitudinal magnetic field. Curves I and I' correspond to $\mathbf{H} \overset{\uparrow\uparrow}{\downarrow\uparrow} \mathbf{E}$, and curves II and II' correspond to $\mathbf{H} \downarrow\uparrow \mathbf{E}$.

sion flux from the central hot zone of autosoliton and the reverse diffusion flux to the autosoliton regions with sizes of $\mathscr{L} < L$ [20], where $\mathscr{L}$ is the autosoliton size and L is the diffusion length. The balance between the thermal-diffusion and diffusion fluxes causes the density of current perpendicular to the autosoliton to tend to zero. An appearance of transverse potential difference $E_\perp$ would bring about an enhancement in one of the fluxes and the establishment of the corresponding dynamic balance between the fluxes. As a result, the autosoliton current would increase or decrease with increasing or decreasing strength of the longitudinal magnetic field. A variation in the autosoliton current implies an increase or decrease in the corresponding excitation level. In a dense EHP, the mean value of current density in the sample is $\langle j \rangle \sim \langle [T(x)]^{3/2} \rangle$; as shown in [20], an increase in the excitation level of a hot autosoliton in a sample of finite size results in a jumplike increase in the mean current, whereas a decrease in the excitation level of autosoliton brings about a jumplike decrease in the mean current.

It was also shown in [20] that a jumplike change in current on gradual variation in the excitation parameter implies fission of autosolitons, their coalescence, or their disappearance. In the case under consideration (Fig. 2, point *2*, curves I, II; point *11*, curves I, II, I'), a longitudinal autosoliton is presumably split into two for a certain value of magnetic-field strength if the latter increases; at a smaller value of the magnetic-field strength when the magnetic field decreases, the new autosolitons either coalesce or some of several autosolitons cease to exist.

Thus, the experiments showed that a weak longitudinal magnetic field affects significantly the behavior of longitudinal autosoliton in indium antimonide samples. In all samples, sharp changes in current were observed for certain magnitudes of the magnetic field; these changes are most likely due to the fission of a longitudinal autosoliton. It was also found that the initial autosoliton current acquires a new stable value under the effect of a magnetic field. In addition, we discovered that the value of initial autosoliton current was restored under a magnetic field with opposite orientation.

ACKNOWLEDGMENTS

We are grateful to V.V. Osipov for his keen interest in this work and his helpful comments and suggestions during discussions of the results.

REFERENCES

1. B. S. Kerner and V. V. Osipov, Zh. Éksp. Teor. Fiz. **61**, 1542 (1976) [Sov. Phys. JETP **44**, 807 (1976)].
2. B. S. Kerner and V. V. Osipov, Pis'ma Zh. Éksp. Teor. Fiz. **41**, 386 (1985) [JETP Lett. **41**, 473 (1985)].
3. B. S. Kerner and V. V. Osipov, Usp. Fiz. Nauk **157**, 201 (1989).
4. B. S. Kerner and V. V. Osipov, Usp. Fiz. Nauk **160**, 1 (1990).
5. B. S. Kerner and V. V. Osipov, Pis'ma Zh. Éksp. Teor. Fiz. **18**, 122 (1973) [JETP Lett. **18**, 70 (1973)].
6. B. S. Kerner and V. V. Osipov, Fiz. Tekh. Poluprovodn. **13**, 891 (1979) [Sov. Phys. Semicond. **13**, 523 (1979)].
7. B. S. Kerner and V. V. Osipov, Fiz. Tverd. Tela **21**, 2342 (1979) [Sov. Phys. Solid State **21**, 1348 (1979)].
8. B. S. Kerner and V. V. Osipov, Fiz. Tekh. Poluprovodn. **13**, 721 (1979) [Sov. Phys. Semicond. **13**, 424 (1979)].
9. A. L. Dubitskiĭ, B. S. Kerner, and V. V. Osipov, Fiz. Tverd. Tela **28**, 1290 (1986) [Sov. Phys. Solid State **28**, 725 (1986)].
10. B. S. Kerner and V. F. Sinkevich, Pis'ma Zh. Éksp. Teor. Fiz. **36**, 359 (1982) [JETP Lett. **36**, 436 (1982)].
11. B. S. Kerner, V. V. Osipov, M. T. Romanko, *et al.*, Pis'ma Zh. Éksp. Teor. Fiz. **44**, 77 (1986) [JETP Lett. **44**, 97 (1986)].

12. V. A. Vashchenko, B. S. Kerner, V. V. Osipov, *et al.*, Fiz. Tekh. Poluprovodn. **23**, 1378 (1989) [Sov. Phys. Semicond. **23**, 857 (1989)].
13. V. A. Vashchenko, B. S. Kerner, V. V. Osipov, *et al.*, Fiz. Tekh. Poluprovodn. **24**, 1705 (1990) [Sov. Phys. Semicond. **24**, 1065 (1990)].
14. V. V. Gafiĭchuk, B. S. Kerner, V. V. Osipov, *et al.*, Fiz. Tverd. Tela **31** (8), 46 (1989) [Sov. Phys. Solid State **31**, 1304 (1989)].
15. M. N. Vinoslavskiĭ, Fiz. Tverd. Tela **31** (8), 315 (1989) [Sov. Phys. Solid State **31**, 1461 (1989)].
16. M. N. Vinoslavskiĭ, B. S. Kerner, V. V. Osipov, *et al.*, J. Phys.: Condens. Matter **2**, 2863 (1990).
17. A. A. Stepurenko, Fiz. Tekh. Poluprovodn. **28**, 402 (1994) [Semicond. **28**, 243 (1994)].
18. I. K. Kamilov and A. A. Stepurenko, Phys. Status Solidi B **194**, 643 (1996).
19. I. K. Kamilov, A. A. Stepurenko, and A. S. Kovalev, Fiz. Tekh. Poluprovodn. **32**, 697 (1998) [Semicond. **32**, 625 (1998)].
20. V. V. Gafiĭchuk, B. S. Kerner, V. V. Osipov, *et al.*, Fiz. Tekh. Poluprovodn. **22**, 2051 (1988) [Sov. Phys. Semicond. **22**, 1298 (1988)].

Translated by A. Spitsyn

Semiconductors, Vol. 34, No. 4, 2000, pp. 422–428. Translated from Fizika i Tekhnika Poluprovodnikov, Vol. 34, No. 4, 2000, pp. 436–442.

ELECTRONIC AND OPTICAL PROPERTIES OF SEMICONDUCTORS

Nonlinearity of Acoustic Effects and High-Frequency Electrical Conductivity in GaAs/AlGaAs Heterostructures under Conditions of the Integer Quantum Hall Effect

I. L. Drichko*, A. M. D'yakonov*, I. Yu. Smirnov*, and A. I. Toropov**

** Ioffe Physicotechnical Institute, Russian Academy of Sciences, Politekhnicheskaya ul. 26, St. Petersburg, 194021 Russia*
e-mail: Irina.L.Drichko@shuvpop.ioffe.rssi.ru

*** Institute of Semiconductor Physics, Siberian Division, Russian Academy of Sciences, pr. Akademika Lavrent'eva 13, Novosibirsk, 630090 Russia*

Submitted October 27, 1999; accepted for publication October 28, 1999

Abstract—The absorption coefficient for surface acoustic wave Γ and variation in the wave velocity $\Delta V/V$ were measured in GaAs/AlGaAs heterostructures; the above quantities are related to interaction of the wave with two-dimensional electron gas and depend nonlinearly on the power of the wave. Measurements were performed under conditions of the integer quantum Hall effect (IQHE), in which case the two-dimensional electron gas was localized in a random fluctuation potential of impurities. The dependences of the components $\sigma_1(E)$ and $\sigma_2(E)$ of high-frequency conductivity $\sigma = \sigma_1 - i\sigma_2$ on the electric field of the surface wave were determined. In the range of the conductivity obeying the Arrhenius law ($\sigma_1 \gg \sigma_2$), the results obtained are interpreted in terms of the Shklovskiĭ theory of nonlinear percolation-based conductivity, which makes it possible to estimate the magnitude of the fluctuation potential of impurities. The dependences $\sigma_1(E)$ and $\sigma_2(E)$ in the range of high-frequency hopping electrical conductivity, in which case $\sigma_1 \ll \sigma_2$ and the theory of nonlinearities has not been yet developed, are reported. © *2000 MAIK "Nauka/Interperiodica".*

1. INTRODUCTION

Studies of the kinetic effects in GaAs/AlGaAs heterostructures with two-dimensional (2D) electron gas in strong constant electric fields [1–4] show that nonlinear effects are adequately accounted for by heating of electron gas. The main issue of controversy in the interpretation of the above results is related to identification of the relevant mechanism of electron-energy relaxation. The theory of electron-gas heating and the energy-relaxation mechanisms in the 2D case were considered in [5]. In [6], the dependence of the coefficient of absorption of a surface acoustic wave (SAW) by 2D electron gas in a GaAs/AlGaAs heterostructure on the SAW intensity was also explained by heating of 2D electron gas by the SAW alternating electric field; it was also shown that the electron-energy relaxation time is controlled by energy dissipation at the piezoelectric potential of acoustic phonons under conditions of strong screening.

In the magnetic-field range where electrons are localized (i.e., under the conditions of IQHE), kinetic effects were also actively studied in a strong constant electric field [7–11]. However, notwithstanding the fact that nonlinear dependences of current on voltage were similar in all cases, these dependences have not been unambiguously interpreted so far. Thus, these nonlinearities were explained by the heating of 2D electron gas [7–9], by impurity breakdown in homogeneous electric field [8], and by resonance tunneling of electrons between the Landau levels [10]; still another explanation was based on the theory of variable-range hopping conduction in a strong electric field [11, 12]. In [13], in order to explain the nonlinearities in the dependence of the width of the IQHE step on the current density in a GaAs/AlGaAs heterostructure at $T = 2.05$ K, the model of heating of 2D electron gas was used. It was found that the dependence of electron temperature T_e on the current I coincided with $T_e(I)$ measured in the absence of a magnetic field. As a plausible reason for this behavior, the authors of [13] could only suggest that it arose from the injection of hot charge carriers from near-contact regions where the Hall voltage was shorted out by the current contacts.

In connection with the above, the acoustic method seems to hold considerable promise for studying the nonlinear effects under the conditions of IQHE; this method is particularly convenient owing to the fact that there is no need for electrical contacts in such measurements.

In this work, we studied the dependences of absorptivity Γ and variations $\Delta V/V$ in the velocity of SAWs in a piezoelectric due to the interaction of SAWs with 2D electron gas in GaAs/AlGaAs heterostructures on the SAW power W absorbed in the sample (or on the SAW electric field E) under the conditions of IQHE ($T =$ 1.5 K), which corresponds to the carrier-localization

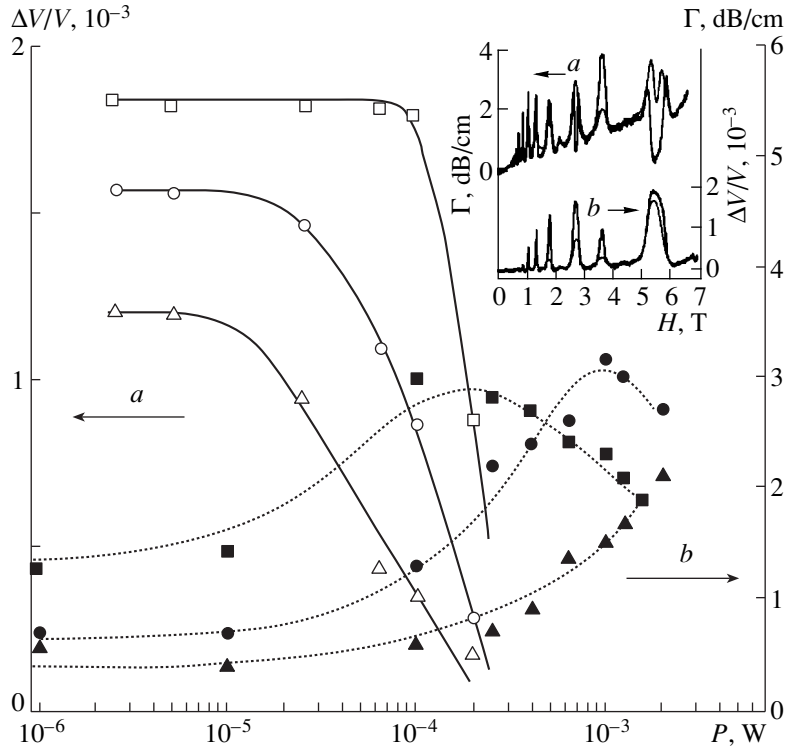

Fig. 1. Dependences of (*a*) relative velocity variation $\Delta V/V$ and (*b*) absorption coefficient Γ of a surface acoustic wave on power P at the output of a generator in magnetic fields of (□ and ▲) 5.5, (○ and ●) 2.7, and (△ and ■) 1.8 T. The insert illustrates the dependences of (*a*) Γ and (*b*) $\Delta V/V$ on the magnetic field H at $T = 1.5$ K for power P at the generator output equal to (*a*) 10^{-5} and (*b*) 2×10^{-6} W (shown by solid lines) and equal to (*a*) 2×10^{-3} and (*b*) 10^{-4} W (shown by dashed lines).

domain. The experimental dependences $\Gamma(E)$ and $\Delta V/V(E)$ were used to calculate the real and imaginary components of high-frequency electrical conductivity $\sigma_1(E)$ and $\sigma_2(E)$, as the high-frequency conductivity is written in the complex form [14] $\sigma(E) = \sigma_1(E) - i\sigma_2(E)$ under the electron-localization conditions. The mechanisms of the nonlinearities were studied by analyzing the dependences of the components of the high-frequency electrical conductivity on the strength (i.e., on absorbed power) of a high-frequency electric field.

2. EXPERIMENTAL METHODS AND RESULTS

In this work, the effect of the SAW power introduced into sample ($f = 30$ MHz) on the absorption coefficient Γ and on the relative variation in the SAW velocity $\Delta V/V$ was measured at $T = 1.5$ K in magnetic fields corresponding to the midpoint of the Hall plateau (i.e., under the conditions of IQHE). We used the GaAs/AlGaAs heterostructures δ-doped with silicon; the density of electrons in 2D gas in the channel was $n = (1.3–2.7) \times 10^{11}$ cm^{-2}, and their mobility was $\mu \approx 2 \times 10^5$ cm^2/(V s). The heterostructures were grown by molecular-beam epitaxy and involved a spacer layer 4×10^{-6} cm in width. The experimental procedure was described in detail elsewhere [15]. Here, we only note that the structure with 2D electron gas was grown on the piezoelectric (lithium niobate) surface over which the SAWs propagated. An alternating electric field having the frequency of SAW and accompanying the strain wave penetrates into the channel with 2D electron gas, induces electric currents and, correspondingly, introduces ohmic losses. As a result of such an interaction, the wave energy is absorbed. Experimentally, we measured the absorption coefficient Γ and the relative variation in the SAW velocity $\Delta V/V$ in relation to the magnetic induction. Since the measured quantities Γ and $\Delta V/V$ are defined by the electric conductivity of 2D electron gas, electron-spectrum quantization resulting in the Shubnikov-de Haas oscillations brings about oscillations in the above effects as well.

Figure 1 shows the dependences of Γ and $\Delta V/V$ on the power P at the output of the RF generator (for a frequency of $f = 30$ MHz) for the filling numbers $\nu = 2$, 4, and 6 for a sample with the 2D-electron gas density of $n = 2.8 \times 10^{11}$ cm^{-2}. Here, $\nu = nch/eH$, where H is the magnetic field strength. In the insert in Fig. 1, the dependences of Γ and $\Delta V/V$ on the magnetic field are shown for several values of the SAW power at a temperature of 1.5 K.

The form of the dependences of Γ on the magnetic field is analyzed in detail in [15]: positions of the peaks in the $\Gamma(H)$ and $\Delta V/V(H)$ curves are equidistant in $1/H$,

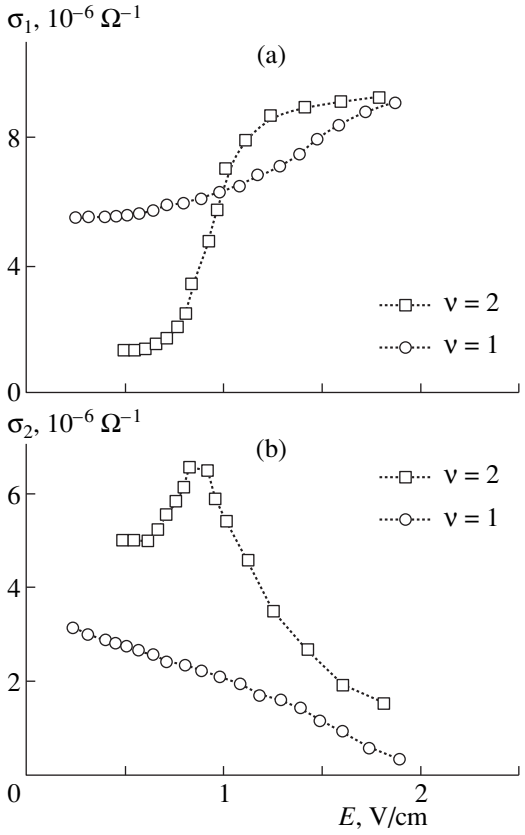

Fig. 2. Dependences of (a) real σ_1 and (b) imaginary σ_2 components of high-frequency electrical conductivity on electric field E for sample AG106 ($n = 1.3 \times 10^{11}$ cm^{-2}) at $T = 1.5$ K.

and the splitting of the $\Gamma(H)$ peaks under the IQHE conditions is related to its relaxation origin. It can be seen from Fig. 1 that an increase in the supplied SAW power results invariably in a decrease in $\Delta V/V$ irrespective of the filling number, which corresponds to an increase in electrical conductivity [6]. The form of dependences $\Gamma(P)$ for dissimilar filling numbers is different: absorption increases with increasing P for $\nu = 2$, whereas, for $\nu = 4$ and 6, Γ increases initially as the SAW power increases, attains a maximum, and then decreases. The smaller the filling number, the higher the power corresponding to the maximum in Γ. It is also evident from Fig. 1 that the higher the magnetic field (the smaller the filling number), the higher is power P corresponding to the onset of the dependences $\Gamma(P)$ and $\Delta V/V(P)$.

3. DISCUSSION OF THE RESULTS

In the experimental configuration of this work, the quantities Γ and $\Delta V/V$ are defined [16, 17] by the formulas

$$\Gamma = 8.68\frac{K^2}{2}qA \times \frac{[4\pi\sigma_1 t(q)/\varepsilon_s V]}{[1+4\pi\sigma_2 t(q)/\varepsilon_s V]^2 + [4\pi\sigma_1 t(q)/\varepsilon_s V]^2},$$

$$A = 8b(q)(\varepsilon_1+\varepsilon_0)\varepsilon_0^2\varepsilon_s \exp[-2q(a+d)],$$

$$\frac{\Delta V}{V} = \frac{K^2}{2}A\frac{[1+4\pi\sigma_2 t(q)/\varepsilon_s V]}{[1+4\pi\sigma_2 t(q)/\varepsilon_s V]^2 + [4\pi\sigma_1 t(q)/\varepsilon_s V]^2},$$

$$\begin{aligned} b(q) &= [b_1(q)[b_2(q)-b_3(q)]]^{-1} \\ t(q) &= [b_2(q)-b_3(q)]/[2b_1(q)], \\ b_1(q) &= (\varepsilon_1+\varepsilon_0)(\varepsilon_s+\varepsilon_0) \\ &-(\varepsilon_1-\varepsilon_0)(\varepsilon_s-\varepsilon_0)\exp(-2qa), \\ b_2(q) &= (\varepsilon_1+\varepsilon_0)(\varepsilon_s+\varepsilon_0) \\ &+(\varepsilon_1-\varepsilon_0)(\varepsilon_s-\varepsilon_0)\exp(-2qd), \\ b_3(q) &= (\varepsilon_1-\varepsilon_0)(\varepsilon_s-\varepsilon_0) \\ &\times \exp(-2qa) + (\varepsilon_1-\varepsilon_0)(\varepsilon_s+\varepsilon_0)\exp(-2q(a+d)), \end{aligned} \quad (1)$$

where the absorption coefficient Γ is expressed in dB/cm; K^2 is the piezoelectric constant of $LiNbO_3$; q and V are the wave vector and the velocity of SAW, respectively; a is the distance between the dielectric and the heterostructure under consideration; d is the depth of the position of the 2D electron-gas layer; ε_1, ε_0, and ε_s are the permittivities of lithium niobate, vacuum, and gallium arsenide, respectively; and σ_1 and σ_2 are the components of the complex high-frequency electrical conductivity of 2D electron gas: $\sigma_{xx}^{hf} = \sigma_1 - i\sigma_2$. The necessity of considering both components of high-frequency conductivity was demonstrated in [14] and was related to localization of electrons under the conditions of IQHE. These formulas make it possible to determine σ_1 and σ_2 from the quantities Γ and $\Delta V/V$ measured experimentally.

Figure 2 shows the dependences of σ_1 and σ_2 on the strength of high-frequency electric field E accompanying the SAW for the sample with $n = 1.3 \times 10^{11}$ cm^{-2} and the filling numbers $\nu = 2$ and 1. It can be seen from Fig. 2 that, for $\nu = 2$ (orbital splitting), σ_1 and σ_2 initially increase with increasing electric field and, beginning with a certain E, σ_2 decreases rapidly while σ_1 continues to increase. In magnetic fields corresponding to the spin splitting ($\nu = 1$), σ_1 increases and σ_2 decreases with increasing E.

Figure 3 shows the dependences of σ_1 and σ_2 on the strength of high-frequency electric field E for the sample with $n = 2.8 \times 10^{11}$ cm^{-2} for the filling numbers of $\nu = 2$, 4, and 6. It can be seen from Fig. 3 that, in the magnetic field H amounting to 5.5 T ($\nu = 2$), both components of high-frequency conductivity are independent of E in a wide range of electric fields; for fields

higher than a certain value E_1, these components increase with E. In a magnetic field of $H = 2.7$ T ($\nu = 4$), an increase in σ_1 and σ_2 sets in an electric field $E_2 < E_1$, and, for $H = 1.8$ T ($\nu = 6$), σ_2 increases initially with increasing E, attains a maximum, and then decreases (similarly to what is shown in Fig. 2 for $H = 2.7$ T in the case of $\nu = 2$).

The high-frequency electric field of SAW is calculated here with the formula reported in [6]. The only difference is that we have $\sigma = \sigma_1 - i\sigma_2$; i.e.,

$$|E|^2 = K^2 \frac{32\pi}{V}(\varepsilon_1 + \varepsilon_2) \times \frac{zq\exp[-2q(a+d)]}{\left[1 + \frac{4\pi\sigma_2}{V\varepsilon_s}t(q)\right]^2 + \left[\frac{4\pi\sigma_1}{V\varepsilon_s}t(q)\right]^2} W, \quad (2)$$

$$z = [(\varepsilon_1 + \varepsilon_0)(\varepsilon_s + \varepsilon_0) - \exp(-2qa)(\varepsilon_1 - \varepsilon_0)(\varepsilon_s - \varepsilon_0)]^{-2},$$

where W is the SAW power supplied to the sample and referred to the sound-scan width.

In order to explain the above dependences of σ_1 and σ_2 on E, we should rely on the fact that, as was shown in [14], electrical conduction in the temperature range of $T = 1.5$–4.2 K is simultaneously governed by the following two mechanisms: (i) the Arrhenius-type mechanism related to activation of charge carriers from the Fermi level, where these carriers are in localized states, to the percolation level and (ii) the mechanism of hopping over localized states in the vicinity of the Fermi level. For $T = 1.5$ K, the contributions of these two mechanisms vary in relation to the filling number (the magnetic field). The smaller the filling number (the higher the magnetic field), the larger the activation energy defined by the value of $0.5\hbar\omega_c$ (ω_c is the cyclotron frequency) and the smaller the Arrhenius contribution to the conductivity. In the case of hopping high-frequency conduction, the imaginary component has the value of $\sigma_2 \approx 10\sigma_1 \gg \sigma_1$ [14] and begins to decrease with an increasing number of delocalized electrons as a result of the activation process. Thus, the ratio σ_1 / σ_2 is a quantity characterizing the contribution of the above two mechanisms to conduction: if $\sigma_1/\sigma_2 \approx 0.1$, the hopping conduction is dominant, whereas, if $\sigma_1 / \sigma_2 \gg 1$, the Arrhenius-law conduction is dominant and the hopping conduction may be ignored.

In view of the above, the nonlinearities should be analyzed separately for two different domains.

3.1. Nonlinearities in the Region of Arrhenius-Type Conduction ($\sigma_1 / \sigma_2 \gg 1$)

The influence of a strong constant electric field on electrical conductivity stemming from activation of charge carriers to the percolation level of the conduction band distorted by random fluctuation potential of charged impurities was considered by Shklovskiĭ in [18]. In fact, we study here the influence of a strong

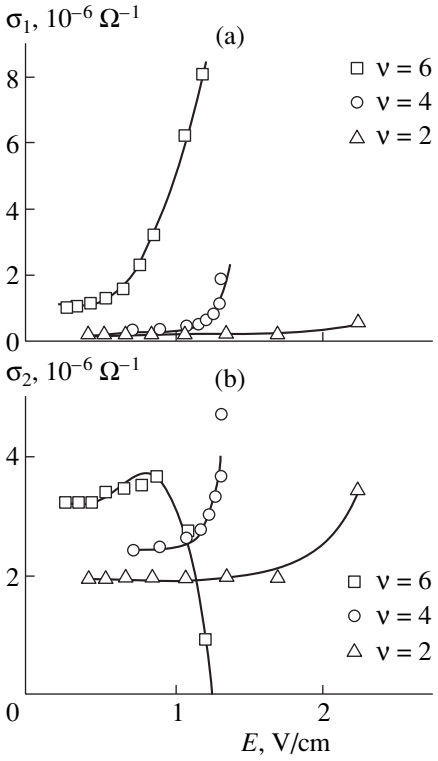

Fig. 3. Dependences of the (a) real σ_1 and (b) imaginary σ_2 components of high-frequency electrical conductivity on electric field E for sample AG49 ($n = 2.8 \times 10^{11}$ cm^{-2}) at $T = 1.5$ K.

electric field on conduction over the percolation level, with the role of the electric field limited to a reduction of activation energy, which may be interpreted as a lowering of the percolation threshold.

In this case, an increase in electrical conductivity in a strong electric field with decreasing activation energy is given by

$$\sigma_1/\sigma_1^0 = \exp[(CeElV_0)^{1/(1+\gamma)}/kT], \quad (3)$$

where σ_1^0 is the conductivity in the linear mode, E is the electric-field strength, T is temperature, C is a numerical coefficient, V_0 is the amplitude of fluctuations in the potential-relief pattern (the characteristic spatial scale of a potential), and γ is the coefficient that depends on dimensionality: $\gamma = 0.9$ for the three-dimensional (3D) case and $\gamma = 4/3$ for the 2D case [19].

Thus, in the 2D case under consideration, formula (3) can be rewritten as

$$\sigma_1/\sigma_1^0 = \exp(\alpha E^{3/7}/kT), \quad (4)$$

where

$$\alpha = (Cel_{sp}V_0)^{3/7}, \quad (5)$$

and l_{sp} is the characteristic spatial scale of the potential, which may be taken as equal to the spacer thickness

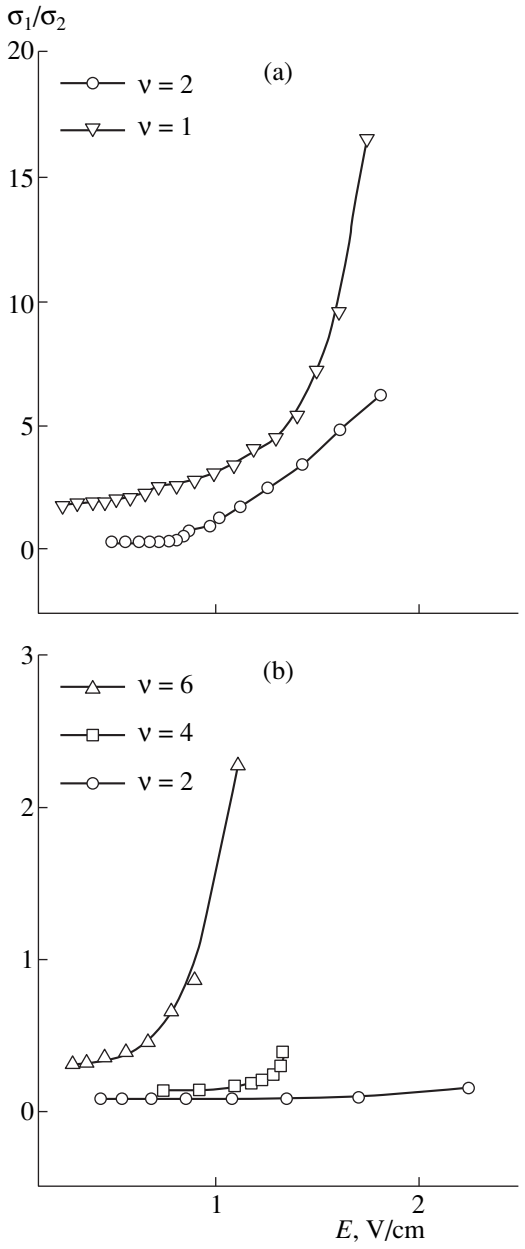

Fig. 4. Dependences of the ratio of the real and imaginary components of high-frequency electrical conductivity σ_1/σ_2 on electric field E for samples (a) AG106 and (b) AG49 at $T = 1.5$ K.

[20] l_{sp} in the heterostructures we studied ($l_{sp} = 4 \times 10^{-6}$ cm).

In the experiment we performed, the following conditions were satisfied:

$$ql_{sp} \ll 1, \quad \omega\tau \ll 1. \tag{6}$$

Here, q and ω are the wave vector and frequency of SAW, respectively, and τ is the electron-momentum relaxation time. Therefore, we may regard the wave as standing and we can use the formulas obtained for the constant electric field in the analysis of dependences of high-frequency conductivity on the alternating SAW electric field.

Figure 4 shows the dependences of σ_1/σ_2 on electric-field strength E calculated according to (2) for two samples in different magnetic fields. It can be seen from Fig. 4 that the condition σ_1/σ_2 is met for sample AG106 alone; therefore, the dependences σ_1/σ_1^0 on E can be analyzed on the basis of [18] only for this sample. Figure 5 shows the dependence of $\ln(\sigma_1/\sigma_1^0)$ on $E^{3/7}$. It can be seen that the dependence is linear; the slope of the corresponding straight line makes it possible to determine (to within a numerical factor) V_0, i.e., the amplitude of fluctuations in the potential relief pattern. We found that $V_0 \approx 1.5$ meV.

Calculation of the fluctuation amplitude by the formula [21]

$$V_0 = (e^2/\varepsilon_s)\sqrt{n}, \tag{7}$$

where n is the density of ionized impurities equal in our case to the carrier density in the 2D channel with $n = 1.3 \times 10^{11}$ cm^{-2}, yields $V_0 = 4.5$ meV, which coincides by an order of magnitude with V_0 determined experimentally to within a numerical factor.

It is stated in [18] that the electric-field range in which formula (3) is valid is limited by the inequalities

$$V_0 \gg eEl_{sp} \gg kT(kT/V_0)^{4/3}. \tag{8}$$

Using the experimental value of V_0, we can estimate the quantities in this inequality:

1.5 meV $\gg 3 \times 10^{-3}$ meV $\approx 5 \times 10^{-3}$ meV at the threshold of nonlinearities; and

1.5 meV $\gg 7 \times 10^{-3}$ meV $> 5 \times 10^{-3}$ meV at the upper limit in our measurements.

Taking into account that the fluctuation amplitude is determined to within a numerical factor, we may consider that the inequality holds and we can use the theory [18] to interpret nonlinearities arising in the case where the conductivity obeys the Arrhenius law.

It is worth noting here that the nonlinearities under a constant electric field E were studied for $E >$ 5–10 V/cm.

The results reported here were obtained for electric fields lower than 2 V/cm. Thus, the following general pattern emerges. In electric fields $E \approx 1$ V/cm corresponding to the prebreakdown region, electrical conductivity increases owing to an increase in concentration in the empty Landau band due to activation of localized electrons from the Fermi level; in this case, the activation energy depends on the electric field (the higher the electric field, the lower the activation energy). In electric fields $E \approx 10$ V/cm, a sharp increase in electron concentration in the empty Landau band due to the impurity breakdown sets in (this phenomenon was clearly observed, for example, in [9]). Electrons

brought into delocalized states of the Landau band are heated in a strong electric field applied to the sample.

3.2 Nonlinearities in the Region of High-Frequency Hopping Conduction ($\sigma_1/\sigma_2 \approx 0.1$)

In the case of electrical conductivity limited by activation, we could use the nonlinearity theory developed for constant fields to interpret the nonlinearities in high-frequency conductivity, because this theory described the influence of a strong electric field on the motion of quasi-free electrons activated to the percolation level. The mechanism of conduction in a constant electric field and that in a high-frequency field are found to be the same. However, in the case where the electrons are localized, the mechanisms of high-frequency hopping conduction and dc hopping conduction are different: in the dc mode, the conduction is accomplished by hops of electrons between two edges of the sample, whereas, in a high-frequency electric field with electrons localized at separate impurity atoms, conduction can be effected by hops of electrons between two impurity atoms separated by a distance smaller than the average one (within an impurity pair with a single electron); in this case, transitions of electrons between different pairs do not occur (a neighbor-site model). Therefore, it is understandable that the theory developed for nonlinearities in the mode of dc hopping conduction [12] cannot be used to interpret the nonlinearities we observed in high-frequency hopping conduction (Figs. 2, 3).

The dependences of resistivities ρ_{xx} and ρ_{xy} on the current density in a GaAs/AlGaAs heterostructure were observed under the IQHE conditions in the region of variable-range hopping conduction at $T < 1$ K [11]. These dependences were analyzed using the theory [12] for variable-range hopping conduction in a strong electric field for 2D electron gas under conditions of the quantum Hall effect. An introduction of effective temperature for hopping conduction in terms of [12] makes it possible to use the above measurements to determine the value of localization length. However, it was found that the value thus obtained was by almost an order of magnitude larger than the localization length determined from the temperature dependence of ρ_{xx} in a linear conduction mode. This fact was related [11] to nonuniformity in the distribution of the electric field.

The theory of nonlinear high-frequency electrical conduction was developed in [22] for the 3D case. However, the dependences $\Delta\sigma^{nl}_{1,2}/\sigma^{0}_{1,2} \propto W^2$ we observed are stronger than those predicted in [21] ($\Delta\sigma \propto W$). Here, $\sigma^{0}_{1,2}$ is the conductivity in linear mode, $\Delta\sigma^{nl}_{1,2} = \sigma_{1,2}(E) - \sigma^{0}_{1,2}$, $\sigma_{1,2}(E)$ is the conductivity measured experimentally, and W is the SAW power absorbed in the sample. At present, the absence of a theory for the 2D case prevents us from analyzing the obtained results. The dependences of σ_1 and σ_2 on the

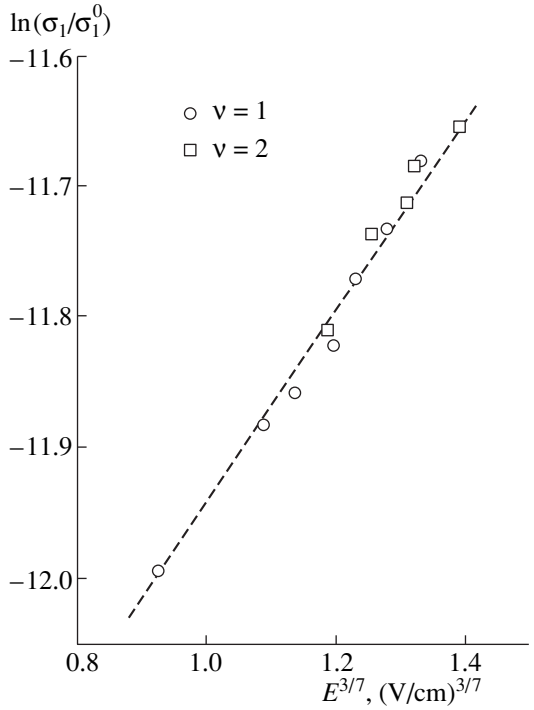

Fig. 5. Dependence of $\ln(\sigma_1/\sigma_1^0)$ on $E^{3/7}$ for different filling numbers in sample AG106.

SAW electric field under conditions of hopping conduction set in under the electric field, which becomes lower as the magnetic-field increases; this fact is qualitatively well explained by assuming that the magnetic field affects the overlap integral for localized states at different impurities and, thus, brings about a depression of hopping conduction and a decrease in the relative nonlinear component [22].

Dependence of absorpitivity of SAW by 2D electron gas on the SAW power in GaAs/AlGaAs heterostructures was previously observed [23, 24] in magnetic fields corresponding to small integer filling numbers when the Fermi level was in midposition between the neighboring Landau levels and when the electrons were localized. However, it is hardly possible to accept the interpretation [23, 24] of these dependences as due to the heating of 2D electron gas, which, as was mentioned above, manifests itself only in the case where the electrons in 2D configuration are delocalized.

4. CONCLUSION

We studied nonlinear dependences of absorptivity and variation in the SAW velocity induced by 2D electron gas on the intensity of sound under the conditions of the integer quantum Hall effect in GaAs/AlGaAs heterostructures.

The nonlinearities were analyzed on the basis of high-frequency electrical conductivity that had a complex form and was calculated from experimental data.

It is shown that the electric-field range corresponding to nonlinearities can be divided into two domains.

In the electric-field domain where $\mathrm{Re}\sigma_1 \gg \mathrm{Im}\sigma = \sigma_2$, the dependence $\sigma_1(E)$ is not only adequately accounted for by the Shklovskiĭ dc nonlinearity theory [18] describing the influence of a strong electric field on the motion of quasi-free electrons activated to the percolation level, but also makes it possible to evaluate the magnitude of the fluctuation impurity potential.

In the electric-field domain where $\mathrm{Im}\sigma = \sigma_2 \gg \mathrm{Re}\sigma = \sigma_1$, the 2D high-frequency hopping conduction apparently takes place; as of yet, the nonlinearity theory for this type of conduction has not been developed.

ACKNOWLEDGMENTS

We thank V.D. Kagan for his helpful participation in discussions of the results.

This work was supported by the Russian Foundation for Basic Research (project no. 98-02-18280) and the Ministry of Science (grant no. 97-1043).

REFERENCES

1. T. J. Drummond, M. Keever, W. Kopp, *et al.*, Electron. Lett. **17**, 545 (1981).
2. J. Shah, A. Pinczuk, H. L. Störmer, *et al.*, Appl. Phys. Lett. **42**, 55 (1983); J. Shah, A. Pinczuk, H. L. Störmer, *et al.*, Appl. Phys. Lett. **44**, 322 (1984).
3. M. G. Blyumina, A. G. Denisov, T. A. Polyanskaya, *et al.*, Pis'ma Zh. Éksp. Teor. Fiz. **44**, 257 (1986) [JETP Lett. **44**, 331 (1986)].
4. E. Chow, H. P. Wei, S. M. Girvin, *et al.*, Phys. Rev. Lett. **77**, 1143 (1996) (and the references therein).
5. P. J. Price, J. Appl. Phys. **53**, 6863 (1982); V. Karpus, Fiz. Tekh. Poluprovod. **22**, 439 (1988) [Sov. Phys. Semicond. **22**, 268 (1988)].
6. I. L. Drichko, A. M. D'yakonov, V. D. Kagan, *et al.*, Fiz. Tekh. Poluprovodn. **31**, 1357 (1997) [Semicond. **31**, 1170 (1997)].
7. G. Ebert, K. von Klitzing, K. Ploog, *et al.*, J. Phys. C **16**, 5441 (1983); P. Streda and K. von Klitzing, J. Phys. C **17**, L483 (1984).
8. M. E. Gage, R. F. Dziuba, B. F. Field, *et al.*, Phys. Rev. Lett. **51**, 1374 (1983).
9. S. Komiyama, T. Takamasu, S. Hiyamizu, *et al.*, Solid State Commun. **54**, 479 (1985).
10. V. L. Pokrovsky, L. P. Pryadko, and A. L. Talapov, J. Phys.: Condens. Matter **2**, 1583 (1990).
11. M. Furlan, Phys. Rev. B.: Condens. Matter **57**, 14818 (1998) (and the references therein).
12. D. G. Polyakov and B. I. Shklovskiĭ, Phys. Rev. B: Condens. Matter **48**, 11167 (1993).
13. A. M. Kreshchuk, E. P. Laurs, T. A. Polyanskaya, *et al.*, Fiz. Tekh. Poluprovodn. **22**, 2162 (1988) [Sov. Phys. Semicond. **22**, 1364 (1988)].
14. I. L. Drichko, A. M. Diakonov, V. D. Kagan, *et al.*, in *Proceedings of 24th International Conference on the Physics of Semiconductors, Jerusalem, Israel, 1998*, Ed. by D. Gershoni (World Scientific, 1998), CD-ROM.
15. I. L. Drichko, A. M. D'yakonov, A. M. Kreshchuk, *et al.*, Fiz. Tekh. Poluprovodn. **31**, 451 (1997) [Semicond. **31**, 384 (1997)].
16. I. L. Drichko, A. M. D'yakonov, I. Yu. Smirnov, *et al.*, Fiz. Tekh. Poluprovodn. **33**, 979 (1999) [Semicond. **33**, 892 (1999)].
17. V. D. Kagan, Fiz. Tekh. Poluprovodn. **31**, 470 (1997) [Semicond. **31**, 407 (1997)].
18. B. I. Shklovskiĭ, Fiz. Tekh. Poluprovodn. **13**, 93 (1979) [Sov. Phys. Semicond. **13**, 53 (1979)].
19. B. I. Shklovskiĭ and A. L. Éfros, *Electronic Properties of Doped Semiconductors* (Nauka, Moscow, 1979; Springer-Verlag, New York, 1984).
20. A. L. Éfros, Zh. Éksp. Teor. Fiz. **89**, 1834 (1985) [Sov. Phys. JETP **62**, 1057 (1985)].
21. A. L. Éfros, F. G. Pikus, and V. G. Barnett, Phys. Rev. B: Condens. Matter **47**, 2233 (1993).
22. Yu. M. Gal'perin and É. Ya. Priev, Fiz. Tverd. Tela **29**, 3016 (1987) [Sov. Phys. Solid State **29**, 1733 (1987)].
23. A. Wixforth, J. Scriba, M. Wassermeier, *et al.*, Phys. Rev. B: Condens. Matter **40**, 7874 (1989).
24. A. Schenstrom, M. Levy, B. K. Sarma, *et al.*, Solid State Commun. **68**, 357 (1988).

Translated by A. Spitsyn

Semiconductors, Vol. 34, No. 4, 2000, pp. 429–432. Translated from Fizika i Tekhnika Poluprovodnikov, Vol. 34, No. 4, 2000, pp. 443–446.

ELECTRONIC AND OPTICAL PROPERTIES OF SEMICONDUCTORS

Variation in the Defect Structure of *p*-CdTe Single Crystals at the Passage of the Laser Shock Wave

A. Baĭdullaeva*, A. I. Vlasenko, B. L. Gorkovenko, A. V. Lomovtsev, and P. E. Mozol'

Institute of Semiconductor Physics, National Academy of Sciences of Ukraine, Kiev, 252650 Ukraine

** e-mail: baidulla@class.semicond.kiev.ua*

Submitted July 7, 1999; accepted for publication November 1, 1999

Abstract—Variations in the minority-carrier lifetime, photoluminescence spectra, dark current and photocurrent temperature dependences of high-resistivity *p*-CdTe crystals under the action of the laser shock wave are investigated. It is shown that the variations in the aforementioned characteristics during the passage of the shock wave are defined by the generation of the nonequilibrium carriers from deep centers, and, after that, the variations are defined by the formation of intrinsic defects and their subsequent interaction with the defects existing in the initial crystals. © *2000 MAIK "Nauka/Interperiodica"*.

Irradiation of II–VI crystals, specifically *p*-CdTe, with ruby laser nanosecond pulses with the power density below the damage threshold leads to the variation in their electrical, photoelectrical, and optical properties. These variations occur both in the near-surface region of the material and at the depth of ~5 μm, which is much larger than the light absorption depth (10^{-5} cm^{-1}) [1–5]. These variations are caused by the formation of intrinsic lattice defects due to lattice "heat-up," the generation of the thermal elastic stresses, and the action of the acoustic and shock waves in the course of irradiation of the crystal. The immediate influence of the laser irradiation on the physical properties of the CdTe crystals is investigated adequately. However, the influence of each phenomenon, which proceeds in the course of the laser irradiation, specifically under the action of the shock wave, is investigated inadequately [5].

In this paper, we report the results of investigation of electrical and photoelectrical properties of high-resistivity *p*-CdTe single crystals both in the course of action of the shock wave with the nondestructive amplitude and after the passage of the wave through the crystal. The shock waves were generated by the ruby laser pulses with the duration of 20 ns and power density varied in the range 10^7–10^9 W/cm^2. The procedures of preparing and irradiating the samples are similar to those described in [4, 5]. The studied sample in the shape of parallelepiped $2 \times 3 \times 2$ mm^3 was placed between the copper foil and quartz substrate. The spacing between the foil and substrate was filled with the epoxy resin so that the distance from the crystal to the foil and substrate would be 25 μm. The copper foil served as an inhibitor of the undesired photoeffect from the forward or scattered laser emission, and the quartz substrate served for outputting the unload wave. The irradiation of the samples was carried out at room temperature. The shock wave pressure was evaluated from the formula reported in [6]:

$$P = \left(I_0 \frac{\gamma - 1}{\gamma} \frac{\rho_1 u_1 \rho_2 u_2}{\rho_1 u_1 + \rho_2 u_2}\right)^{1/2}, \quad (1)$$

where I_0 is the laser-radiation power density; γ is the effective specific-heat ratio of the plasma formed; $\rho_1 u_1$ and $\rho_2 u_2$ are the shock impedances of the condensed medium and absorbing substance, respectively; ρ is the substance density; and u is the velocity of the shock wave.

The shock wave pressure was determined from the ratio of pressures of the transmitted wave P_2 and incident wave P_1, taking into account the reflection from the interfaces foil-resin and resin-crystal [6]:

$$\frac{P_2}{P_1} = \frac{2}{1 + \rho_2 u_2 / \rho_1 u_1}. \quad (2)$$

EXPERIMENTAL RESULTS AND DISCUSSION

The dependence of the concentration variation (Δp) of nonequilibrium charge carriers on the shock wave pressure is shown in Fig. 1 (curve *1*). At low shock wave pressures, the concentration of nonequilibrium charge carriers increases exponentially and reaches saturation at the shock wave pressure higher than 3 kbar. The relaxation time of the nonequilibrium charge carriers depends on the pressure of the shock wave propagating through the crystal. The relaxation time initially decreases with the shock wave pressure up to 2.5 kbar. On the further increase in the shock wave pressure, namely, in the region of Δp saturation, the relaxation time varies only slightly (Fig. 1, curve *2*). The observed initial increase in Δp can be explained by an increase in the concentration of nonequilibrium charge carriers because of the propagation of the thermal and shock

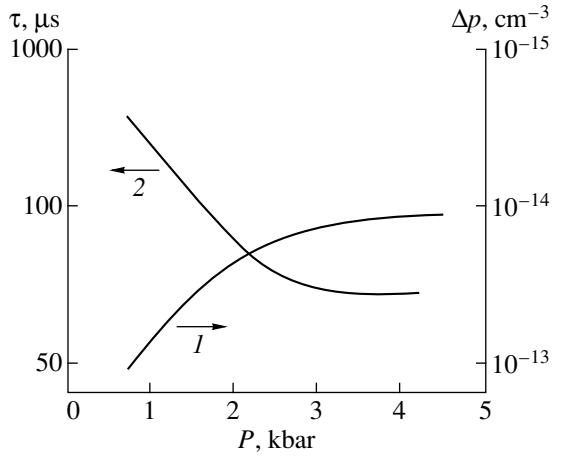

Fig. 1. Dependences of (*1*) concentration Δp and (*2*) relaxation time τ of nonequilibrium charge carriers in the CdTe single crystal on the shock wave pressure *P*.

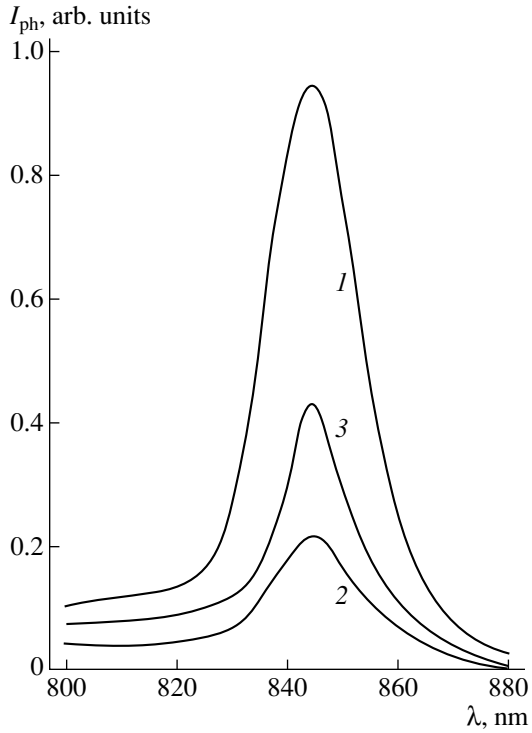

Fig. 2. Spectral dependences of photoconductivity for the CdTe single crystal (*1*) before and (*2*) after the passage of the shock wave with the pressure $P > 2$ kbar. The curve *3* was measured after the irradiated sample was kept in air for one month.

waves, which are formed in the course of the irradiation of the crystals by the laser emission.

The penetration depth of the thermal wave, which is formed under irradiation of the samples, was ~1.5 μm, much less than the foil thickness. For this reason, the variation in concentration of the nonequilibrium charge carriers in the crystals cannot result from heating. The energy of defect ionization decreases because of a decrease in the bandgap energy E_g under the shock wave action. The estimate shows that the variation of E_g in the studied range of the shock wave pressures amounts to ~0.01 eV, whereas the conductivity increases by a factor of 2–2.5. This indicates that the concentration of the nonequilibrium charge carriers released from the traps is comparable to the equilibrium concentration. However, the slight variation of E_g cannot bring about ionization of all traps. In relation to the aforementioned, the increase in the concentration of the nonequilibrium charge carriers at low (below 2 kbar) pressures can be explained by their generation from deep-level point defects (traps). The saturation of the concentration with the increase in the shock wave pressure above 3 kbar can be explained by the accumulation of residual defects generated by the shock wave [4].

The photoconductivity spectra, as well as the temperature dependences of the photocurrent and dark current before and after the passage of the shock wave through the crystal, were also investigated. We note that, in the course of investigations of the photoconductivity and photocurrent, the samples were illuminated from the back side. The spectral dependences of the photoconductivity of CdTe single crystals before and after the passage of the shock wave with $P > 2$ kbar, as well as after keeping the samples in air for one month, are presented in Fig. 2. The photoconductivity spectrum of the initial sample includes a single band with the peak at $\lambda_{max} = 840$ nm. Subsequent to the shock wave action, the photoconductivity diminishes. The shape and position of the photoconductivity band remain unchanged. The photoconductivity increases as a result of keeping the samples for one month after the shock wave action. However, photoconductivity does not reach the initial value.

The photocurrent of initial crystals depends only slightly on temperature in the range of 100–300 K. At higher temperatures, the photocurrent becomes thermally activated and the dependence $I_{ph}(T)$ follows the Arrhenius law with the activation energy $E_i = 0.8$–0.9 eV (Fig. 3, curve *1*). Subsequent to the passage of the shock wave with the pressure $p < 2$ kbar, quenching of the photoconduction with the activation energy $E_{vt} = 0.13$ eV is observed in the low-temperature region. The thermal activation region of the photocurrent remains unchanged above room temperature, and the photocurrent decreases by almost an order of magnitude (Fig. 3, curve *2*). The appearance of the temperature range of quenching of the photocurrent subsequent to the passage of the shock wave with $P < 2$ kbar can be related to the formation of shallow-level centers with the activation energy of ~0.13 eV. At low temperatures and low excitation levels in the region of intrinsic light absorption, a strong optical charge redistribution between *r*-centers ($E_r = 0.9$ eV) and shallow acceptors ($E_{vt} =$

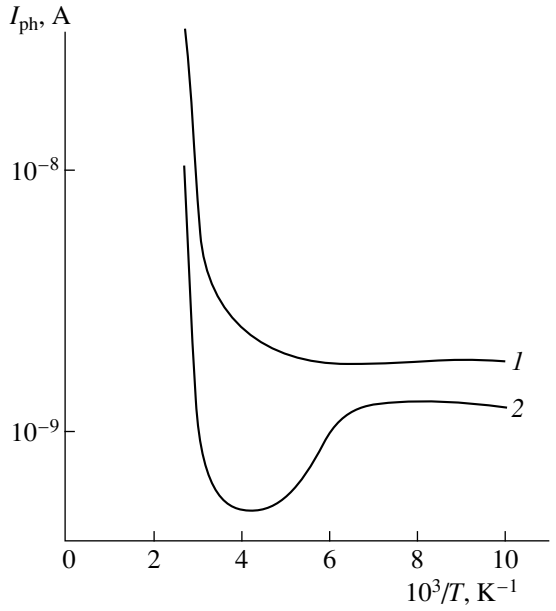

Fig. 3. Temperature dependences of the photocurrent I_{ph} for the CdTe single crystal (*1*) before and (*2*) after the passage of the shock wave.

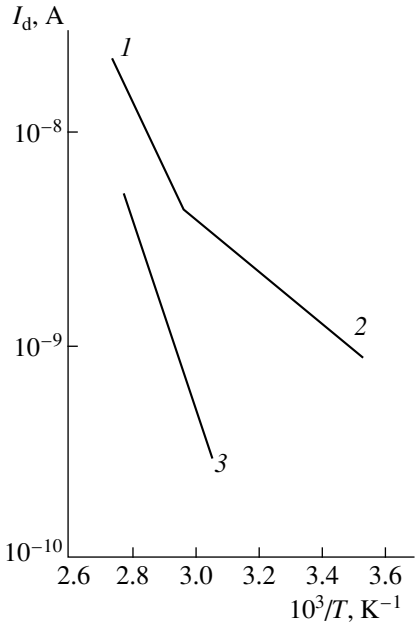

Fig. 4. Temperature dependences of the dark current I_d for the CdTe single crystal (*1*) before and (*2*, *3*) after the passage of the shock wave.

0.13 eV) proceeds in CdTe crystals. Namely, the photoholes are trapped by shallow levels, and the hole population of *r*-centers is decreased; i.e., the quasi-dark formation of the center population by the minority carriers with the concentration N_r^0 takes place [7]. Consequently, the rise in N_r^0 causes a decrease in τ ($\tau \propto 1/N_r^0$) and in the photocurrent. This is also evidenced by an increase in τ after the passage of the shock wave with a pressure of $P < 2$ kbar. The photocurrent decreases further by an order of magnitude after the repeated passage of the shock wave with $P > 2$ kbar. In this case, the form of the temperature dependence is retained, excluding the region of the temperature quenching of the photoconductivity, which disappears.

A region with the activation energy $E_1 = 0.6$ eV is observed in the temperature dependence of the dark current (I_d) of the crystal (Fig. 4, curve *1*). The dark current remains unchanged after the passage of the shock wave with the pressure $P < 2$ kbar. However, the additional region with $E_2 = 0.14$ eV appears (Fig. 4, curve *2*). The dark current decreases with further increase in the shock wave pressure, and the activation energies E_1 and E_2 disappear in the temperature dependence of the dark current. However, the level with the energy $E_3 = 0.8$ eV corresponding to deep *r*-centers (Fig. 4, curve *3*) emerges. This fact testifies that, after the passage of the shock wave with $P > 2$ kbar, charge carriers are generated from the deeper levels compared to the case of the initial crystal. The level with the energy $E_2 = 0.14$ eV in CdTe crystals corresponds to the energy position of the acceptor, which is known to be the cadmium vacancy [8], and the level $E_1 = 0.6$ eV corresponds to the double-charged cadmium vacancy [9].

Since the metal vacancies (acceptors) in *p*-type crystals manifest themselves in the equilibrium conductivity, we can suppose that a decrease in the equilibrium conductivity after the passage of the shock wave with $P > 2$ kbar is related to the variation in the concentration of acceptor centers in crystals. Let us consider the behavior of the acceptor centers after the repeated passage of the laser shock wave. The Frenkel pairs, isolated vacancies, and interstitial atoms are formed in the crystal under the wave action. They can interact with impurity atoms and form stable defect complexes [10]. In the course of the multiple passage of the shock wave, these stable defects accumulate as the number of pulses of the laser radiation increases. This process is similar to that in the case of high-energy radiation of semiconductors [11]. It is possible that the cadmium vacancy forms during the first passage of the shock wave as is evidenced by the appearance of the level with $E_2 = 0.14$ eV (Fig. 3 and 4, curves *2*). The cadmium vacancies are transferred to dislocations at the second passage of the shock wave with $P > 2$ kbar. The energy of the vacancy formation decreases because of the repeated passage of the shock wave through the crystal. For this reason, a large amount of excess vacancies form, which brings about the additional distortion of material [12]. This distortion can in turn bring about concentration fluxes and cause “uphill” diffusion. The formed elastically strained layer dramatically enhances the vacancy diffusion in a bulk material. The enhanced

diffusion can be related to the crowdion mechanism of displacement of the lattice site atoms, the diffusion to sinks, the diffusion along the dislocations with the enhanced diffusivity, or the drift in the gradient of elastic strains, i.e., the "uphill" diffusion [12]. The migration rate of atoms within the local volumes during the uphill diffusion can be several orders of magnitude higher than the average mobility level of atoms in crystals at a given temperature. As a result, the vacancies are localized in the compressed regions, which are formed by both the vacancies themselves and the shock wave, and form clusters. Depending on the number of vacancies, the clusters take a form of the sphere or the disk of monoatomic thickness, i.e., the dislocation loop. We previously observed the formation of the dislocation loop and appearance of the band $\lambda_{max} = 840$ nm in the photoluminescence spectra, which was related to the dislocation loop [5]. In many works of other authors, this dislocation-related band is associated with the point centers of recombination, which include cadmium vacancies [13]. Notice that the appearance of the dislocation loop and band $\lambda_{max} = 840$ nm was observed only after the repeated passage of the shock wave. This agrees with the results of this work.

Thus, we can conclude that the shock wave, which is formed on irradiation of crystals by the laser pulses, is one of the mechanisms of defect formation in *p*-CdTe.

REFERENCES

1. V. N. Babentsov, A. Baĭdullaeva, A. I. Vlasenko, *et al.*, Fiz. Tekh. Poluprovodn. (St. Petersburg) **27**, 1618 (1993) [Semicond. **27**, 894 (1993)].
2. V. N. Babentsov, A. Baĭdullaeva, S. I. Gorban', *et al.*, Poverkhnost, No. 12, 144 (1988).
3. A. Baĭdullaeva, B. M. Bulakh, B. K. Dauletmuratov, *et al.*, Fiz. Tekh. Poluprovodn. (St. Petersburg) **26**, 801 (1992) [Sov. Phys. Semicond. **26**, 450 (1992)].
4. V. A. Yanushkevich, A. V. Polyaninov, E. G. Prutskaya, *et al.*, Izv. Akad. Nauk SSSR, Ser. Fiz., No. 5, 1146 (1986).
5. A. Baĭdullaeva, A. I. Vlasenko, Yu. V. Vlasenko, *et al.*, Fiz. Tekh. Poluprovodn. (St. Petersburg) **30**, 1438 (1996) [Semicond. **30**, 756 (1996)].
6. L. I. Ivanov, Yu. N. Nikiforov, and V. A. Yanushkevich, Zh. Éksp. Teor. Fiz. **67**, 147 (1975) [Sov. Phys. JETP **40**, 75 (1975)].
7. R. Bube, *Photoconductivity of Solids* (Wiley, New York, 1960; Nauka, Moscow, 1962).
8. N. V. Agrinskaya, E. N. Arkad'eva, O. A. Matveev, *et al.*, Fiz. Tekh. Poluprovodn. (Leningrad) **2**, 932 (1968) [Sov. Phys. Semicond. **2**, 776 (1968)].
9. A. A. Sokolova, V. S. Vavilov, A. F. Plotnikov, *et al.*, Fiz. Tekh. Poluprovodn. (Leningrad) **3**, 720 (1969) [Sov. Phys. Semicond. **3**, 612 (1969)].
10. G. G. Bondarenko, L. I. Ivanov, and V. A. Yanushevich, Fiz. Khim. Obrab. Mater., No. 4, 147 (1973).
11. A. I. Vlasenko, V. V. Gorbunov, A. V. Lyubchenko, *et al.*, Ukr. Fiz. Zh. **29**, 423 (1984).
12. V. B. Brik, *Diffusion and Phase Transformations in Metals and Alloys* (Naukova Dumka, Kiev, 1985).
13. I. M. Figueroa, F. Sánchez-Sinencio, and J. G. Mendoza-Álvarez, J. Appl. Phys. **60**, 452 (1986).

Translated by N. Korovin

Semiconductors, Vol. 34, No. 4, 2000, pp. 433–437. Translated from Fizika i Tekhnika Poluprovodnikov, Vol. 34, No. 4, 2000, pp. 447–451.

ELECTRONIC AND OPTICAL PROPERTIES OF SEMICONDUCTORS

Optical Spectra and Electronic Structure of Cubic Silicon Carbide

V. V. Sobolev and A. N. Shestakov

Udmurt State University, Krasnoarmeĭskaya ul. 71, Izhevsk, 426034 Russia

Submitted June 17, 1999; accepted for publication November 3, 1999

Abstract—A full set of fundamental optical functions of 3*C*-SiC is calculated from reflectance spectra in the range of 2–16 eV. The integral curve of the dielectric constant is for the first time resolved into 11 components. Peak energy, half-width, and oscillator strength are determined for each component. The obtained results are analyzed in terms of the known theoretical calculations of the band structure and spectra of optical functions. *© 2000 MAIK "Nauka/Interperiodica".*

Owing to its unique properties, silicon carbide is a rather promising material for near-UV optoelectronics and high-temperature and radiation-resistant electronics. Theoretically, this material is of interest as the only compound formed by Group IV elements. It is characterized by a great number of polytypes and a wide spectral region of changeover from indirect to direct optical transitions [1, 2]. Therefore, the recent upsurge of theoretical calculations of its band structure is not accidental [3–11]. However, only two experimental investigations of reflectivity and dielectric constant have been performed recently in a wide energy range of 4–9.5 eV [11, 12].

In this work, a full set of optical functions has been calculated for cubic silicon carbide (3*C*-SiC). A complete set of transitions and parameters of these have been determined, and a theoretical analysis of the data obtained was performed.

1. CALCULATION PROCEDURE

The most comprehensive information about the specific features of the electronic structure in a wide range of characteristic absorption energies is contained in a set of fundamental optical functions [13]. These include the spectra of reflection (R); refractive index (n); extinction coefficient (k); real (ε_1) and imaginary (ε_2) parts of the dielectric constant; bulk ($-\mathrm{Im}\varepsilon^{-1}$) and surface ($-\mathrm{Im}[1 + \varepsilon]^{-1}$) losses; absorption coefficient μ; electrooptical functions α and β; and also $\varepsilon_2 E^2$, θ, n_{eff}, and $\varepsilon_{\mathrm{eff}}$.

Generally, only the reflection spectrum is measured in a wide spectral range, with the same done for ε_1, ε_2, and $-\mathrm{Im}\varepsilon^{-1}$ spectra very rarely. That is why the spectra of a full set of functions are most commonly calculated using the integral Kramers–Kronig relations and an experimental reflection spectrum. For this purpose, we used the known procedure [13, 14] with the reflection spectrum reported in [15] as input data.

Fundamental absorption of cubic SiC at the longest wavelengths is due to indirect transitions corresponding to an energy gap $E_{gi} \approx 2.4$ eV [16–18]. At shorter wavelengths, the absorption exceeds the value calculated for indirect transitions. Therefore, the existence of two more indirect-transition edges has been assumed: at $E_{gi} \approx 3.55$ and 4.20 eV [16]. However, the second edge is very weakly pronounced and may have some other nature. The region of the third indirect-transition edge has been measured at unacceptably large optical densities (μd = 4–9), and, therefore, these data are questionable. It should be emphasized that indirect transitions can be revealed conclusively only in the following way. Temperature dependences of $\mu(E, T)$ spectra should be measured in a wide temperature (T) range on perfect samples, with any influence of impurities or imperfections ruled out, and a theoretical analysis of the spectra should be made. This has not been done for the spectral region $E > 2.5$ eV. Therefore, the issue concerning the $\mu(E)$ spectrum for $E > 3.2$ eV and its nature remains open.

3*C*-SiC reflection spectra have been taken at room temperature in the spectral ranges 3–13 [15], 1–12 [17], 1–12.5 [19], and 4–9.5 eV [11]. The data of [15, 17, 19] were analyzed in [2, 19]. The spectrum of [17] is strongly distorted for unknown reasons. The refractive index can be used to readily calculate the expected R values at 1.8 eV: $R \approx 0.20$. Therefore, the reflection in [11] is markedly underestimated, with all spectral features strongly broadened. Curves having the most distinct structure were obtained in [15, 19], with peak positions in good agreement. The strongest reflection was observed in [15]. Therefore, just these data were used to calculate the set of optical functions.

2. RESULTS AND DISCUSSION

Let us briefly discuss the main results (Figs. 1, 2). The experimental reflectance spectrum of 3*C*-SiC in

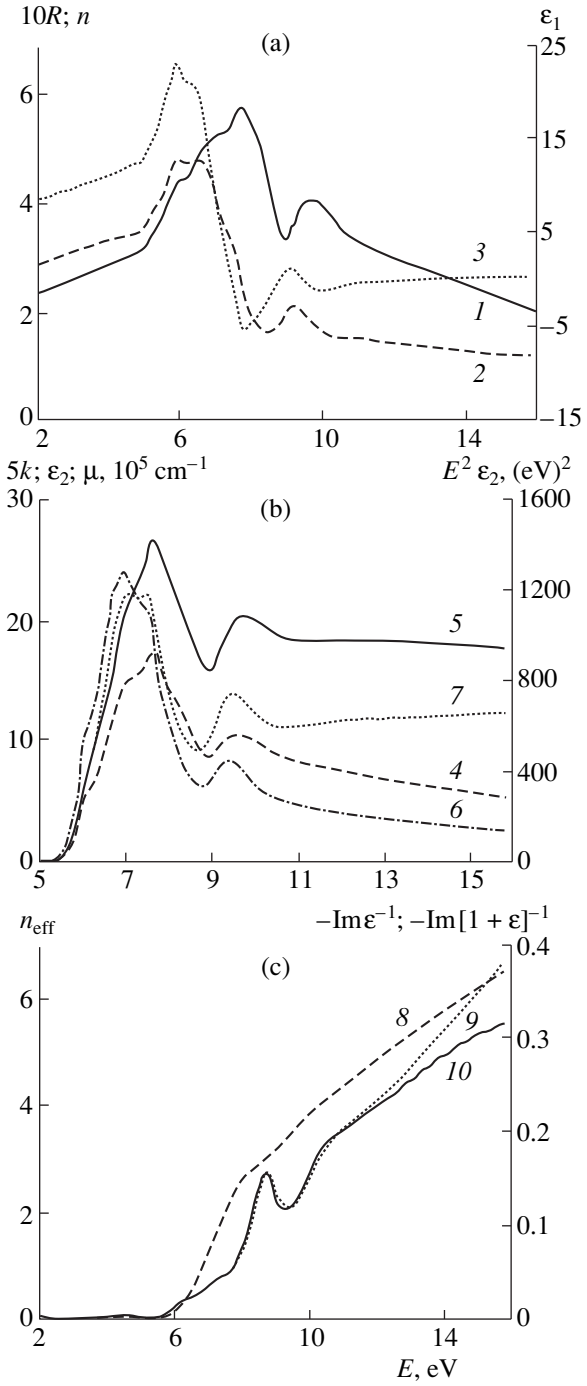

Fig. 1. (a) Experimental spectrum of reflectance R (*1*), and calculated spectra of n (*2*) and ε_1 (*3*). (b) Calculated spectra of (*4*) k, (*5*) μ, (*6*) ε_2, and (*7*) $\varepsilon_2 E^2$. (c) Calculated spectra of (*8*) n_{eff}, (*9*) $-\text{Im}\varepsilon^{-1}$, and (*10*) $-\text{Im}[1+\varepsilon]^{-1}$.

Fig. 1a shows the strongest peak at $E = 7.75$ eV; a broad peak at $E = 9.7$ eV; and weak features at ~4.6, 6.0, 7.1, and 8.3 eV. Extrapolation of the reflectance to shorter and longer wavelengths gives approximately equal values at $E = 0.2$ and 16 eV ($R \approx 0.2$). For the main peak at 7.75 eV, $R \approx 0.58$. The calculated $n(E)$ and $\varepsilon_1(E)$ spectra (Fig. 1a) are rather similar in shape. It looks as if they are shifted to lower energies with respect to R by approximately 0.5 eV with peak intensities in the 5.5–9.0 eV range redistributed in favor of longer-wavelength peaks. Consequently, analogues of weak reflection peaks become strongest in these spectra. For peaks at ~6 and 9.2 eV, $n = 4.84$ and 2.10, and $\varepsilon_1 = 22.7$ and 1.1, respectively. At $E = 16$ eV, these values decrease to $n = 1.1$ and $\varepsilon_1 = 0.2$.

The calculated spectra of k, μ, ε_2, and $\varepsilon_2 E^2$ in Fig. 1b are similar in shape. They include a doublet–triplet main band with a maximum at ~7.5 eV and a separate peak at ~9.6 eV. The k, μ, and ε_2 values are 3.4, 2.7×10^6 cm^{-1}, and 24, respectively, for the first band, and 2.1, 2×10^6 cm^{-1}, and 8.3, for the second. With the energy increasing to 16 eV, these values decrease to 1.1, 1.8×10^6 cm^{-1}, and 2.6. The $n(E)$ and $k(E)$ spectra calculated from experimental data in the 5–12.5 eV range [21] are erroneous: $n < 1$ for $E > 10$ eV instead of the expected $n > 1$, and $k \sim 0.2$ (i.e., $\mu \approx 10^5$ cm^{-1}) at 5 eV instead of the expected $\mu < 10^4$ cm^{-1}. At $E = 3.5$–5 eV, the ε_2 values reported in [12] are markedly overestimated (whereas the values of ε_1 are underestimated) as compared with those expected on the basis of absorption [16, 17] and refraction data [20].

With increasing energy, the effective number $n_{\text{eff}}(E)$ of valence electrons involved in transitions to the given energy E (Fig. 1c) increases from 0.1 at $E = 6$ eV to 2, 4, and 6 for $E = 7.5$, 10.3, and 14.7 eV, respectively. This agrees well with the known theoretical band-structure calculations: all four electrons of the uppermost valence bands participate in transitions at $E < 10.3$ eV. At higher energies, electrons from lower valence bands become involved.

The spectra of bulk and surface characteristic losses $-\text{Im}\varepsilon^{-1}$ and $-\text{Im}[1+\varepsilon]^{-1}$ in Fig. 1c nearly coincide. Their peak at $E = 8.8$ eV is shifted by ~1.1 eV with respect to the main absorption peak, which is indicative of a very strong, longitudinal–transverse splitting of the related transitions.

In the $E = 2$–6 eV range, the electrooptical function β is very small. Therefore, the contribution from changes in the imaginary part of the dielectric constant can be neglected in analyzing modulated spectra. In the rest of the spectral region, the functions α and β nearly coincide.

In the available publications, theoretical spectra have been reported for R (4–10 eV) [10] and ε_2 (5.5–12 eV [10], 4.5–10 eV [9], 5–17 eV [7], 5.7–11 eV [8], and 3–13 eV [22]). With normalization used, the theoretical reflectance spectrum nearly coincides with the experimental one in the 4–7.6 eV range. In the vicinity of broad experimental bands (E = 6–8.5 and 9.2–11 eV), the theoretical spectrum also contains bands with a rather intricate structure, each comprising four components. The main contradiction between the

Parameters E_i, H_i, S_i, and f_i of oscillators O_i for 3*C*-SiC crystal, their possible interpretation and energies in band diagrams, according to [3–8, 10, 22]

O_i	Our data				[3]	[4]	[5]	[6]	[7]	[8]	[10]	[22]
	E_i	H_i	f_i	S_i								
1	6.03	0.26	0.48	0.48	–	*LM* 5.7; *LA* 5.8	*X* 6.0	X 5.7	Γ*X* 5.5	Γ 5.8; *X* 6.0	*X* 5.6	*X* 5.3
2	6.33	0.65	0.82	1.64	*X* 6.2	Γ*K* 6.4		Γ*X* 5.9	*K* 6.4	Γ 6.4		Γ 5.9
3	6.51	0.28	0.14	0.39	Δ 6.5	*KM* 6.5	*K* 7.1	–		Γ*X* 6.5	–	*L* 6.6
4	6.85	0.67	1.1	5.42	Σ 6.7	*KM* 7.2		–	–	7.3 volume of BZ	–	–
5	7.15	0.3	0.15	1.01	*U* 7.1	Γ 7.4	Γ 7.2	Γ 7.2	Γ 7.2		–	–
6	7.55	0.6	0.52	4.8	*U* 7.4	Γ*K* 7.6; *LA* 7.7				Σ 7.6	Γ 7.6; *L* 7.6	–
7	7.95	0.3	0.03	0.3	Λ 8.3	*KM* 7.7	Γ 7.7	Γ*L* 7.6	*L* 7.7	8.1 volume of BZ	*X* 8.5	Γ 7.8 *X* 7.9
8	8.24	0.54	0.08	0.91	Σ 8.3	*LM* 8.5	*X* 9.1	Γ*K* 8.5	Λ 8.2	Γ*L* 9.0	Γ 8.7	
						KM 8.2; 8.7	Γ 8.4					*L* 9.0
						Γ 8.1; 8.5						
9	9.5	0.92	0.21	2.7	Σ 9.2	*LM* 9.5	*L* 9.7	Γ*X* 9.3	Γ*X* 9.2	*X* 9.2	*L* 9.4	
					Δ 9.3; Λ 10	*LA* 10			*XW* 9.0	Γ*L* 9.2		
10	10.9	2.42	0.37	5.1	Σ 12	Γ*K* 10.5	Γ*K* 11.0	Γ*K* 10	*KW* 10.7	Γ*X* 10.2	9.9 volume of BZ	Σ 10
						KM 10.5		*L* 10	*XW* 10.3			
									Γ*L* 10.4			
11	14.2	4.4	0.35	4.9	Σ 13.5; 15	*KM* 14.5	*L* 13.2	*W* 13.8	*KW* 14.2	Γ 13.2	–	–
					Λ 13.3	*LM* 12.7		*L* 12.4				
						Γ*K* 15.5						

Note: All energies are given in eV.

theoretical and experimental spectra of R is that the intensities of both the theoretical bands are strongly overestimated. Both these bands are rather broad, and, therefore, the contradiction cannot be eliminated in a conventional manner by taking into account their additional broadening.

All the reported theoretical ε_2 spectra contain two bands in the vicinity of the bands calculated in this work from the reflection spectrum. However, these spectra widely vary in absolute intensity, ratio of the intensities of these two bands, their half-widths, area under the bands, and band positions. This is no accident. Up to now, there have not been any adequate theoretical $\varepsilon_2(E)$ spectra even for the simplest model crystals, such as Si and C [13]. This is due to the necessity of calculating the band structure over the entire volume of the Brillouin zone (BZ), taking into account the dependences of oscillator strengths on the energy and wave vector, $f(E, k)$, and many-particle effects. Therefore, the knowledge of a set of spectra of fundamental optical functions in a wide range of fundamental absorption energies, including the set obtained by us for cubic silicon carbide, is of particular importance for solving these rather complicated problems.

Further steps in obtaining information about the fine structure of optical spectra and the related transitions involve the problem of resolving these spectra into components [13]. The Argand diagram method [13, 14] was used to resolve the total $\varepsilon_2(E)$ spectrum of a 3*C*-SiC crystal in the 5.5–16 eV range into 11 Lorentz oscillators O_i, with three parameters determined for each of these: peak energy E_i, half-width H_i, and oscillator strength f_i (Fig. 2, table). Commonly, the $n_{\text{eff}}(E)$

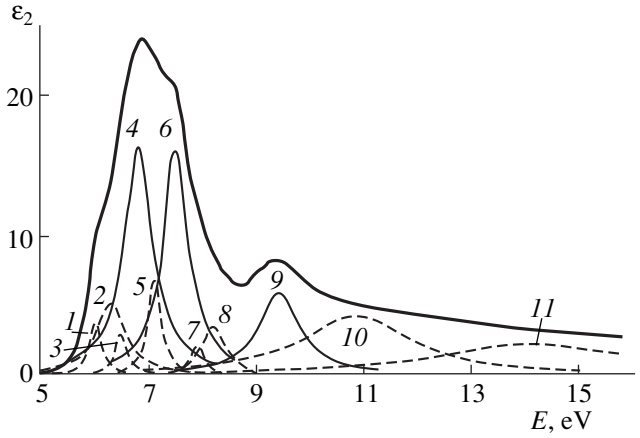

Fig. 2. Integral spectrum of ε_2 (the upper curve) and its components for a 3*C*-SiC crystal.

spectrum is unavailable and, therefore, the oscillator strength is determined as the area S_i under a peak in the $\varepsilon_2(E)$ spectrum divided by the total number of valence electrons. In the case under consideration, the transition intensities are determined in both ways, using S_i and f_i. On decomposing the $\varepsilon_2(E)$ spectrum into components, not only a very weakly pronounced triplet structure of the main intensive band was resolved (*2, 4, 6*), but also new bands (*1, 3, 5, 7, 8, 10, 11*) were revealed, totally hidden in the integral curve due to their strong overlapping.

In the Argand method, this decomposition is performed in a unique manner without any fitting parameters. True, the model of symmetric Lorentzian oscillators, used in the process, is rather simplified. It can be adopted as a zero approximation for developing further, more perfect approaches. Each component combines transitions with close energies, but not necessarily of the same nature. In the general case, the employed method gives the smallest number of components. Their theoretical analysis may suggest whether the obtained components should be resolved into several more parts.

In [21], the $k(E)$ and $n(E)$ spectra of a SiC crystal in the range 5–12 eV were reproduced with a set of four oscillators, using 14 fitting parameters. For this purpose, analytical formulas proposed for $k(E)$ and $n(E)$ were derived in a rather artificial approximation of parabolic bands in terms of the model of Lorentzian symmetric oscillators. The set of oscillators proposed in [21] markedly differs from our data in all the three parameters (E_i, H_i, f_i). This confirms the arbitrariness and ambiguity of reproduction of the $n(E)$ and $k(E)$ spectra in [13], as was expected [13]. Only simultaneous use of spectra of two functions, $\varepsilon_1(E)$ and $\varepsilon_2(E)$, allows us to resolve, in terms of the Argand diagram, the integral curves $\varepsilon_1(E)$ and $\varepsilon_2(E)$ into components in a unique manner and without fitting parameters. No unambiguous and conclusive interpretation can be proposed yet for each of the 11 components of the $\varepsilon_2(E)$ spectrum. Above, a brief mention was made of wide discrepancies between theoretical integral $\varepsilon_2(E)$ spectra of 3*C*-SiC crystal, reported in different works, and also between theoretical and experimental $R(E)$ and $\varepsilon_2(E)$ spectra. This can be explained by oversimplifications in theoretical calculations commonly based on the model of direct interband transitions as the best developed and simplest. Another extreme model, based on metastable excitons, is considered rather promising. However, it has only been used up to now for obtaining integrated $\varepsilon_2(E)$ spectra for silicon and diamonds, without resolving the spectra into components [13].

According to the general theory, the most intense transitions must be observed between pairs of bands that are parallel in a certain volume of the Brillouin zone. We used this model to analyze the theoretical schemes proposed in [3–10, 22]. For brevity, the table lists energy spacings between different pairs of bands in the vicinity of the points Γ, *X*, *K*, *L*, *W*, *U*, Σ, Δ, and Λ without indicating the upper and lower bands. Analysis of these data indicates a pronounced inconsistency of band schemes employed in different works and their substantial faults. Therefore, the proposed interpretation of 11 $\varepsilon_2(E)$ components for the 3*C*-SiC crystal (see table) is one of the first attempts to compare in detail the predictions of the band theory with the fine structure of transitions in the $\varepsilon_2(E)$ spectrum calculated from experimental data.

The long history of theoretical calculations has shown that the problem of the electronic structure of solids is rather complicated. Until recently, the possibility of fitting and selecting tentative model concepts for a crystal was limited to the integral curve of the reflection spectrum. The complete set of optical fundamental functions and components of the dielectric constant spectrum supplements the available experimental data, providing very thorough and extensive information. This provides a fundamentally new basis for much more precise theoretical calculations of a detailed electronic structure of crystals, including those for cubic silicon carbide.

The principal results of this work are the following. A complete set of optical fundamental functions of the 3*C*-SiC crystal was obtained for the first time in the range of 2–16 eV at 300 K. The ε_2 spectrum was found to comprise 11 components. Parameters of these components were determined, and a general scheme was proposed that is applicable to their interpretation based on the known theoretical band calculation procedures.

ACKNOWLEDGMENTS

The authors are grateful to P.A. Ivanov, V.E. Chelnokov, F. Bechstedt, K.J. Chang, and W.R L. Lambrecht for paper reprints.

This work was supported by the Center for Basic Natural Science (St. Petersburg University).

REFERENCES

1. P. A. Ivanov and V. E. Chelnokov, Fiz. Tekh. Poluprovodn. **29**, 1921 (1995) [Semicond. **29**, 1003 (1995)].
2. V. V. Sobolev, *Native Energy Levels in A^4 Solids* (Shtiintsa, Kishinev, 1978).
3. B. Wenzien, P. Kackell, F. Bechstedt, *et al.*, Phys. Rev. B: Condens. Matter **52**, 10897 (1995).
4. C. H. Park, B.-Ho Cheong, K.-Ho Lee, *et al.*, Phys. Rev. B: Condens. Matter **49**, 4485 (1994).
5. M. Rohlfing, P. Kruger, and J. Pollmann, Phys. Rev. B: Condens. Matter **48**, 17791 (1993).
6. W. R. L. Lambrecht and B. Segall, Phys. Rev. B: Condens. Matter **43**, 7070 (1991).
7. A. R. Lubinsky, D. E. Ellis, and G. S. Painter, Phys. Rev. B: Condens. Matter **11**, 1537 (1975).
8. L. A. Hemstreet and C. Y. Fong, Phys. Rev. B: Condens. Matter **6**, 1464 (1972).

9. K.-Ho Lee, C.H. Park, B.-Ho Cheong, *et al.*, Solid State Commun. **92**, 869 (1994).
10. W. R. L. Lambrecht, C. H. Lee, K. Kim, *et al.*, in *Wide Band Gap Electronic Materials* (Kluwer Acad., Dodrecht, 1995), p. 335.
11. W. R. L. Lambrecht, B. Segall, M. Joganathan, *et al.*, Phys. Rev. B: Condens. Matter **50**, 10722 (1994).
12. S. Logothetidis and J. Petalas, J. Appl. Phys. **80**, 1768 (1996).
13. V. V. Sobolev and V. V. Nemoshkalenko, *Methods of Calculational Physics in Solid-State Theory. Electronic Structure of Semiconductors* (Naukova Dumka, Kiev, 1988).
14. V. V. Sobolev and V. Val. Sobolev, Fiz. Tverd. Tela **36**, 2560 (1994) [Phys. Solid State **36**, 1393 (1994)].
15. B. E. Wheeler, Solid State Commun. **4**, 173 (1966).
16. W. J. Choyke and L. Patrick, Phys. Rev. **187**, 1041 (1969).
17. M. L. Belle, N. K. Prokof'eva, and M. B. Reĭfman, Fiz. Tekh. Poluprovodn. **1**, 383 (1967) [Sov. Phys. Semicond. **1**, 315 (1967)].
18. D. S. Nedzvetskiĭ, B. V. Novikov, N. K. Prokof'eva, *et al.*, Fiz. Tekh. Poluprovodn. **2**, 1089 (1968) [Sov. Phys. Semicond. **2**, 914 (1968)].
19. V. V. Sobolev, Izv. Akad. Nauk SSSR, Neorg. Mater. **6**, 2073 (1970).
20. P. T. B. Shaffer, Appl. Opt. **10**, 1034 (1971).
21. A. R. Forouhi and J. Bloomer, Phys. Rev. B: Condens. Matter **38**, 1865 (1988).
22. F. Herman, J. P. Van Dyke, and R. L. Kortum, Mater. Res. Bull. **4**, S167 (1969).

Translated by M. Tagirdzhanov

Semiconductors, Vol. 34, No. 4, 2000, pp. 438–440. Translated from Fizika i Tekhnika Poluprovodnikov, Vol. 34, No. 4, 2000, pp. 452–454.

SEMICONDUCTOR STRUCTURES, INTERFACES, AND SURFACES

On the Theory of Anomalous Photovoltage in Multilayer Structures with *p–n* Junctions

V. N. Agarev and N. A. Stepanova

Nizhni Novgorod State University, pr. Gagarina 23, Nizhni Novgorod, 603600 Russia

Submitted July 19, 1999; accepted for publication October 21, 1999

Abstract—Steady- and nonsteady-state photovoltages appearing in a multilayer structure with *p–n* junctions under the conditions of nonuniform illumination are considered for an arbitrary ratio between the diffusion length L and the sizes d of the *p*- and *n*-regions. It is shown that, for $d \ll L$, the photovoltage is substantially lower (by $d^2/12L^2$ times) than in the case of $d \gg L$ owing to the mutual influence of neighboring *p–n* junctions. Relaxation of the photovoltage is controlled by recharging of the barrier capacitances of *p–n* junctions, and the relaxation time exceeds by several orders of magnitude the lifetime of nonequilibrium charge carriers in the *p*- and *n*-regions. The results obtained make it possible to explain the special features of the effect of anomalous photovoltage in polycrystalline films. © *2000 MAIK "Nauka/Interperiodica".*

The effect of anomalous photovoltage has been observed in polycrystalline films based on various materials [1–4]. This effect is caused by the fact that the film includes a large number of crystallites with *p–n* junctions [1]. If the film is illuminated at an angle, the neighboring *p–n* junctions are illuminated nonuniformly owing to the irregular relief pattern of the surface. As a result, the photovoltage arises across the film; this photovoltage is equal to the sum of the differences between photovoltages across the neighboring *p–n* junctions. A multilayer structure with *p–n* junctions is a convenient model of a polycrystalline film. Recently, in connection with the development of the δ-doping technology, additional interest in fabricated multilayer structures with specified properties has been aroused [5].

The largest photovoltage in a multilayer structure can attain values on the order of mkT/e ($2m$ is the number of *p–n* junctions). However, the actual values of the photovoltage observed experimentally are lower by an order of magnitude [2, 4]. In order to explain this fact, it was assumed in [1] that a conducting bypass existed in the bulk of the film. The relaxation time of the photovoltage is much longer than the lifetime of the nonequilibrium charge carriers, which is explained in [2] by the presence of capture levels. The influence of barrier capacitances and the assembly capacitance of connections on the photovoltage-relaxation time was considered phenomenologically in [3, 4]. In the latter, a multilayer structure composed of uncoupled *p–n* junctions was considered; it was shown that the relaxation time of photovoltage is defined by the largest of two characteristic times: τ_1 (the relaxation time of the photocurrent) and τ_2 (the time it takes to recharge the barrier capacitances).

Since the crystallites have dimensions on the order of 10^{-4}–10^{-5} cm, the issue concerning the ratio between the crystallite size d and the diffusion length L is open to discussion. In [1], it was invariably assumed that $d \gg L$. It is obvious that, if $d \leq L$, the influence of neighboring *p–n* junctions can reduce the photovoltage.

Transient processes in a multilayer structure with coupled *p–n* junctions (for $d \leq L$) were studied in detail in [6–8] where it was shown that the influence of barrier capacitances brought about an appreciable increase in the relaxation time of nonequilibrium electrical conductivity and photoconductivity.

In this work, we studied a multilayer structure with nonuniformly illuminated *p–n* junctions for an arbitrary value of d/L. We consider a one-dimensional homogeneous multilayer structure with $2m$ *p–n* junctions having the same thicknesses for the *p*- and *n*-regions ($d_n = d_p = d$). We assume that the parameters of charge carriers are identical in the *p* and *n* regions; i.e., we have $\tau_n = \tau_p = \tau$ for the lifetime of nonequilibrium charge carriers, $D_n = D_p = D$ for the diffusion coefficient, $L_n = L_p = L$ for the diffusion length, and $P_n = N_p$ for the equilibrium concentration of holes in *n*-regions and electrons in *p*-regions. We also assume that the rate of bulk generation of charge carriers by light in the *p*- and *n*-regions decreases linearly from the value of g in the vicinity of *p–n* junctions to the value of αg ($\alpha < 1$) away from *p–n* junctions. The continuity equation and the boundary conditions for the concentration of equilibrium charge carriers in the *n*-region between the jth and $(j + 1)$th *p–n* junctions can be written as

$$\frac{d^2\Delta p}{dx^2} = \frac{\Delta p}{L^2} - \frac{g}{D}\left[1 - \frac{(1-\alpha)x}{d}\right],$$

$$\Delta p(0) = P_j = P_n\left[\exp\left(\frac{eV_j}{kT}\right) - 1\right], \quad (1)$$

$$\Delta p(d) = P_{j+1} = P_n\left[\exp\left(\frac{eV_{j+1}}{kT}\right) - 1\right].$$

Solving equation (1), we find the currents of the jth and $(j+1)$th p–n junctions, and we then determine the total photovoltage across the multilayer structure under the open-circuit conditions as

$$V_{\text{ph}} = m(V_j - V_{j+1}) = \frac{mkT}{e}$$

$$\times \ln\left\{\left[1 + \frac{g\tau}{P_n}\left[1 - (1-\alpha)\frac{L}{d}\left(\coth\frac{d}{L} - \operatorname{cosech}\frac{d}{L}\right)\right]\right] \Big/ \left[1\right.\right. \quad (2)$$

$$\left.\left. + \frac{g\tau}{P_n}\left[\alpha + (1-\alpha)\frac{L}{d}\left(\coth\frac{d}{L} - \operatorname{cosech}\frac{d}{L}\right)\right]\right]\right\}.$$

For low intensities of illumination ($g\tau \ll P_n$), the photovoltage across the structure is given by

$$V_{\text{ph}} = \frac{mkT}{e}\frac{g\tau}{P_n}(1-\alpha) \times \left[1 - 2\frac{L}{d}\left(\coth\frac{d}{L} - \operatorname{cosech}\frac{d}{L}\right)\right], \quad (3)$$

whence, for $d \gg L$, we have

$$V_{\text{ph}} = \frac{mkT}{e}\frac{g\tau(1-\alpha)}{P_n}. \quad (4)$$

In the case of $d \ll L$, we arrive at

$$V_{\text{ph}} = \frac{mkT}{e}\frac{g\tau(1-\alpha)}{P_n}\left(\frac{1}{12}\frac{d^2}{L^2}\right). \quad (5)$$

Thus, it can be seen from (4) and (5) that, for small sizes of crystallites as compared to the diffusion length ($d \ll L$), the influence of neighboring p–n junctions brings about an appreciable decrease in photovoltage. For moderate sizes of crystallites ($d \leq L$), the variation in charge at barrier capacitances of p–n junctions (when the voltage applied to them is varied) substantially exceeds the variation in charge of nonequilibrium electrons and holes in the p- and n-regions [6].

We now consider the relaxation of charge at the barrier capacitances of p–n junctions after switching off the illumination. Voltages across the p–n junctions in the course of relaxation are defined by the charges at barrier capacitances; i.e.,

$$Q_j(t) = \frac{Q_0}{2}\sqrt{1 - \frac{V_j(t)}{\varphi}}, \quad Q_{j+1}(t) = \frac{Q_0}{2}\sqrt{1 - \frac{V_{j+1}(t)}{\varphi}}, \quad (6)$$

where φ is the contact potential difference, $Q_0 = eNW$ is the equilibrium charge at barrier capacitances, N is the concentration of the majority charge carriers, and W is the thickness of the space-charge layer of the p–n junction. Charges at the barrier capacitances vary under the effect of currents through the p–n junctions; thus,

$$\frac{dQ_j}{dt} = I_j, \quad \frac{dQ_{j+1}}{dt} = -I_{j+1}. \quad (7)$$

Since variation in the diffusion currents of p–n junctions in response to changes in the boundary concentrations occurs with a characteristic time on the order of $d^2/2D$, which is much shorter than the photovoltage-relaxation time [6], we may assume that the currents through p–n junctions are quasi-equilibrium; i.e.,

$$I_j(t) = -\frac{eD}{L}\left(P_{j+1}\operatorname{cosech}\frac{d}{L} - P_j\coth\frac{d}{L}\right),$$

$$I_{j+1}(t) = -\frac{eD}{L}\left(P_{j+1}\coth\frac{d}{L} - P_j\operatorname{cosech}\frac{d}{L}\right),$$

$$P_j(t) = \Delta p(0) = P_n\left[\exp\left(\frac{eV_j(t)}{kT}\right) - 1\right], \quad (8)$$

$$P_{j+1}(t) = \Delta p(d) = P_n\left[\exp\left(\frac{eV_{j+1}(t)}{kT}\right) - 1\right].$$

For low illumination intensities ($V_j < kT/e$ and $V_{j+1} < kT/e$), system (6)–(8) has the following analytical solution:

$$V_j(t) = \frac{1}{2}\left\{\left[V_j(0) + V_{j+1}(0)\operatorname{cosech}\frac{d}{L}\right] \times \exp\left[\left(-\coth\frac{d}{L} + 1\right)\frac{t}{\tau_0}\right] + \left[V_j(0) - V_{j+1}(0)\operatorname{cosech}\frac{d}{L}\right] \times \exp\left[\left(-\cot\frac{d}{L} - 1\right)\frac{t}{\tau_0}\right]\right\},$$

$$V_{j+1}(t) = \frac{1}{2}\left\{\left[V_j(0)\sinh\frac{d}{L} + V_{j+1}(0)\right] \times \exp\left[\left(-\coth\frac{d}{L} + 1\right)\frac{t}{\tau_0}\right] + \left[V_{j+1}(0) - V_j(0)\sinh\frac{d}{L}\right]\right.$$

$$\times \exp\left[\left(-\cot\frac{d}{L} - 1\right)\frac{t}{\tau_0}\right]\Bigg\}.$$

Here, $V_j(0)$ and $V_{j+1}(0)$ are solutions to time-independent equation (1) and are given by

$$V_j(0) = \frac{kT}{e}\frac{g\tau}{P_n}\left[(1-\alpha)\frac{L}{d}\left(\operatorname{cosech}\frac{d}{L} - \coth\frac{d}{L}\right) + 1\right],$$

$$V_{j+1}(0) = \frac{kT}{e}\frac{g\tau}{P_n}\left[(1-\alpha)\frac{L}{d}\left(\coth\frac{d}{L} - \operatorname{cosech}\frac{d}{L}\right) + \alpha\right].$$

The relaxation time τ_0 is defined by recharging of the barrier capacitances; i.e., we have

$$\tau_0 = \frac{1}{4}\frac{N}{P_n}\frac{W}{L}\frac{kT}{e\varphi}\tau.$$

For $kT/e\varphi \approx 10^{-2}$, $W/L \approx 10^{-1}$, and $N/P_n \approx 10^{16}/10^4$, we have $\tau_0 \approx 10^{10}\tau$; i.e., the characteristic relaxation time τ_0 for the photovoltage exceeds the lifetime of nonequilibrium charge carriers by many orders of magnitude.

For $d \ll L$, the photovoltage-relaxation time $\tau_{ph} \approx \tau_0 d/L$ decreases with decreasing d/L; however, τ_{ph} still remains much larger than τ.

Thus, the model of a multilayer structure with small-size p- and n-regions ($d \leq L$ or $d \ll L$) accounts adequately both for the value of the steady-state photovoltage and for the long photovoltage-relaxation time without using additional assumptions concerning the conducting bypasses and capture levels.

REFERENCES

1. É. I. Adirovich, É. M. Mastov, and Yu. M. Yuabov, Fiz. Tekh. Poluprovodn. **5** (7), 1415 (1971) [Sov. Phys. Semicond. **5**, 1241 (1971)].
2. É. I. Adirovich, Fiz. Tekh. Poluprovodn. **4** (4), 745 (1970) [Sov. Phys. Semicond. **4**, 629 (1970)].
3. É. I. Adirovich, É. M. Mastov, and Yu. M. Yuabov, Dokl. Akad. Nauk SSSR **188**, 1254 (1969).
4. I. A. Karpovich and M. V. Shilova, Izv. Vyssh. Uchebn. Zaved., Fiz. **4**, 128 (1969).
5. V. V. Osipov, A. Yu. Selyakov, and M. Foygel, Fiz. Tekh. Poluprovodn. **32** (2), 221 (1998) [Semicond. **32**, 201 (1998)].
6. V. I. Stafeev, Fiz. Tekh. Poluprovodn. **6**, 2134 (1972) [Sov. Phys. Semicond. **6**, 1811 (1972)].
7. V. N. Agarev and V. I. Stafeev, Radiotekh. Élektron. **22** (1), 169 (1977).
8. V. N. Agarev and V. I. Stafeev, Radiotekh. Élektron. **22** (11), 2335 (1977).

Translated by A. Spitsyn

Semiconductors, Vol. 34, No. 4, 2000, pp. 441–444. Translated from Fizika i Tekhnika Poluprovodnikov, Vol. 34, No. 4, 2000, pp. 455–458.

SEMICONDUCTOR STRUCTURES, INTERFACES, AND SURFACES

Equilibrium Distributions of Shallow-Level Impurity and Potential in the Near-Surface Region of a Semiconductor in a Model with a Completely Depleted Layer

V. V. Gavrilovets, V. B. Bondarenko, Yu. A. Kudinov, and V. V. Korablev

St. Petersburg State Technical University, ul. Politekhnicheskaya 29, St. Petersburg, 195251 Russia

Submitted October 18, 1999; accepted for publication November 16, 1999

Abstract—A model of completely depleted layer was used to derive analytical expressions for equilibrium distributions of shallow-level impurity, electric field, and potential in the near-surface region of a semiconductor. The results of calculation were used to estimate the variation in the parameters of a finite-size structure. It was found that, in the approximation used, it was possible to reduce the concentration of electrically active defects by several times for semiconductor layers ~1 μm thick. © *2000 MAIK "Nauka/Interperiodica".*

A model according to which the doping impurity is distributed uniformly and the coordinate dependence of potential is either parabolic (for a completely depleted layer) or exponential (for the case of Debye screening) is typically used in analyzing the processes in the near-surface depleted layers in semiconductors and contact structures. At the same time, it is evident that such a state of a semiconductor is basically far from equilibrium; as shown in [1–6], in any uniformly doped semiconductor crystal, redistribution of charged impurity caused by diffusion and drift occurs in the field initiated by the surface charge after the crystal was cleaved. For example, in the surface-cleaning stage (often conducted at temperatures departing widely from those corresponding to intrinsic conduction), charged impurity is bound to be redistributed in the space-charge region (SCR), which would influence the potential-relief pattern of the band bending. Distribution of impurity by the time the diffusion and drift components of ionic current are balanced tends to a nonuniform state. A uniform state is realized if the driving force (electric field) is absent or if the ultimate solubility of impurity in a given matrix is attained.

In the majority of cases, the problem of equilibrium distributions of impurity and potential at the surface and interfaces of semiconductors can be only solved numerically; an analytical solution can be derived only in rare cases. For example, in [6], a solution of the problem in the case of deep impurity levels is outlined in detail, with consistent presentation based on a low degree of ionization of impurity and on linear screening of space charge in most of the near-surface region. It is noteworthy that this model is invalid for large band bendings and for doping with shallow-level impurity, which is characteristic of a wide range of semiconductor structures. As will be shown below, an analytical solution is also possible in this case if certain conditions are met.

The equilibrium state of the SCR in a semiconductor can be described if the time-independent diffusion equation and the Poisson equation are solved simultaneously. For the sake of definiteness, we consider a semi-infinite semiconductor doped with donor impurity. In the case where the impurity is completely and singly ionized, the electron gas in the conduction band is nondegenerate, and the space charge of holes in the valence band is ignored, we have

$$\frac{dN(z)}{dz} - e\mathscr{E}(z)\frac{N(z)}{kT} = 0, \qquad (1)$$

$$\frac{d^2U(z)}{dz^2} = \frac{4\pi e^2}{\varepsilon}\left\{N(z) - N_0\exp\left[-\frac{U(z)}{kT}\right]\right\}. \qquad (2)$$

Here, z is the coordinate along the axis directed from the surface to the bulk of the semiconductor; $N(z)$ is the donor concentration; $N_0 = N(\infty)$ is the doping level; $U(z)$ is the potential energy in the electric field; $\mathscr{E}(z) = (1/e)dU(z)/dz$ is the electric field in the band-bending region; and ε is the permittivity of the semiconductor (for elemental semiconductors, III–V, IV–VI, and some other compounds, $\varepsilon \sim 10$). Differential equation (1) is written under the assumption that $|\mathscr{E}(z)|$ in the main region of its existence is small; i.e., we have at least $e|\mathscr{E}(z)|a \ll kT$ (a is the diffusion-jump length of an impurity atom [7, 8] and, as such, is typically on the order of interatomic distance), which is virtually always valid for the near-surface fields lower than 10^6 V/cm. The right-hand side of equation (2) is written similarly to the case of a uniformly distributed shallow-level impurity of a single type (see, for example, [9]). Henceforth, we measure the potential from the conduction-band bottom.

System (1)–(2) should be supplemented with physically meaningful boundary conditions. Equation (1)

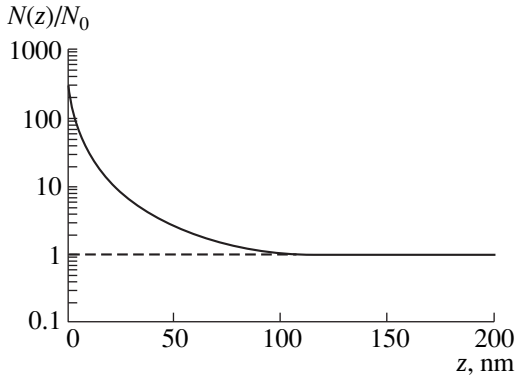

Fig. 1. Equilibrium distribution of shallow-level impurity in the SCR for constant magnitude of band bending (the solid curve) and the uniform distribution (the dashed straight line) with the parameters $N_0 = 10^{16}$ cm^{-3}, $U_0 = 0.3$ eV, and $T = 600$ K.

implies that the transport is steady-state, in which case the total flux of particles is equal to zero. Therefore, the most reasonable condition at the surface corresponds to the requirement that there is a balance between the diffusion- and drift-related components of the charged-impurity flux, which is equivalent to the case of reflecting interface. Correspondingly, for $z = \infty$, the diffusion flux equals zero, because $\mathscr{E}(\infty) = 0$. It is noteworthy that such a boundary condition at the surface for equation (1) presupposes a known and constant $\mathscr{E}(0)$. This is feasible if the surface charge remains unchanged in the course of redistribution of the space charge. This situation can be realized if either the surface states are completely occupied or the so-called slow surface states brought about by an adsorbate or a passivating coating are present at the surface. There exist intrinsic states at atomically clean surfaces; typically, these states have a high density, which brings about a pinning of the Fermi level. In this case, a variation in the space charge in the near-surface region only slightly affects the magnitude of the band bending. It is apparent that, in this case, the boundary condition at the surface consists in the requirement that the potential be constant. Under any physically meaningful boundary conditions, the general solution to equations (1) and (2) can be obtained only numerically. However, there exists a model simplification which admits of analytical integration of the system and derivation of a self-consistent solution; we have in mind the model with a completely depleted layer. This approximation is valid for appropriate magnitudes of the band bending.

Let the magnitude of the band bending be $U_0 \gg kT$ and let it be unchanged on redistribution of the charged impurity. We also assume that there are no electrons in a certain near-surface layer. We may then ignore the exponentially small term accounting for the screening of ionized donors on the right-hand side of (2). In this case, the problem is formulated in the following way:

$$\frac{dN(z)}{dz} - \frac{dU(z)}{dz}\frac{N(z)}{kT} = 0, \tag{3}$$

$$\frac{d^2U(z)}{dz^2} = \frac{4\pi e^2}{\varepsilon}N(z), \tag{4}$$

$$N|_{z=L} = N_0, \quad \left.\frac{dN}{dz}\right|_{z=L} = 0, \quad U|_{z=0} = U_0,$$

$$U|_{z=0} = 0, \quad \left.\frac{dU}{dz}\right|_{z=L} = 0.$$

The parameter L corresponds to the width of the depletion region. We now separate out the logarithmic derivative of $N(z)$ in (3) and differentiate the obtained expression with respect to z. On substituting (4) and introducing a new function $W(z) = \ln[N(z)/N_0]$, we have

$$\frac{d^2W(z)}{dz^2} = \frac{4\pi e^2}{\varepsilon kT}N_0 \exp W(z) \tag{5}$$

with homogeneous boundary conditions $W|_{z=L} = 0$ and $\left.\frac{dW}{dz}\right|_{z=L} = 0$. Applying the conventional algorithm for solving a nonlinear equation to (5), we arrive at

$$\exp W = \cos^{-2}\left(\frac{L-z}{2l}\right)$$

or

$$N(z) = N_0 \cos^{-2}\left(\frac{L-z}{2l}\right), \tag{6}$$

where $l = \sqrt{\dfrac{\varepsilon kT}{8\pi e^2 N_0}}$.

Thus, we obtained the distribution of the charged impurity in the SCR. In order to determine the potential, we can now rewrite (4) with the known coordinate dependence on the right-hand side; i.e.,

$$\frac{d^2U(z)}{dz^2} = \frac{4\pi e^2}{\varepsilon}N_0 \cos^{-2}\left(\frac{L-z}{2l}\right). \tag{7}$$

The first integration of (7) with allowance made for the condition $dU/dz(L) = 0$ yields the electric-field distribution

$$\frac{dU}{dz} = -\frac{kT}{l}\tan\left(\frac{L-z}{2l}\right). \tag{8}$$

The second integration under the condition that $U(L) = 0$ results in

$$U = -2kT \ln\cos\left(\frac{L-z}{2l}\right). \tag{9}$$

The condition $U(0) = U_0$ completes the definition of parameter L:

$$L = 2l\arccos\left[\exp\left(-\frac{U_0}{2kT}\right)\right]. \quad (10)$$

Thus, the self-consistent (and, consequently, equilibrium) solution to the problem defined by (3) and (4) in the depletion-layer model involves the functions $N(z)$ and $U(z)$. It is noteworthy that these dependences (they are shown in Figs. 1 and 2, respectively) are significantly different from those in the case of uniformly distributed impurity. The impurity-atom concentration in the immediate vicinity of the surface can attain values on the order of $N(0) = N_0\exp(U_0/kT)$. For example, if $U_0 = 0.3$ eV and $T = 600$ K, $N(0)/N_0 \approx 320$. As can be seen from a plot of $U(z)$, in this case [$N_0 = 10^{16}$ cm and $\varepsilon = 12$ (Si)], the electric field becomes appreciably higher (in the case under consideration, by a factor of about 8) at the semiconductor surface. It is worth noting that the result was obtained without taking into account the restrictions imposed on the near-surface impurity concentration at comparatively low temperatures (~300–400 K) and for high doping levels (~10^{18}–10^{19} cm^{-3}). Apparently, under these conditions, the ultimate solubility of impurity in a semiconductor crystal can be attained.

The distribution of impurity in the case of a large magnitude of the band bending (6) was obtained on the assumption that the electric fields in the SCR are low. However, if, in the case of a uniform distribution of impurity, the initial electric-field strength is moderate (<10^6 V/cm), the equilibrium electric field at the surface ($z = 0$) as defined by expressions (8) and (10)

$$\left.\frac{dU}{dz}\right|_{z=0} = -\frac{kT}{l}\sqrt{\exp\left(\frac{U_0}{kT}\right) - 1}$$

can exceed in magnitude the fields for which E appears linearly in diffusion equation (1) [or (3)]. For example, for $N_0 = 10^{17}$ cm^{-3}, $U_0 = 0.3$ eV, $\varepsilon = 12$, and $T = 600$ K, the value of $\mathscr{E}(0)$ is attained at the order of 10^6 V/cm, whereas, if the equilibrium state is attained at $T = 500$ K, the field at the surface exceeds the above value. In such cases, a substantial asymmetry in the impurity-atom jumps along and opposite to the field should be taken into account.

Distributions of impurity and potential in a finite layer of a semiconductor are also of theoretical and practical interest, as an appreciable redistribution of impurity in the SCR can bring about a variation in the doping level of semiconductor structures with micrometer and submicrometer sizes. The specificity of the above-outlined model and the results obtained make it possible to assess rather easily the influence of impurity diffusion within the in-built field of the band bending on the electron concentration in the conduction band; this concentration is an important electrical parameter of the system.

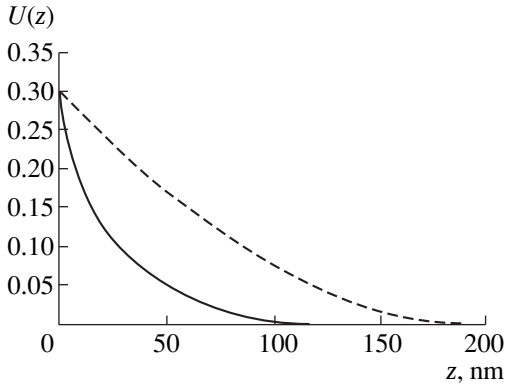

Fig. 2. The equilibrium band-bending profile (the solid line) for a constant potential at the surface and the parabolic band bending (the dashed line) with the parameters $N_0 = 10^{16}$ cm^{-3}, $U_0 = 0.3$ eV, and $T = 600$ K.

The following condition for a balance of impurity atoms should be fulfilled for a finite semiconductor layer:

$$N_0^{(0)}D = \int_0^L N(z)dz + N_0^{(1)}(D - L). \quad (11)$$

Here, D is the layer thickness and $N_0^{(0)}$ and $N_0^{(1)}$ are the initial and final impurity concentrations in the bulk. In this case, it is assumed that the electric field is zero for any value of the coordinate z in the interval $[L, D]$. It is significant that the distribution $N(z)$, the SCR width L, and other dependences (those of field and potential) have forms similar to (6) and (8)–(10), although with different parameters. This is related to the equivalence of the systems and boundary conditions in the adopted model of SCR.

On evaluating the integral in equation (11), we obtain

$$N_0^{(0)}D = N_0^{(1)}\left(2l\tan\frac{L}{2l} + D - L\right), \quad (12)$$

where now $l = \sqrt{\dfrac{\varepsilon kT}{8\pi e^2 N_0^{(1)}}}$ and $L = 2l\arccos\left[\exp\left(-\dfrac{U_0^{(1)}}{2kT}\right)\right]$. When the equilibrium state is attained, the magnitude of the band bending is changed as

$$U_0^{(1)} = U_0^{(0)} + \Delta E_F, \quad (13)$$

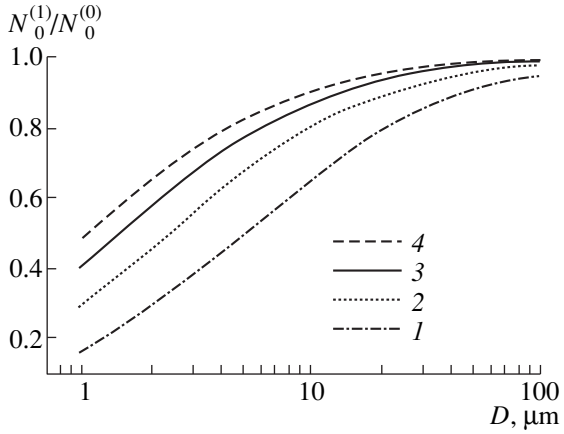

Fig. 3. Dependences of concentration of shallow-level impurity on the structure size D for several temperatures T in the state of equilibrium. T = (*1*) 400, (*2*) 500, (*3*) 600, and (*4*) 700 K.

where $\Delta E_F = kT\ln\dfrac{N_0^{(1)}}{N_0^{(0)}}$ is a variation in the position of the Fermi level in the system. Here, as above, it is assumed that the concentrations of donors and free electrons are equal in value in the bulk of the sample.

In what follows, we perform calculations for thick layers: $D \gg l$ and $D \gg L$ (for large magnitudes of band bending, $L \approx \pi l$). In these cases, the third term in the right-hand side of equation (12) can be ignored. In view of expression (13), we can simplify the first term in (12) as

$$2l\tan\frac{L}{2l} = 2l\sqrt{\exp\left(\frac{U_0^{(1)}}{kT}\right)-1}$$

$$\approx 2l\exp\left(\frac{U_0^{(0)}}{2kT}\right)\sqrt{\frac{N_0^{(1)}}{N_0^{(0)}}} = \exp\left(\frac{U_0^{(0)}}{2kT}\right)\sqrt{\frac{\varepsilon kT}{2\pi e^2 N_0^{(0)}}}.$$

As a result of the above simplifications, we obtain the following explicit expression for the so-far unknown parameter of the system (the impurity concentration in the bulk of a finite layer under the conditions of equilibrium):

$$N_0^{(1)} = N_0^{(0)}D\left[\exp\left(\left(\frac{U_0^{(0)}}{2kT}\right)\sqrt{\frac{\varepsilon kT}{2\pi e^2 N_0^{(0)}}}+D\right)\right]^{-1}. \quad (14)$$

We now replace the relevant parameters (the band bending and the bulk concentration of impurity) in expressions (6) and (8)–(10) by the corresponding expressions (13) and (14) and derive the equilibrium distributions of impurity, field, and potential in the SCR of a finite structure.

We now analyze the resulting expression (14). We note first of all that, in the limit of $D \longrightarrow \infty$ (a semi-infinite sample), the bulk impurity concentration tends towards its initial value. Typical dependences of $N_0^{(1)}$ on structure size and on the temperature corresponding to the establishment of equilibrium are shown in Fig. 3. The presence of a term that increases exponentially with decreasing temperature in the denominator in expression (14) causes the concentration to decrease several times. The temperature for which the quantity $N_0^{(1)}$ is half the initial concentration can be found from the following transcendental equation:

$$\exp\left(\frac{U_0^{(0)}}{2kT}\right)\sqrt{\frac{\varepsilon kT}{2\pi e^2 N_0^{(0)}}} = D.$$

For the aforementioned values of the parameters ($N_0^{(0)} = 10^6$ cm^{-3}, $U_0^{(0)} = 0.3$ eV, $\varepsilon = 12$, and $D = 2 \times 10^{-4}$ cm), such a variation occurs at ≈540 K and, for $D = 1 \times 10^{-4}$ cm, at ~700 K.

REFERENCES

1. V. S. Kuznetsov and V. B. Sandomirskiĭ, Kinet. Katal. **3**, 724 (1962).
2. W. Nuyts and R. van Overstraeten, Phys. Status Solidi A **15**, 329 (1973).
3. R. Sh. Malkovich and V. A. Pokoeva, Phys. Status Solidi A **48**, 329 (1978).
4. R. Shrivastava and A. H. Marshak, Solid-State Electron. **23**, 73 (1980).
5. O. Holdebrand, Phys. Status Solidi A **72** (2), 575 (1982).
6. F. F. Vol'kenshteĭn, *Electronic Processes at the Surface of Semiconductors in the Course of Chemisorption* (Nauka, Moscow, 1987).
7. J. P. Stark, *Solid State Diffusion* (Wiley, New York, 1976; Energiya, Moscow, 1980).
8. P. V. Kovtunenko, *Physical Chemistry of Solids: Crystals with Defects* (Vysshaya Shkola, Moscow, 1993).
9. V. L. Bonch-Bruevich and S. G. Kalashnikov, *Physics of Semiconductors* (Nauka, Moscow, 1977).

Translated by A. Spitsyn

Semiconductors, Vol. 34, No. 4, 2000, pp. 445–447. Translated from Fizika i Tekhnika Poluprovodnikov, Vol. 34, No. 4, 2000, pp. 459–461.

LOW-DIMENSIONAL SYSTEMS

On the Static Conductivity of a Disordered Quantum System with the Mirror Symmetry

A. G. Moiseev

Novosibirsk State Technical University, Novosibirsk, 630092 Russia

Submitted March 23, 1999; accepted for publication October 13, 1999

Abstract—The low-frequency portion of electrical conductivity in a disordered quantum system with the mirror symmetry is examined. The system is described by the Hubbard Hamiltonian, and the number of electrons is assumed to be equal to the number of sites. It is demonstrated that, given the strong attraction of electrons residing at the same site and the strong repulsion of electrons at the neighboring sites, the conductivity of the system at $T = 0$ increases with its size. It is shown that the metal-insulator transition does not occur in such a system. © *2000 MAIK "Nauka/Interperiodica".*

As noted in [1], a disordered one-dimensional system undergoes a metal-insulator transition at $T \longrightarrow 0$. In this author's opinion, the occurrence of such a transition is not a universal property featured by any one-dimensional disordered system. Thus, in a disordered mirror-symmetrical system with strong electron attraction at the same site and strong repulsion at neighboring sites, the low-frequency portion of conductivity diverges with an increase in the length of the system at $T \longrightarrow 0$, provided the number of electron is equal to the number of the sites. The metal-insulator transition at $T \longrightarrow 0$ does not occur in such a system. Conductivity of the one-dimensional disordered system with mirror symmetry was studied in [2, 3]. In [2], the electron-electron interaction was neglected. It was found that, in an unbounded medium, an electron located at $-\infty$ can, in an infinitely long time, be transferred to $+\infty$. This distinguishes a disordered system with the mirror symmetry from a disordered system uniform on average, where an electron cannot escape to infinity [4]. Meanwhile, the static conductivity of the disordered system considered in [2] vanishes at $T \longrightarrow 0$. In [3], the conductivity of a disordered system with the mirror symmetry has been studied for the case of strong repulsion between the electrons occupying the same site, the number of electrons being equal to the number of sites. In this situation, the static conductivity also amounts to zero, and the system proves to be an insulator. However, the conductivity diverges at a certain frequency of the external field.

In this paper, we study the conductivity of the mirror-symmetrical disordered system with the number of electrons equal to the number of sites. Strong attraction between electrons occupying the same site and strong repulsion between electrons occupying the neighboring sites is assumed. The system's Hamiltonian is written in the context of the Hubbard model as

$$\hat{H} = \sum_{n=1}^{n=N} \varepsilon_n(\hat{c}^+_{n;\uparrow}\hat{c}_{n;\uparrow} + \hat{c}^+_{n;\downarrow}\hat{c}_{n;\downarrow} + \hat{c}^+_{-n;\uparrow}\hat{c}_{-n;\uparrow} + \hat{c}^+_{-n;\downarrow}\hat{c}_{-n;\downarrow}) - |U|\sum_{n=-N}^{n=N} \hat{c}^+_{n;\uparrow}\hat{c}_{n;\uparrow}\hat{c}^+_{n;\downarrow}\hat{c}_{n;\downarrow}$$
$$+|\overline{U}|\sum_{n=1}^{n=N-1} (\hat{c}^+_{n;\uparrow}\hat{c}_{n;\uparrow}\hat{c}^+_{n+1;\uparrow}\hat{c}_{n+1;\uparrow} + \hat{c}^+_{n;\uparrow}\hat{c}_{n;\uparrow}\hat{c}^+_{n+1;\downarrow}\hat{c}_{n+1;\downarrow} \quad (1)$$
$$+ \hat{c}^+_{n;\downarrow}\hat{c}_{n;\downarrow}\hat{c}^+_{n+1;\uparrow}\hat{c}_{n+1;\uparrow} + \hat{c}^+_{n;\downarrow}\hat{c}_{n;\downarrow}\hat{c}^+_{n+1;\downarrow}\hat{c}_{n+1;\downarrow})$$
$$+\sum_{n=1}^{n=N} t_n(\hat{c}^+_{n;\uparrow}\hat{c}_{-n;\uparrow} + \hat{c}^+_{n;\downarrow}\hat{c}_{-n;\downarrow} + \hat{c}^+_{-n;\uparrow}\hat{c}_{n;\uparrow} + \hat{c}^+_{-n;\uparrow}\hat{c}_{n;\uparrow}).$$

Here, ε_n are random negative quantities, $2N$ is the total number of sites (N being an even quantity), $t_n = \Delta\exp(-aa_n)$, a is the distance between the sites, n is the number of a site, and $a_n = a(n - 0.5)$ is the coordinate of the nth site ($n \geq 1$). The model Hamiltonian (1) accounts for the transitions between the mirror-symmetrical sites $(n, -n)$ only, which are characterized by equal energy parameters: $\varepsilon_n = \varepsilon_{-n}$.

Since two electrons experience a strong attraction when they occupy the same site and a strong repulsion when they occupy neighboring sites, they pair up by two electrons with opposite spins at a site, with an empty site between each pair. Then, if $t \ll \Delta\varepsilon \ll |U| \approx |\overline{U}|$ (where $\Delta\varepsilon$ is the spread in ε_n), the following vector basis $|1\rangle$ and $|2\rangle$ are appropriate for the treatment of the ground and the first excited states:

1063-7826/00/3404-0445$20.00

$$\begin{cases} |1\rangle = \underset{-N;}{|0} \quad \underset{-N+1;}{\updownarrow} \quad \ldots \quad \underset{-3;}{\updownarrow} \quad \underset{-2;}{0} \quad \underset{-1;}{\updownarrow} \quad \underset{1;}{0} \quad \underset{2;}{\updownarrow} \quad \underset{3;}{0} \quad \ldots \quad \underset{N-1}{0} \quad \underset{N}{\updownarrow}\rangle, \\ |2\rangle = \underset{-N;}{|\updownarrow} \quad \underset{-N+1;}{0} \quad \ldots \quad \underset{-3;}{0} \quad \underset{-2;}{\updownarrow} \quad \underset{-1;}{0} \quad \underset{1;}{\updownarrow} \quad \underset{2;}{0} \quad \underset{3;}{\updownarrow} \quad \ldots \quad \underset{N-1}{\updownarrow} \quad \underset{N}{0}\rangle. \end{cases} \tag{2}$$

Here, numerals represent the site number and arrows indicate the spin direction. To compose the ground and the first excited state from vectors $|1\rangle$ and $|2\rangle$, we introduce an effective Hamiltonian $\hat{H}_0$, represented in the basis $|1\rangle$ and $|2\rangle$ as

$$\langle 1|\hat{H}_0|1\rangle = \langle 2|\hat{H}_0|2\rangle = \varepsilon_0; \quad \langle 2|\hat{H}_0|1\rangle = -|A|.$$

The eigenvectors and eigenvalues of the effective Hamiltonian are then given by

$$\begin{cases} |\psi_1\rangle = (|1\rangle + |2\rangle)/\sqrt{2}, & \varepsilon_1 = \varepsilon_0 - |A|, \\ |\psi_2\rangle = (|1\rangle - |2\rangle)/\sqrt{2}, & \varepsilon_2 = \varepsilon_0 + |A|. \end{cases} \tag{3}$$

To analyze the conductivity of the system under study, one needs to calculate the transition amplitude $\langle 2|\hat{U}(t')|1\rangle$ (where $\hat{U}(t')$ is the evolution operator) between the states $|1\rangle$ and $|2\rangle$ and the rate

$$\bar{\omega}_0 = 2|A|/\hbar = \frac{2|\langle 2|\hat{H}_0|1\rangle|}{\hbar}$$

of the transition between the states $|\psi_1\rangle$ and $|\psi_2\rangle$. It is expedient to express the model Hamiltonian (1) as a sum

$$\hat{H} = \hat{H}' + \hat{V}, \tag{4}$$

where the operator $\hat{V}$ describes the electron transitions between the mirror-symmetrical sites:

$$\hat{V} = \sum_{n=1}^{N} t_n(\hat{c}^+_{n;\uparrow}\hat{c}_{-n;\uparrow} + \hat{c}^+_{n;\downarrow}\hat{c}_{-n;\downarrow} + \hat{c}^+_{-n;\uparrow}\hat{c}_{n;\uparrow} + \hat{c}^+_{-n;\downarrow}\hat{c}_{n;\downarrow}). \tag{5}$$

Then, the evolution operator in the interaction representation can be expressed as

$$\hat{U}(t') = \exp(-i\hat{V}t'/\hbar). \tag{6}$$

Nonvanishing transition amplitude $\langle 2|\hat{U}(t')|1\rangle$ appears only in the $2N$th order of the perturbation theory and is equal to

$$\langle 2|\hat{U}(t')|1\rangle = \left\langle 2\left|\frac{1}{(2N)!}\left(-\frac{i\hat{V}t'}{\hbar}\right)^{2N}\right|1\right\rangle = \prod_{n=1}^{n=N}\{-[\Delta^2(t')^2\exp(-2aa_n)]/\hbar\}. \tag{7}$$

The product of exponentials in (7) can be expressed as an exponential of the sum argument

$$\sum_{n=1}^{n=M}(-2aa_n).$$

For even N, this expression can be calculated as a sum of the arithmetical progression:

$$\sum_{n=1}^{n=N}(-2aa_n) = -aaN^2.$$

This makes it possible to write the transition amplitude $\langle 2|\hat{U}(t')|1\rangle$ as

$$\langle 2|\hat{U}(t')|_1\rangle = \left(\frac{\Delta t'}{\hbar}\right)^{2N}\exp(-aaN^2). \tag{8}$$

It can be seen from (8) that, for small t' (i.e., $\Delta t'/\hbar < 1$), the transition amplitude becomes zero at $N \longrightarrow \infty$:

$$\lim\langle 2|\hat{U}(t')|1\rangle = 0 \quad \text{for} \quad N \longrightarrow \infty.$$

The off-diagonal Hamiltonian matrix element $\langle 2|\hat{H}_0|1\rangle$ and, thus, the transition rate, $\bar{\omega}_0 = 2|\langle 2|\hat{H}_0|1\rangle|/\hbar$ can be evaluated from the requirement that for small t'

$$\langle 2|\hat{U}(t')|1\rangle = -\frac{i}{\hbar}\langle 2|\hat{H}_0|1\rangle t'. \tag{9}$$

Since, according to (8), for small t' the transition amplitude $\langle 2|\hat{U}(t')|1\rangle$ approaches zero as $N \longrightarrow \infty$ faster than $\exp(-aaN^2)$, then, according to (9), the matrix element $\langle 2|\hat{H}_0|1\rangle$ also approaches zero as $N \longrightarrow \infty$ faster than $\exp(-aaN^2)$. Thus, one can argue that, in a long system (i.e., for large N), the transition rate $\bar{\omega}_0$ is bounded by an exponentially small quantity:

$$\bar{\omega}_0 < \Omega\exp(-aaN^2). \tag{10}$$

Conducting the calculations, we assume that $|\psi_1\rangle$ is a steady state with the energy $E_1 = \varepsilon_0 - |A|$ and that $|\psi_2\rangle$ is a state with the finite lifetime τ and complex energy given by

$$E_2 = \varepsilon_0 + |A| + i\Gamma. \tag{11}$$

The imaginary part Γ of the energy is related to the lifetime τ by

$$\frac{\Gamma}{\hbar} = \bar{\Gamma} = -\frac{1}{\tau}. \quad (12)$$

The finite lifetime τ may be related to the natural level broadening due to the spontaneous emission of a photon accompanied by a transition of the system from the state $|\psi_2\rangle$ to $|\psi_1\rangle$ [5]:

$$\frac{1}{\tau} = \frac{4}{3}\frac{\bar{\omega}_0^3}{\hbar c^3}\left|\langle\psi_2|\hat{d}|\psi_1\rangle\right|^2, \quad (13)$$

where $\hat{d}$ is the dipole moment operator

$$\hat{d} = q_e\sum_1^N a_n(\hat{c}^+_{n;\uparrow}\hat{c}_{n;\uparrow} + \hat{c}^+_{n;\downarrow}\hat{c}_{n;\downarrow} - \hat{c}^+_{-n;\uparrow}\hat{c}_{-n;\uparrow} - \hat{c}^+_{-n;\downarrow}\hat{c}_{-n;\downarrow}).$$

To calculate the conductivity, we introduce the Hamiltonian $\hat{W}(t)$ describing the interaction of the disordered system with the external electric field

$$\hat{W}(t) = 0 \quad (t<0); \quad \hat{W}(t) = \hat{W}_E\cos(\omega t) \quad (t<0), \quad (14)$$

where $\hat{W}_E = -E_0\hat{d}$, and E_0 is the component of the electric field strength along the axis of the system. The system state is represented by the vector

$$|\psi(t)\rangle = |\psi_1\rangle\exp\left(-\frac{iE_1t}{\hbar}\right)C_1(t) + |\psi_2\rangle\exp\left(-\frac{iE_2t}{\hbar}\right)C_2(t). \quad (15)$$

The amplitudes $C_1(t)$ and $C_2(t)$ can be calculated by the perturbation theory with the initial condition $|\psi(t=0)\rangle = |\psi_1\rangle$:

$$C_1(t) = 1, \qquad C_2(t) = \frac{\langle\psi_2|\hat{W}_E|\psi_1\rangle}{2\hbar}\frac{[1-\exp i(\omega_0-\omega)t]}{(\omega_0-\omega)}. \quad (16)$$

Here, $\omega_0 = \hat{\omega}_0 + i\hat{\Gamma}$. Using the expressions for $C_1(t)$ and $C_2(t)$, one can calculate the average electron coordinate $\hat{X}(t)$:

$$\hat{X}(t) = \langle\psi(t)|\hat{X}|\psi(t)\rangle, \quad (17)$$

where $\hat{X} = \frac{1}{2Nq_e}\hat{d}$ is the operator of the average electron coordinate of the disordered system. Taking the expression for $C_2(t)$ into account, one obtains the following formula for $\bar{X}(t)$:

$$\bar{X}(t) = \frac{aW_{21}}{4\hbar}\frac{[\exp(-i\omega_0t)-\exp(-i\omega t)]}{\omega_0-\omega} + \text{c.c.} \quad (18)$$

In the steady state ($t \longrightarrow \infty$),

$$\bar{X}(t) = \frac{aW_{21}}{2\hbar}\frac{(\omega-\bar{\omega}_0)\cos(\omega t)+\bar{\Gamma}\sin(\omega t)}{(\bar{\omega}_0-\omega)^2+\bar{\Gamma}^2}, \quad (19)$$

where $W_{21} = \langle\psi_2|\hat{W}_E|\psi_1| = -q_eE_0aN$. The electron velocity is $\bar{X}(t)$, and the steady-state ($t \longrightarrow \infty$) electric current density $J(t)$ at resonance ($\omega = \bar{\omega}_0$) is given by

$$J(t) = -E_0\frac{q_e^2}{\hbar}aN\frac{\bar{\omega}}{\bar{\Gamma}}\cos(\bar{\omega}_0t) = E_0\sigma_0\cos(\bar{\omega}_0t). \quad (20)$$

In view of expressions by (12) and (13) for $\bar{\Gamma}$, the resonance conductivity σ_0 is given by

$$\sigma_0 = \frac{3}{8}\frac{c^3}{Na\bar{\omega}_0^2} = \frac{3}{4}\frac{c^3}{L\bar{\omega}_0^2}, \quad (21)$$

where $L = 2aN$ is the length of the system.

Based on the deduced formula (21) for σ_0 and the upper estimate (10) for $\bar{\omega}_0$, we can state that, in a very long system, (i.e., for large N) the resonance conductivity increases with N faster than $\frac{1}{N}\exp(2aaN^2)$.

Thus, a metal-insulator transition does not occur at $T \longrightarrow 0$ in the investigated disordered system with mirror symmetry.

ACKNOWLEDGMENTS

The author is grateful to M.V. Éntin for his attention to this work and the discussion of the results.

REFERENCES

1. A. A. Abrikosov, *Fundamentals of the Theory of Metals*, (Nauka, Moscow, 1987).
2. A. G. Moiseev and M. V. Éntin, Fiz. Tekh. Poluprovodn. (St. Petersburg) **28**, 1282 (1994) [Semicond. **28**, 727 (1994)].
3. A. G. Moiseev, Fiz. Tekh. Poluprovodn. (St. Petersburg) **30**, 2127 (1996) [Semicond. **30**, 1108 (1996)].
4. V. L. Berezinskiĭ, Zh. Éksp. Teor. Phys. **65**, 125 (1973) [Sov. Phys. JETP **38**, 61 (1974)].
5. E. Fermi, *Nuclear Physics* (University of Chicago Press, Chicago, 1950; Inostrannaya Literatura, Moscow, 1951).

Translated by M. Skorikov

Semiconductors, Vol. 34, No. 4, 2000, pp. 448–452. Translated from Fizika i Tekhnika Poluprovodnikov, Vol. 34, No. 4, 2000, pp. 462–466.

LOW-DIMENSIONAL SYSTEMS

A Numerical Calculation of Auger Recombination Coefficients for InGaAsP/InP Quantum Well Heterostructures

N. A. Gun'ko, A. S. Polkovnikov, and G. G. Zegrya

Ioffe Physicotechnical Institute, Russian Academy of Sciences, Politekhnicheskaya ul. 26, St. Petersburg, 194021 Russia

Submitted March 24, 1999; accepted for publication September 27, 1999

Abstract—Auger recombination coefficients are calculated numerically for InGaAsP/InP quantum well heterostructures. In narrow quantum wells, the quasi-threshold and thresholdless mechanisms mainly contribute to the Auger recombination coefficient. For the processes involving two electrons and a heavy hole (CHCC) or an electron and two heavy holes with a transition of one of the holes to the spin–orbit split-off band (CHHS), the Auger recombination coefficients depend on temperature only slightly in a wide temperature range. The dependence of the Auger coefficient on the quantum well width is analyzed and found to be nonmonotonic.

1. INTRODUCTION

Two recombination processes, radiative recombination and nonradiative Auger recombination (AR), are dominant in semiconductors at high excitation levels [1, 2]. Usually, the AR process in narrow gap semiconductors predominates over radiative recombination at high concentrations of nonequilibrium carriers [2–9]. In particular, the current of Auger recombination constitutes a significant part of the total threshold current in long-wavelength lasers [1]. The AR current affects not only the laser threshold current but also its temperature dependence (i.e., the characteristic temperature T_0) [1, 2]. The stronger the temperature dependence of the AR rate, the lower the characteristic temperature and the lower the temperature stability of the laser [1, 2].

For homogeneous semiconductors, mechanisms of AR have been extensively studied [3–8]. For quantum well (QW) heterostructures, this has been done theoretically by the authors of this work [9, 10]. It was shown that three AR mechanisms of threshold, quasi-threshold, and thresholdless types exist in QWs. For sufficiently narrow QWs, the two latter mechanisms prevail. Therefore, the temperature dependence of the overall AR coefficient is weak and the recombination process is enhanced as compared with the same AR process in bulk semiconductors (the thresholdless AR mechanism for QWs has been studied by Dyakonov *et al.* [11]). However, no results of numerical calculations of the AR coefficients for particular structures were reported in [9, 10]. Meanwhile, such calculations are necessary for analyzing the effect of AR on the operation of optoelectronic devices with QWs.

This work is concerned with a numerical calculation of AR coefficients for QWs. The results for the best-known InGaAsP/InP heterostructures are presented. The dependence of the AR coefficients on temperature and QW width is given.

2. MODEL

To adequately describe electron and hole wave functions in III–V semiconductors, one should use Kane's model. The wave functions and energy spectrum of charge carriers in QWs have been studied in detail [9, 10]. Here, we note only that, if $m_h \gg m_c$ and T, $E_1 \gg (\Delta_{so}, E_g)$, heavy holes do not mix with light and spin–orbit split-off holes (m_h and m_c are the heavy hole and electron masses, E_1 is the electron size-quantization energy, Δ_{so} is the constant of spin–orbit interaction, and E_g is the band gap). Because of the relatively large mass of heavy holes, their penetration into barrier regions can be neglected.

The derivation of the matrix element of an Auger transition for the CHCC process (involving two electrons and a heavy hole) was outlined in detail in [9, 10]. It was shown that the matrix element for the transition of an excited particle into the continuous spectrum splits into two terms corresponding to the thresholdless ($M^{(1)}$) and quasi-threshold ($M^{(2)}$) AR processes:

$$M = M^{(1)} + M^{(2)}, \tag{1}$$

where

$$M^{(1)} \approx \frac{8\pi e^2}{\kappa_0(q^2 + k_4^2)(q^2 + k_3^2)}$$
$$\times\left(\frac{3V_c + V_v}{4E_g} - \frac{\kappa_0 - \tilde{\kappa}_0}{\kappa_0 + \tilde{\kappa}_0}\right)[\psi_4^*(a/2)\psi_1(a/2)] \tag{2}$$
$$\times[\psi_3^*(a/2)\psi_2(a/2)]'(1 \pm e^{-qa}).$$

Here V_c, V_v are the barrier heights for electrons and holes, respectively; a is the QW width; q is the in-plane heavy hole quasi-momentum component; κ_0 and $\tilde{\kappa}_0$ are the dielectric constants of semiconductors inside the

QW and in the barrier region, respectively; $\psi_\alpha(x)$ is the Fourier amplitude of the wave function of the bound electron ($\alpha = 1, 2$), the highly excited electron ($\alpha = 4$), and the hole ($\alpha = 3$); k_3 is the size-quantization momentum for the heavy hole; k_4 is the excited-electron momentum component perpendicular to the quantum well plane. The signs "+" and "–" correspond to even and odd parities, respectively, of the product $\psi_3^*(x)\psi_2(x)$. In the case of $qa \gg 1$, the exponent in (2) is close to zero and the matrix element $M^{(1)}$ then corresponds to independent scattering from the two heteroboundaries. The term $(\kappa_0 - \tilde{\kappa}_0)/(\kappa_0 + \tilde{\kappa}_0)$ appears owing to consideration of the additional Coulomb potential $\tilde{\Phi}(\mathbf{r}_1, \mathbf{r}_2)$ associated with the presence of heteroboundaries [10]. It should be noted that the matrix element $M^{(1)}$ is zero if the parities of the products $\psi_3^*(x)\psi_2(x)$ and $\psi_4^*(x)\psi_1(x)$ differ. For the quasi-threshold process, the matrix element is given by

$$M^{(2)} \approx \frac{\pi e^2}{\kappa_0(q^2 + k_4^2)} e^{i\delta} \frac{\hbar\gamma}{E_g} \frac{1 + 2/3\alpha}{1 + \alpha} A_c A_f A_c A_h \times \frac{\sin(k_f - k_{c1} - k_{c2} - k_h)a/2}{k_f - k_{c1} - k_{c2} - k_h} \times \begin{cases} q_h k_c e^{i\phi_{2,3}} + q_c k_h, & \nu_c = \pm\nu_h, \\ q_c q_h \sin\phi_{2,3}, & \nu_c = \mp\nu_h. \end{cases} \quad (3)$$

Here, δ is an insignificant phase coefficient, A_i are normalization constants, ν_c and ν_h are the spin indexes, $\phi_{2,3}$ is the angle between the lateral wave vectors of electron and hole, and γ is Kane's matrix element. From (3) it follows that, in the limit of $a \longrightarrow \infty$, the matrix element $M^{(2)}$ is proportional to $\delta(k_f - k_1 - k_2 - k_h)$ and, hence, becomes the bulk matrix element. On the other hand, $M^{(1)}$ has no extremum in the same limit and vanishes as $a \longrightarrow \infty$. That is why the Auger processes corresponding to $M^{(1)}$ and $M^{(2)}$ are referred to as thresholdless and quasi-threshold processes, respectively.

Thus, the matrix element of the Auger transition splits into two parts. The first of these corresponds to scattering from heteroboundaries and the second, to scattering by the short-range Coulomb potential with large momentum transfer. We note that both $M^{(1)}$ and $M^{(2)}$ are in fact thresholdless matrix elements. Indeed, they do not obey the conservation law for the localized particles momenta k_1, k_2, and k_3. However, the mechanisms responsible for lifting the restrictions imposed by the momentum conservation law (with $k_1 + k_2 \neq k_3 + k_4$) in $M^{(1)}$ and $M^{(2)}$ are different. For $M^{(1)}$, the momentum nonconservation is associated with the electron scattering from heteroboundaries. The same mechanism gives rise to a thresholdless Auger process in scattering from a single heterobarrier [12]. The reason why the momentum conservation law breaks down for $M^{(2)}$ is that the carriers are localized in the QW and, hence, their momenta have an uncertainty on the order of $\hbar/a$.

The threshold Auger process is associated with the transition of an excited electron into the discrete spectrum. The corresponding matrix element $M^{(3)}$ describes the transition without change in the degree of electron size quantization:

$$M^{(3)} \approx \frac{4\pi e^2}{\kappa_0(q^2 + k_4^2)} \int_{-a/2}^{a/2} (\psi_4^*\psi_1)(\psi_3^*\psi_2)dx. \quad (4)$$

As a rule, the threshold Auger process is of minor importance for QWs and, therefore, no explicit expression for $M^{(3)}$ will be presented here. The following three AR coefficients are related to the three AR mechanisms:

$$C = C_1 + C_2 + C_3, \quad (5)$$

where C_1 corresponds to the thresholdless process with the matrix element $M^{(1)}$; C_2, to the quasi-threshold process with the matrix element $M^{(2)}$; and C_3, to the threshold process with the matrix element $M^{(3)}$.

Let us consider expressions for the coefficients associated with different Auger processes. For the CHCC process, we have

$$C_1 \approx \frac{32\pi^2 e^4}{\kappa_0^2} \frac{\hbar\gamma^2}{E_g^3} \frac{F(\Delta_{so}/E_g)}{a(a + 2/\kappa_c)^2} \frac{k_c^2\kappa_c^2}{(k_c^2 + \kappa_c^2)^2} \frac{V_c}{E_g} \times \left(\frac{3V_c + V_v}{4E_g} - \frac{\kappa - \tilde{\kappa}_0}{\kappa_0 + \tilde{\kappa}_0}\right)^2 \left\langle \frac{q_h^2 k_h^2}{(q_h^2 + k_h^2)^3} \frac{1}{k_4(q_h)} \right\rangle, \quad (6)$$

where

$$F(x) = \left(\frac{1 + 2x/3}{1 + x}\right)^3 \frac{1 + 7x/9 + x^2/6}{(1 + x/2)(1 + 4x/9)},$$

$$x = \Delta_{so}/(E_g).$$

The broken brackets in (6) and below denote averaging over the heavy hole distribution function.

For the CHHS process (involving an electron and two heavy holes, one of which is transferred to the spin–orbit split-off band), the expression for the coefficient C_1 takes the form

$$C_1 \approx \frac{2\pi^2 e^4}{\kappa_0^2 \hbar} \frac{V_c}{E_g} \frac{k_c^2\kappa_c^2}{(k_c^2 + \kappa_c^2)^2} \frac{\tilde{F}(\Delta_{so}/E_g)}{a^2(a + 2/\kappa_c)} \times \frac{\hbar^3}{m_{so}^3(E_g - \Delta_{so})^3} \left\langle \frac{k_{h1}^2 k_{h2}^2 q_{h1}^2 (q_{h1}^2 + q_{h2}^2)}{(q_{h1}^2 + k_{h1}^2)^3 (q_{h2}^2 + k_{h2}^2)} \right\rangle, \quad (7)$$

where

$$\tilde{F}(x) = \frac{[2x + 3(1-x)(1-m_{so}/m_h)]^2}{2x^2 + [x + 3(1-x)(1-m_{so}/m_h)]^2}\frac{1+2x/3}{1+x}.$$

In the latter case, averaging is performed over the distribution functions of two heavy holes. In deriving (7), we assumed that $E_g - \Delta_{so} \gg T(m_h/m_{so})$.

Let us now consider the quasi-threshold AR mechanism. In the case of the CHCC process, the coefficient C_2 is given by

$$C_2 \approx \frac{\pi^2 e^4 \hbar^3 \gamma^4}{\kappa_0^2 E_g^5}\frac{F(\Delta_{so}/E_g)}{a(a+2/\kappa_c)^2} \times\left\langle \frac{q_c^2 k_h^2 + q_h^2[k_c^2 + (1/2)q_c^2]}{(q_h^2 + k_h^2)k_f} \times \frac{1-\cos(k_f - k_h - 2k_c)a}{2(k_f - k_h - 2k_c)^2}\right\rangle. \quad (8)$$

For the CHHS process, direct calculation of the coefficient C_2 yields a cumbersome result. Therefore, we restrict our consideration to the case of relatively narrow QWs with $k_c \gg q_c$; thus, we have

$$C_2 \approx \frac{\pi^2 e^4}{4\kappa_0^4}\frac{E_c}{E_g}\frac{\hbar^3}{m_{so}^2(E_g-\Delta)^3}\frac{\tilde{F}(\Delta_{so}/E_g)}{a^2(a+2/\kappa_c)} \times\left\langle \frac{1-\cos(k_{so}-k_{h1}-k_{h2}-k_c)a}{2(k_{so}-k_{h1}-k_{h2}-k_c)^2}\frac{q_{h_2}^2\{(k_{so}^2+k_{h1}^2)q_{h1}^2 + q_{h2}^2k_{h1}^2 + 2k_{h1}^2(\mathbf{q}_{h1}\mathbf{q}_{h2}) + [\mathbf{q}_{h1}\times\mathbf{q}_{h2}]^2\}}{(q_{h1}^2+k_{h1}^2)(q_{h2}^2+k_{h2}^2)k_{so}}\right\rangle. \quad (9)$$

Finally, for the CHCC process, the coefficient C_3 is written as

$$C_3 \approx \frac{32\pi^2 e^4}{\kappa_0^2 \hbar E_g}\frac{a}{(a+1/\kappa_c)^3}\frac{1+(7/9)x+(1/6)x^2}{(1+x/3)^2} \times\frac{1+(2/3)x}{1+x}\left\langle \frac{q_{\text{th}}^2}{q_T^2}\frac{q_c^2}{(q_{\text{th}}^2+k_h^2)}e^{-q_{\text{th}}^2/q_T^2}\alpha^2\right\rangle_n, \quad (10)$$

where α is a multiplier on the order of unity. In (10), averaging is only done over different discrete states of heavy holes. The threshold momentum is found from the conservation law for the energy and the longitudinal component of the momentum:

$$q_{\text{th}} \approx \sqrt{\frac{4m_c E_g}{\hbar^2} + \frac{3}{2}\left(k_c^2 + \frac{m_c}{m_h}k_h^2\right)}. \quad (11)$$

If the QW width tends to infinity, the threshold momentum approaches its bulk value [4].

We note that, for narrow QWs, the threshold process is much less intense than thresholdless and quasi-threshold processes and makes practically no contribution to the overall AR coefficient. For this reason, no corresponding expressions are given for the coefficient C_3 in the case of the CHHS process. Such an expression can be found in [9, 10]. The quasi-threshold and thresholdless coefficients depend on temperature only slightly, thereby leading to a weak temperature dependence of the overall Auger coefficient.

3. NUMERICAL RESULTS

Let us make a numerical analysis for a strained QW based on the $In_{0.533}Ga_{0.467}As/InP$ compound (numerical results for some other compounds can be found in the database [13]). The following parameters of the heterostructure are used: $x = 0.467$, $E_g = 0.75$ eV, $V_c = 0.234$ eV, $V_v = 0.366$ eV, $\Delta_{so} = 0.32$ eV, $\kappa = 12.68$, $m_c = 0.041m_0$; $m_{so} = 0.144m_0$, $m_{hh} = 0.432m_0$, and $m_{lh} = 0.052m_0$.

Figure 1 shows the overall AR coefficient $C = C_1 + C_2 = C_3$ for the CHCC process as a function of the QW width a at different temperatures. The dependence of C on a exhibits a clearly pronounced maximum. It is significant that the position of the maximum is virtually temperature-independent. For small a and low temperatures, the main contribution to the coefficient C comes from the thresholdless and quasi-threshold AR processes. The thresholdless AR coefficient C_1 shows a more pronounced dependence on the QW width a than does the coefficient C_2 for the quasi-threshold process. The coefficient C_1 decreases with increasing a as $1/a^3$, $1/a^5$, or $1/a^7$. In any case, even on passing to the three-dimensional case (by way of multiplication by a^2), C_1 remains a decreasing function of the QW width. Thus, the thresholdless process can be dominant only for sufficiently narrow quantum wells. For $a \approx 1/\kappa_c$, C has a maximum associated with the fact that, with the QW width decreasing further, the overlap of the electron

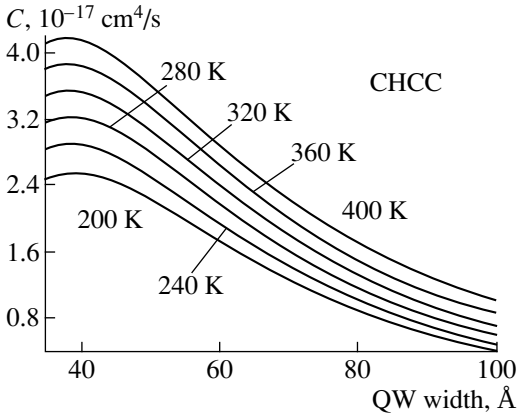

Fig. 1. AR coefficient C as a function of quantum well (QW) width for the CHCC process at different temperatures.

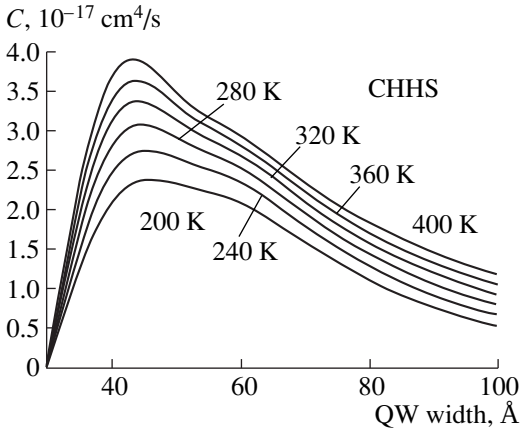

Fig. 2. AR coefficient C as a function of quantum well (QW) width for the CHHS process at different temperatures.

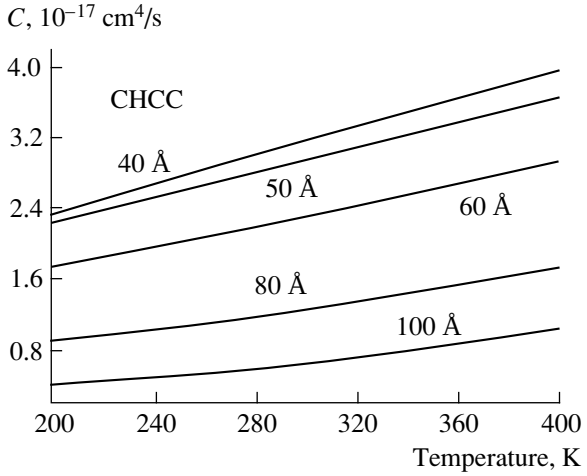

Fig. 3. Temperature dependence of the AR coefficient C for the CHCC process at different quantum well widths.

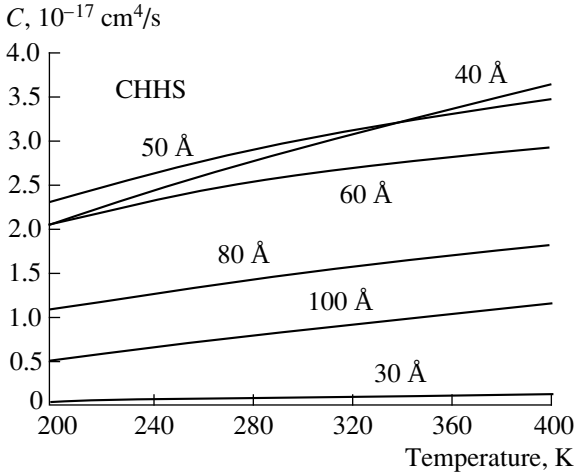

Fig. 4. Temperature dependence of the AR coefficient C for the CHHS process at different quantum well widths.

and hole wave functions becomes less pronounced. With increasing temperature, the quasi-threshold AR process becomes more important than the thresholdless one. In the limit of $a \longrightarrow \infty$, the sum of the quasi-threshold and threshold AR coefficients multiplied by squared QW width, $C_2a^2 + C_3a^2$, tends to its bulk value C_{3D} [9, 10]. Figure 2 shows the dependence of the AR coefficient on the QW width for the CHHS process. The shape of the dependence $C(a)$ coincides qualitatively with that for the CHCC process. However, for small a, the AR coefficient for the CHHS process diminishes with decreasing a faster than in the case of the CHCC process.

Figure 3 shows the temperature dependence of the overall AR coefficient for the CHCC process at different QW widths. It can be seen that, for any of the QW widths considered, the temperature dependence of the AR coefficient is weak in conformity with the above analysis. The temperature dependence of the AR coefficient for the CHHS process is qualitatively the same as that observed for the CHCC process (see Fig. 4).

4. SUMMARY

Our investigation has shown that in QW heterostructures the quasi-threshold and thresholdless AR mechanisms make the major contribution to the AR coefficient. For sufficiently narrow QWs, it is the prevalence of the thresholdless and quasi-threshold AR processes that is responsible for the fact that the two-dimensional AR coefficient multiplied by a^2 exceeds the corresponding bulk value. Thus, in the case of QWs, the AR process is enhanced as compared to a homogeneous semiconductor. This enhancement is more pronounced at low temperatures. Under these conditions, the bulk AR coefficient C_{3D} is small because of the presence of a small exponential multiplier [9, 10]. More

detailed numerical data for QW heterostructures are given in the database [13].

ACKNOWLEDGMENTS

This work was supported in part by the Russian Foundation for Basic Research (project nos. 98-07-09336, 97-02-18151, and 99-02-16796) and the Russian State Program "Physics of Solid State Nanostructures" (grant nos. 97-0003 and 97-1035).

REFERENCES

1. G. P. Agrawal and N. K. Dutta, *Long-Wavelength Semiconductor Lasers* (Van Nostrand Reinhold, New York, 1993).
2. *Quantum Well Lasers*, Ed. by P. S. Zory, Jr. (Academic, New York, 1993).
3. A. R. Beattie and P. T. Landsberg, Proc. R. Soc. A **249**, 16 (1959).
4. B. I. Gel'mont, Zh. Éksp. Teor. Fiz. **75**, 536 (1978) [Sov. Phys. JETP **48**, 268 (1978)].
5. V. N. Abakumov, V. I. Perel', and I. N. Yasievich, *Nonradiative Recombination in Semiconductors* (Peterb. Inst. Yad. Fiz. Ross. Akad. Nauk, St. Petersburg, 1997).
6. B. L. Gel'mont and Z. N. Sokolova, Fiz. Tekh. Poluprovodn. **16**, 1670 (1982) [Sov. Phys. Semicond. **16**, 1067 (1982)]; B. L. Gel'mont, Z. N. Sokolova, and V. B. Khalfin, Fiz. Tekh. Poluprovodn. **18**, 1803 (1984) [Sov. Phys. Semicond. **18**, 1128 (1984)]; B. L. Gel'mont, Z. N. Sokolova, and N. Yasievich, Fiz. Tverd. Tela **29**, 2351 (1987) [Sov. Phys. Solid State **29**, 1355 (1987)].
7. A. Haug, J. Phys. C: Solid State Phys. **16**, 4159 (1983).
8. M. Takeshima, Phys. Rev. B: Condens. Matter **28**, 2039 (1983).
9. G. G. Zegrya and A. S. Polkovnikov, Zh. Éksp. Teor. Fiz. **113**, 1491 (1998) [JETP **86**, 815 (1998)].
10. A. S. Polkovnikov and G. G. Zegrya, Phys. Rev. B: Condens. Matter **58**, 4039 (1998).
11. M. I. Dyakonov and V. Yu. Kachorovskiĭ, Phys. Rev. B: Condens. Matter **49**, 17 130 (1994).
12. G. G. Zegrya and V. A. Kharchenko, Zh. Éksp. Teor. Fiz. **101**, 327 (1992) [Sov. Phys. JETP **74**, 173 (1992)].
13. Interactive database *New Semiconductor Materials. Characteristics and Properties*, /http://www.ioffe.rssi.ru/SVA/NSM/.

Translated by S. Gupalov

Semiconductors, Vol. 34, No. 4, 2000, pp. 453–461. Translated from Fizika i Tekhnika Poluprovodnikov, Vol. 34, No. 4, 2000, pp. 467–476.

LOW-DIMENSIONAL SYSTEMS

Recombination Emission from InAs Quantum Dots Grown on Vicinal GaAs Surfaces

V. G. Talalaev*, B. V. Novikov*, S. Yu. Verbin*, A. B. Novikov*, Dinh Son Thath*, I. V. Shchur*, G. Gobsch, R. Goldhahn**, N. Stein**, A. Golombek**, G. É. Tsyrlin***, V. N. Petrov***, V. M. Ustinov****, A. E. Zhukov****, and A. Yu. Egorov******

** Institute of Physics (Petrodvorets Branch), St. Petersburg State University, Petrodvorets, 198904 Russia*
e-mail: tantal@sbor.ru
*** Institute für Physik, Technische Universität Ilmenau, 98684 Ilmenau, Germany*
**** Institute of Analytical Instrument Making, Russian Academy of Sciences, Rizhskiĭ pr. 26, St. Petersburg, 198103 Russia*
***** Ioffe Physicotechnical Institute, Russian Academy of Sciences, Politekhnicheskaya ul. 26, St. Petersburg, 194021 Russia*
Submitted October 19, 1999; accepted for publication October 22, 1999

Abstract—Photoluminescence (PL) spectra of InAs/GaAs heteroepitaxial structures with quantum dots (QDs) have been studied. The structures were grown by submonolayer migration-enhanced epitaxy on vicinal substrates with the amount of deposited InAs close to the critical value of 1.8 monolayer (ML). The origin and evolution of the structure of PL spectra were studied in relation to the direction and angle of misorientation, temperature, and power density and spectrum of the exciting radiation. A blue shift and narrowing of the PL band with increasing misorientation angle was established experimentally. The fact that QDs become smaller and more uniform in size is explained in terms of a lateral confinement of QDs on terraces with account taken of the step bunching effect. The temperature dependences of the positions and full widths at half-maximum (FWHM) of PL bands are fundamentally different for isolated and associated QDs. The exciton ground states contribute to all low-temperature spectral components. The excited exciton state contributes to the recombination emission from QDs, as evidenced by the temperature dependence of the integrated intensity of the PL bands. A quantitative estimate is given of the electronic structure of different families of InAs QDs grown on GaAs substrates misoriented by 7° in the [001] direction. © *2000 MAIK "Nauka/Interperiodica".*

1. INTRODUCTION

The interest in low-dimensional semiconductor structures is mainly due to the demand of modern microelectronics for efficient solid-state light emitters. The possibility of a technologically directed adjustment of the emission spectrum of heteroepitaxial structures is the best pronounced for self-organized arrays of quantum dots (QDs).

The occurrence of self-organization effects in III–V semiconductor structures grown by molecular-beam epitaxy and its varieties has been confirmed experimentally in recent years (see review [1]). The influence of the lateral size, surface density, and ordering of QDs on the photoluminescence (PL) spectrum has been established. In turn, most of these factors are governed by technological conditions and growth kinetics. For example, the use of submonolayer migration-stimulated epitaxy (SMSE) and vicinal GaAs substrates yields arrays of InAs QDs with the closest lateral dimensions and the resulting narrowing of the PL band [2–8].

A more complicated QD PL spectrum is observed in some cases: the main band, assigned to excitonic recombination of an electron and a heavy hole in the ground state of a QD, is inhomogeneously broadened. Additional emission peaks are occasionally observed. The origin of these peaks is being actively discussed [9–14].

The nature of various spectral components of the PL from two-dimensional InAs QD arrays on vicinal GaAs substrates is the subject of this communication. The structure of the PL spectrum is shown to be due to QD families belonging to terraces having discrete widths because of mono-atomic step bunching. The intense high-energy PL component observed in samples with relatively large misorientation angles (5° and 7°) is interpreted as the recombination emission of QDs isolated from the base array through the wetting-layer (WL) continuity disruptions at terrace edges. The dependence of the PL spectrum structure on temperature and on the spectral composition of the exciting radiation agrees with the proposed model. From the temperature dependence of the PL spectral components, their excitonic nature is inferred and the excited exciton state is shown to be responsible, among other factors, for the QD recombination emission spectrum. A quantitative estimate is made of the energy structure of different InAs QD groups on GaAs substrates misoriented by 7° in the [001] direction (InAs/GaAs 7° [001]).

1063-7826/00/3404-0453$20.00

2. EXPERIMENTAL

InAs QD arrays were grown by SMSE [15]. Semi-insulating (100) GaAs substrates without surface misorientation (singular) and misoriented (vicinal) by 3°, 5°, and 7° in the [001], [010], [011], and [$0\bar{1}1$] directions were used.

The epitaxial structures under study consisted of a two-dimensional array of InAs QDs confined on the substrate side with a 300-nm-thick buffer GaAs layer, a $Al_{0.25}Ga_{0.75}As$/GaAs superlattice (5 2 nm/2 nm periods), and a 6-nm-thick GaAs layer. On the other side, the active QD layer was overgrown symmetrically with a GaAs layer (6 nm) and a superlattice of a similar thickness. The lower confining superlattice was grown to suppress carrier diffusion into the substrate, with the upper one eliminating the influence of surface recombination.

In preparing the active InAs QD layer by SMSE, the shutters of In and As molecular sources were opened in the following order. On depositing an In layer necessary to form a 0.5 monolayer (ML) of InAs, the surface was exposed to As flux for $\tau = 10$ s. The total thickness of the InAs active layer was between 1 (2 cycles) and 3 ML (6 cycles). The growth conditions were maintained the same in all technological experiments: arsenic vapor pressure $\sim 4 \times 10^{-6}$ Pa, InAs growth rate 0.1 ML s^{-1}, InAs growth temperature 470°C, and As/In flux ratio maintained at 10. The state of the surface was monitored *in situ* using the reflection high-energy electron diffraction (RHEED) technique.

The PL spectra were studied with a DFS-12 automated spectrometer. A cooled photomultiplier was used as the photodetector; the signal received was amplified and fed into a computer. The PL was excited with helium–neon and argon lasers. The exciting radiation power was attenuated with calibrated optical filters. It was also possible to vary the exciting radiation spectrum by using a halogen lamp and an MDR-12 wide-aperture monochromator matched to the basic detection system. Low-temperature measurements were carried out in special cryostats, with the temperature varied in the range $T = 5$–300 K and maintained constant to within ±0.1 K.

3. RESULTS AND DISCUSSION

A study of additional recombination emission peaks implies that they are separated from the main PL band either instrumentally (resolution criterion is satisfied) or by computer processing (if an adequate algorithm of spectral resolution is known). For the latter purpose, a QD PL spectrum is commonly deconvoluted into Gaussian components under the assumption that the emission line contour describes the statistical size distribution of QDs. In this case, the spectral position of the peak characterizes the mean QD size, and its full width at half-maximum (FWHM) characterizes the QD size variance.

In order to use the instrumental factor to full advantage, we carried out a preliminary study aimed at obtaining QD arrays with the narrowest possible band of radiation recombination. Among the techniques and conditions that allow the achievement of this goal are the SMSE process [2, 4], vicinal substrates [3, 8], initial stages of QD self-organization [4, 8, 16], and high-temperature annealing [17–20].

It is known [21–23] that QDs are formed in the InAs/GaAs system on singular and vicinal surfaces by molecular-beam epitaxy in two stages. In the first stage, a pseudomorphic strained InAs layer is formed. After its thickness attains the critical value (1.5–1.7) ML, the second stage sets in. The pseudomorphic layer spontaneously disintegrates into a system of crystal islands (QDs) and a wetting InAs layer with a thickness of about 1 ML, in accordance with the Stranski–Krastanov growth mechanism. Up to thicknesses of (3–4) ML, the quasi-three-dimensional islands remain coherently strained, i.e., dislocation-free. Simultaneously, the surface density of QDs and their mean size increase, attaining a limiting (equilibrium) value. Further InAs growth leads to emergence of mesoscopic clusters containing dislocations.

In submonolayer InAs deposition on a vicinal GaAs surface, QDs can be formed following a different scenario. The structural features of the vicinal surface (steps and terraces) limit the surface-potential continuity [24]. Terrace edges form a system of potential barriers hindering the migration of adsorbed substance over the WL surface. Under certain SMSE conditions (low flux rates and appropriate growth temperature), this may lead to rupture of the submonolayer coating at terrace edges and produce InAs clusters bounded by these terraces [7, 24]. Pseudomorphic-layer continuity violations are rather likely if the terrace edges have irregularities of height amounting to 2 nm, as observed in [21]. Therefore, QDs can be formed in SMSE on the vicinal surface at smaller amounts of the deposited substance. In the case of conventional molecular beam epitaxy (in the absence of WL continuity violation), the critical InAs layer is thicker on vicinal surfaces [26].

In our experiments, SMSE on vicinal substrates with a misorientation angle of 5° produced QD arrays for InAs layers thicker than 1.8 ML. Well-defined RHEED reflections and a pronounced QD PL in the range of 1.1–1.45 eV were always observed in this case. At the same time, only PL from a strained GaAs barrier layer was detected around 1.5 eV (photon emission by excitons and carbon impurities) for smaller InAs layer thicknesses. Making the InAs pseudomorphic layer thicker (3 ML instead of 1.8 ML) caused, along with a shift of the QD PL band to longer wavelengths, its broadening. This indicates that the QDs become larger and less uniform in size and shape. For this reason, all investigations of the InAs QD PL fine structure were carried out on QD arrays grown by SMSE on vicinal GaAs substrates from a 1.8-ML-thick

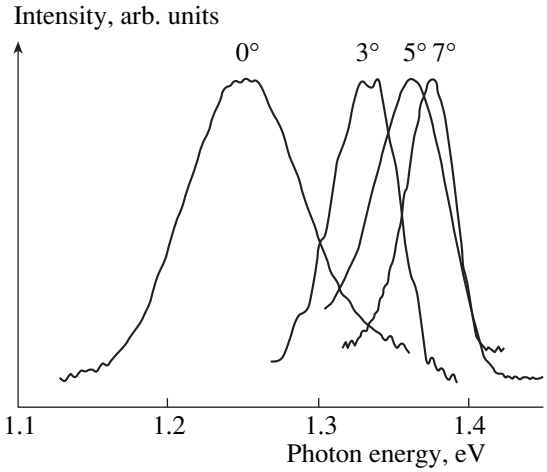

Fig. 1. PL spectra of InAs QDs grown on vicinal GaAs (100) substrates with a varied angle of misorientation in the [011] direction. $T = 5$ K.

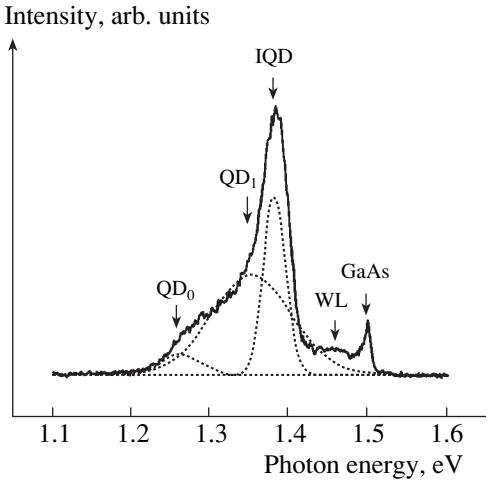

Fig. 2. PL spectrum of InAs/GaAs 5° [011] QDs at $T = 5$ K and its Gaussian decomposition. Excitation by a 20 mW He–Ne laser. WL denotes the spectral feature related to the wetting layer; the same for Figs. 2–5.

InAs layer. With all these factors combined, we could achieve the highest hardware resolution of the PL spectrum for such QDs and investigate its additional fine structure.

3.1. Groups of Quantum Dots on Misoriented Substrates

Experiments with vicinal substrates demonstrated that, technological conditions being the same, InAs QD size and its variance depend on the angle and direction of GaAs substrate misorientation. Analysis of the low-temperature PL spectra reveals a general tendency for all the studied directions and angles of misorientation: a short-wavelength shift of the QD PL peak, its narrowing, and appearance of an additional feature in the emission spectrum.

In a set of samples misoriented in the [011] direction, a steady short-wave shift of the QD emission peak (from 1.255 to 1.375 eV) and its narrowing (from 95 to 33 meV) were observed with the misorientation angle increasing from 0° to 7° (see Fig. 1). Another characteristic feature of the PL spectra of QDs grown on substrates misoriented in the [011] and $[0\bar{1}1]$ directions is a wide structureless wing on the long-wave slope of the main band (Fig. 2).

A somewhat different evolution of the low-temperature PL spectrum was observed for samples with larger misorientation in the [001] and [010] directions. The spectral features of PL were changing nonmonotonically. The PL band of InAs QDs for a vicinal sample misoriented by 3° corresponded to the radiation band of InAs QDs prepared on the singular GaAs surface. The PL spectra of the samples misoriented by 5° and 7° were identical and showed a sharp intense band at 1.37 eV and a low-intensity structure on the low-energy side of the spectrum (Fig. 3).

The observed behavior obviously stems from the presence of stepped terraces restricting the QD size on the vicinal surfaces. With allowance made for the growth conditions used, it seems unlikely that a single QD could occupy several terraces, although participation of neighboring terraces in QD formation is conceivable. Nevertheless, direct comparison of the QD pedestal size and terrace width suggests that the QD distribution over a real vicinal surface is far from being ideal. Indeed, it follows from data reported in [3, 8] that the width of terraces on the vicinal surface samples with misorientation angle A must be $W = 5.2$ nm for $A = 3°$, 3.5 nm for 5°, and 2.3 nm for 7°. At the same time, an estimate of the lateral QD size from the spectral position of the main PL peak (see [27]) and from the data of scanning tunneling spectroscopy yields for our singular samples $B = 8$–9 nm. The coincidence of growth conditions and QD lateral sizes of this work with the data of [28] gives us reason to believe that, in our case, QDs are pyramidal with a square base and height $H \approx B/2$. From the relation between the sizes of QDs and those of terraces, it follows that the InAs QDs are to be formed on vicinal GaAs surfaces with terrace width exceeding severalfold that calculated for the ideal case.

It is known [29] that monoatomic step bunching occurs on actual vicinal surfaces, which makes the terraces several times wider. The frequency and amount of bunching are mainly determined by the surface diffusion length of adsorbed atoms in the GaAs buffer layer in comparison with the terrace width determined by the misorientation angle. According to experimental data [26], the steps on the GaAs vicinal surface misoriented by 6° may be as high as 10 ML. This means that for the

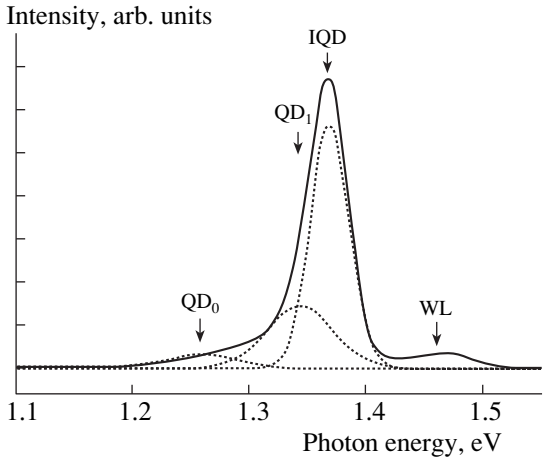

Fig. 3. PL spectrum of InAs/GaAs 7° [001] QDs at $T = 5$ K and its Gaussian decomposition. Excitation by a 20 mW Ar^+ laser.

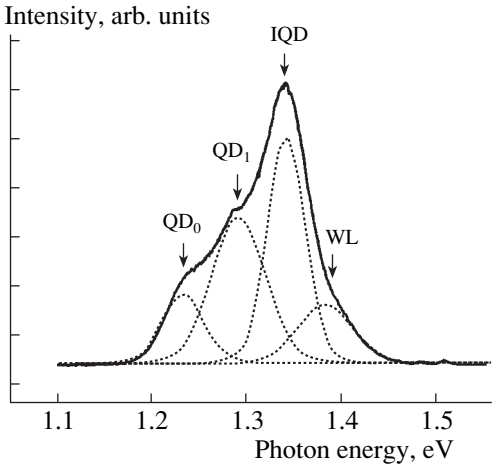

Fig. 4. PL of InAs/GaAs 7° [001] QDs at $T = 80$ K and its Gaussian decomposition. Excitation by a 20 mW He–Ne laser.

structures with misorientation angle in the range of 3°–7°, studied in this work, the terrace width may exceed the critical value necessary for pyramidal InAs QDs to be formed.

This model was applied to the case of a quasi-two-dimensional network of square terraces (GaAs misoriented in the [001] and [010] directions), which allowed us to explain the features of InAs QD PL spectra. A component with the longest wavelength QD_0 was found in the Gaussian decomposition of low-temperature PL spectra of InAs/GaAs QDs grown on substrates with different misorientation angles in the above directions (Fig. 3). The spectral position of this band (1.265 eV) coincides with that for the PL band of a singular-surface sample (Fig. 1). This allows us to identify this component as an emission from wide terraces on which the largest QDs grow, characteristic of the singular surface ($B = 8$–9 nm). It may be supposed that such QDs start to grow by the Stranski-Krastanov mechanism on terraces broadened by a factor $Q = 3$ ($W = 10.5$ nm) for a sample misoriented by 5° and $Q = 4$ ($W = 9.2$ nm) for a sample misoriented by 7°.

In terms of the proposed model, the QD_1 component (1.345 eV) of the PL spectrum (Fig. 3) is the emission from the QDs confined to terraces with broadening factor Q smaller by unity than that for QD_0, i.e., $Q = 2$ ($W = 7$ nm) for misorientation angle $A = 5°$ and $Q = 3$ ($W = 6.9$ nm) for $A = 7°$. The nanosize islands formed under these lateral confinement conditions must differ from those in the limiting case of a singular surface not only in base length but also in strain distribution, which must inevitably affect their energy-band structure. For example, in passing from QDs characterized by QD_0 to those with QD_1, the energy separation of the electron and heavy-hole levels increases by 80 meV.

For a vicinal GaAs surface misoriented by 3°, terraces with $Q = 2$ ($W = 10.4$ nm) ensure necessary and sufficient conditions for growth of InAs QDs of the largest size ($B = 8$–9 nm), corresponding to the singular surface.

It should be noted that a set of terraces with a Gaussian size distribution corresponds to a given terrace-broadening factor Q for an actual vicinal surface. This spread in sizes, in turn, gives rise to fluctuations of the QD base side length. Moreover, QDs show intrinsic height variance that can be reduced by increasing the misorientation angle [26]. All this leads to a narrowing of the radiative recombination band in the InAs QD PL spectra with increasing GaAs surface misorientation.

The modulation of the InAs QD size distribution function for misorientation in the [011] and $[0\bar{1}1]$ directions may be very weak. Lowering the terrace symmetry changes not only the size but also the shape of QDs. A corrugated island structure may form in this case [30], with emergence of quantum wires being more likely for misorientation in the $[0\bar{1}1]$ direction [5]. These are the reasons why the QD size distribution function must be broadened for terraces with a given Q. Another apparent consequence is the structureless asymmetric shape of the QD_1 QD PL band observed on InAs/GaAs (100) samples misoriented in the [011] and $[0\bar{1}1]$ directions. For samples misoriented in the [001] and [010] directions, the structure of the PL spectra was preserved even at higher temperatures and was best resolved in the range of 80–90 K (Fig. 4).

Thus, the adopted model describes well the experimentally observed dependence of the QD PL on the direction and angle of misorientation of the vicinal substrate. In the context of this model, the QD bands (QD_0 and QD_1) are ascribed to InAs QD arrays emitting from terraces having closely related broadening factors because of the monostep bunching effect on the misoriented GaAs surface.

3.2. Isolated Quantum Dots

Of certain interest is the situation on narrow terraces with small broadening factor ($Q = 1$ for $A = 3°$, 5° and $Q = 1, 2$ for $A = 7°$). The corresponding QD sizes are below the threshold ($B = 6$ nm) above which localized electron states exist in QDs [27, 31, 32]. Such QDs must not luminesce even in the case of their clearly pronounced faceting. It is more probable that, by analogy with the case of submonolayer coatings [5, 33], nanosize islands of a small height are formed without clearly pronounced faceting, which can be regarded as WL islands of varied thickness. In any case, so intense a band of recombination emission as the band related to isolated quantum dots (IQDs) at 1.37 eV in samples misoriented by 5° and 7° (Figs. 2 and 3) must not be observed in such samples.

The intense band in the high-energy part of the PL spectrum may be associated with several processes [34]. In the case of inefficient phonon relaxation ("bottleneck" effect), this may be a manifestation of QD excited states even for a low excitation level of PL. For this reason, in our previous work [35], the IQD band was assigned to radiative recombination involving excited QD states. However, further investigation failed to confirm this interpretation. No intensity redistribution between QD and IQD bands was observed in the low-temperature PL spectra of InAs/GaAs QDs. Emission in the region of 1.37 eV has also been observed in similar structures by other authors [5, 36, 37], but its origin was not explained. Elucidating the origin of this emission band was the subject of a special investigation in this work.

Comparison of the PL spectra of the InAs/GaAs 7° [001] sample (Figs. 3 and 5) shows that the low-temperature intensity distribution is reproduced at higher temperatures and high excitation densities. This means that both cases reflect the relative density-of-states distribution in the QD groups. The stability of the spectral position and width of the QD and IQD bands in such experiments rules out any contribution from many-particle mechanisms (biexcitons and exciton complexes). In addition, the growth conditions used (low overgrowth temperature and no postgrowth annealing) rule out any significant contribution to the PL spectrum from such a mechanism of inhomogeneous broadening as indium segregation at the surface [11, 38]. The multicomponent nature of the PL spectrum, due to the nonuniform thickness of a deposited layer [10, 28], was excluded by rotating substrates during sample growth.

The nature of the IQD band was established in studies of the PL spectrum in relation to the temperature and spectrum of exciting light. Figures 6 and 7 show the FWHMs and peak energy positions (E_m) of the PL spectrum components as functions of the InAs/GaAs 7° [001] sample temperature. A fundamental difference is observed between the QD and IQD bands. The QD_0 (at $T > 120$ K) and QD_1 (at $T > 80$ K) bands are narrowing, and the IQD band is broadening (at $T > 80$ K) with

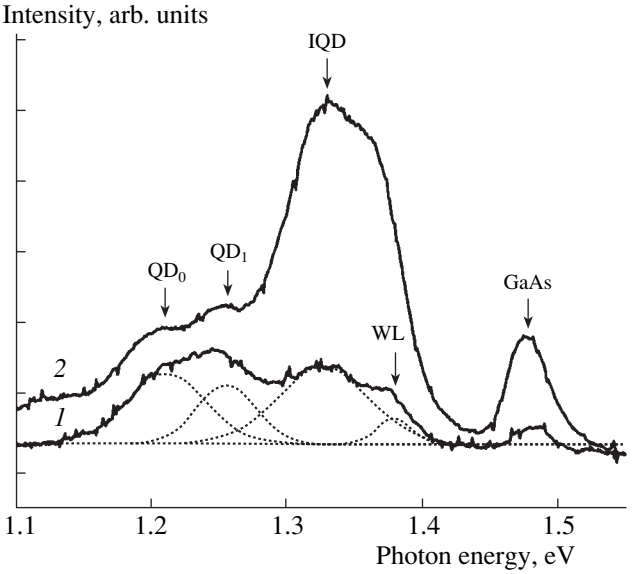

Fig. 5. PL spectrum of InAs/GaAs 7° [001] QDs at T = 155 K at different excitation levels by Ar^+ laser. Excitation power is equal to (*1*) 200 and (*2*) 400 mW.

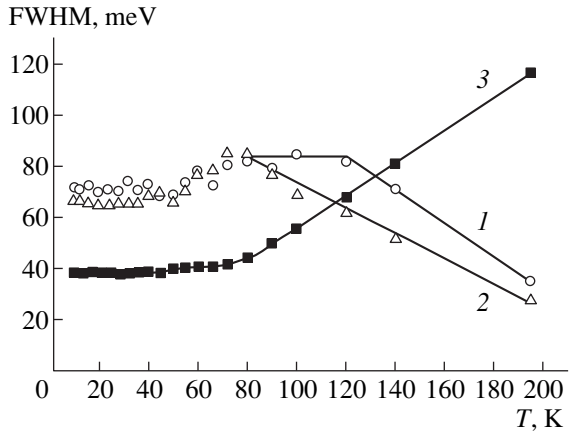

Fig. 6. FWHM for different PL bands of InAs/GaAs 7° [001] QDs as a function of temperature for (*1*) QD_0, (*2*) QD_1, and (*3*) IQD.

increasing sample temperature (Fig. 6). The relative constancy of the FWHM for all components of the PL spectrum at temperatures lower than those mentioned above indicates that exciton states are involved in the emission process [39]. The temperature dependence of the peak position E_m of the IQD band follows the bandgap E_g behavior for InAs [40] over the entire temperature range studied, whereas the QD_1 band peak starts to deviate from the Varshni law at $T = 80$ K. A similar behavior of E_m is observed for the QD_0 band above 120 K (Fig. 7).

The above evolution of the QD bands with increasing temperature fits the concept of a random occupation

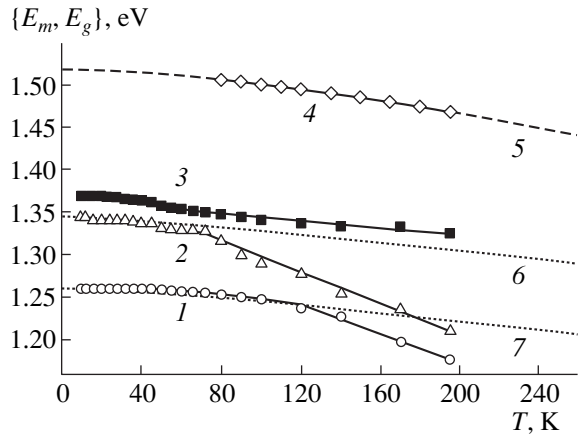

Fig. 7. Spectral peak positions E_m for different bands in PL spectra of InAs/GaAs 7° [001] QDs as a function of temperature under excitation by an Ar^+ laser (100 mW). Experimental data correspond to (*1*) QD_0, (*2*) QD_1, (*3*) IQD, and (*4*) GaAs; calculated dependences are for (*5*) $E_g(T)$ for GaAs and (*6*, *7*) $E_g(T)$ for InAs (shifted along the energy axis).

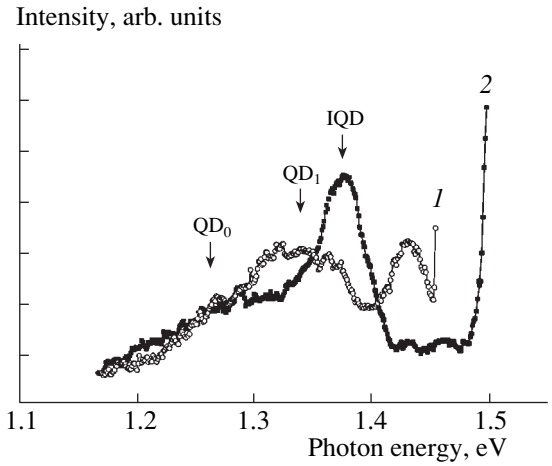

Fig. 8. PL spectra of InAs/GaAs 7° [001] QDs at excitation energy equal to (*1*) 1.46 and (*2*) 1.52 eV. $T = 5$ K.

by carriers of localized QD states at low temperatures, their thermal activation (mainly from shallow QDs) into the WL, and subsequent capture of the carriers by localized states of larger QD [9, 41]. Because of carrier redistribution in favor of larger QD, the situation approaches the thermodynamic equilibrium. An important point is that there exists a transport mechanism ensuring carrier exchange between neighboring QD for QD families emitting from terraces with broadening factors differing by unity. In our opinion, the InAs WL is involved in this mechanism.

Quite a different situation takes place on terraces with QDs responsible for the emission in the IQD band. The absence of carrier exchange between QDs of this family suggests that there are no allowed states in the WL because of its becoming thinner and/or lack of a WL itself because of ruptures. As mentioned above, the WL continuity violations are most likely at terrace edges. Studies of the QD growth kinetics have shown [20, 21, 23, 42, 43] that QDs mainly nucleate at base, at step edges. When a pseudomorphic layer shrinks into a QD in accordance with the Stranski-Krastanov mechanism, layer discontinuities (ruptures) are formed at the terrace edges and places of thinning (constrictions) appear at "gateways" connecting neighboring terraces. Hence, we believe that IQDs are mainly formed on terraces with small broadening factors. Thus, the QDs emitting in the QD_1 and IQD bands are confined to terraces with equal broadening factors, but the former are connected via WL while the latter are isolated.

This conjecture was confirmed by a study of the PL spectra with excitation by light of varied spectrum. The emission in the QD bands appeared upon excitation of the InAs WL, and that in the IQD band, only when exciting the GaAs barrier. This feature is illustrated in Fig. 8.

The above-barrier excitation of the IQD band can also be explained in terms of the indirect transitions ⟨electron in GaAs barrier⟩–⟨hole in InAs QD⟩. An analogue of a type-II heterostructure in the InAs/GaAs QD system may appear in two cases. Significant strain arises near the lateral faces of the pyramidal QDs deformed both through lateral confinement on terraces and because of overgrowth [37, 44–46]. This strain may lead to inversion of the Γ and *X* valleys of the conduction band at the InAs/GaAs interface [47]. Another possibility [48] is that QDs on narrow terraces ($W < 6$ nm) have localized states only for holes. Remaining spatially separated from QDs, barrier electrons are confined to the vicinity of QDs by the Coulomb interaction. However, the recombination emission spectrum must depend on the excitation density in both cases [49, 50]. No dependence of this kind was observed for the IQD band.

3.3. Specific Manifestations of Excited States in Quantum Dots

The results obtained in studying the temperature dependence of the integrated intensity of the QD PL spectral components for InAs/GaAs 7° [001] are presented in Fig. 9 and in the table.

The parameters of the PL spectral bands and of the corresponding QD families were determined using the Arrhenius equation:

$$I/I_m = [1 + \beta \exp(-E_A/kT)]^{-1} \equiv F, \qquad (1)$$

where I is the integrated intensity of a given PL band, I_m is the peak intensity, and k is the Boltzmann constant.

The activation energy E_A was estimated from the slope of the dependence of $-\ln(I_m/I - 1)$ on $1/kT$. For each QD family, two temperature intervals with constant slopes, E_{A0} and E_{A1}, were found (see table). The

obtained E_{A0} values were used to fit the function F to the experimental data on I/I_m by varying the parameter β. The results of the fit are presented in the table.

The obtained temperature dependences (Figs. 6, 7, 9) suggest that all components of the low-temperature QD PL spectrum for InAs/GaAs 7° [001] are related to the radiative recombination of the exciton in the ground state $n = 0$.

If the thermal dissociation energy (binding energy) G of the exciton is estimated as in [51, 52], from the onset of the QD PL band intensity decrease, then the Arrhenius law (Fig. 9, curves *2*) yields $G = 5$ meV for QD families related to QD_1 and $G = 6$ meV for QD_0 QDs. These values of G are in agreement with the available published data [51–53]. The coincidence of the exciton-binding energies for QD_1 and IQD QDs may be due to the existence of a high lateral potential for QDs confined to terraces with a small broadening factor. In this case, excitons become insensitive to the QD size [54].

Noteworthy in Fig. 9 is the deviation of the I/I_m experimental dependence from the Arrhenius law, the most pronounced for the IQD band. A similar phenomenon was observed in [19]. We attribute this behavior to the influence of the excited ($n = 1$) electron state in the QD. Direct observation of this state is difficult, since the transition $e|100\rangle - hh|000\rangle$ is not allowed because of the weak overlapping of the excited electron state with the ground state of a heavy hole [31, 55, 56]. With increasing temperature, one of the channels for the population of the ground state $n = 0$ by carriers disappears because of the thermally activated depletion of the higher ($n = 1$) level. The deviation of the experimental dependence I/I_m (curve *1*) from the function F calculated for E_{A0} (curve *2*) depends on the efficiency of this channel.

Thus, the thermal activation energy E_{A0} corresponds to the depth ΔE_0 of the electron ground state in a QD (see table): relative to the InAs WL level (E_{WL} = 1.46 eV) for QD families and relative to the GaAs barrier level (E_{BR} = 1.52 eV) for IQDs. Following the approach used in [57], we calculated the hole level depth (ΔE_h) for various QD families (see table): $\Delta E_h = E_{IF} - (E_m + \Delta E_0)$, where $E_{IF} = E_{WL}$ for QDs and $E_{IF} = E_{BR}$ for IQDs, and ΔE_0 accounts for the Coulomb interaction (exciton binding energy G). The results obtained for the ionization energy of the electron and hole states in InAs/GaAs QDs agree with the known published data [9, 27, 31, 47, 49, 51, 57–60] and are representative of the dependences of ΔE_0 on the QD volume and ΔE_h on the QD shape [31, 61]. Indeed, simple calculations show that the volume of the deposited substance forming an IQD on a 7-nm-wide terrace exceeds that for the pyramidal QD associated with QD_0 with a base length of 8–9 nm. It is also evident that, under the conditions of lateral confinement by the terrace edges, IQDs must be characterized by an H/B ratio larger than

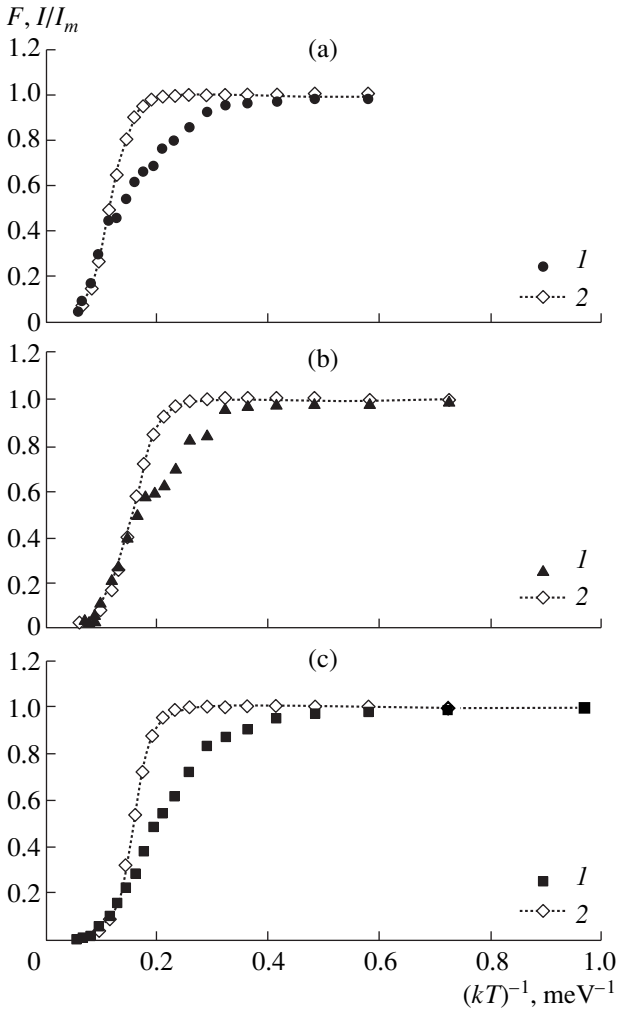

Fig. 9. Fitting of the function F (*2*) to the experimental dependence of I/I_m (*1*) on reciprocal temperature for the following bands in the PL spectrum of InAs/GaAs 7° [001] QDs: (a) QD_0, (b) QD_1, and (c) IQD. Excitation by an Ar^+ laser (100 mW).

that in QD_0-related QDs and, consequently, have a shallower hole level [61].

The difference between the contributions from excited states to the temperature dependence of I/I_m for the PL bands associated with different QD families can be understood if the energy spacing ΔE_{1-0} between the first excited and the ground electronic states is estimated. Assuming, as before, for ΔE_h that the electron and hole levels approach each other in exciton formation through lowering of the electron level, we obtain for IQDs a ΔE_{1-0} value of 35 meV coinciding with the energy of the LO phonon at the InAs/GaAs interface [62]. It may be expected that this resonance leads to a rather effective relaxation of the electronic excitation to the ground state, i.e., to a very short electron lifetime in the excited state. The low-level occupancy is another reason for the absence of contribution to the PL spec-

Characteristics of the PL spectrum components and of the corresponding QD groups in InAs/GaAs 7° [001]

Parameter	QD_0	QD_1	IQD
E_m, eV	1.265	1.345	1.37
$E_{A0} \equiv \Delta E_0$, meV	50	43	56
$E_{A1} \equiv \Delta E_1$, meV	14	12	16
G, meV	6	5	5
ΔE_{1-0}, meV	30	26	35
ΔE_h, meV	145	72	94
β	350	750	7500

Note: E_{A0} and E_{A1} are the activation energies, ΔE is the ionization energy (level depth) of the ground (ΔE_0) and the first excited (ΔE_1) electronic states, G is the energy of thermal dissociation (binding energy) of the exciton, ΔE_{1-0} is the energy spacing between the first excited and the ground electronic states in a QD, ΔE_h is the heavy-hole level depth, and β is the fitting parameter for the Arrhenius function F.

trum from transitions involving the excited electronic state. Naturally, the disappearance of such a relaxation mechanism with increasing temperature leads to a substantial distortion of the temperature dependence of I/I_m for the PL spectrum of IQDs (Fig. 9c). A sharp decrease in the relative intensity of the IQD band for IQDs in the temperature range 5–80 K is shown in Figs. 3 and 4. The ΔE_{1-0} values obtained in this work for all QD families (see table) agree with the results of [63], where an energy spacing of 30 meV between the excited and ground states of "ultrasmall" InAs/GaAs QDs under lateral confinement conditions was obtained.

A study of the role played by excited states and other competing channels for excitation relaxation in InAs QDs grown on vicinal GaAs (100) surfaces by measuring excitation spectra and PL decay times is underway.

ACKNOWLEDGMENTS

The authors thank N.K. Polyakov, D.N. Demidov, N.P. Korneev, and Yu.B. Samsonenko for participation in growth experiments and N.N. Ledentsov, D. Bimberg, V.G. Dubrovskiĭ, and V.P. Evtikhiev for their helpful participation in discussions.

This work was supported in part by the Russian Scientific Program "Physics of Solid State Nanostructures" (grant no. 98-2029), the Russian Foundation for Basic Research (project nos. 98-02-18317 and 99-02-17780), and the Russian Scientific Program "Integration of the Fundamental Science and Higher School, 1997–2000" (grant no. 326.75).

G.É. Tsyrlin acknowledges the support of INTAS (grant no. YSF 98-54).

REFERENCES

1. N. N. Ledentsov, V. M. Ustinov, V. A. Shchukin, *et al.*, Fiz. Tekh. Poluprovodn. **32**, 385 (1998) [Semicond. **32**, 343 (1998)].
2. G. É. Tsyrlin, V. N. Petrov, M. V. Maksimov, *et al.*, Fiz. Tekh. Poluprovodn. **31**, 912 (1997) [Semicond. **31**, 777 (1997)].
3. A. F. Tsatsul'nikov, B. V. Volovik, N. N. Ledentsov, *et al.*, Fiz. Tekh. Poluprovodn. **32**, 95 (1998) [Semicond. **32**, 84 (1998)].
4. P. D. Wang, N. N. Ledentsov, C. M. Sotomayor Torres, *et al.*, Appl. Phys. Lett. **64**, 1526 (1994).
5. S. Ruvimov, P. Werner, K. Scheerschmidt, *et al.*, Phys. Rev. B: Condens. Matter **51**, 14766 (1995).
6. V. P. Evtikhiev, I. V. Kudryashov, E. Y. Kotel'nikov, *et al.*, Fiz. Tekh. Poluprovodn. **32**, 1482 (1998) [Semicond. **32**, 1323 (1998)].
7. O. Brandt, L. Tapfer, K. Ploog, *et al.*, Phys. Rev. B: Condens. Matter **44**, 8043 (1991).
8. Y. Nabetani, A. Wakahara, and A. Sasaki, J. Appl. Phys. **78**, 6461 (1995).
9. L. Brusaferri, S. Sanguinetti, E. Grilli, *et al.*, Appl. Phys. Lett. **69**, 3354 (1996).
10. M. Colocci, F. Bogani, L. Carraresi, *et al.*, Appl. Phys. Lett. **70**, 3140 (1997).
11. H.-W. Ren, K. Nishi, S. Sugou, *et al.*, Jpn. J. Appl. Phys. **37**, 1548 (1998).
12. S. Noda, T. Abe, and M. Tamura, Phys. Rev. B: Condens. Matter **58**, 7181 (1998).
13. G. L. Rowland, T. J. C. Hosea, *et al.*, Appl. Phys. Lett. **73**, 3268 (1998).
14. W. G. Stallard, A. S. Plaut, S. Thoms, *et al.*, Appl. Phys. Lett. **73**, 1898 (1998).
15. G. É. Tsyrlin, V. N. Petrov, V. G. Dubrovskiĭ, *et al.*, Fiz. Tekh. Poluprovodn. **31**, 902 (1997) [Semicond. **31**, 768 (1997)].
16. Y. Nabetani, N. Yamamoto, T. Tokuda, *et al.*, J. Cryst. Growth **146**, 363 (1995).
17. S. J. Xu, X. C. Wang, S. J. Chua, *et al.*, Appl. Phys. Lett. **72**, 3335 (1998).
18. Q. W. Mo, T. W. Fan, Q. Gong, *et al.*, Appl. Phys. Lett. **73**, 3518 (1998).
19. H. Lee, R. Lowe-Webb, T. J. Johnson, *et al.*, Appl. Phys. Lett. **73**, 3556 (1998).
20. H.-W. Ren, K. Nishi, S. Sugou, *et al.*, Jpn. J. Appl. Phys. Part 1 **36**, 4118 (1997).
21. D. Leonard, K. Pond, and P. M. Petroff, Phys. Rev. B: Condens. Matter **50**, 11687 (1994).
22. J. M. Moison, F. Houzay, F. Barthe, *et al.*, Appl. Phys. Lett. **64**, 196 (1994).
23. N. Ikoma and S. Ohkouchi, Jpn. J. Appl. Phys. **34**, L724 (1995).
24. O. Brandt, G. C. La Rocca, A. Heberle, *et al.*, Phys. Rev. B: Condens. Matter **45**, 3803 (1992).
25. Y. Tokura, H. Saito, and T. Fukui, J. Cryst. Growth **94**, 46 (1989).
26. V. P. Evtikhiev, V. E. Tokranov, A. K. Kryzhanovskiĭ, *et al.*, Fiz. Tekh. Poluprovodn. **32**, 860 (1998) [Semicond. **32**, 765 (1998)].

27. M. Grundmann, O. Stier, and D. Bimberg, Phys. Rev. B: Condens. Matter **52**, 11969 (1995).
28. P. M. Petroff, K. H. Schmidt, G. M. Ribeiro, *et al.*, Jpn. J. Appl. Phys. Part 1 **36**, 4068 (1997).
29. T. Ide, A. Yamashita, and T. Mizutani, Phys. Rev. B: Condens. Matter **46**, 1905 (1992).
30. G. M. Guryanov, G. E. Cirlin, A. O. Golubok, *et al.*, Surf. Sci. **352–354**, 646 (1996).
31. M. Grundmann, R. Heitz, N. Ledentsov, *et al.*, Superlattices Microstruct. **19**, 81 (1996).
32. M. A. Cusack, P. R. Briddon, and M. Jaros, Phys. Rev. B: Condens. Matter **54**, R2300 (1996).
33. N. N. Ledentsov, P. D. Wang, S. M. Sotomayor Torres, *et al.*, Phys. Rev. B: Condens. Matter **50**, 12171 (1994).
34. S. Raymond, S. Fafard, P. J. Poole, *et al.*, Phys. Rev. B: Condens. Matter **54**, 11548 (1996).
35. S. Yu. Verbin, B. V. Novikov, R. B. Jufer, *et al.*, in *Proceedings of Seventh International Symposium on Nanostructures: Physics and Technology* (St. Petersburg, Russia, 1999), p. 63.
36. M. J. Steer, D. J. Mowbray, W. R. Tribe, *et al.*, Phys. Rev. B: Condens. Matter **54**, 17738 (1996).
37. T. Saitoh, H. Takeuchi, J. Konda, *et al.*, Jpn. J. Appl. Phys. **35**, 1217 (1996).
38. A. Bossacchi, F. Colonna, S. Franchi, *et al.*, J. Cryst. Growth **150**, 185 (1995).
39. K. Mukai, N. Ohsuka, and M. Sugawara, Appl. Phys. Lett. **70**, 2416 (1997).
40. Z. M. Fang, K. Y. Ma, D. H. Jaw, *et al.*, J. Appl. Phys. **67**, 7034 (1990).
41. W. Yang, R. R. Lowe-Webb, H. Lee, *et al.*, Phys. Rev. B: Condens. Matter **56**, 13314 (1997).
42. P. B. Joyce, T. J. Krzyzewski, G. R. Bell, *et al.*, Phys. Rev. B: Condens. Matter **58**, R15981 (1998).
43. P. Chen, Q. Xie, A. Madhukar, *et al.*, J. Vac. Sci. Technol. B **12**, 2568 (1994).
44. H. Saito, K. Nishi, and S. Sugou, Appl. Phys. Lett. **73**, 2742 (1998).
45. G. D. Lian, J. Yuan, L. M. Brown, *et al.*, Appl. Phys. Lett. **73**, 49 (1998).
46. J. M. García, T. Mankad, P. O. Holtz, *et al.*, Appl. Phys. Lett. **72**, 3172 (1998).
47. A. J. Williamson and A. Zunger, Phys. Rev. B: Condens. Matter **58**, 6724 (1998).
48. A. J. Williamson, A. Zunger, and A. Canning, Phys. Rev. B: Condens. Matter **57**, R4253 (1998).
49. I. E. Itskevich, S. G. Lyapin, I. A. Troyan, *et al.*, Phys. Rev. B: Condens. Matter **58**, R4250 (1998).
50. F. Hatami, N. N. Ledentsov, M. Grundmann, *et al.*, Appl. Phys. Lett. **67**, 656 (1995).
51. D. I. Lubyshev, P. P. González-Borrero, E. Marega, Jr., *et al.*, Appl. Phys. Lett. **68**, 205 (1996).
52. G. Wang, S. Fafard, D. Leonard, *et al.*, Appl. Phys. Lett. **64**, 2815 (1994).
53. P. D. Wang, N. N. Ledentsov, C. M. Sotomayor Torres, *et al.*, Phys. Rev. B: Condens. Matter **50**, 1604 (1994).
54. M. Bayer, S. N. Walck, T. L. Reinecke, *et al.*, Phys. Rev. B: Condens. Matter **57**, 6584 (1998).
55. M. A. Cusack, P. R. Briddon, and M. Jaros, Phys. Rev. B: Condens. Matter **56**, 4047 (1997).
56. H. Jiang and J. Singh, Phys. Rev. B: Condens. Matter **56**, 4696 (1997).
57. P. N. Brounkov, A. Polimeni, S. T. Stoddart, *et al.*, Appl. Phys. Lett. **73**, 1092 (1998).
58. H. Lee, W. Yang, and P. C. Sercel, Phys. Rev. B: Condens. Matter **55**, 9757 (1997).
59. F. Bogani, L. Carraresi, R. Mattolini, *et al.*, Solid-State Electron. **40**, 363 (1996).
60. H. Yu, S. Lycett, C. Roberts, *et al.*, Appl. Phys. Lett. **69**, 4087 (1996).
61. J. Kim, L.-W. Wang, and A. Zunger, Phys. Rev. B: Condens. Matter **57**, R9408 (1998).
62. R. Heitz, M. Grundmann, N. N. Ledentsov, *et al.*, Appl. Phys. Lett. **68**, 361 (1996).
63. S. Fafard, D. Leonard, J. L. Merz, *et al.*, Appl. Phys. Lett. **65**, 1388 (1994).

Translated by S. Ktitorov

Semiconductors, Vol. 34, No. 4, 2000, pp. 462–472. Translated from Fizika i Tekhnika Poluprovodnikov, Vol. 34, No. 4, 2000, pp. 477–487.

LOW-DIMENSIONAL SYSTEMS

Charge Carrier Interference in Modulated Quantum Wires

N. T. Bagraev*, W. Gehlhoff, V. K. Ivanov***, L. E. Klyachkin*, A. M. Malyarenko*, and I. A. Shelykh*****

** Ioffe Physicotechnical Institute, Russian Academy of Sciences, ul. Politekhnicheskaya 26, St. Petersburg, 194021 Russia*

*** Institut für Festkörperphysik, Technische Universität Berlin, D-10623, Berlin, Germany*

**** St. Petersburg State Technical University, ul. Politekhnicheskaya 29, St. Petersburg, 195251 Russia*

Submitted October 25, 1999; accepted for publication October 26, 1999

Abstract—Quantized conductance as a function of the charge carrier energy in modulated quantum wires is investigated for the first time. The energy dependence of the coefficient of transit through a modulated quantum wire was calculated, with the δ-potential approximation used to describe the charge carrier quantum interference in the system of ultrasteep internal barriers. The current steps and oscillations in the quantized conductance plateaus, observable as the oscillating features in the quantum wire conductance under varying longitudinal voltage, are predicted. Such oscillations, resulting from the quantum interference of the ballistic holes, are observed experimentally for the first time by recording quantized conductance plateaus as a function of the voltage applied along the silicon modulated quantum wire. © *2000 MAIK "Nauka/Interperiodica".*

1. INTRODUCTION

With the high level of nanotechnology achieved in recent years, quantum wires with one or several one-dimensional (1D) channels with a shorter length than the charge-carrier free-path length can be fabricated by the split-gate technique [1–3], cleaved edge overgrowth [4], as well as by the use of metallic point contacts [5] or electrostatic ordering of the impurity dipoles [6]. Due to the suppression of the inelastic scattering processes, the charge carrier transport in such channels is not accompanied by Joule losses. Thus, ballistic electron and hole motion can take place in the case of the 1D transport [7, 8].

One of the most important achievements resulting from the fabrication of the 1D ballistic channels, based on the GaAs-AlGaAs heterostructures [2–5] and silicon superlattices [6], was the observation of the quantum wire conductance quantization. It reveals itself through a series of plateaus in the 1D conductance recorded as a function of the gate voltage controlling the wire width (see Figs. 1a and 1b); the plateaus are separated by steps of height $g_s g_v e^2/h$ (g_s and g_v being the spin and the valley degeneracy factors, respectively) [7, 8]. Increasing the gate voltage results in an increase of the quantum wire width, which leads to an increase in the number of the occupied quantum-confinement subbands. Hence, we have a clearly pronounced steplike shape of the $G(V_g)$ dependence: a step in the wire conductance occurs each time the Fermi level crosses the bottom of a quantum-confinement subband [2–6]; i.e.,

$$G_0 = g_s g_v \frac{e^2}{h} N, \qquad (1)$$

where N is the number of occupied subbands, which corresponds to the serial number of the highest occupied 1D subband in the quantum wire.

It should be noted that the actual height of the quantized conductance steps is usually slightly smaller than $g_s g_v e^2/h$ (Fig. 1b), which may result from the influence of the zero-magnetic-field spin polarization of the charge carriers [9] or from the coherence destruction due to electron–electron interaction, as well as due to impurity scattering [4, 10–13]. Furthermore, it is the residual impurities distributed along the quantum wire boundaries that provide the basis for the formation of the internal barriers modulating the 1D transport characteristics. The strength of these barriers can be adjusted by the voltage on the gate controlling the width of the quantum wire and, especially effectively, by the additional "finger" gates (see Fig. 1a) [13], which are used to form quantum dots between two neighboring barriers. It is important that the existence of modulating barriers results in the appearance of the periodic oscillations in the regions of the quantized conductance plateau as a function of the gate voltage [6, 12–17]. Two types of such oscillations related to the transit of the individual charge carriers through the modulated quantum wire were observed experimentally. One of them, the Coulomb oscillations, occur due to the recharging of the quantum dots formed between the fixed barriers, whose parameters are determined by the charge correlations and the quantum confinement conditions [12–14, 17, 18]. In this case, recharging of the quantum dots is performed by varying the barrier potential via finger gates (Fig. 1a) under the given constant energy of the tunneling carriers (U_{ds} = const). Another type of oscillations in the quantized conductance plateaus is related to the interference effects

induced by the elastic backscattering between the modulating barriers [15]. Interference of the ballistic carriers should be most pronounced, if their kinetic energy varies with the voltage on the main and (or) finger gates (which is often the case in submicron-scale nanoelectronics devices). Thus, identification of the interference effects against the background of the Coulomb oscillations is quite complicated. To solve it here, we precisely adjusted the kinetic energy of the carriers tunneling through the quantum wire, so that this energy increased linearly and directly during the recording of the quantized conductance plateaus.

In what follows, we first analyze the energy dependence of the transit coefficient $T(E)$ through a modulated quantum wire to demonstrate the existence of the oscillations in the quantized conductance

$$G = G_0 T(E), \tag{2}$$

which appear due to the ballistic carrier interference. Next, we present experimental data on the observation of the oscillations in the quantized conductance plateaus as a function of the source-drain voltage applied along the axis of an electrostatically modulated quantum wire formed within a self-organized silicon quantum well. Since the ballistic-carrier kinetic energy is largely determined by the source-drain voltage, we show the observation of such oscillations to be proof that charge carrier interference in the modulated quantum wires does occur.

2. ENERGY DEPENDENCE OF THE COEFFICIENT OF TRANSIT THROUGH A SYSTEM OF δ-LIKE BARRIERS IN A MODULATED QUANTUM WIRE

We assume that the modulated quantum wire may be regarded as a regular quantum 1D structure, i.e., that the potential of this system (with no external fields applied) can be expressed as a sum corresponding to a finite set of equally spaced barriers. The actual profile $V(x)$ of each barrier can be, to a certain approximation, substituted by the δ-like one. Then, the single-barrier potential is given by $\alpha\delta(x - R)$, where R represents the barrier location and α is determined from the condition

$$\alpha = \int_{-\infty}^{\infty} V(x)dx, \tag{3}$$

which represents the strength equality of the actual and the model (δ-like) barriers. Thus, the quantum wire potential can be expressed as

$$U(x) = \alpha \sum_{j=0}^{n-1} \delta(x - Lj), \tag{4}$$

where n is the number of barriers and L is the distance between them. Below, this potential is used to calculate the energy dependence of the transit coefficient $T(E)$ via the transfer matrix technique [19, 20].

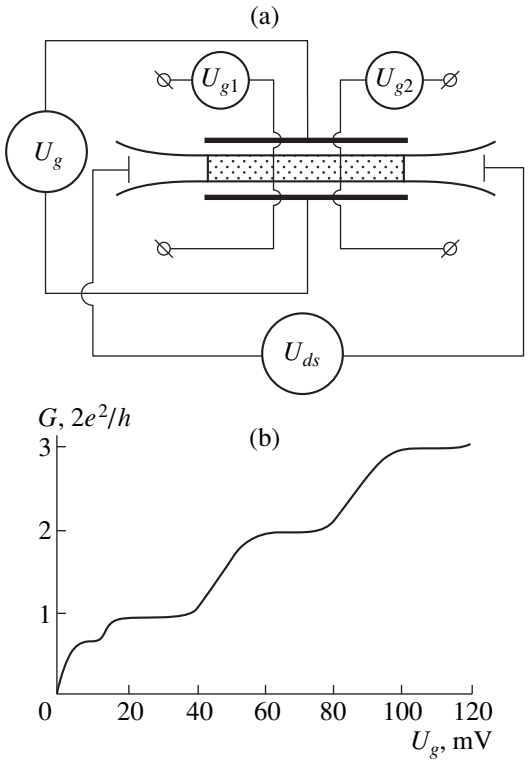

Fig. 1. (a) Layout of the split gate (under the bias of U_g) employed to create modulated quantum wires in a quantum well. The voltages U_{g1} and U_{g2} are applied to the "finger" gates used to form quantum dots [13, 27]. (b) Quantized conductance $G(U_g)$ observed at $T = 77$ K in a narrow (2×2 nm^2) 1D channel in a p-type self-organized silicon quantum well. The Fermi level position corresponds to the filling of the heavy-hole 1D subbands, thus $G = (2e^2/h)T(E)$.

2.1. T(E) Dependence in the Absence of the Longitudinal Electric Field

In this case, the scattering potential can be represented by (4), and the $T(E)$ dependence can be derived analytically.

In the context of the model under consideration, it is expedient to separate the x-axis (coinciding with the wire axis) into $n + 1$ segments (see the inset in Fig. 2b); let us number them by 0, 1,…, n. The particle wave function $\psi_j(x)$ in the jth region can be represented as a linear combination of the two counterpropagating plane waves:

$$\psi_j(x) = A_j \exp(ikx) + B_j \exp(-ikx), \tag{5}$$

where k is the particle wave vector, related to its momentum by $p = \hbar k$. The reflected wave should be absent at the exit from the wire; thus, $B_n = 0$. Setting the incident wave amplitude equal to unity ($A_0 = 1$), we obtain for the transit coefficient

$$T = \left|\frac{A_n}{A_0}\right|^2 = A_n^2 < 1. \tag{6}$$

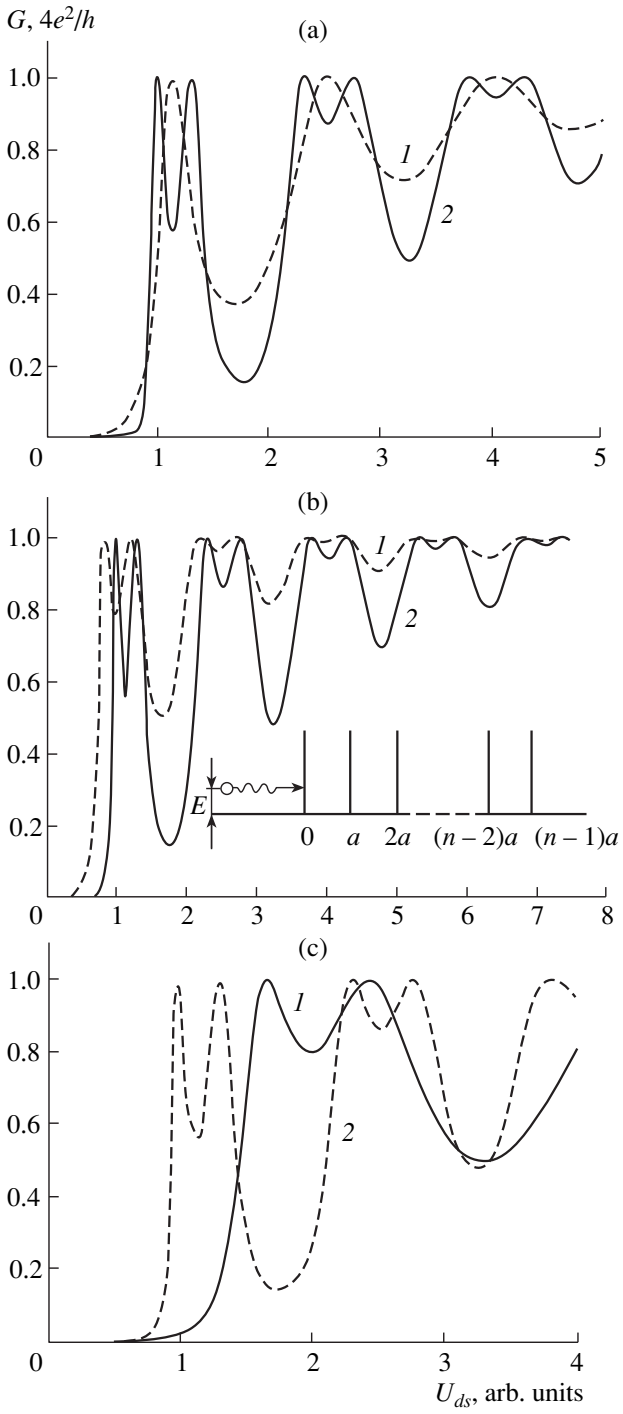

Fig. 2. Oscillations caused by the charge carrier quantum interference in the plateau of the quantized conductance G in relation to the source-drain voltage U_{ds} applied to the modulated quantum wire. The curves are calculated for the following parameters: (a) barrier strength $\alpha = 1$, distance between the barriers $L = 1$, and number of the barriers (*1*) $n = 2$ and (*2*) $n = 3$; (b) $L = 2$, $n = 3$, and the barrier strength (*1*) $\alpha = 1$ and (*2*) $\alpha = 2$; and (c) $\alpha = 1$, $n = 3$, and the distance between the barriers (*1*) $L = 1$ and (*2*) $L = 2$. The parameters α and L are expressed in atomic units. Fig. 1b, inset: a 1D system of separate δ-like barriers in the absence of an external electric field.

At each barrier, the wave function is continuous and its derivative, discontinuous; the functions ψ_j and ψ_{j+1} should be sewn together at the point $x = Lj$ according to the following conditions, which result from the definition of the δ-potential:

$$(\psi_{j+1} - \psi_j)\big|_{x=Lj} = 0,$$
$$(\psi'_{j+1} - \psi'_j)\Big|_{x=Lj} = \frac{2m\alpha}{\hbar^2}\psi_j\Big|_{x=Lj}. \quad (7)$$

Let us express A_{j+1} and B_{j+1} in terms of A_j and B_j. The following set of two linear algebraic equations can be derived from the boundary conditions (7):

$$A_{j+1}\exp(ikLj) + B_{j+1}\exp(-ikLj) = A_j\exp(ikLj) + B_j\exp(-ikLj),$$
$$ik[A_{j+1}\exp(ikLj) - B_{j+1}\exp(-ikLj)] - ik[A_j\exp(ikLj) - B_j\exp(-ikLj)] = \frac{2m\alpha}{\hbar^2}[A_j\exp(ikLj) + B_j\exp(-ikLj)]. \quad (8)$$

Substituting the variables

$$A'_{j+1} = A_{j+1}\exp(ikLj),$$
$$B'_{j+1} = B_{j+1}\exp(-ikLj),$$
$$A'_j = A_j\exp(ikLj),$$
$$B'_j = B_j\exp(-ikLj), \quad (9)$$

we get

$$A'_{j+1} + B'_{j+1} = A'_j + B'_j,$$
$$A'_{j+1} - B'_{j+1} - A'_j + B'_j = \frac{2m\alpha}{ik\hbar^2}(A'_j + B'_j). \quad (10)$$

Therefore,

$$A'_{j+1} = \left(1 - \frac{im\alpha}{k\hbar^2}\right)A'_j - \frac{im\alpha}{k\hbar^2}B'_j,$$
$$B'_{j+1} = \frac{im\alpha}{ik\hbar^2}A'_j + \left(1 + \frac{im\alpha}{k\hbar^2}\right)B'_j. \quad (11)$$

Employment of the matrix notation will be appropriate in the further treatment for the sake of convenience. Thus, we introduce the column of new complex amplitude as

$$\mathbf{X}'_{j+1} = \begin{pmatrix} A'_{j+1} \\ B'_{j+1} \end{pmatrix}, \quad \mathbf{X}'_j = \begin{pmatrix} A'_j \\ B'_j \end{pmatrix},$$
$$\mathbf{X}_{j+1} = \begin{pmatrix} A_{j+1} \\ B_{j+1} \end{pmatrix}, \quad \mathbf{X}_j = \begin{pmatrix} A_j \\ B_j \end{pmatrix}. \quad (12)$$

In the 0th region, the incident wave amplitude is set equal to 1, and, in the nth region, the reflected wave is absent; thus,

$$\mathbf{X}_0 = \begin{pmatrix} 1 \\ B \end{pmatrix}, \quad \mathbf{X}_n = \begin{pmatrix} A \\ 0 \end{pmatrix}. \tag{13}$$

Next, using (9), we have

$$\begin{aligned} \mathbf{X}'_{j+1} &= \mathbf{C}_j \mathbf{X}_{j+1}, \\ \mathbf{X}'_j &= \mathbf{C}_j \mathbf{X}_j, \end{aligned} \tag{14}$$

where the matrix $\mathbf{C}_j$ is defined as

$$\begin{aligned} \mathbf{C}_j &= \begin{pmatrix} \exp(ikLj) & 0 \\ 0 & \exp(-ikLj) \end{pmatrix}, \\ \mathbf{C}_j^{-1} &= \begin{pmatrix} \exp(-ikLj) & 0 \\ 0 & \exp(ikLj) \end{pmatrix}. \end{aligned} \tag{15}$$

The relationship between $\mathbf{X}'_{j+1}$ and $\mathbf{X}'_j$ can be found from (11) as

$$\mathbf{X}'_{j+1} = \mathbf{D}\mathbf{X}'_j,$$

where

$$\mathbf{D} = \begin{pmatrix} 1 - \dfrac{im\alpha}{k\hbar^2} & -\dfrac{im\alpha}{k\hbar^2} \\ \dfrac{im\alpha}{k\hbar^2} & 1 + \dfrac{im\alpha}{k\hbar^2} \end{pmatrix} = \begin{pmatrix} 1 - i\beta & -i\beta \\ i\beta & 1 + i\beta \end{pmatrix} \tag{16}$$

and $\beta = m\alpha/k\hbar^2$. Then,

$$\begin{aligned} \mathbf{C}_j \mathbf{X}_{j+1} &= \mathbf{D}\mathbf{C}_j \mathbf{X}_j, \\ \mathbf{X}_{j+1} &= \mathbf{C}_j^{-1}\mathbf{D}\mathbf{C}_j \mathbf{X}_j. \end{aligned} \tag{17}$$

The matrix $\mathbf{C}_j$ can be represented as the jth power of the matrix $\mathbf{C}$, so that the following relationships are valid for the equally spaced barriers:

$$\mathbf{C}_j = (\mathbf{C})^j, \quad \mathbf{C}_j^{-1} = (\mathbf{C}^{-1})^j. \tag{18}$$

Using (18), we can express $\mathbf{X}_n$ in terms of $\mathbf{X}_0$ as

$$\mathbf{C}_{n-1}\mathbf{X}_n = (\mathbf{D}\mathbf{C})^{n-1}\mathbf{D}\mathbf{X}_0. \tag{19}$$

Setting the position of the first barrier at $x = L$ (instead of $x = 0$), we obtain, similar to (19):

$$\mathbf{C}_n\mathbf{X}_n = (\mathbf{D}\mathbf{C})^n\mathbf{X}_0. \tag{20}$$

It is this expression that we use in the following presentation. To calculate $(\mathbf{D}\mathbf{C})^n$, we diagonalize the matrix $\mathbf{D}\mathbf{C}$:

$$\mathbf{D}\mathbf{C} = \mathbf{G}\begin{pmatrix} \lambda_1 & 0 \\ 0 & \lambda_2 \end{pmatrix}\mathbf{G}^{-1},$$

where λ_1 and λ_2 are the eigenvalues of the matrix $\mathbf{D}\mathbf{C}$ and the transfer matrix $\mathbf{G}$ is composed of the eigenvectors $\mathbf{Y}_1$ and $\mathbf{Y}_2$: $\mathbf{G} = \{\mathbf{Y}_1; \mathbf{Y}_2\}$. We now determine the eigenvalues and eigenvectors; we have

$$\begin{aligned} \mathbf{D}\mathbf{C} &= \begin{pmatrix} (1 - i\beta)\exp(ikL) & i\beta\exp(-ikL) \\ i\beta\exp(ikL) & (1 + i\beta)\exp(-ikL) \end{pmatrix} \\ &= \begin{pmatrix} a^* & b^* \\ b & a \end{pmatrix}, \end{aligned} \tag{21}$$

where

$$a = (1 + i\beta)\exp(-ikL), \quad b = i\beta\exp(ikL). \tag{22}$$

The eigenvalues are determined from the equation

$$\begin{aligned} \begin{vmatrix} a^* - \lambda & b^* \\ b & a - \lambda \end{vmatrix} &= (a^* - \lambda)(a - \lambda) - bb^* \\ &= \lambda^2 - (a + a^*)\lambda + (aa^* - bb^*) = 0. \end{aligned} \tag{23}$$

It can be easily shown that

$$\begin{aligned} \lambda_1 &= \cos kL + \beta\sin kL + \sqrt{[\cos kL + \beta\sin kL]^2 - 1}, \\ \lambda_2 &= \cos kL + \beta\sin kL - \sqrt{[\cos kL + \beta\sin kL]^2 - 1}. \end{aligned} \tag{24}$$

Then, using the transformation matrix

$$\mathbf{G} = \begin{pmatrix} \dfrac{\lambda_1 - a}{b} & \dfrac{\lambda_2 - a}{b} \\ 1 & 1 \end{pmatrix} \tag{25}$$

and the corresponding inverse matrix $\mathbf{F} = \mathbf{G}^{-1}$ and taking (20) into account, we arrive at

$$\mathbf{F}\mathbf{C}_n\mathbf{X}_n = \mathrm{diag}\{\lambda_1^n; \lambda_2^n\}\mathbf{F}\mathbf{X}_0, \tag{26}$$

$$\begin{aligned} \mathbf{C}_n\mathbf{X}_n &= \begin{pmatrix} \exp(iknL) & 0 \\ 0 & \exp(-iknL) \end{pmatrix}\begin{pmatrix} A \\ 0 \end{pmatrix} \\ &= \exp(iknL)\begin{pmatrix} A \\ 0 \end{pmatrix}, \end{aligned} \tag{27}$$

$$\begin{aligned} \mathbf{F}\mathbf{X}_n &= \frac{1}{\det(\mathbf{G})}\begin{pmatrix} 1 & \dfrac{a - \lambda_2}{b} \\ -1 & \dfrac{\lambda_1 - a}{b} \end{pmatrix}\begin{pmatrix} A \\ 0 \end{pmatrix} \\ &= \frac{1}{\det(\mathbf{G})}\begin{pmatrix} A \\ -A \end{pmatrix}, \end{aligned} \tag{28}$$

$$\mathrm{diag}\{\lambda_1^n;\ \lambda_2^n\}\mathbf{F}\mathbf{X}_0 = \frac{1}{\det(\mathbf{G})}\begin{pmatrix} \lambda_1^n\left(1-\dfrac{a-\lambda_2}{b}B\right) \\ \lambda_2^n\left(-1+\dfrac{\lambda_1-a}{b}B\right)\end{pmatrix}. \quad (29)$$

From (13) and (26), we obtain a set of two linear equations for the amplitudes A and B of the transmitted and reflected waves:

$$\begin{cases} \lambda_1^n\left(1-\dfrac{a-\lambda_2}{b}B\right) = A\exp(iknL), \\ \lambda_2^n\left(1-\dfrac{a-\lambda_1}{b}B\right) = A\exp(iknL). \end{cases} \quad (30)$$

Therefore,

$$B = \frac{b(\lambda_2^n-\lambda_1^n)}{\lambda_2^n(a-\lambda_1)-\lambda_1^n(a-\lambda_2)}. \quad (31)$$

Thus, the transit coefficient

$$T = 1 - BB^* \quad (32)$$

depends primarily on the wave vector k of the incident particle.

In the specific case of a single barrier inside a quantum wire, equation (31) is reduced to the known formula

$$A(k) = \frac{ik\hbar^2}{ik\hbar^2 - m\alpha}, \qquad B(k) = \frac{m\alpha}{ik\hbar - m\alpha}\exp(2ikx_0), \quad (33)$$

where x_0 indicates the location of the barrier. Hence,

$$T(k) = AA^* = \frac{k^2\hbar^4}{m^2\alpha^2 + k^2\hbar^4}. \quad (34)$$

One can see that the transit coefficient increases steadily from zero to unity as the charge-carrier kinetic energy increases.

When several barriers are present, damped oscillations appear in the $T(k)$ curve, with their frequency and amplitude being dependent on the number and strength of the barriers and the distance between them (see Fig. 2, where the dependences for the quantized conductance plateau calculated from (2) and (32) are shown). These oscillations are related to the interference of the waves that experienced multiple scattering between the barriers. To illustrate more conveniently the influence of interference on the shape of the $T(E)$ curve (k being proportional to E), let us consider the particular case of a 1D system with two barriers that need not be either identical or δ-like.

Let t_1 and t_2 be the absolute values of the transit amplitude and let r_1 and r_2 be the absolute values of the reflection amplitude from the first and second barrier, respectively. Next, let φ_{11} and φ_{22} stand for the phase change of the wave transmitted through the first and second barrier, respectively; φ_{12}, for the phase change of the wave propagating from the right to the left upon reflection from the first barrier; and φ_{21}, for the phase change of the wave propagating from the left to the right upon reflection from the second barrier. Then, the amplitude of the wave transmitted through the double-barrier system is given by

$$A = t_1t_2\exp[i(\varphi_{11}+\varphi_{22})]\sum_{j=1}^{\infty} r_1r_2\exp[i(\varphi_{12}+\varphi_{21})] = \frac{t_1t_2\exp[i(\varphi_{11}+\varphi_{22})]}{1-r_1r_2\exp[i(\varphi_{12}+\varphi_{21})]}. \quad (35)$$

Due to the presence of the factor $\exp[i(\varphi_{12}+\varphi_{21})]$, the transmission coefficient of the double-barrier system can, at certain energies of the incident particle, increase, as compared to the single-barrier case. The transmission coefficient reaches unity for certain incident particle energies, their spectrum being determined by the different combinations of the multiple scattering events. Treating multiple-barrier systems, it is convenient to use the following terminology: if a particle residing between the barriers undergoes many scattering events before it escapes, its energy is said to correspond to a quasi-level. The time spent by the particle between the barriers is then increased, i.e., a quasi-bound state is formed. If the incident particle energy is in resonance with some quasi-level energy of the system, then the transmission coefficient becomes equal to unity. The transmission amplitude in the resonance neighborhood is expressed by the Breit–Wigner formula [21, 22]:

$$A = C\frac{i\Gamma/2}{\varepsilon-\varepsilon_n+i\Gamma/2}, \quad (36)$$

where ε is the particle energy and ε_n and Γ are the nth quasi-level energy position and width, respectively.

One can see that interference effects change the $T(k)$ dependence dramatically, leading to an increase in the transmission probability up to unity for some values of k and to its significant reduction for others. Note that, for small k, interference results in a significant decrease of the transmission coefficient.

Let us note some regular features typical of the calculated dependences presented in Fig. 2.[1] The values of the wave vector corresponding to zero reflection from

[1] The calculations were carried out in the context of the δ-like barrier model assuming a zero voltage drop along the quantum wire, $G = (4e^2/h)T(E)$, and correspond to the case of the 1D subband filling in a (100)-oriented n-type silicon wire with $g_s = 2$ and $g_v = 2$, as well as to the Fermi level position on 1D light- and heavy-hole subband filling in the p-type silicon wire.

the barrier system with the number of barriers $n > 1$ can be separated into groups of $n - 1$ elements each. The dips between the quasi-levels belonging to the same group are rather shallow, while those between the different groups are much deeper. The depth of the dips within a group depends on the barrier strength and the distance between the barriers. The dips between groups also become deeper with an increase in these parameters. The energy of a given quasi-level increases with barrier strength and decreases with the distance between the barriers, the former dependence being much weaker than the latter. It can be easily inferred from (31) that the quasi-level spectrum of a system with an even number of barriers comprises a subset corresponding to the quasi-levels of a double-barrier system. This statement is illustrated in Fig. 3a: the quasi-level spectrum (i.e., the set of k values corresponding to the transmission coefficient of unity) of a six-barrier system comprises all quasi-levels of the double- and triple-barrier systems, as well as additional ones. Other features, already noted above, can also be deduced from (31): the quasi-levels of a system with an arbitrary number of barriers are grouped naturally by $n - 1$ elements, and the energy of a quasi-level with some given number p decreases with an increase in the distance between the barriers.

The model outlined, which implies that no potential drop occurs between the barriers, is valid if the external electric field only accelerates the carriers prior to their injection in the interbarrier region, their further motion being purely ballistic. Then, the wave vector k is proportional to the applied field E: $k \propto E \propto U_{ds}$, where U_{ds} is the source-drain voltage. The wire conductivity is calculated as

$$\sigma(E) = \frac{J_{\text{tr}}}{E} = \frac{T(k)J_f}{E} \propto \frac{T(k)k}{E} \propto T[k(E)], \quad (37)$$

where J_f and J_{tr} denote the incident and the transmitted carrier flux, respectively.

We note that the shape of the conductance dependence on the longitudinal electric field strength (which is determined by the source-drain voltage) is identical to the dependence of the transmission coefficient on the carrier wave vector. Thus, due to the interference of the tunneling charge carriers, the modulated quantum wire conductance should exhibit oscillating behavior as a function of their kinetic energy (Fig. 3b).

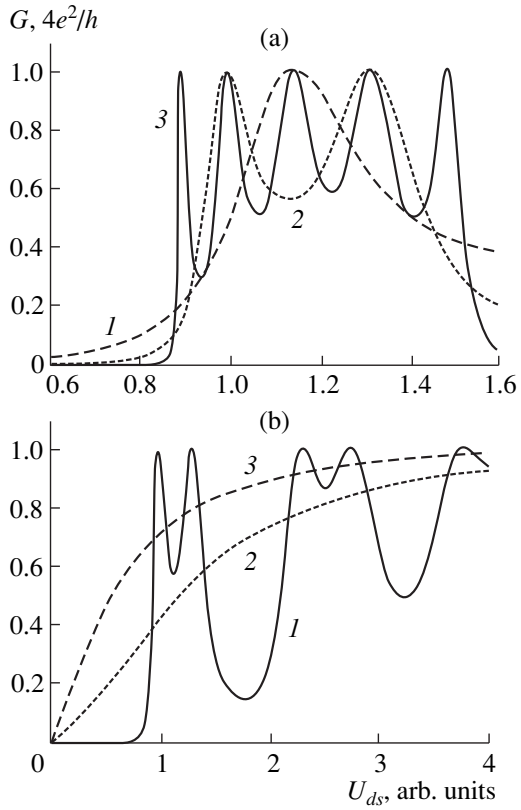

Fig. 3. (a) The shape of a single oscillation in the quantized conductance plateau in a modulated quantum wire, calculated for $\alpha = 1$, $L = 2$, and the number of barriers equal to (*1*) 2, (*2*) 3, and (*3*) 6. (b) The quantized conductance G in the plateau region as a function of the source-drain voltage U_{ds} applied to the modulated quantum wire, calculated (*1*) with and (*2*) without considering the charge carrier quantum interference. Curve (*3*) is calculated for the modulated quantum wire with a single barrier.

2.2. Energy Dependence of the Transmission Coefficient T(E) in the Presence of the Longitudinal Electric Field

If the potential drop between the barriers is to be accounted for, the model has to become more complicated. In this case, the potential $U_{\text{ext}}(x)$ due to the external sources should be taken into consideration, along with the potential (4) describing the wire itself. It is reasonable to assume that U_{ext} depends linearly on the external electric field applied along the quantum wire:

$$U_{\text{ext}} = -eEx. \quad (38)$$

However, the wave function would then be given by a superposition of the Airy functions $\text{Ai}(x)$ and $\text{Bi}(x)$ instead of the plane waves, which makes further analysis very complicated. Thus, we consider a simplified model, assuming a stepwise potential drop along the wire. Then, the scattering potential takes the following form (see the inset in Fig. 4b):

$$U(x) = \sum_{j=0}^{n-1} \delta(x - Lj) + U_{\text{exp}}(x),$$
$$U_{\text{ext}}(x) = \begin{cases} 0, & x < 0, \\ -eEjL, & x \in [(j-1)a, ja], \\ -eEnL, & x > (n-1)a. \end{cases} \quad (39)$$

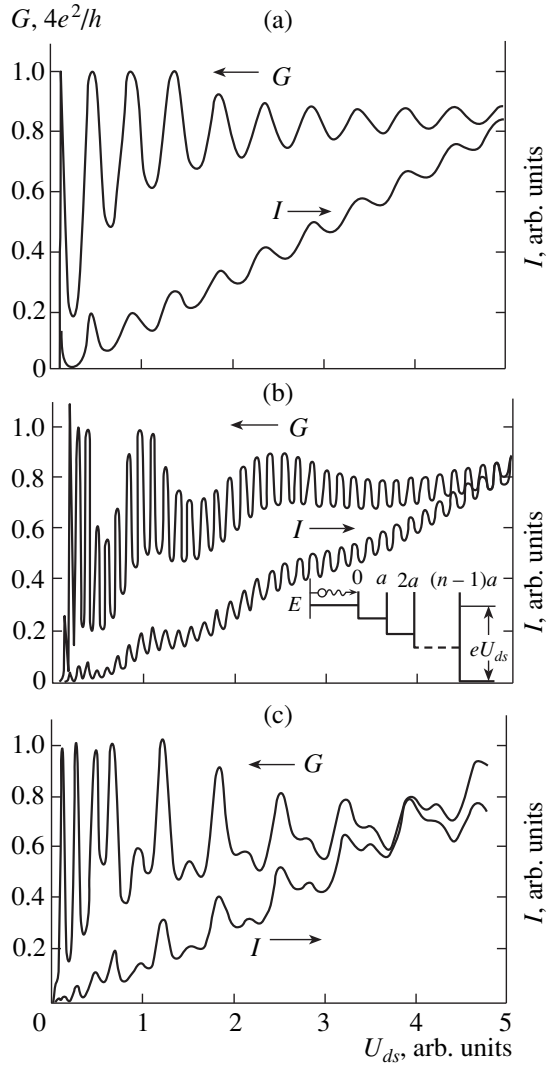

Fig. 4. Periodic oscillations in the regions of the current steps and quantized conductance plateaus numerically calculated for the following parameters of the structure (here, α and L are the strength and the distance between the barriers, respectively, given in atomic units, and n is the number of the barriers): (a) $n = 2$, $L = 20$, and $\alpha = 0.2$; (b) $n = 2$, $L = 40$, and $\alpha = 0.4$; and (c) $n = 3$, $L = 15$, and $\alpha = 0.2$. Fig. 4b, inset: a 1D system of separate δ-like barriers under applied external electric field.

The wave number of the incident charge carrier is proportional to the field strength

$$k_0 \propto E, \tag{40}$$

with the proportionality coefficient being the free parameter of the model. The wave number varies during the particle motion. In the jth region (between the barriers j and $j + 1$), it is equal to

$$k_j = \sqrt{k_0^2 + 2meELj}. \tag{41}$$

Then, the wave function in this region can be expressed as

$$\psi_j(x) = A_j \exp(ik_j x) + B_j \exp(-ik_j x). \tag{42}$$

Accordingly, the sewing conditions at the boundary of the regions j and $j + 1$ are

$$\begin{aligned} &A_{j+1}\exp(ik_{j+1}Lj) + B_{j+1}\exp(-ik_{j+1}Lj) \\ &\quad = A_j \exp(ik_jLj) + B_j \exp(-ik_jLj), \\ &ik_{j+1}(A_{j+1}\exp(ik_{j+1}Lj) - B_{j+1}\exp(-ik_{j+1}Lj)) \\ &\quad - ik_j[A_j \exp(ik_jLj) - B_j \exp(-ik_jLj)] \\ &\quad = \frac{2m\alpha}{\hbar^2}[A_j \exp(ik_jLj) + B_j \exp(-ik_jLj)]. \end{aligned} \tag{43}$$

Next, introducing [similar to (12)] the vectors

$$\mathbf{X}_{j+1} = \begin{pmatrix} A_{j+1} \\ B_{j+1} \end{pmatrix} \text{ and } \mathbf{X}_j = \begin{pmatrix} A_j \\ B_j \end{pmatrix},$$

we get

$$\mathbf{X}_{j+1} = \mathbf{D}_j \mathbf{X}_j, \tag{44}$$

where

$$\mathbf{D}_j = \begin{pmatrix} M & N \\ Q & S \end{pmatrix}, \tag{45}$$

$$M = \left(-\frac{im\alpha}{\hbar^2} + \frac{1}{2} + \frac{k_j}{2k_{j+1}}\right)\exp[i(k_j - k_{j+1})Lj],$$

$$N = \left(-\frac{im\alpha}{\hbar^2 k_{j+1}} + \frac{1}{2} - \frac{k_j}{2k_{j+1}}\right)\exp[-i(k_j + k_{j+1})Lj],$$

$$Q = \left(\frac{im\alpha}{\hbar^2 k_{j+1}} + \frac{1}{2} - \frac{k_j}{2k_{j+1}}\right)\exp[i(k_j + k_{j+1})Lj],$$

$$S = \left(\frac{im\alpha}{\hbar^2 k_{j+1}} + \frac{1}{2} + \frac{k_j}{2k_{j+1}}\right)\exp[-i(k_j - k_{j+1})Lj].$$

The amplitudes of the transmitted and reflected waves are determined from the system of two linear algebraic equations that are written in the matrix notation as follows:

$$\begin{aligned} &\mathbf{X}_n = \mathbf{D}_{n-1}\mathbf{X}_{n-1} = \mathbf{D}_{n-1}\mathbf{D}_{n-2}\ldots\mathbf{D}_0\mathbf{X}_0 = \Re\mathbf{X}_0, \\ &\Re = \prod_{j=0}^{n-1}\mathbf{D}_j, \\ &\mathbf{X}_0 = \begin{pmatrix} 1 \\ B \end{pmatrix}, \quad \mathbf{X}_n = \begin{pmatrix} A \\ 0 \end{pmatrix}. \end{aligned} \tag{46}$$

The solution is given by

$$B = -\frac{\Re_{21}}{\Re_{22}}, \quad A = \Re_{11} - \frac{\Re_{12}\Re_{21}}{\Re_{22}}. \tag{47}$$

Unlike the case considered in the previous section, the matrix product $\Re = \mathbf{D}_{n-1}\mathbf{D}_{n-2}\ldots\mathbf{D}_0$ cannot be calculated analytically for arbitrary n; only numerical analysis is possible.

The transmission coefficient is calculated as a ratio of the transmitted and incident particle flux densities:

$$T = \frac{J_{\text{tr}}}{J_f} = \frac{k_n}{k_0}|A|^2. \quad (48)$$

The current–voltage characteristics $I(U_{ds})$ and conductance G calculated for different parameters of the modulated wire are shown in Fig. 4. Periodic oscillations in I and G appear owing to the quantum interference of the charge carriers between the modulated quantum wire barriers. It can be seen that, for some parameter values, the voltage dependence of the conductance is similar to that obtained for the case of no potential drop between the barriers; for others, the curves are radically different. An example of the second type is given in Fig. 4c, where additional, higher-frequency modulation of the oscillations in the quantized conductance plateau is evident. Interestingly, such a modulation also arises in the $G(V_g)$ dependences obtained in the split-gate technique experiments demonstrating Coulomb oscillations in quantized conductance plateaus [12, 13]. It should be emphasized that the condition necessary for the manifestation of ballistic carrier interference, evidenced by the conductance oscillations, is the abruptness of the potential barriers formed in the modulated quantum wire. With this requirement violated, the interference vanishes, which is caused by the suppression of the ballistic carrier backscattering between the barriers, as well as by the enhanced carrier scattering within the single-particle subbands. Similar problems also arise in detecting the Coulomb oscillations in the system of the quantized conductance plateaus [13].

Thus, with the proposed model of the modulated quantum wire, it is possible to describe the oscillations in the quantized conductance plateau by the effects of the charge carrier quantum interference between the ultrasteep internal barriers. This is experimentally demonstrated for the first time in this work by the results obtained with the modulated silicon quantum wires.

3. QUANTIZED CONDUCTANCE IN MODULATED SILICON QUANTUM WIRES: EXPERIMENTAL RESULTS

Quantum wires of this type are formed electrostatically in the ultrashallow p^+-diffusion profiles at the single-crystalline Si(100) surface [6, 23, 24]. Such impurity profiles were obtained by nonequilibrium boron diffusion by precisely controlling the self-interstitial and vacancy fluxes generated by the Si–SiO_2 interface. The presence of these defects stimulate the dopant diffusion via a kick-out or a dissociative vacancy mechanism, respectively [6, 24, 25]. Varying the parameters of the surface oxide layer, changing the chlorine-containing component concentration in the gas phase and the diffusion temperature, one can define the conditions leading to the balance of these two competing mechanisms. Due to the strong reduction of the diffusion rate, which occurs under the conditions of balance, we managed to obtain ultrashallow p^+-profiles on the (100) surface of the n-type (bulk concentration of phosphorus $N(P) = 2 \times 10^{14}$ cm^{-3}) silicon by performing short-term boron diffusion from the gas phase at 900°C. The front and back surfaces of the wafer were previously thermally oxidized. The impurity diffusion was carried out at the front surface of the wafer through the Hall-bridge-shaped window in the oxide mask defined by photolithography (Fig. 5a). The depth and the boron concentration within the hyperabrupt diffusion profile, as measured by the secondary-ion mass-spectroscopy, were 7 nm and 10^{21} cm^{-3}, respectively.

The p^+-ultrashallow diffusion profiles thus obtained were studied by the cyclotron resonance (CR) and the quantized conductance measurements. The CR angle dependences were recorded at 3.8 K with an X-band 9.1–9.5 GHz EPR spectrometer [26]. The 180° symmetry of the CR line quenching and shift under magnetic field rotation in the {110} plane (perpendicular to the p^+–n junction plane) was established. This indicates the existence of a single, self-organized longitudinal quantum well (LQW) located between the highly doped two-dimensional impurity barriers within an ultrashallow diffusion p^+-profile (Fig. 5b).

The EPR and thermal-emf measurements revealed pyroelectric properties of such ultraheavily boron-doped two-dimensional barriers, caused by the existence of the reconstructed trigonal-symmetry impurity B^+–B^- dipoles (Fig. 5c) [6]. As electrostatic ordering in the pyroelectric barriers occurs, the reconstructed boron dipoles impose restrictions on the transverse charge-carrier motion in the plane of the LQW, which results in the formation of the quantum wires, either smooth or modulated (see [6]). Such a type of quantum wire is formed under the external voltage $U_{DS} = U_g + U_{ds}$ applied along the LQW (Fig. 5b). The voltage component U_g serves to maintain the transverse confinement because of the impurity dipole ordering, and U_{ds} serves to initiate the individual charge carrier transport.

The width of a dynamic quantum wire formed between the two pyroelectric barriers should increase as electrostatic ordering of the impurity dipoles proceeds, while the depth of the wire modulation is determined by the number of unreconstructed dipoles, which can be considered as δ-like barriers. It should be noted that the number of unreconstructed dipoles can be controlled by varying the concentrations of the Cl-containing compounds, which are responsible for the uniform dopant distribution inside the 2D pyroelectric barriers.

The quantized conductance resulting from the 1D transport of individual holes was observed at 77 K, both

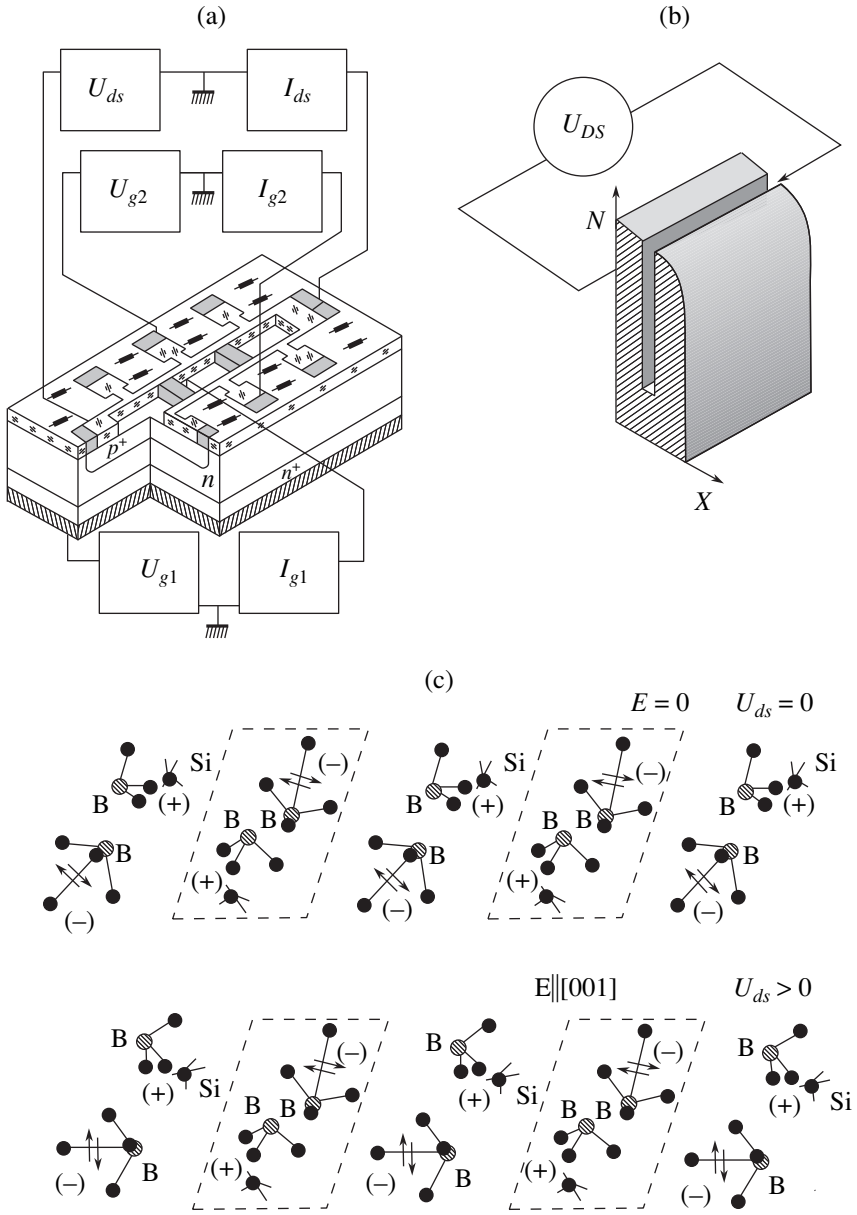

Fig. 5. (a) Layout of the planar Hall-geometry p^+–n structure fabricated for the studies of the quantized conductance as a function of the source-drain voltage. (b) Three-dimensional representation of an ultrashallow p^+-profile with a single quantum well confined between the heavily doped ultrathin barriers. (c) A system of the reconstructed trigonal B^+–B dipoles within the pyroelectric ultrathin barriers; under an applied external electric field, these dipoles confine the transverse motion of the charge carriers in the self-organized quantum well.

in the smooth and modulated quantum wires formed in the LQW under applied U_{DS} voltage (Fig. 6). The cross section of the dynamic quantum wires under study is determined by the width of the LQW and the width of the electrostatically induced lateral-channel, which are close to the distance between the dipoles (about 2 nm) defined by the boron concentration in the pyroelectric barriers. These parameters, along with the 2D hole concentration (1.6×10^9 cm^{-2}) and the effective 1D channel length (5 μm, much less than the inelastic backscattering length), determine the contribution of the light and heavy holes to the quantized conductance, which is reflected in the height of the conductance steps (compare the data in Fig. 6 and Fig. 1b). The widths of the LQW and of the 1D channel can also be determined from the CR angle dependences [26], as well as from the characteristics of the Coulomb oscillations observed in the split-gate technique experiments on a pyroelectric-barrier-confined quantum well (Fig. 5a) [6].

Since the cross section of the quantum wire is small (2×2 nm^2), one can expect that the energy gaps

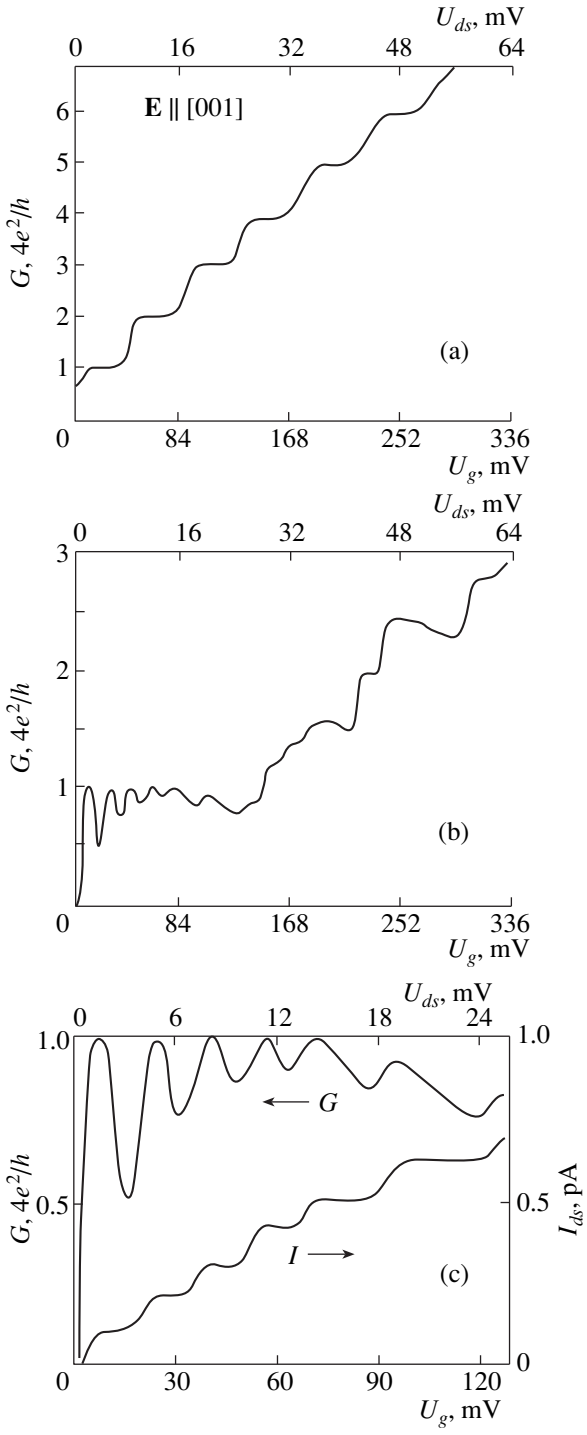

Fig. 6. The quantized conductance G observed at 77 K as a function of the voltages U_g and U_{ds} (a) in a smooth and (b), (c) in modulated 2×2 nm^2 quantum wires formed in the self-organized p-type silicon quantum wells. The Fermi level position corresponds to the filling of both heavy- and light-hole subbands.

between the 1D subbands are large, much greater than the temperature broadening at 77 K. Nevertheless, the conductance quantization decays with an increase in the number of the highest occupied subband. Apparently, this is caused by the nonlinear noise fluctuations of the conductance that develop when eU_{ds} becomes comparable to the energy gaps between the subbands [27]. This assumption was verified by the technique employed in [27] to study the nonlinear behavior of the quantized conductance as a function of the source-drain voltage. Both U_{DS} components (U_g and U_{ds}), as well as the value of the energy gap between the 1D subbands (96 meV, in good agreement with the calculation based on the known wire cross section) were deduced from the data on the quenching of the quantized conductance with the growth of U_{DS}. It should be noted that the linear variation of U_g and U_{ds} was observed in the entire range of the U_{DS} variation, up to the region where the quantum staircase disappears in the dependence $G(U_g)$ (Fig. 6); this fact is very important for identifying the mechanism responsible for the oscillations in the quantized conductance plateaus by varying the charge carrier kinetic energy.

It follows from the above discussion that the oscillations observed in the plateaus of the quantized conductance of the modulated quantum wires develop if the kinetic energy of the ballistic holes varies (Figs. 6b, 6c). Apparently, the oscillations are caused by the interference effects brought about by the elastic backscattering from the δ-like barriers, their damping with an increase in the highest occupied state number (Fig. 6b) being attributable to the extreme sensitivity of the ballistic hole interference to the width of the quantum wire and the abruptness of the modulating barriers. It should be mentioned that the oscillating behavior of the conductance as a function of U_{ds} in the plateau region appears to present an experimental test to recognize the quantum interference effects in modulated quantum wires against the background of the Coulomb oscillations that arise owing to the formation of the quantum dots between the δ-barriers. Such an interplay between the Coulomb oscillations and interference effects has been observed previously in split-gate structures [15], which was possibly caused by small deviations in U_{ds} on varying the gate voltage U_g.

4. CONCLUSION

Thus, the proposed model for the conductance of a modulated quantum wire, based on the use of the δ-potential to describe the elastic backscattering of the charge carriers from the ultrasteep internal barriers, makes identifying the quantum interference contribution to the experimentally observed oscillations in the quantized conductance plateaus possible.

The appearance of steps in the current–voltage characteristics and oscillations in the region of the quantized conductance plateaus, which should reveal themselves as oscillating features in the quantum wire conductance as a function of the longitudinal voltage, follows from the energy dependence of the charge carrier transit through a modulated quantum wire, calculated in the context of this model.

Such conductance oscillations resulting from the quantum interference of the ballistic holes at the δ-like potential barriers were observed in this work by recording the quantized conductance plateaus as a function of voltage applied along the modulated quantum wire.

ACKNOWLEDGMENTS

This work was supported by the Program "Physics of the Solid-State Nanostructures" (project no. 97-1040), the Federal Program "Promising Technologies and Devices of Micro- and Nanoelectronics" (project no. 02.04.301.89.5.2) and by the "Integration" Program (project no. 75:2.1).

REFERENCES

1. T. J. Thornton, M. Pepper, H. Ahmed, *et al.*, Phys. Rev. Lett. **56**, 1198 (1986).
2. D. A. Wharam, T. J. Thornton, R. Newbury, *et al.*, J. Phys. C **21**, L209 (1988).
3. B. J. van Wees, H. van Houten, C. W. J. Beenakker, *et al.*, Phys. Rev. Lett. **60**, 848 (1988).
4. A. Yacoby, H. L. Stormer, Ned S. Wingreen, *et al.*, Phys. Rev. Lett. **77**, 4612 (1996).
5. J. I. Pascual, J. Méndez, J. Gómez-Herrero, *et al.*, Phys. Rev. Lett. **71**, 1852 (1993).
6. N. T. Bagraev, L. E. Klyachkin, A. M. Malyarenko, *et al.*, Superlattices Microstruct. **23**, 1333 (1998).
7. R. Landauer, IBM J. Res. Dev. **1**, 233 (1957).
8. M. Büttiker, Phys. Rev. Lett. **57**, 1761 (1986).
9. K. J. Thomas, J. T. Nicholls, M. Y. Simmons, *et al.*, Phys. Rev. Lett. **77**, 135 (1996).
10. B. L. Altshuler, A. G. Aronov, and D. E. Khmelnitsky, J. Phys. C **15**, 7367 (1982).
11. S. Tarucha, T. Honda, and T. Saku, Solid State Commun. **94**, 413 (1995).
12. U. Meirav, M. A. Kastner, S. J. Wind, *et al.*, Phys. Rev. Lett. **65**, 771 (1990).
13. C.-T. Liang, M. Y. Simmons, C. G. Smith, *et al.*, Phys. Rev. Lett. **81**, 3507 (1998).
14. D. V. Averin, A. N. Korotkov, and K. K. Likharev, Phys. Rev. B: Condens. Matter **44**, 6199 (1991).
15. T. Heinzel, S. Manus, D. A. Wharam, *et al.*, Europhys. Lett. **26**, 689 (1994).
16. T. J. Thornton, Rep. Prog. Phys. **58**, 311 (1995).
17. M. A. Kastner, Phys. Today **46** (1), 24 (1993).
18. K. Likharev and T. Claeson, Sci. Am., No. 6, 50 (1992).
19. R. Tsu and L. Esaki, Appl. Phys. Lett. **22**, 562 (1973).
20. M. R. Vladimirova and A. V. Kavokin, Fiz. Tverd. Tela (St. Petersburg) **37**, 2163 (1995) [Phys. Solid State **37**, 1178 (1995)].
21. A. Yacoby, M. Heiblum, D. Mahalu, *et al.*, Phys. Rev. Lett. **74**, 4047 (1995).
22. R. Schuster, E. Bucks, M. Heiblum, *et al.*, Nature (London) **385**, 417 (1997).
23. N. T. Bagraev, W. Gehlhoff, V. K. Ivanov, *et al.*, Proc. SPIE-Int. Soc. Opt. Eng. **3687**, 112 (1998).
24. N. T. Bagraev, W. Gehlhoff, L. E. Klyachkin, *et al.*, Defect Diffus. Forum **143–147**, 1003 (1997).
25. U. Cösele and T. Y. Tan, Defect Diffus. Forum **59**, 1 (1988).
26. W. Gehlhoff, N. T. Bagraev, and L. E. Klyachkin, Mater. Sci. Forum **196–201**, 467 (1995).
27. L. P. Kouwenhoven, B. J. Weels, C. J. P. M. Harmans, *et al.*, Phys. Rev. B: Condens. Matter **39**, 8040 (1989).

Translated by M. Skorikov

Semiconductors, Vol. 34, No. 4, 2000, pp. 473–476. Translated from Fizika i Tekhnika Poluprovodnikov, Vol. 34, No. 4, 2000, pp. 488–491.

LOW-DIMENSIONAL SYSTEMS

Dependence of the Energy Spectrum of a Strained ZnSe/ZnS Superlattice on the Charge-Carrier Concentration

R. M. Peleshchak and B. A. Lukiyanets

Drogobych State Pedagogical University, Drogobych, 293720 Ukraine

Submitted October 27, 1999; accepted for publication October 28, 1999

Abstract—The model of self-consistent electron-deformation coupling was used to show that additional periodic local electron-deformation wells and barriers arise in the vicinity of heterocontact in a strained ZnSe/ZnS superlattice within the main quantum well (ZnSe) and above the main barrier (ZnS). It is found that, for the thickness of the ZnSe overgrown layer in the range from 10 to 20 Å, the electron ground-state energy E_{0c} decreases steadily with increasing conduction-electron concentration n_c; however, for the layer thickness exceeding 20 Å, the concentration dependence $E_{0c} = f(n_c)$ becomes nonmonotonic and features a maximum, which shifts to lower concentrations n_c as the layer thickness increases. © *2000 MAIK "Nauka/Interperiodica".*

1. INTRODUCTION

Semiconductor heterostructures, including those subjected to strain, are widely used in modern microelectronics [1, 2]. A number of technologies (such as, e.g., molecular-beam epitaxy) aimed at fabricating the strained heterostructures have been developed [2–5]. The phenomena related to the strained layer in heterosystems are actively studied; the results of these studies make it possible, on the one hand, to suppress the undesirable effects and, on the other hand, to use these phenomena in the design of microelectronic devices having the specified characteristics.

The deformation model describing the heterostructures with strains takes into account the lattice distortions that arise in the vicinity of contacts between crystalline systems owing to a mismatch of lattice parameters or as a result of fluctuations either in the thickness of an overgrown layer or in the solid-solution composition [3–7].

Actually, interaction between lattice distortions and conduction electrons also affects the strained state of a heterosystem. The electron-deformation interaction, which depends appreciably on the charge-carrier concentration, may be taken into account on the basis of the so-called electron-deformation model [8]. It is this model that is used in this work to describe the strained states of heterosystems.

2. THEORY

We consider a superlattice whose layers are under strain arising as a result of a mismatch in lattice constants or other crystallographic characteristics of the materials in contact. As is known, such a situation takes place in the case of ZnSe/ZnS heterostructures [5, 9].

Calculation of energy spectrum of a strained superlattice with allowance made for electron-deformation interaction is based on solving the time-independent Schrödinger equation

$$\left[-\frac{\hbar^2}{2m_\alpha^{*\beta}}\frac{\partial^2}{\partial x^2} + V_\alpha^\beta(x, L_w, b, n_\alpha)\right] \times \Psi_\alpha^\beta(E, x) = E\Psi_\alpha^\beta(E, x), \quad (1)$$

where the subscript $\alpha = c$ or v refers to the conduction or valence bands, respectively; $\beta = i$ or j, with the superscript i corresponding to the region $-L_w \le x \le 0$ of a narrow-gap material (ZnSe with the bandgap of E_{0g} = 2.822 eV) with the layer thickness L_w (see Fig. 1) and superscript j corresponding to the region $0 < x \le b$ in a wide-gap material (ZnS with the bandgap of E_{0g} = 3.840 eV) with the layer thickness equal to b; $m_\alpha^{*\beta}$ is the effective mass of an electron (hole); n_α is the charge-carrier concentration; and $V_\alpha^\beta(x, L_w, b, n_\alpha)$ is the periodic superlattice potential given by

$$V_\alpha^\beta(x, L_w, b, n_\alpha) = \Delta E_{0\alpha} + \Delta E_{\alpha\,\mathrm{mech}}(L_w, b) + \Delta E_{\alpha\,\mathrm{el\text{-}d}}^\beta(x, L_w, b, n_\alpha). \quad (2)$$

The first term in (2) $\Delta E_{0\alpha} = E_{0\alpha}^j - E_{0\alpha}^i$ accounts for the discontinuity in the conduction or valence bands of contacting materials in an unstrained superlattice.

The second term $\Delta E_{\alpha\,\mathrm{mech}}(L_w, b)$ accounts for a variation in the potential energy of electrons (holes) as a result of lattice distortions arising at the heteroboundary owing to the mismatch in the lattice constants a^i and a^j; thus,

$$\Delta E_{\alpha\,\mathrm{mech}}(L_w, b) = (-1)^n[a_\alpha^j\varepsilon_{\mathrm{mech}}^j(L_w, b) - a_\alpha^i\varepsilon_{\mathrm{mech}}^i(L_w, b)]. \quad (3)$$

1063-7826/00/3404-0473$20.00 © 2000 MAIK "Nauka/Interperiodica"

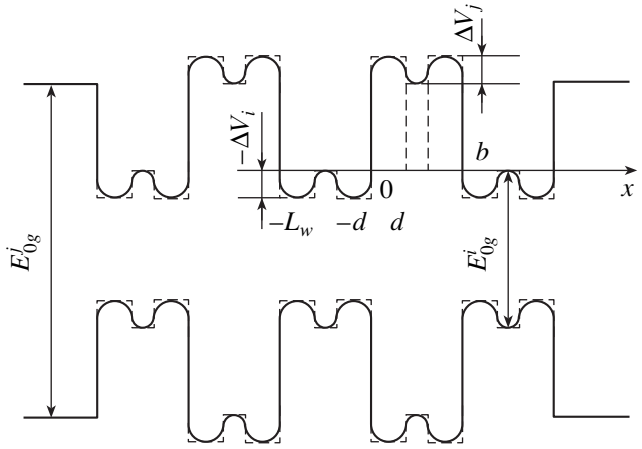

Fig. 1. Schematic representation of an energy-band diagram for a strained superlattice with local electron-deformation wells and barriers (the modified Kronig-Penney model). The dashed line shows an approximation of the periodic potential V_α^β (2) of a strained superlattice with allowance made for electron-deformation interaction.

Here, $n = 0$ for $\alpha = c$ and $n = 1$ for $\alpha = v$; a_α^j and a_α^i are the constants of the homogeneous deformation potential for the α band of the jth and ith materials,

$$\varepsilon_{\text{mech}}(L_w, b) \equiv \text{Sp}\,\varepsilon_{\text{mech}}^\beta = \frac{1}{\alpha^\beta}[2a_\parallel + a_\perp^\beta] - 3, \qquad (4)$$

where $a_\parallel$ is the lattice constant in the heterocontact plane and $a_\perp^\beta$ is the lattice constant along the superlattice axis [6]. For the above lattice constants, we have

$$a_\parallel(L_w, b) = \frac{a^i G^i L_w + b a^j G^j}{G^i L_w + b G^j}, \qquad (5)$$

with G^i and G^j standing for the shear moduli in the ith and jth materials and

$$a_\perp^\beta = a^\beta\left[1 - D^\beta\left(\frac{a_\parallel}{\alpha^\beta} - 1\right)\right], \qquad (6)$$

where D^β is a coefficient that is defined by the ratio of elastic constants and depends on the crystallographic orientation of the lattice (in particular, we have $D^\beta = 2C_{12}^\beta/C_{11}^\beta$ [6] for the [001] orientation).

The third term in (2) accounts for a variation in the potential energy of charge carriers in the band α; this variation is caused by local redistribution of the electron density $\Delta n_\alpha^\beta(x, L_w, b, n_\alpha)$ in the vicinity of the heteroboundary strained locally as a result of the electron-deformation interaction [8]. In other words, the above corresponds to a local distortion in profile of the potential $V_\alpha^\beta(x, L_w, b, n_\alpha)$; i.e., we have

$$\Delta E_{\alpha\ \text{el-d}}^\beta(x, L_w, b, n_\alpha) = -\frac{(a_\alpha^\beta)^2}{K^\beta}\Delta n_\alpha^\beta(x, L_w, b, n_\alpha), \quad (7)$$

where K^β is the uniform elastic constant of material β and Δn_α^β ($\Delta n_\alpha^i > 0, \Delta n_\alpha^j < 0$) is the local variation in the electron (hole) density. Expressions for Δn_α^β were obtained by the Fourier transforms of the relevant correlators on the basis of single-particle Green's functions. Such Green's functions can be derived as a result of searching for a self-consistent solution to a system of five equations [10] involving the following quantities: (i) charge-carrier concentration; (ii) electrostatic potential emerging in the vicinity of the strained heteroboundary owing to a variation in the electron (hole) density Δn_α^β; (iii) the wave function of electron (hole) in the vicinity of the strained heteroboundary; (iv) the Green functions; and (v) the chemical potential.

Finally, we have

$$\begin{aligned}&\Delta n_\alpha^\beta(x, L_w, b, n_\alpha)\\ &= R_\alpha^\beta[e\varphi_\alpha^\beta(x) - [\Delta E_{0\alpha} + \Delta E_{\alpha\ \text{mech}}^\beta(L_w, b)]],\end{aligned} \qquad (8)$$

where

$$\begin{aligned}R_\alpha^\beta &= \left(\frac{3}{8\pi^4}\right)^{1/3}\frac{2m_\alpha^{*\beta}}{\hbar^2}\frac{n_\alpha^{1/3}[1 + P_\alpha^\beta n_\alpha^{1/3}]^{1/2}}{1 - (3/2)P_\alpha^\beta n_\alpha^{1/3}[1 + P_\alpha^\beta n_\alpha^{1/3}]},\\ P_\alpha^\beta &= \frac{2(a_\alpha^\beta)^2 m_\alpha^{*\beta}}{(3\pi^2)^{2/3}\hbar^2 K^\beta}.\end{aligned} \qquad (9)$$

Electrostatic potential $\varphi_\alpha^\beta(x)$ arising in the vicinity of the strained heteroboundary as a result of local redistribution of electrons (holes) can be derived by solving the Poisson equations for the ith and jth regions of the superlattice.

As the origin of potential in the quantum well of the strained superlattice, we choose the bottom of the well for electrons and the top of the barrier for holes; thus, we have

$$\begin{aligned}&\frac{d^2\varphi_\alpha^i}{dx^2} - (\lambda_\alpha^i)^2\varphi_\alpha^i = 0,\\ &(\lambda_\alpha^i)^2 = e^2 R_\alpha^i/\varepsilon^i\varepsilon_0 \quad \text{for} \quad -L_w \le x \le 0;\end{aligned} \qquad (10)$$

$$\frac{d^2\varphi_\alpha^j}{dx^2} - (\lambda_\alpha^j)^2\varphi_\alpha^j = -\frac{(\lambda_\alpha^j)^2}{e}[\Delta E_{0\alpha} + \Delta E_{\alpha\,\mathrm{mech}}^j(L_w, b)],$$
$$(\lambda_\alpha^j)^2 = e^2 R_\alpha^j/\varepsilon^j\varepsilon_0 \quad \text{for} \quad 0 \le x \le b. \tag{11}$$

Here, ε^β are the static permittivities. Solutions to equations (10) and (11) can be written as

$$\varphi_\alpha^i = A_\alpha^i \exp(\lambda_\alpha^i x) + B_\alpha^i \exp(-\lambda_\alpha^i x), \tag{12}$$

$$\varphi_\alpha^j = A_\alpha^j \exp(\lambda_\alpha^j x) + B_\alpha^j \exp(-\lambda_\alpha^j x) + \frac{1}{e}[\Delta E_{0\alpha} + \Delta E_{\alpha\,\mathrm{mech}}^j(L_w, b)], \tag{13}$$

where A_α^i, B_α^i, A_α^j, and B_α^j are constants that are determined from the condition for the continuity of the electrostatic potential $\varphi_\alpha^i(x)$ and $\varphi_\alpha^j(x)$ at the heteroboundary (i.e., for $x = 0$) and the condition for the periodicity of the potential

$$\varphi_\alpha^i(b) = \varphi_\alpha^i(-L_w)$$

and the normal component of the electric-displacement vector

$$D_\alpha^{in}(0) = D_\alpha^{jn}(0) \quad \text{and} \quad D_\alpha^{jn}(b) = D_\alpha^{in}(-L_w).$$

$$\Delta E_{\alpha\,\mathrm{el\text{-}d}}^i(x, L_w, b, n_\alpha) = -\frac{(a_\alpha^i)^2 R_\alpha^i}{K^i}[A_\alpha^i \exp(\lambda_\alpha^i x) + B_\alpha^i \exp(-\lambda_\alpha^i x)] \quad \text{for} \quad -L_w \le x \le 0; \tag{14}$$

$$\Delta E_{\alpha\,\mathrm{el\text{-}d}}^j(x, L_w, b, n_\alpha) = -\frac{(a_\alpha^j)^2 R_\alpha^j}{K^j}[A_\alpha^j \exp(\lambda_\alpha^j x) + B_\alpha^j \exp(-\lambda_\alpha^j x)] \quad \text{for} \quad 0 \le x \le b. \tag{15}$$

3. RESULTS OF CALCULATION AND DISCUSSION

The spectrum of charge carriers in a strained superlattice with periodic potential accounting for the electron-deformation interaction is defined as a solution to the one-dimensional Schrödinger equation (1) with an approximating piecewise constant electron-deformation potential $\tilde{V}_\alpha^\beta(x, L_w, b, n_\alpha)$ (Fig. 1, the dashed line), which describes the periodic potential $\tilde{V}_\alpha^\beta(x, L_w, b, n_\alpha)$ (2) of a strained superlattice. The latter potential is obtained by the method of self-consistent electron-deformation coupling [8] as

$$\tilde{V}_\alpha^\beta(x, L_w, b, n_\alpha) = \begin{cases} -\Delta V_\alpha^i(\varepsilon_{\mathrm{mech}}, n_\alpha) & \text{for } -L_w \le x \le -L_w + d, \\ 0 & \text{at } -L_w + d < x < -d, \\ -\Delta V_\alpha^i(\varepsilon_{\mathrm{mech}}, n_\alpha) & \text{for } -d \le x \le 0, \\ V_{0\alpha}(\varepsilon_{\mathrm{mech}}) + \Delta V_\alpha^j(\varepsilon_{\mathrm{mech}}, n_\alpha) & \text{for } 0 < x \le d, \\ V_{0\alpha}(\varepsilon_{\mathrm{mech}}) & \text{for } d < x \le b - d, \\ V_{0\alpha}(\varepsilon_{\mathrm{mech}}) + \Delta V_\alpha^j(\varepsilon_{\mathrm{mech}}, n_\alpha) & \text{for } b - d < x \le b, \end{cases} \tag{16}$$

where $\Delta V_\alpha^i(\varepsilon_{\mathrm{mech}}, n_\alpha) \equiv \Delta E_{\alpha\,\mathrm{el\text{-}d}}^i(x \longrightarrow 0-; L_w, b, n_\alpha)$ is the depth of the additional local well formed at the heterocontact in the main quantum well (ZnSe) as a result of electron-deformation interaction (see Fig. 1). In particular, for a ZnSe/ZnS superlattice with $n_c = 10^{17}$ cm^{-3} and $L_w = 10$ Å, we have $\Delta V_c^{\mathrm{ZnSe}} \approx 0.07$ meV, and we have $\Delta V_c^{\mathrm{ZnSe}} \approx 0.3$ meV for $n_c = 10^{19}$ cm^{-3} and $L_w = 10$ Å. Here, $\Delta V_\alpha^j(\varepsilon_{\mathrm{mech}}, n_\alpha) \equiv \Delta E_{\alpha\,\mathrm{el\text{-}d}}^j(x \longrightarrow 0+; L_w, b, n_\alpha)$ is the height of local additional barrier appearing at the heteroboundary above the main barrier (ZnS) as a result of electron-deformation interaction, and $V_{0\alpha}(\varepsilon_{\mathrm{mech}}) \equiv \Delta E_{0\alpha} + \Delta E_{\alpha\,\mathrm{mech}}(L_w, b)$.

The width of the local additional electron-deformation well d_α^i (of the local barrier d_α^j) was chosen from

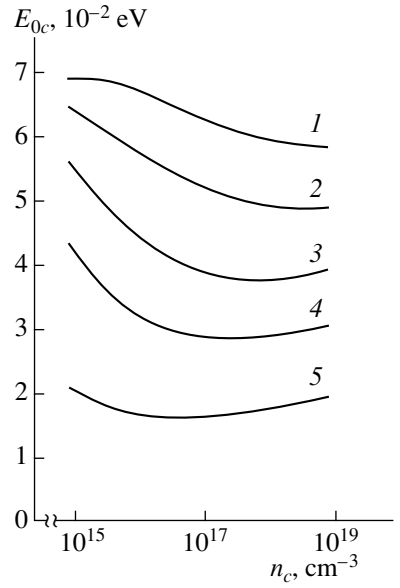

Fig. 2. The energy of the electron ground-state energy in a strained ZnSe/ZnS superlattice as a function of conduction-electron concentration n_c for the thickness of the ZnSe overgrown layer L_w = (*1*) 12, (*2*) 20, (*3*) 30, (*4*) 40, and (*5*) 60 Å.

the condition $d_\alpha^\beta = (1/e)\sqrt{\varepsilon^\beta \varepsilon_0 / R_\alpha^\beta}$, where ε^β is the static permittivity of the βth material and ε_0 is the permittivity of vacuum.

We used the condition for the continuity of the wave function $\Psi_\alpha^\beta(E, x)$ and its derivative at the boundaries between the regions ($x = -L_w + d$, $x = -d$, $x = 0$, and $x = b - d$) of the superlattice and the condition for periodicity $\Psi_\alpha^\beta(b) = \Psi_\alpha^\beta(-L_w)\exp[ik(L_w + b)]$ to derive the dispersion equation; the latter was solved to determine the dependence of the charge-carrier spectrum on the average carrier concentration n_α for various values of the thickness L_w of the ZnSe overgrown layer.

Figure 2 shows the results of numerical calculation of the electron ground-state energy E_{0c} in a strained ZnSe/ZnS superlattice. The following parameters of the materials and their energy-band structure were used in the calculations: $m_{0c}^{*\mathrm{ZnSe}} = 0.17m_0$, $a_c^{\mathrm{ZnS}} = -2.78$ eV, $a_c^{\mathrm{ZnSe}} = -3.65$ eV, $K^{\mathrm{ZnSe}} = 0.379$ eV/Å^3, $a^{\mathrm{ZnSe}} = 5.6687$ Å, $a^{\mathrm{ZnS}} = 5.4093$ Å, $b = 59.5$ Å, $\Delta E_{0c} = 0.198$ eV, $\varepsilon^{\mathrm{ZnSe}} = 8.1$, and $\varepsilon^{\mathrm{ZnS}} = 8.3$ [5, 6]. As follows from Fig. 2, for the range of electron concentrations under consideration (10^{15}–10^{19} cm^{-3}), the dependence of the position of the ground-state level on concentration is dissimilar for different values of thickness L_w of the overgrown layer. For the thickness of 10–20 Å, this dependence is monotonic, whereas, for the thickness L_w exceeding 20 Å, the dependence becomes nonmonotonic and features a minimum whose position is defined by the thickness L_w: the larger is L_w, the lower is the concentration corresponding to the minimum in the ground-state level. Such nontrivial behavior of the ground-state level can be quantitatively accounted for using the following reasoning. The ground-state energy is defined by two factors related to a variation in the charge-carrier concentration. On the one hand, an increase in this concentration is accompanied by a lowering of the potential-well bottom owing to the electron-deformation interaction. This effect by itself brings about a lowering of the ground-state level. On the other hand, an increase in charge-carrier concentration causes a decrease in the width d (see Fig. 1) and, as a result, a rise in the level. Thus, the final position of the level is defined by competition between the aforementioned opposing factors. As follows from the above, the first factor of these is proportional to $n_c^{1/3}$, whereas the second is proportional to $n_c^{-1/3}$, which is responsible for the fact that the resulting dependence becomes nonmonotonic. On the basis of the above reasoning, we may assume that the dependence of the position of the ground-state level on carrier concentration would also be nonmonotonic for the thickness L_w in the range of 10–20 Å but for concentrations higher than those considered in this work.

The above reasoning makes it possible to qualitatively account for the existence of a minimum in the dependence $E_{0c}(n_c)$. Quantitatively, the level position is defined by effects that were not adequately taken into account in this work.

REFERENCES

1. *Molecular-Beam Epitaxy and Heterostructures*, Ed. by L. L. Cheng and K. Ploog (Martinus Nihoff, Amsterdam, 1985; Mir, Moscow, 1989).
2. A. E. Zhukov, A. Yu. Egorov, V. M. Ustinov, *et al.*, Fiz. Tekh. Poluprovodn. **31**, 19 (1997) [Semicond. **31**, 15 (1997)].
3. A. V. Kavokin, S. I. Kokhanovskiĭ, A. I. Nesvizhskiĭ, *et al.*, Fiz. Tekh. Poluprovodn. **31**, 1121 (1997) [Semicond. **31**, 950 (1997)].
4. M. S. Brodin, V. V. Tishchenko, N. V. Bondar', *et al.*, Ukr. Fiz. Zh. **37**, 1802 (1992).
5. T. Taguchi, Y. Kawakami, and Y. Yamada, Physica B **191**, 23 (1993).
6. G. Chris and Van de Walle, Phys. Rev. B: Condens. Matter **39**, 1871 (1989).
7. V. Ya. Aleshkin, V. I. Gavrilenko, I. V. Erofeeva, *et al.*, Fiz. Tekh. Poluprovodn. **32**, 1240 (1998) [Semicond. **32**, 1106 (1998)].
8. I. V. Stasyuk and R. M. Peleshchak, Ukr. Fiz. Zh. **36**, 1744 (1991).
9. M. Herman, *Semiconductor Superlattices* (Akademie-Verlag, Berlin, 1986; Mir, Moscow, 1989), Chap. 3.
10. R. M. Peleshchak and B. A. Lukiyanets, Pis'ma Zh. Tekh. Fiz. **24**, 37 (1998) [Tech. Phys. Lett. **24**, 57 (1998)].

Translated by A. Spitsyn

Semiconductors, Vol. 34, No. 4, 2000, pp. 477–480. Translated from Fizika i Tekhnika Poluprovodnikov, Vol. 34, No. 4, 2000, pp. 492–495.

AMORPHOUS, VITREOUS, AND POROUS SEMICONDUCTORS

Structure and Properties of *a*-Si:H Films Grown by Cyclic Deposition

V. P. Afanas'ev*, A. S. Gudovskikh*, O. I. Kon'kov, M. M. Kazanin**, K. V. Kougiya***, A. P. Sazanov*, I. N. Trapeznikova**, and E. I. Terukov****

** St. Petersburg State University of Electrical Engineering, St. Petersburg, 197022 Russia*

*** Ioffe Physicotechnical Institute, Russian Academy of Sciences, Politekhnicheskaya ul. 26, St. Petersburg, 194021 Russia*

**** St. Petersburg State Pediatric Academy, St. Petersburg, 194100 Russia*

Submitted November 16, 1999; accepted for publication November 17, 1999

Abstract—Amorphous hydrogenated silicon films obtained by cyclic deposition with intermediate annealing in hydrogen plasma were studied. *a*-Si:H films deposited under optimal conditions are photosensitive (photoconductivity to dark conductivity ratio σ_{ph}/σ_d is as high as 10^7 under 20 mW cm^{-2} illumination in the visible region of the spectrum) and have an optical gap (E_g) and activation energy of conductivity (E_a) of 1.85 and 0.91 eV, respectively. Electron microscopy studies revealed a clearly pronounced layered structure of *a*-Si:H films and the presence of nanocrystalline inclusions in the amorphous matrix. © *2000 MAIK "Nauka/Interperiodica".*

INTRODUCTION

As compared to other amorphous semiconductors, amorphous hydrogenated silicon (*a*-Si:H) possesses such properties as high photoconductivity, a high absorption coefficient, and the possibility of being effectively doped. However, despite the fact that *a*-Si:H has been used for more than twenty years, the problem of obtaining high-quality material with well-reproducible and stable parameters still remains to be solved.

One way to obtain high-quality *i*-layers of *a*-Si:H at relatively low substrate temperatures consists in using the intermittent (cyclic) deposition regime, when a cycle of plasma-enhanced chemical vapor deposition (PECVD) of a 1–10-nm-thick layer of *a*-Si:H from monosilane is followed by its "annealing" in hydrogen plasma [1]. It has been noticed that optimizing the ratio of the deposition and annealing times markedly improves the photosensitivity of *i*-layers. However, when this ratio is made lower than a certain critical value, the volume fraction of microcrystalline silicon increases and photosensitivity falls [1–4].

The authors developed and then modified a technological system that allows varying cyclic PECVD regimes over wide range [5]. Placing the rf PECVD system on the lateral surface of a cylindrical vacuum chamber and substrates on a rotating substrate-holder drum enabled depositing of thin layers of the material, which could be subjected to layer-by-layer thermal annealing in hydrogen plasma to produce *a*-Si:H films of a highly uniform thickness.

GROWTH TECHNOLOGY AND MEASUREMENT PROCEDURE

Undoped *a*-Si:H films were deposited onto Pyroceram, quartz, and silicon substrates by cyclic PECVD in a diode rf system (13.56 MHz). The technological regimes used were the optimal for cyclic deposition in a constant-composition gas mixture (80% Ar + 20% SiH_4) [5]: substrate temperature 250°C, rf discharge power 40 W, rotation velocity of substrate-holder drum 4 rpm, and gas mixture pressure 25 Pa.

In optimizing the cyclic deposition process, the gas mixture composition was varied using leak valves controlled by time relays, with the times of deposition (t_{dep}) and thermal treatment in hydrogen (t_{tr}) preset and the ratio of these also varied. The annealing time was constant and equal to 2 min. The layer thickness deposited in a single run was varied by changing the deposition time in the range from 1 to 4 min. In the process, the transition to a steady gas mixture composition took several tens of seconds, i.e., was comparable to the times of deposition and annealing. This led to fundamentally nonequilibrium conditions of film deposition.

The thickness, absorption coefficient, and refractive index of *a*-Si:H films deposited onto quartz substrates were determined from transmission spectra of the samples by a procedure described in [6]. The optical gap was found using the Tauc method from the spectral dependence of the absorption coefficient.

The dark conductivity σ_d and photoconductivity σ_{ph} of *a*-Si:H films on Pyroceram substrates were determined using aluminum electrodes with interelectrode spacing of 0.2 mm and form factor of 0.018. Since the

1063-7826/00/3404-0477$20.00

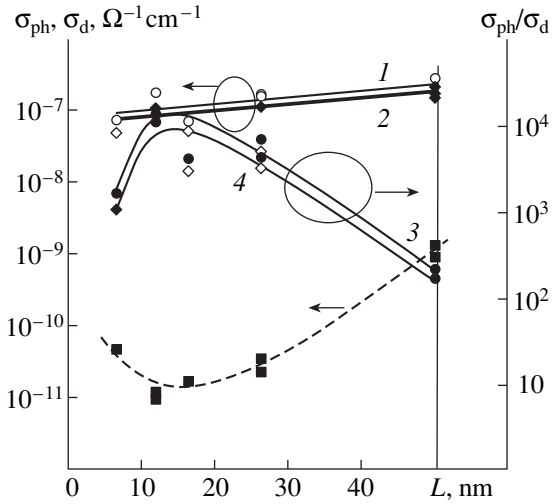

Fig. 1. Dark conductivity σ_d and photoconductivity σ_{ph} of *a*-Si:H films and the ratio σ_{ph}/σ_d in relation to the thickness *L* of a layer deposited in a run. Curves *1* and *2* correspond to σ_{ph}; *3* and *4*, to σ_{ph}/σ_d; and dashed curve, to σ_d. Illumination wavelength λ was (*1*, *3*) 436 and (*2*, *4*) 365 nm. Vertical straight line corresponds to uninterrupted deposition mode; the same for Figs. 3 and 4.

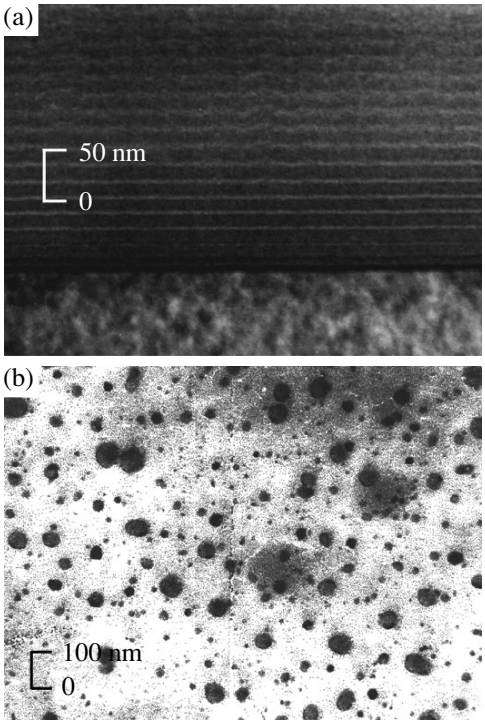

Fig. 2. Micrographs taken by (a) scanning and (b) transmission electron microscopy of an *a*-Si:H film (thickness of layer deposited in a single run was 16 nm).

thicknesses of the deposited films varied within 0.47–0.63 μm, it was necessary to eliminate the effect of thickness on the photosensitivity of *a*-Si:H films. For this purpose, the photoconductivity was measured at 365 and 463 nm, with photons mainly absorbed in a 100-nm-thick near-surface layer. The measurements were done on a probing setup, which enabled photoelectric studies in two illumination modes (i) at 365 and 436 nm with light intensity of 0.17 mW cm^{-2} and (ii) in the visible region of the spectrum with intensity of 20 mW cm^{-2}.

Temperature dependences of the dark conductivity were used to determine its activation energy.

By processing IR absorption spectra of *a*-Si:H films deposited onto silicon substrates, the concentrations and the bonding configuration of hydrogen were determined.

Structural features of the films were studied by scanning and transmission electron microscopy (SEM and TEM, respectively).

RESULTS AND DISCUSSION

The dark σ_d and photoconductivity σ_{ph} and the ratio of these σ_{ph}/σ_d are shown in Fig. 1 as functions of layer thickness deposited in a single cycle. It can be seen that, as the layer thickness decreases, the photosensitivity σ_{ph}/σ_d increases, with this increase resulting from a decrease in dark conductivity. Such behavior of the dark conductivity of *a*-Si:H films obtained in this work by cyclic deposition is a distinctive feature of the films. Other authors, conversely, have reported that the dark conductivity of *a*-Si:H films either increases [2] or remains unchanged [1] with decreasing layer thickness deposited in a single run.

In our previous work [7], we suggested that the observed behavior of the dark conductivity is associated with the following. The distribution of hydrogen is nonuniform, and, therefore, the energy gap varies across the layer deposited in a single run under transient conditions. This results in a layered variable-gap structure with potential barriers at layer boundaries, and it is the presence of these barriers that possibly reduces the dark conductivity by making smaller the effective area of a film possessing higher conductivity.

This assumption is supported by the results obtained in an SEM study of a section of an *a*-Si:H film deposited in the cyclic mode (Fig. 2a). The micrograph clearly demonstrates the layered structure of the film, with thicknesses of separate layers corresponding to the layer thickness deposited in a single run. Light stripes in the film image apparently correspond to regions created in the film during treatment in hydrogen plasma and enriched with hydrogen to the greatest extent. With the thickness *L* of a layer deposited in a single cycle decreasing further, the dark conductivity starts to increase, which may be due to an increase in the fraction of the nanocrystalline phase in the *a*-Si:H film. The formation of nanocrystalline inclusions in the *a*-Si:H films is confirmed by TEM data (Fig. 2b). The micrograph clearly shows crystalline inclusions several tens of nanometers in size.

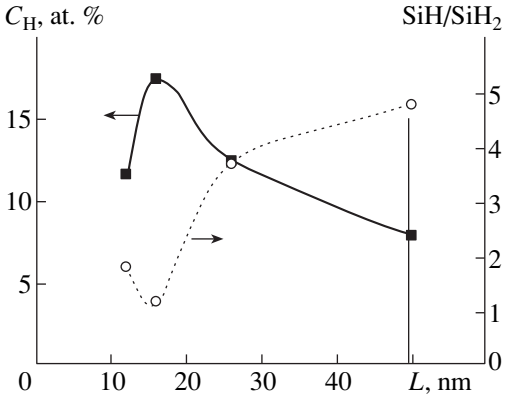

Fig. 3. Averaged content of hydrogen C_H and SiH/SiH$_2$ ratio in *a*-Si:H films in relation to the thickness L of a layer deposited in a single run.

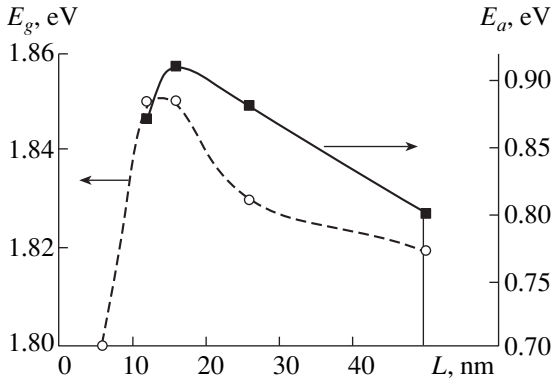

Fig. 4. Optical gap E_g and activation energy of conductivity E_a of *a*-Si:H films in relation to the thickness L of a layer deposited in a single run.

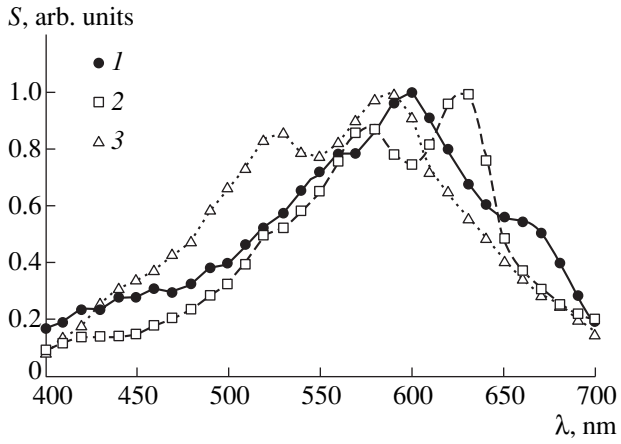

Fig. 5. Relative photoconductivity spectra of *a*-Si:H films deposited (*1*) in uninterrupted mode and in cyclic mode with the thickness L of a layer deposited in a single cycle equal to (*2*) 26 and (*3*) 16 nm.

To gain insight into the processes occurring in cyclic deposition, it is of interest to study such characteristics of *a*-Si:H films as hydrogen content, ratio of SiH/SiH$_2$ bond concentrations (Fig. 3), optical gap, and activation energy of conductivity (Fig. 4) in relation to the thickness L of a layer deposited in a single run. It can be seen that, with decreasing layer thickness, the hydrogen concentration increases, with the optical gap and activation energy of conductivity also increasing and the fraction of the SiH$_2$ bonds becoming larger. Then, the hydrogen concentration passes through a maximum and starts to decrease, as do the optical gap, activation energy of conductivity, and fraction of SiH$_2$ bonds. In our opinion, the decreasing hydrogen concentration furnishes additional evidence that the fraction of the nanocrystalline phase increases with decreasing thickness of a film subjected to hydrogen plasma treatment. According to [8], a decrease in the SiH/SiH$_2$ concentration ratio with increasing hydrogen concentration may be due to passivation of the surface of silicon nanocrystals by hydrogen forming SiH$_2$ bonds.

A specific feature of the obtained *a*-Si:H films is the presence of doublets in their photoconductivity spectra, previously observed in [9]. This feature is clearly seen from the spectra of relative photoconductivity of *a*-Si:H films prepared by the cyclic method with different thicknesses of layers deposited in a single run (Fig. 5). We believe that the occurrence of doublets is associated with the variable-gap structure of the film. This assumption is confirmed by the energy separation of 0.1–0.3 eV between the peaks, corresponding to optical-gap fluctuations caused by nonuniform distribution of hydrogen across the film.

CONCLUSION

A study of the structural and electrical properties of *a*-Si:H films shows that intermediate annealing in hydrogen plasma in the course of cyclic deposition enriches the films with hydrogen, thereby making the optical gap wider and the activation energy of conductivity higher. The distribution of hydrogen across the *a*-Si:H film is not uniform, which, in turn, leads to a variable-gap structure of the film and gives rise to potential barriers at boundaries of layers subjected to annealing.

At the same time, a nanocrystalline silicon phase is formed on increasing hydrogen content in the films. With a film subjected to treatment in hydrogen plasma becoming thinner, the fraction of the nanocrystalline phase increases.

The dependences of σ_d, E_g, E_a, C_H, and the [SiH]/[SiH$_2$] ratio on the thickness of a layer deposited in a single run can be described in terms of two competing processes: (i) film enrichment with hydrogen passivating dangling bonds and (ii) formation of nanocrystals. On the basis of the results obtained, the optimal thickness (corresponding to the maximum photosensi-

tivity, optical gap, and activation energy of dark conductivity of the resulting *a*-Si:H films) of layers subjected to hydrogen plasma treatment can be estimated as 14–16 nm.

ACKNOWLEDGMENTS

The authors thank A. A. Sitnikova for conducting the electron-microscopy studies.

The work was supported by Copernicus (grant no. IC15-CT98-0819, TIMOC) and INTAS (grant no. 97-1910).

REFERENCES

1. S. Okamoto, Y. Hishikawa, S. Tsuge, *et al.*, Jpn. J. Appl. Phys. **33** (4A), 1773 (1994).
2. A. Asano, Appl. Phys. Lett. **56** (6), 533 (1990).
3. M. Otobe and S. Oda, Jpn. J. Appl. Phys. **31** (6B), 1948 (1992).
4. S. Koynov, R. Schwartz, T. Fischer, *et al.*, Jpn. J. Appl. Phys. **33** (8), 4534 (1994).
5. V. P. Afanas'ev, A. A. Lyanguzov, and A. P. Sazanov, Peterb. Zh. Élektron. **2**, 7 (1995).
6. R. Swanepoel, J. Phys. E: Sci. Instrum. **16**, 1214 (1983).
7. V. P. Afanas'ev, A. S. Gudovskikh, O. I. Kon'kov, *et al.*, in *Proceedings of Tenth International Symposium on Thin Films in Electronics, Yaroslavl, Russia, 1999* (Inst. Mikroélektr. Ross. Akad. Nauk, Yaroslavl, 1999), p. 150.
8. A. A. Andreev, A. V. Andrianov, B. Ya. Averbukh, *et al.*, Fiz. Tverd. Tela **38** (1), 19 (1996) [Phys. Solid State **38**, 10 (1996)].
9. O. A. Golikova and M. M. Kazanin, Fiz. Tekh. Poluprovodn. **33**, 110 (1999) [Semicond. **33**, 97 (1999)].

Translated by M. Tagirdzhanov

Semiconductors, Vol. 34, No. 4, 2000, pp. 481–487. Translated from Fizika i Tekhnika Poluprovodnikov, Vol. 34, No. 4, 2000, pp. 496–503.

PHYSICS OF SEMICONDUCTOR DEVICES

Lasing in the Vertical Direction in InGaN/GaN/AlGaN Structures with InGaN Quantum Dots

I. L. Krestnikov*, A. V. Sakharov*, W. V. Lundin*, Yu. G. Musikhin*, A. P. Kartashova*, A. S. Usikov*, A. F. Tsatsul'nikov*, N. N. Ledentsov*, Zh. I. Alferov*, I. P. Soshnikov,[1] E. Hahn**, B. Neubauer**, A. Rosenauer**, D. Litvinov**, D. Gerthsen**, A. C. Plaut***, A. A. Hoffmann****, and D. Bimberg******

** Ioffe Physicotechnical Institute, St. Petersburg, 194021 Russia*

*** Laboratorium für Electronenmikroskopie der Universität Karlsruhe, Postfach 6980, D-76128 Karlsruhe, Germany*

**** Exeter University, Stocker Road, Exeter EX44QL, UK*

***** Institut für Festkörperphysik, Technische Universität Berlin, D-10623 Berlin, Germany*

Submitted October 27, 1999; accepted for publication October 28, 1999

Abstract—InGaN/GaN structures with dense arrays of InGaN nanodomains were grown by metallorganic chemical vapor deposition. Lasing in vertical direction occurs at low temperatures, indicating ultrahigh gains ($\sim 10^5$ cm^{-1}) in the active region. Fabrication of an effective AlGaN/GaN distributed Bragg reflector with reflectivity exceeding 90% enables vertical lasing at room temperature in structures with a bottom distributed Bragg reflector, despite the absence of a well-reflecting upper mirror. The lasing wavelength is 401 nm, and the threshold excitation density is 400 kW/cm^2. © *2000 MAIK "Nauka/Interperiodica".*

1. INTRODUCTION

Currently, much attention is given to the fabrication and study of semiconductor lasers based on heterostructures with quantum dots [1, 2]. Semiconductor lasers based on the Group III nitrides (III–N) emitting in the UV spectral region appear to be the most promising for the fabrication of optical devices to be used for data recording and storage. To obtain high-quality structures, the following difficulties are to be surmounted:

(i) the high density of defects [currently, epitaxial lateral overgrowth technique (ELOG [3]) is used, which strongly complicates the technology of laser structure fabrication];

(ii) the absence of the appropriate cleavage planes for creating mirrors in the stripe-geometry lasers grown on the best technologically developed sapphire substrates of (0001) orientation; and

(iii) the high series resistance of thick GaN layers with *p*-type conduction.

In addition, for these devices to become widely used, their cost would have to be substantially reduced, their laser beam characteristics improved, and high device integration should be realized on a single chip. Vertical cavity surface emitting lasers (VCSELs) make it possible to solve many of the above-listed problems. Multilayer distributed Bragg reflectors (DBR) integrated in the laser structure eliminate the problem of cleavage planes. The possibility of preparing VCSELs with very small lateral dimensions makes the requirements to the density of threading dislocations in the structure less stringent.

The basic elements of the VCSELs are high-reflectivity DBRs that make the external optical losses lower than the possible maximum gain, and thus ensuring the conditions for lasing. In structures with quantum wells (QWs), the maximum gain is limited by the effect of gain saturation at a relatively low level, which requires the use of DBRs with very high reflectivity, 99% or higher. It is difficult to obtain such a reflectivity in the GaN/AlGaN system because of the strong GaN and AlN lattice mismatch and the small difference between the refractive indices of these materials. The use of dielectric DBRs as a bottom mirror involves a very complicated lift-off fabrication technique [4].

Thus, moderately reflecting (~90%) mirrors are to be used in fabricating the monolithic GaN-VSCELs, which requires obtaining a mode gain saturation level of no less than 2×10^4 cm^{-1}. The most promising way to achieve high gains is to use dense arrays of quantum dots (QD) as the active region of the device [1]. For example, in the case of an inhomogeneous broadening of ~100 meV and a QD concentration of ~10^{18} cm^{-3}, the mode gain may exceed 10^5 cm^{-1}. Such QD densities are quite attainable for wide-gap semiconductors having a Bohr radius for an exciton of less than 5 nm [5]. The total three-dimensional localization of excitons in QDs eliminates the problem of radiative recombination of nonzero-momentum excitons predominant at high excitation densities [6]. Also eliminated, through the

[1] On leave from the Ioffe Institute.

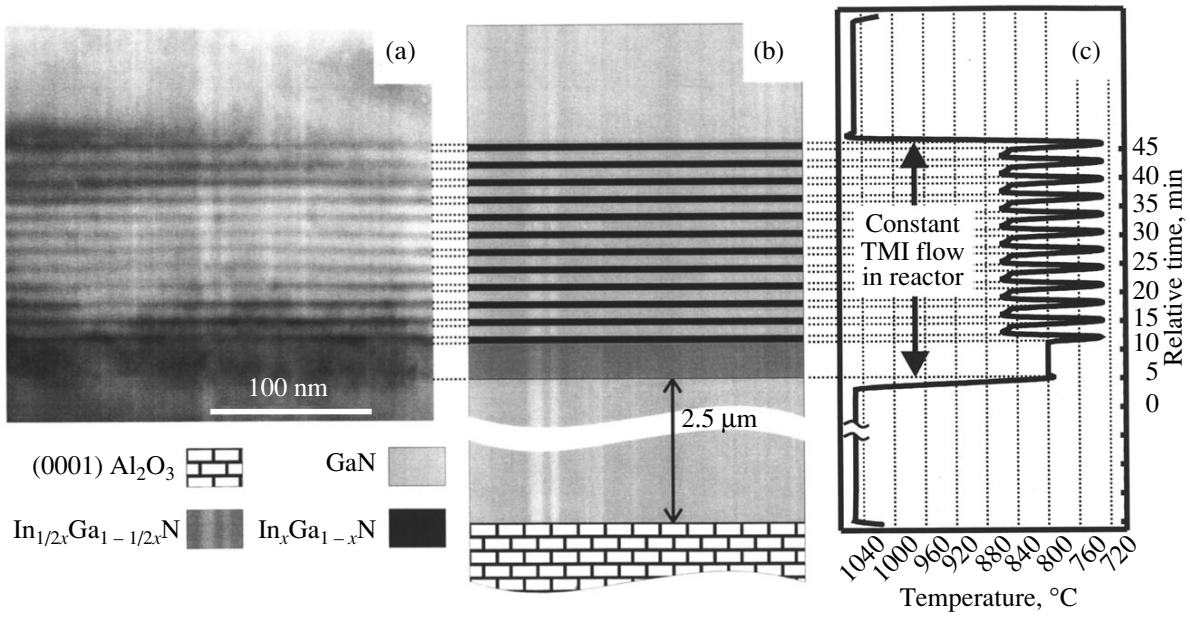

Fig. 1. Cross-sectional TEM image (a), schematic representation (b), and temperature cycling diagram (c) for a structure without DBR.

suppression of transport in the lateral direction, is the problem of nonradiative recombination via defects and dislocations. In the present work, dense QD arrays were obtained by means of the vertical stacking of ultrathin InGaN layers that disintegrate into QDs.

2. EXPERIMENTAL

The structures studied in this work were grown by metalorganic chemical vapor deposition onto (0001) sapphire substrates, using a low-temperature AlGaN nucleation layer. Ammonia, trimethylgallium (TMG), trimethylaluminum (TMA), and trimethylindium (TMI) served as precursors. Hydrogen and argon were used as carrier gases in GaN–AlGaN and InGaN growth, respectively.

Figure 1b schematically shows a sample without a bottom DBR, with an InGaN/GaN active region sandwiched between a 2.5-μm-thick GaN buffer layer and a 0.1-μm-GaN cap layer, both grown at 1050°C. The active region comprised a relaxed 25-nm-thick InGaN sublayer with a low In content (~10%), grown at 800°C, and a 12-period InGaN/GaN structure, grown on this sublayer, and, on the average, lattice-matched with it. The structure was formed by a cyclic variation of the substrate temperature between 730 and 860°C, with all gas flow rates in the reactor maintained constant (see Fig. 1c) [7]. Since incorporation of indium into a growing layer heavily depends on temperature, the temperature cycling at constant flow rates of the source compounds produces a periodical InGaN/GaN heterostructure.

For structures containing DBR, a 1.1-μm-thick $Al_{0.08}Ga_{0.92}N$ layer grown directly on the low-temperature nucleation layer was used as a buffer [8]. The DBR contained 37 pairs of quarter-wave GaN/$Al_{0.15}Ga_{0.85}N$ layers. The average content of aluminum in the DBR corresponded to the buffer layer composition, and the thickness of the quarter-wave layers was substantially smaller than the critical thickness for a mismatch dislocation to be formed in the AlGaN/GaN system [9]. The use of a strain-compensated DBR made it possible to avoid having cracks appear in the case of DBR grown on the GaN buffer layer [10]. An active region similar to that described above was grown on the DBR, except that different growth temperatures were used: 850°C for the InGaN sublayer with low indium content and 780–910°C during temperature cycling. The distance between the DBR (bottom mirror) and the surface of the entire structure (upper mirror) was equal to two wavelengths of light in the crystal.

A Philips EM 420 microscope with 100 kV accelerating voltage was used for transmission electron microscopy (TEM). High resolution TEM (HRTEM) was performed with a Philips CM 200 FEG/ST microscope with a 0.24-nm resolution. The distribution of indium in the structures was studied by means of digital image processing of cross-sectional $[1\bar{1}00]$ images by the DALI program [11].

Photoluminescence spectra were taken at 16–300 K in a closed-cycle helium cryostat. The excitation was effected by an N_2 pulse laser (λ = 337.1 nm) beam focused onto the sample. The excitation density was varied using neutral glass filters. The emitted radiation was detected using an MDR-23 monochromator, a

cooled FEU-83 photomultiplier, and a lock-in amplifier. Optical reflectivity spectra were obtained in normal-incidence geometry using a halogen lamp.

3. RESULTS AND DISCUSSION

3.1. Structural Properties of InGaN Incorporations

As can be seen from Fig. 1a demonstrating a TEM image of a structure without DBR, thermal cycling leads to formation of In-enriched (dark regions) and In-depleted (light regions) layers. The layer thicknesses found from this micrograph are 5 and 6 nm, respectively. These values agree both with the growth-rate calibrations and with X-ray diffraction data, the latter indicating a structure period of 11 nm [12]. Yet, these visualization conditions give no way of evaluating the type of In distribution within a single InGaN layer. To tackle this problem, thin (~20 nm) samples were studied by HRTEM with subsequent digital processing (DALI) of the obtained cross-sectional images. Figure 2 presents the results obtained by treating the cross-sectional images. Black color corresponds to GaN, and the gradations of gray, to InGaN of different compositions (the lighter the shade of gray, the higher the In content). It follows from the structural analysis that InGaN incorporations are dense arrays of nanodomains with increased (up to 60%) In content. The vertical dimension of nanodomains is 2–3 nm; two typical nanodomain dimensions are revealed in the lateral direction: 3–4 and 6–9 nm. The surface density of nanodomains in each layer is $(2–5) \times 10^{11}$ cm^{-2}.

3.2. Lasing in Structures without DBR

The high density of nanodomains, $(2–4) \times 10^{17}$ cm^{-3} with regard for the vertical stacking, makes possible vertical lasing from the structure surface even without DBR at low temperatures ($T < 200$ K). The dependence of photoluminescence (PL) spectra on the excitation density P_{exc} at $T = 150$ K is presented in Fig. 3a. It is clearly seen that the PL spectra are modulated by modes of the Fabry–Perot microcavity formed by the GaN/Al_2O_3 heterointerface and the GaN/air interface. For high excitation densities ($P_{exc} > 600$ kW/cm^2), one of the cavity modes becomes dominant in the PL spectra, with the intensity of this mode increasing superlinearly with excitation density (see Fig. 3b). The single-mode character of the emission and the threshold behavior of the differential efficiency is indicative of the appearance of a feedback in this structure, despite the very low Q-factor of the cavity [13].

A specific feature of the given cavity consists in high external optical losses (α_{ext}), which can be calculated by the following formula:

$$\alpha_{ext} = (1/2L)\ln(1/R_bR_t), \quad (1)$$

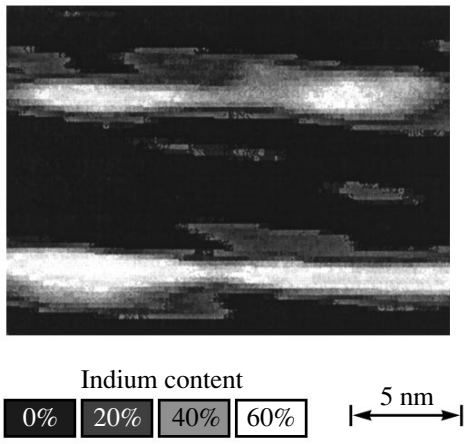

Fig. 2. Mathematically processed (DALI) HRTEM image.

where L is the cavity length, and R_b and R_t are the reflectivities of the bottom and upper mirrors, respectively. The threshold modal gain in the structure (g_{th}) should be equal to the optical losses determined by (1) (note that, here, the internal optical losses are neglected as compared with the very high external losses) divided by the optical confinement factor (Γ). Accordingly, we obtain:

$$g_{th} = \frac{1}{\Gamma}\alpha_{ext} = \frac{1}{2L_{act}}\ln(1/R_bR_t), \quad (2)$$

where L_{act} is the thickness of the active region of the structure. With a knowledge of the refractive indices of Al_2O_3 (1.75), GaN (2.4), and air (1), one can determine the reflectivities of the Al_2O_3/GaN heterointerface, 2.4%, and the GaN/air interface, 17%. Taking into account that the active region thickness is 150 nm, we obtain the mode gain of 2×10^5 cm^{-1}, which is necessary to compensate for the exit losses.

As follows from Fig. 3a, a shift of the microcavity mode to shorter wavelengths occurs with increasing excitation density. The maximum shift is characteristic of modes with higher photon energies, with low-energy modes hardly shifting at all. This effect is described in terms of the Kramers–Kronig formulas relating the real and imaginary parts of the dielectric constant of the material. Since the gain (absorption) spectrum has a sharp feature near the lasing energy, the refractive index modulation occurs in the same spectral region [14]. For the cavity mode to be shifted so significantly (3.2 nm), the refractive index must change by 0.4. However, as follows from [15], such a drastic change of the refractive index agrees with the calculated gain (~10^5 cm^{-1}) necessary for the onset of lasing. In addition, theoretical estimates [16] show that, for small (~4 nm) InGaN nanodomains, the maximum gain and the variation of the refractive index may be ~1.6×10^5 cm^{-1} and (0.2–0.5), respectively. Thus, the theoret-

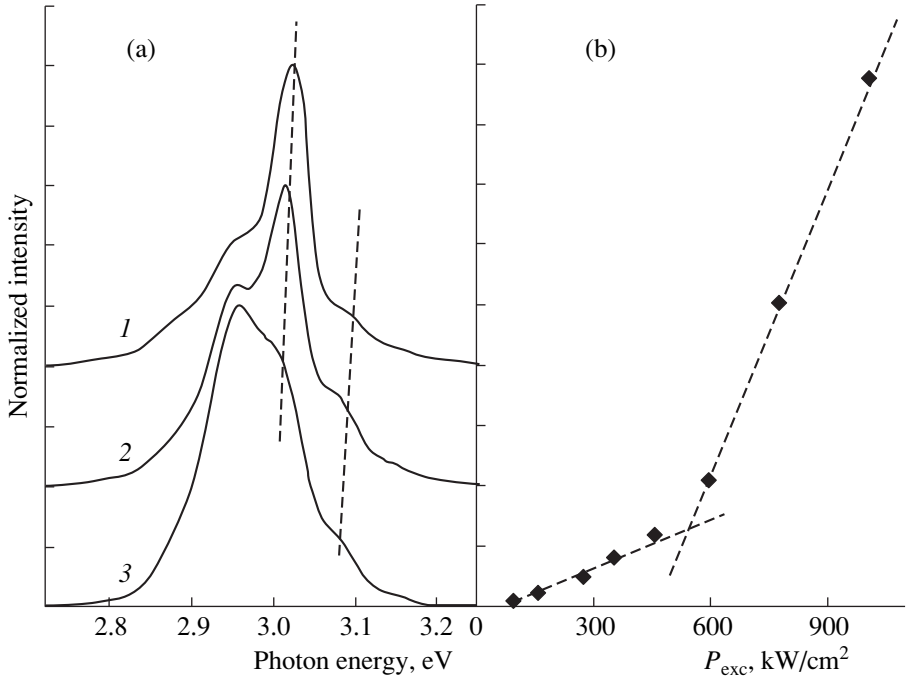

Fig. 3. Photoluminescence spectra of a structure without DBR at different excitation densities (a) and dependence of the lasing mode intensity on excitation density (b). In (a), P_{exc} = (*1*) 1000, (*2*) 590, and (*3*) 160 kW/cm^2. T = 150 K.

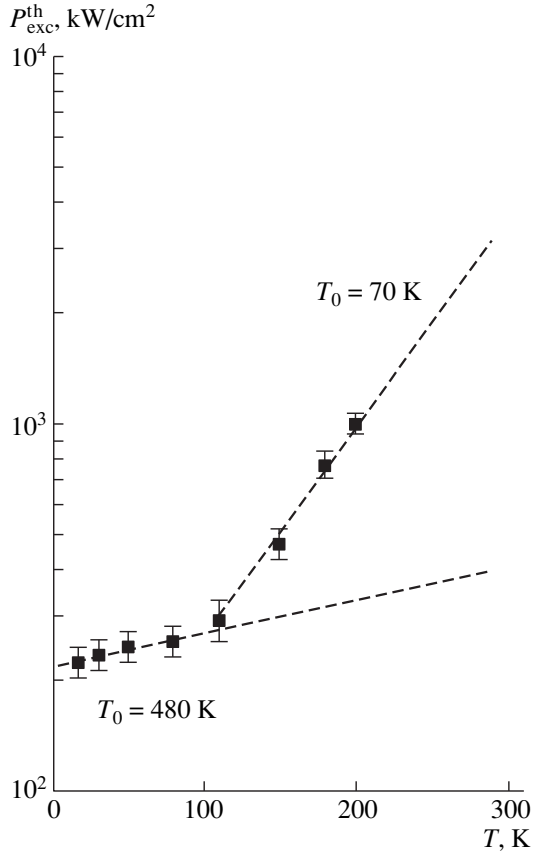

Fig. 4. Temperature dependence of the threshold excitation density for a structure without DBR.

ical assumptions of [15, 16] are well confirmed by the experiment.

The temperature dependence of the threshold excitation density (P^{th}_{exc}) is presented in Fig. 4. In the temperature range T = 16–110 K, the threshold excitation density depends only slightly on temperature, but, at higher temperatures, this dependence becomes very strong. In both regions, the temperature dependence is well approximated by the following empirical relation:

$$P^{th}_{exc} = P_0 \exp\left(\frac{T}{T_0}\right), \quad (3)$$

with T_0 = 480 K in the low-temperature region and T_0 = 70 K in the high-temperature one. The high values of T_0 at low temperatures are associated with lasing via the QD states, with the abrupt decrease of this parameter due to the thermal emission of carriers from the QDs [17].

3.3. Influence of Bottom DBR on Lasing

In spite of the very high gain achieved at low temperatures in structures without DBR, the threshold excitation density grows sharply with increasing temperature. To minimize this effect, it seems of interest to use a DBR with a narrow spectral region of high reflectivity, which coincides with the region of emission from QDs having the maximum energy of exciton localization. Figure 5 presents optical reflectivity spectra of a structure grown in the form of an AlGaN/GaN DBR. No special effort was made to reduce the nonuniformity

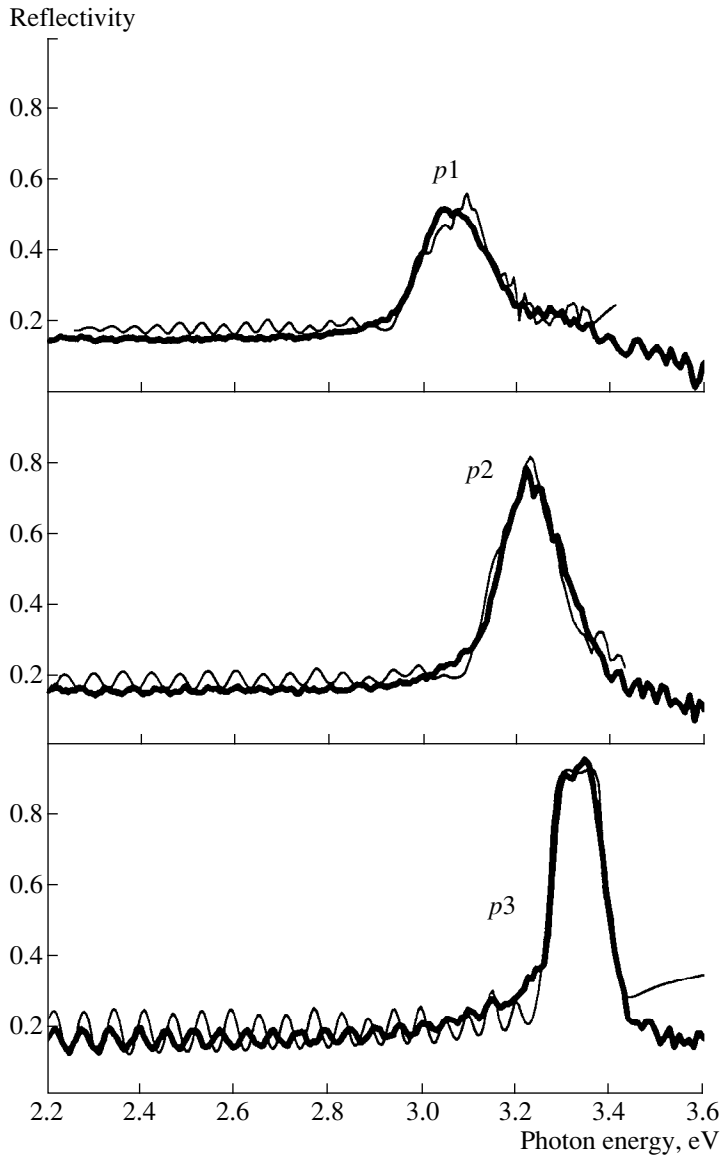

Fig. 5. Experimental spectra of optical reflectance from AlGaN/GaN DBR, obtained at different points of the substrate $p1$–$p3$ (bold lines), and their numerical fits (fine lines).

of layer thickness during growth, which led to a dependence of the reflectivity peak position on the coordinate. In addition, the peak reflectivity value increases as the peak wavelength becomes shorter (Fig. 5). This is due to a noticeable dispersion of the GaN refractive index near the interband absorption edge [18], and the difference between the GaN and AlGaN refractive indices near this edge greatly exceeds that far from the edge. By fitting the calculated reflectivity spectra (the fine line in Fig. 5) to the experimental data, the thickness of the quarter-wave AlGaN and GaN layers was determined: (39 ± 1.5) and (43 ± 1.5) nm for point $p1$; (36.5 ± 1.0) and (40.5 ± 1.0) nm for point $p2$; and (34.5 ± 0.5) and (38.5 ± 0.5) nm for point $p3$, respectively. These values agree with growth calibration data and results of X-ray diffraction analysis [19].

Fabrication of an efficient DBR (with maximum reflectivity > 90%) made possible vertical lasing at room temperature. Similar results were obtained in [20] using an upper dielectric mirror. In our case, with QDs used as an active medium, there is no need to form a high-Q cavity, which simplifies the technology and allows the GaN/air interface to act as an upper mirror. The dependence of PL spectra on the excitation density at room temperature is presented in Fig. 6. It can be seen that, with an increasing excitation density, the PL line becomes narrower and a threshold-like rise in differential efficiency is observed. Both these facts are indicative of the appearance of a stimulated vertical emission, with a threshold excitation density of 400 kW/cm^2.

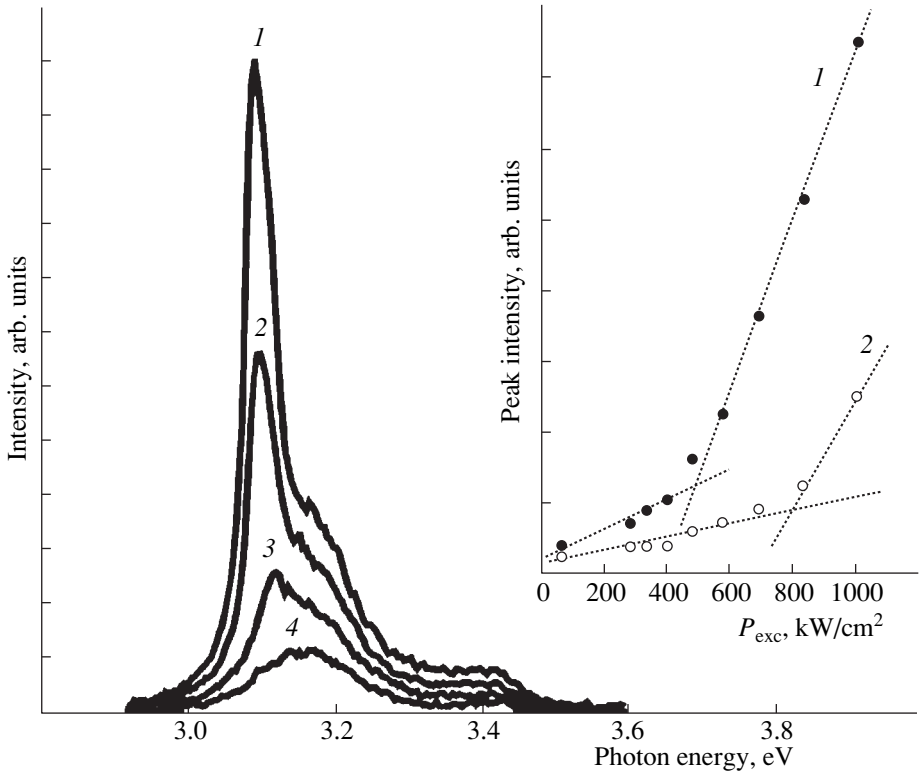

Fig. 6. PL spectra of structures with DBR at room temperature and P_{exc} = (*1*) 1000, (*2*) 700, (*3*) 480, and (*4*) 63 kW/cm^2. Inset: dependence of the intensity of the PL lasing mode on excitation density is shown for the cases of (*1*) DBR matched with the active region and (*2*) no matching.

As mentioned above, the layer thickness gradient gives rise to a dependence of the spectral position of the reflectivity peak on the coordinate. At the same time, the wavelength of the emission from the InGaN/GaN active region is practically constant over the entire structure area. This allowed us to study the influence of the DBR reflectivity on the threshold excitation density. The inset in Fig. 6 presents the PL intensity as a function of excitation density for two different points. In the first case (point *1*), the emission wavelength of the InGaN/GaN active region coincides with the peak DBR reflectivity wavelength, while, in the second case (point *2*), it does not. This inconsistency leads to a substantial increase in the threshold excitation density (from 400 to 700 kW/cm^2) and to a twofold decrease of the differential efficiency. These facts point to the important role of an efficient DBR in lowering the lasing threshold [21].

In some cases, it seems important to distinguish the lasing and the stimulated emission. The stimulated emission can also exhibit a threshold dependence on the excitation density, followed by a narrowing of the luminescence spectrum. The stimulated emission and the lasing have a common origin, determined by the existence of a gain in the system. However, the role of the cavity is fundamentally different in these two cases. Laser emission has a narrow far-field distribution and, accordingly, a selected direction associated with the existence of a feedback in the system. At the same time, the far fields of stimulated and spontaneous emissions from the surface have similar angular dependences, since light propagating at any angle with the surface is amplified. In our case, the PL spectra in Figs. 6 and 7a were recorded using a short-focus lens with a collecting aperture amounting to 60°. In this geometry, all kinds of emission-spontaneous, stimulated, and lasing emissions—enter the detecting system. Figure 7a shows both the narrow line of stimulated emission and the broad spectrum of spontaneous emission. Of importance is the fact that, when the collecting angle is narrowed to 10°, the PL spectra change substantially (Fig. 7b): the relative intensity of the broad band of spontaneous emission decreases sharply, with the intensity of the narrow line remaining practically unchanged (Fig. 7b, solid line). However, even a small tilt of the sample, with the normal to the sample surface making an angle of 15° with the optical axis of the detection system, makes the narrow PL line disappear completely (Fig. 7b, dashed line). At the same time, the intensity of spontaneous emission remains unchanged [22]. It follows from these results that the narrow PL line, which demonstrates a superlinear increase in intensity with increasing excitation density (see insert in Fig. 6), corresponds to vertical lasing from the sam-

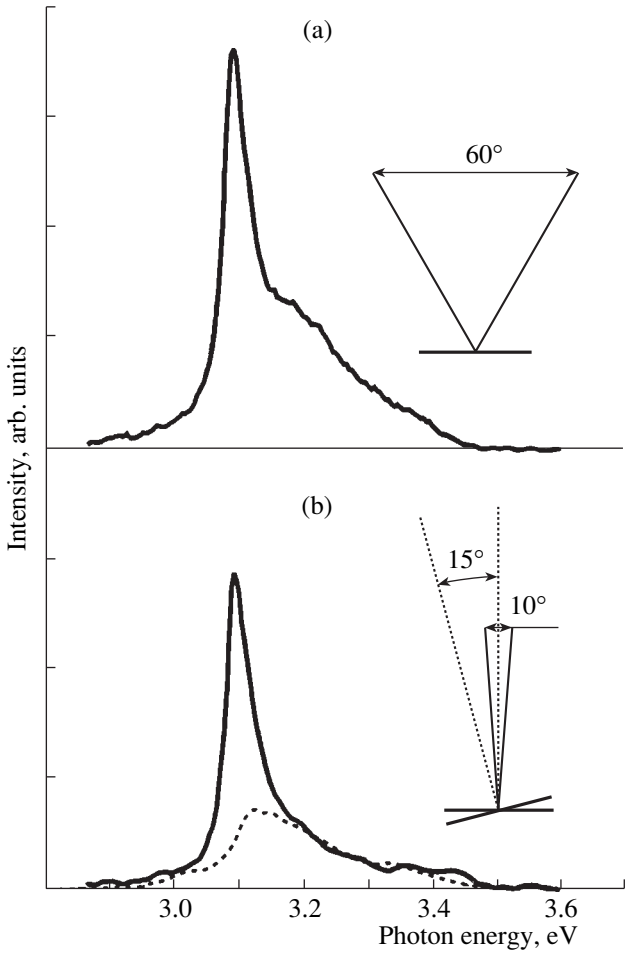

Fig. 7. PL spectra of structures with DBR at room temperature and P_{exc} = 1000 kW/cm^2. Detection system collecting angle 60° (a) or 10° (b). The solid line corresponds to normal-incidence geometry (the normal of the sample is parallel to the detection system axis), and the dashed line corresponds to a 15° tilt of the normal from the axis.

ple surface, since it has a narrower far-field distribution compared with a wide far-field distribution of the spontaneous or stimulated emission.

4. CONCLUSIONS

(I) Ultrathin InGaN incorporations in GaN disintegrate to give arrays of nanoislands with typical dimensions of 2–3 nm in the vertical direction and 3–4 and 6–9 nm in the lateral direction, with a surface density of $(2–5) \times 10^{11}$ cm^{-2}.

(II) The ultrahigh modal gain (~10^5 cm^{-1}) in the structures with InGaN QDs makes possible lasing in vertical direction at low temperatures (<200 K), even in structures without DBR.

(III) Fabrication of an effective AlGaN/GaN DBR and growth of the active region based on InGaN QDs produce a vertically emitting laser operating at room temperature.

ACKNOWLEDGMENTS

We are grateful to N.N. Faleev and M.V. Baĭdakova for the X-ray diffraction studies of the samples.

The work was supported by the Russian Foundation for Basic Research, NATO SfP (grant no. 972614), and NanoOp.

REFERENCES

1. D. Bimberg, M. Grundmann, and N. N. Ledentsov, *Quantum Dot Heterostructures* (Wiley, Chichester, 1999), p. 328.
2. K. Tachibana, T. Someya, Y. Arakawa, *et al.*, Appl. Phys. Lett. **75**, 2605 (1999).
3. A. Usui, H. Sunakawa, A. Sakai, *et al.*, Jpn. J. Appl. Phys., Part 2 **36**, L899 (1997).
4. Y.-K. Song, H. Zhou, M. Diagne, *et al.*, Appl. Phys. Lett. **74**, 3441 (1999).
5. I. L. Krestnikov, M. Strassburg, M. Caesar, *et al.*, Phys. Rev. B: Condens. Matter **60**, 8695 (1999).
6. N. N. Ledentsov, I. L. Krestnikov, M. V. Maximov, *et al.*, Appl. Phys. Lett. **69**, 1343 (1996).
7. A. S. Usikov, W. V. Lundin, A. V. Sakharov, *et al.*, *Proc. EW MOVPE VIII* (Prague, 1999), p. 57.
8. A. V. Sakharov, W. V. Lundin, A. S. Usikov, *et al.*, MRS Internet J. Nitride Semicond. Res. **3**, 28.
9. I. Akasaki and H. Amano, Jpn. J. Appl. Phys. **36**, 5393 (1997).
10. T. Someya and Y. Arakawa, Appl. Phys. Lett. **73**, 3653 (1998).
11. A. Rosenauer, S. Kaiser, T. Reisinger, *et al.*, Optik (Stuttgart) **102**, 63 (1996).
12. A. V. Sakharov, W. V. Lundin, I. L. Krestnikov, *et al.*, Phys. Status Solidi B **216** (1999).
13. A. V. Sakharov, W. V. Lundin, I. L. Krestnikov, *et al.*, Appl. Phys. Lett. **74**, 3921 (1999).
14. I. L. Krestnikov, S. V. Ivanov, P. S. Kop'ev, *et al.*, J. Electron. Mater. **27**, 72 (1998).
15. N. N. Ledentsov, D. Bimberg, V. M. Ustinov, *et al.*, Semicond. Sci. Technol. **13**, 99 (1999).
16. F. Jain and W. Huang, J. Appl. Phys. **85**, 2706 (1999).
17. N. Kirstaedter, N. N. Ledentsov, M. Grundmann, *et al.*, Electron. Lett. **30**, 1416 (1994).
18. H. Amano, N. Watanabe, N. Koide, *et al.*, Jpn. J. Appl. Phys., Part 2 **32**, L1000 (1993).
19. W. V. Lundin, A. S. Usikov, I. L. Krestnikov, *et al.*, *Proc. EW MOVPE VIII* (Prague, 1999), p. 49.
20. T. Someya, Y. Arakawa, R. Werner, *et al.*, Phys. Status Solidi B **216** (1999).
21. I. L. Krestnikov, W. V. Lundin, A. V. Sakharov, *et al.*, Appl. Phys. Lett. **75**, 1192 (1999).
22. I. L. Krestnikov, W. V. Lundin, A. V. Sakharov, *et al.*, Phys. Status Solidi B **216** (1999)

Translated by D. Mashovets

Semiconductors, Vol. 34, No. 4, 2000, pp. 488–492. Translated from Fizika i Tekhnika Poluprovodnikov, Vol. 34, No. 4, 2000, pp. 504–508.

PHYSICS OF SEMICONDUCTOR DEVICES

Spectral Characteristics of Lasers Based on InGaAsSb/InAsSbP Double Heterostructures (λ = 3.0–3.6 μm)

M. Aĭdaraliev*, N. V. Zotova*, S. A. Karandashev*, B. A. Matveev*, M. A. Remennyĭ*, N. M. Stus'*, G. N. Talalakin*, T. Beyer, and R. Brunner****

** Ioffe Physicotechnical Institute, Russian Academy of Sciences, Politekhnicheskaya ul. 26, St. Petersburg, 194021 Russia*

*** Fraunhofer Institute of Physical Measurement Techniques, Freiburg, 79110 Germany*

Submitted November 9, 1999; accepted for publication November 17, 1999

Abstract—It is shown that an increase in the internal losses beyond the lasing threshold in the lasers based on InGaAsSb/InAsSbP double heterostructures (wavelength range λ = 3.0–3.6 μm, temperature T = 77 K) causes the current-related shift of the laser mode to shorter wavelengths. This shift is as large as 80 cm^{-1}/A and can explain the broadening of the laser line from 5 to 7 MGz as the pump current increases. © *2000 MAIK "Nauka/Interperiodica".*

1. INTRODUCTION

Infrared injection lasers find applications in spectroscopy, atmospheric pollution monitoring, and fibre-optics communication. The strongest absorption bands of methane CH_4, formaldehyde H_2CO, and other hydrocarbons fall within the wavelength range λ = 3–4 μm. This determines the prospects of the application of the lasers emitting in this range as the tunable sources of radiation for diode-laser spectroscopy and gas analysis.

More than 30 years have passed from the fabrication of the first semiconductor diode lasers emitting near λ = 3 μm [1]. The lasers on the basis of lead salts (IV–VI compounds) emitting in the wavelength region λ > 3 μm operate in a pulsed mode up to a temperature T = 290 K [2] and in continuous wave mode, up to T = 223 K [3]. However, such lasers have low power due to the low thermal conductivity of IV–VI solid solutions and their tendency to degrade. For narrow-gap II–VI semiconductors, such as HgCdTe, the diode lasers emitting at λ = 2.86 μm up to 90 K were reported. The materials on the basis of III–V solid solutions possess a high thermal conductivity and structural perfection. Because of this, the development of III–V semiconductor lasers seems to be the most promising. More attention is focused on the studies of low-dimensional (lasers on the basis of superlattices and quantum dots), quantum cascade, vertical (VCSEL) lasers, and others. However, the traditional lasers based on double heterostructures [4–7] are still the objects of intense interest.

In this paper, the spectral characteristics of the lasers based on InGaAsSb/InAsSbP double heterostructures and emitting in the range λ = 3–4 μm are considered. It was shown previously [8, 9] that the main mechanism of the internal losses in these lasers was an intraband absorption by holes with their transition to the spin–orbit split-off band. The intraband-absorption factor $k_0 \approx 5.6 \times 10^{-16}$ cm^2 is more than an order of magnitude higher than that of InGaAsP (λ = 1.55 μm), since the bandgap and the energy of spin–orbit splitting are close in solid solutions based on InAs. This work is a continuation of the above studies and shows that the current tuning of the lasing wavelength and broadening of the laser line with pumping current can be explained by the increase in the internal losses beyond the lasing threshold due to the intraband absorption.

2. EXPERIMENTAL

The double heterostructures were grown by liquid epitaxy. They consisted of an undoped n-InAs(111)A substrate with an electron concentration $n = (1–2) \times 10^{16}$ cm^{-3} and three epitaxial layers. The latter included a wide-gap n-$InAs_{1-x-y}Sb_xP_y$ ($0.05 \le x \le 0.09$, $0.09 \le y \le 0.18$) confining layer adjacent to the substrate, n-$In_{1-v}Ga_vAs_{1-w}Sb_w$ ($v \le 0.07$, $w \le 0.07$) active laser layer, and a wide-gap p(Zn)-$InAs_{1-x-y}Sb_xP_y$ ($0.05 \le x \le 0.09$, $0.09 \le y \le 0.18$) contact layer of an emitter. The thicknesses of the wide-gap layers were 4–6 μm, while an active layer was 1–4 μm thick. The lasers were similar to those described in [10] and had a deep mesa-stripe design with the stripe width w = 20 μm and resonator length L = 100–300 μm.

The measurements were performed in the continuous-wave mode at a temperature T = 80 K. The electroluminescence spectra were recorded with a spectral resolution no worse than 0.75 cm^{-1}. The laser linewidth was measured with a heterodyne detection technique [11].

3. EXPERIMENTAL RESULTS AND DISCUSSION

3.1. Emission Spectra

A single-mode operation is retained, as a rule, at currents which exceed the threshold current I_{th} by no

more than $\Delta I \approx (2–3)I_{th} \approx 30–100$ mA; in this case, the ratio of the power of a dominant mode to the total radiation power was as large as ~96%. At larger currents, the multimode spectra are usually observed regardless of I_{th} with a spacing between the longitudinal modes $\Delta\lambda = 20–90$ Å according to $\Delta\lambda = \lambda^2/2\bar{n}L$ ($\bar{n}$ is the refractive index of the active region). A decrease in the resonator length causes only one resonance frequency to be available in the amplification loop due to an increase in $\Delta\lambda$. A simultaneous reduction in the *p–n* junction area increases the probability of obtaining the homogeneous active region. Because of this, the single-mode lasing in the current range $\Delta I \approx 100$ mA and the monotonic current dependence of the output power without kinks are more often attainable for lasers with $L < 200$ μm. For $L < 75$ μm, an increase in the internal losses because of an increase in the threshold concentration [8] rendered the lasing impossible.

The evolution of the emission spectra of a laser with a resonator length $L = 275$ μm from the spontaneous emission to the lasing mode at $2I_{th}$ is shown in Fig. 1. The spontaneous emission is modulated by the condition for the longitudinal resonance. The ratio of the intensities of spontaneous and laser emission reaches 1% at $I = 2I_{th}$. An increase in the intensity of spontaneous emission beyond the lasing threshold is readily seen. This attests that an increase in the intensity of laser emission with current is accompanied by an increase in absorption and, correspondingly, in the carrier concentration in the active region, which is necessary for the fulfillment of the threshold condition for the gain and internal losses equality.

3.2. Current Tuning

The current tuning of the wavelength of the longitudinal modes of the Fabry–Perot resonator is known to occur due to the variation of the refractive index in an active region according to $\lambda = 2\bar{n}L/q$ (q is an integer). The variation of the refractive index of an active region $\bar{n}$ with the current I is defined by the effect of the injected carriers N and temperature T and described by the formula

$$\frac{d\bar{n}}{dI} = \frac{\partial\bar{n}}{\partial N}\frac{\partial N}{\partial I} + \frac{\partial\bar{n}}{\partial T}\frac{\partial T}{\partial I}. \quad (1)$$

The current dependences of the intensity of a spontaneous emission P_{sp} and of the wave number $\bar{\nu}$ of the longitudinal mode of resonator, at which the lasing occurs, are compared in Fig. 2. The dependence $P_{sp}(I)$ similar to that characterizing the current tuning of the wavelength (wave number) has a kink near the lasing threshold $I = I_{th}$. In addition, the rate of current tuning of the resonator mode tends to diminish with a decrease in a $P_{sp}(I)$ slope. The increase in the intensity of a spontaneous emission beyond the threshold can be associated with the increase in the concentration of minority carriers [12]:

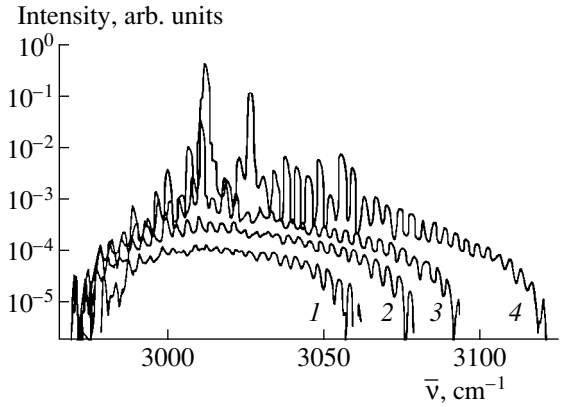

Fig. 1. Emission spectra at the currents below and beyond the lasing threshold $I_{th} = 83$ mA. The magnitudes of the current I are (*1*) 0.074 mA, (*2*) 0.077 mA, (*3*) 0.09 A, and (*4*) 0.15 A.

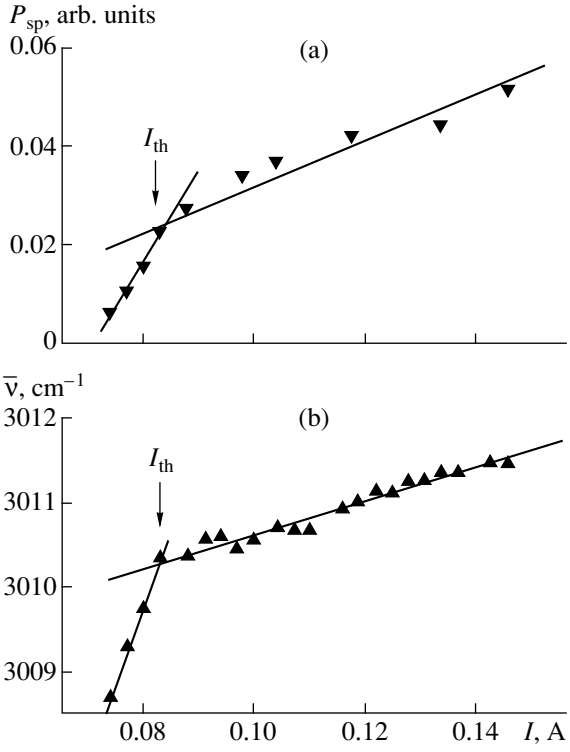

Fig. 2. Current dependences of the spontaneous-emission intensity (a) and of the mode shift of the Fabry-Perot resonator (b).

$$\frac{dP_{sp}}{dI} = 2\frac{P_{sp}(I_{th})}{N_{th}}\frac{dN}{dI}, \quad (2)$$

where $P_{sp}(I_{th})$ is the intensity of a spontaneous emission at a lasing threshold, and $N_{th} = 2 \times 10^{17}$ cm^{-3} [8] is the threshold concentration. Using the data of Fig. 2a, we

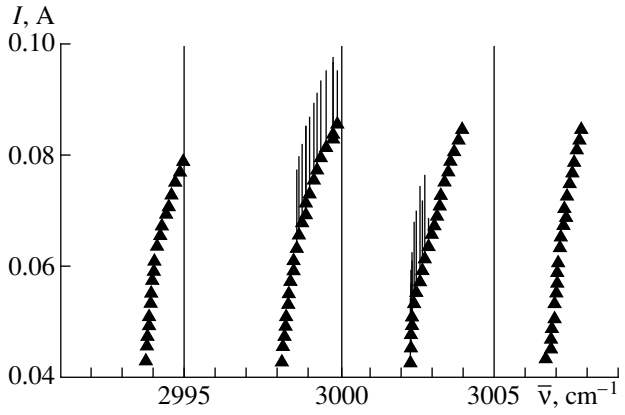

Fig. 3. Modes of the laser emission. The rate of current tuning is $d\bar{\nu}/dI \approx 60$ cm^{-1}/A. Vertical lines are the intensities of the laser mode.

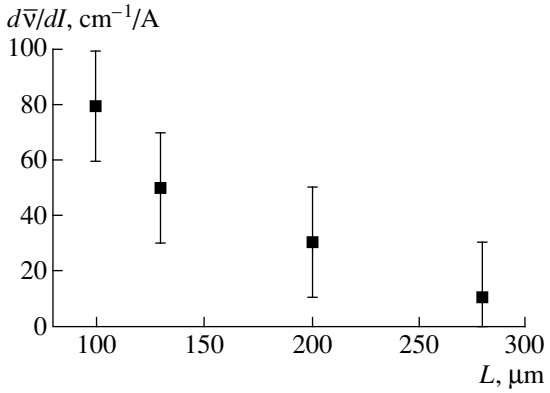

Fig. 4. Dependence of the rate of current tuning on the resonator length for the lasers fabricated from the same epitaxial wafer.

obtain $dN/dI \approx 3 \times 10^{17}$ cm^{-3}/A. The variation of the refractive index of the narrow-gap semiconductors with a carrier injection is mainly due to the saturation of the fundamental absorption. The contribution of the latter can be reduced to the form [13]

$$\frac{\partial \bar{n}}{\partial N} \approx -3 \times 10^{-17} T^{-1} (h\nu)^{-2} J(h\nu). \qquad (3)$$

Here, $J(h\nu)$ is a dimensionless function of the photon energy $h\nu$, which is equal to unity at the expected absorption edge and decreases approximately fivefold at a distance of about kT from it. The effect of free carriers on the refractive index with a consideration of the saturation of the fundamental absorption, band-gap narrowing, and effect of plasma transitions for indium arsenide was studied in [14]. The estimations based on (2) and (3) yield $\partial \bar{n}/\partial N \sim -(10^{-18}$–$10^{-19})$ cm^3 and the magnitude of the first term in (1) $(\partial \bar{n}/\partial N)(\partial N/\partial I) \sim 1$ A^{-1}.

The Auger recombination and intraband absorption increase the temperature of the active region, which has an opposite effect on the refractive index; i.e.,

$$\frac{\partial \bar{n}}{\partial T} \approx 4 \times 10^{-4} - 3 \times 10^{-3} \text{ K}^{-1}. \qquad (4)$$

The estimates of the heating up of the active region made in [16] ($\partial T/\partial I \approx 10^2$ K A^{-1}) allow us to conclude that the contribution of the temperature term in (1) is insignificant, being no more than 10^{-1} A^{-1}. The conclusion on the predominant influence of the change in the concentration of the injected carriers on the refractive index was also confirmed by the current tuning in such lasers in [17]. Thus, the evaluations of the effect of the injected carriers on the refractive index yield the value of the current tuning $d\bar{\nu}/dI$, which comprises hundreds of cm^{-1}/A and agrees with the experimental values by an order of magnitude (see Fig. 3).

We relate the increase in the concentration of the minority carriers beyond the lasing threshold to the intraband transitions in the valence band. The intraband absorption and the amount of the current tuning would thus be expected to decrease with the reduction of the band gap of material in the active region and corresponding violation of the resonance between the energies of the band gap and spin–orbit splitting. It seems likely that for this reason the smallest mean magnitude of the current tuning is observed in lasers on the basis of InAsSb/InAsSbP double heterostructures ($\lambda = 3.6$ μm).

As the resonator length decreases, the threshold concentration of the minority carriers and accordingly the intraband absorption increase. As a consequence, in lasers with a short resonator ($L < 150$ μm), the rate of current tuning is observed to increase as compared to lasers having $L = 300$ μm (see Fig. 4). The dependences of the rate of current tuning on the relationship between the energies of the band gap and spin–orbit splitting and on the threshold concentration of carriers support the assumption that the increase in the minority-carrier concentration beyond the lasing threshold and, by this means, the current tuning of the laser mode are associated with the intraband transitions in the valence band.

The effect of gain on the current tuning must be taken into account in addition to the nonlinearities described above. In the lasing mode, the condition for the equality of the gain and total losses $g = \alpha_i + \alpha_r$ should be met, where α_i are the total losses, $\alpha_r = L^{-1}\ln(1/R)$, and R is the reflectivity. As a consequence, an increase in the internal losses beyond the lasing threshold results in the current dependence of the extinction coefficient $\bar{k}$ (an imaginary part of the complex refractive index $\bar{N} = \bar{n} - i\bar{k}$); thus,

$$-g = 4\pi\bar{k}/\lambda_0,$$

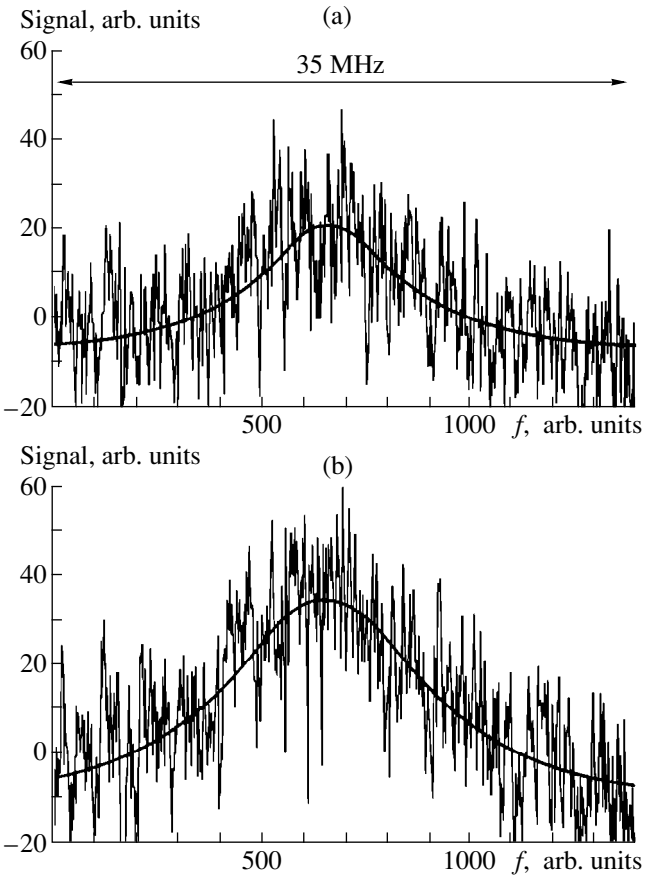

Fig. 5. Frequency dependence of the laser line on the screen of spectrum analyzer for (a) I = 58 mA, $\Delta f \approx 5.1$ MHz and (b) I = 130 mA, $\Delta f \approx 7.5$ MHz.

where λ_0 is the wavelength in a free space. It was shown in [8] that, in the lasers studied, dg/dI is about 1.5×10^3 cm^{-1}/A beyond the lasing threshold. This results in the current dependence of the extinction coefficient $d\bar{k}/dI \sim 0.01$ A^{-1} and appears to be much less significant than the contribution described by (1). Therefore, the effect of gain on the current tuning can be neglected.

3.3. Linewidth of Laser Emission

It is well known that the laser linewidth is inversely proportional to the emission power and, being caused by the fluctuations of the phase and intensity of a spontaneous emission, is defined by [18]

$$\Delta f = \frac{v_g^2 h\nu g n_{sp} \alpha_i (1+\alpha^2)}{8\pi P}, \quad \alpha = \frac{\Delta \bar{n}}{\Delta \bar{k}}. \qquad (5)$$

Substituting $v_g = c/\bar{n}$, $\bar{n} = 3.52$, $\alpha_i = 40$ cm^{-1}, $g = 80$ cm^{-1}, $h\nu = 0.33$ eV, spontaneous-emission factor $n_{sp} = 1$, and the emission power $P = 1$ mW in (5), we obtain $\Delta f/(1+\alpha^2) \approx 7$ MGz.

In Fig. 5, the spectrograms obtained on the screen of a spectrum analyzer for currents I = (a) 58 and (b) 130 mA, which correspond to the FWHM of the laser line $\Delta f \approx 5.1$ and 7.5 MGz, are shown.

The internal losses can be expressed in the form $\alpha_i = \alpha_0 + k_0 N$, where α_0 are the internal losses in the absence of injection, $k_0 \approx 5.6 \times 10^{-16}$ cm^2 is the intraband-absorption factor, and N is the carrier concentration [8]. An increase in the current from 58 to 130 mA is accompanied by an increase in α_i from 40 to 100 cm^{-1}. On the other hand, the power of the laser mode obtained by integrating the frequency-distribution curve of the laser line increases approximately twofold in this case. The narrowing of the laser line with an increase in power is not observed experimentally. This is presumably due to the increase in Δf, caused by the rise in α_i. The line shape is approximated well by a Gaussian function. The transition from the Lorentzian to Gaussian shape can be caused by the fluctuations of a pumping current [19]. The parameter α is generally taken to be equal to 4.6–6.2 [18]; thus, a small experimental value of Δf is still unexplained. This issue will be studied in a separate paper.

4. CONCLUSION

It was shown that, in the lasers based on InGaAsSb/InAsSbP double heterostructures (λ = 3.0–3.6 μm), the intraband absorption by holes in the valence band caused the increase in the internal losses beyond the laser threshold and was accompanied by the current tuning of the laser line to shorter wavelengths and its broadening. An increase in the rate of current tuning approaching $d\bar{\nu}/dI \approx 80$ cm^{-1}/A and in the spectral range of single-mode lasing up to ΔI = 100 mA with the decrease in the resonator length to 100 μm were observed. The laser characteristics obtained show that the lasers based on InGaAsSb/InAsSbP double heterostructures are promising for use in diode-laser spectroscopy.

ACKNOWLEDGMENTS

The part of the work performed at the Ioffe Physicotechnical Institute was supported by the Ministry for Science and Technology of the Russian Federation within the framework of the Program “Optics. Laser Physics” (project no. 4.14) and the European Office of Aerospace Research and Development, Air Force Office of Scientific Research, Air Force Lab under SPC-994016 Contract No. F61775-99-WE016.

REFERENCES

1. I. Melngailis and R. H. Rediker, J. Appl. Phys. **37** (2), 899 (1966).
2. Z. Shi, M. Tacke, A. Lambrecht, *et al.*, Appl. Phys. Lett. **66**, 2537 (1995).

3. Z. Feit, M. McDonald, R. J. Woods, *et al.*, Appl. Phys. Lett. **68**, 738 (1996).
4. M. Aydaraliev, N. V. Zotova, S. A. Karandashev, *et al.*, Semicond. Sci. Technol. **8**, 1575 (1993).
5. H. K. Choi, G. W. Turner, and Z. L. Liau, Appl. Phys. Lett. **65** (18), 2251 (1994).
6. A. Rybaltowski, Y. Xiao, D. Wu, *et al.*, Appl. Phys. Lett. **71** (17), 2430 (1997).
7. A. N. Baranov, A. N. Imenkov, V. V. Sherstnev, *et al.*, Appl. Phys. Lett. **64** (19), 2480 (1994).
8. M. Aĭdaraliev, N. V. Zotova, S. A. Karandashev, *et al.*, Fiz. Tekh. Poluprovodn. (St. Petersburg) **33** (6), 759 (1999) [Semicond. **33**, 700 (1999)].
9. N. A. Gun'ko, G. G. Zegrya, N. V. Zotova, *et al.*, Fiz. Tekh. Poluprovodn. (St. Petersburg) **31** (11), 1396 (1997) [Semicond. **31**, 1204 (1997)].
10. M. Aĭdaraliev, N. V. Zotova, S. A. Karandashev, *et al.*, Fiz. Tekh. Poluprovodn. (St. Petersburg) **33** (2), 233 (1999) [Semicond. **33**, 200 (1999)].
11. T. Okoshi, K. Kikuchi, and A. Nakayama, Electron. Lett. **16** (16), 630 (1980).
12. I. Joindot and J. L. Beylat, Electron. Lett. **29** (7), 604 (1993).
13. P. G. Eliseev and A. P. Bogatov, Tr. Fiz. Inst. im. P. N. Lebedeva, Akad. Nauk SSSR (Ross. Akad. Nauk) **166**, 15 (1986).
14. P. P. Paskov, Solid State Commun. **82** (9), 739 (1992).
15. N. C. Gasey, Jr. and M. B. Panise, *Heterostructure Lasers* (Academic, New York, 1978, Part A; Mir, Moscow, 1981), Vol. 1.
16. M. Aĭdaraliev, N. V. Zotova, S. A. Karandashev, *et al.*, Pis'ma Zh. Tekh. Fiz. (St. Petersburg) **24** (12), 40 (1998) [Tech. Phys. Lett. **24**, 472 (1998)].
17. T. N. Danilova, A. P. Danilova, A. N. Imenkov, *et al.*, Fiz. Tekh. Poluprovodn. (St. Petersburg) **33** (2), 243 (1999) [Semicond. **33**, 210 (1999)].
18. C. H. Henry, IEEE J. Quantum Electron. **18** (2), 259 (1982).
19. W. H. Burkett, B. Lu, and M. Xiao, IEEE J. Quantum Electron. **33** (11), 2111 (1997).

Translated by Yu. Aleshchenko

Semiconductors, Vol. 34, No. 4, 2000, pp. 493–494. Translated from Fizika i Tekhnika Poluprovodnikov, Vol. 34, No. 4, 2000, pp. 509–510.

IN MEMORIAM

Aleksandr Aleksandrovich Rogachev

Aleksandr Aleksandrovich Rogachev, a distinguished physicist, Doctor of Physics and Mathematics, Professor, recipient of the Lenin and State Prizes of the USSR, the head of a laboratory at the Ioffe Physicotechnical Institute of the Russian Academy of Sciences, passed away on October 23, 1999.

A. A. Rogachev, widely renowned for his profound knowledge and scientific intuition and daring, contributed significantly to the physics of semiconductors by enriching it with a wealth of discoveries and fruitful ideas in the areas of many-electron systems, optoelectronics, and semiconductor technology.

A. A. Rogachev was born on December 18, 1937, in Leningrad. He lived through all the hard 1941–1944 years in the besieged city. From 1955 to 1960, he studied at the Physical faculty of the Leningrad State University. For forty years, from 1960 to his untimely death, he worked at the Ioffe Physicotechnical Institute of the Academy of Sciences of the USSR (from 1992 onwards, the Russian Academy of Sciences), in succession, as a senior technician, a postgraduate student, a junior researcher, a senior researcher, and as the head of a department; from 1974, he headed the Laboratory of Electronic Semiconductors. In 1967, the Scientific Council of the Ioffe Institute awarded A.A. Rogachev a degree of Doctor of Science in Physics and Mathematics for the work he submitted as his Candidate dissertation. From 1973 onwards, he was a full professor at the optoelectronics chair of the Leningrad Electrotechnical Institute.

The scope of his scientific interests was extremely broad, and the results achieved in his studies span diverse branches of the physics of semiconductors. Semiconductor lasers, infrared lasers based on type-II heterojunctions, exciton condensation and the electron–hole liquid, many-exciton complexes, many-electron phenomena at the insulator-metal transition, Auger transistors—these are the areas covered by research at the Ioffe Institute that were enriched by his personal achievements. Among A.A. Rogachev's most brilliant scientific contributions were the observation of exciton condensation in electron–hole liquid drops in germanium, which was made in 1964, and the discovery of stimulated emission in gallium arsenide, a work for which he, together with several colleagues, was awarded the Lenin Prize. Aleksandr Rogachev was the youngest scientist honored with this prize during the history of its existence. In 1986, he was the first to devise, together with a group of co-workers, an efficient infrared laser based on a type-II heterojunction. In 1988, he was one of a group of physicists who received the USSR State Prize for a series of studies on many-exciton complexes in semiconductors.

A. A. Rogachev belonged to the category of scientists, never very large, which combine the rich talent of a theoretician with the skills of a true experimentalist. He was a harmoniously educated, brilliant, and fascinating person, who succeeded in generating a unique creative atmosphere in his laboratory and uniting quite a number of able scientists around him. He was not only an unquestionable leader in his team but a pioneer in establishing a whole new direction in the physics of many-electron systems as well. The scientific school founded by him presently occupies a well-deserved place in world science. Aleksandr Rogachev loved

1063-7826/00/3404-0493$20.00 © 2000 MAIK "Nauka/Interperiodica"

music, had an intimate understanding of art, and was a sparkling and witty companion. Friends and colleagues often visited him just to talk about science and life in general. His intellect, charm, and power of logic were attractive to others. His unique contributions to science are well recognized by the world scientific community.

In appreciation of his scientific contributions, Aleksandr Rogachev was selected by the Editorial Board of the International Biographical Center (Cambridge, UK) as one of *2000 Outstanding Intellectuals of the 20th Century* and *2000 Outstanding Scientists of the 20th Century* and by the Board of Directors of the American Biographical Institute as one of the *1000 World Leaders of Influence*. He was also nominated by the ABI as the *1999 Man of the Year*, and by the IBC, as the *International Man of the Millennium.*

Aleksandr Rogachev will long be remembered by those who were privileged to be his friends and colleagues.

Zh. I. Alferov, P. D. Altukhov,
V. V. Afrosimov, V. S. Bagaev,
D. A. Varshalovich, B. A. Volkov,
I. V. Grekhov, A. G. Zabrodskiĭ,
B. P. Zakharchenya, V. A. Zayats,
Yu. V. Kopaev, V. I. Korol'kov, P. S. Kop'ev,
E. P. Mazets, G. V. Mikhaĭlov,
E. V. Ostroumova, R. V. Parfen'ev, V. I. Perel',
M. P. Petrov, Ya. E. Pokrovskiĭ,
N. I. Sablina, N. N. Sibel'din,
V. I. Stepanov, R. A. Suris, and V. B. Timofeev

Translated by G. Skrebtsov